
Insights into binary black hole formation from gravitational waves

Simon Stevenson, MPhys

Submitted in fulfilment of the requirements
for the Degree of Doctor of Philosophy

School of Physics & Astronomy
University of Birmingham

May 2017

© S. Stevenson 2017



UNIVERSITY OF
BIRMINGHAM

UNIVERSITY OF
BIRMINGHAM

University of Birmingham Research Archive

e-theses repository

This unpublished thesis/dissertation is copyright of the author and/or third parties. The intellectual property rights of the author or third parties in respect of this work are as defined by The Copyright Designs and Patents Act 1988 or as modified by any successor legislation.

Any use made of information contained in this thesis/dissertation must be in accordance with that legislation and must be properly acknowledged. Further distribution or reproduction in any format is prohibited without the permission of the copyright holder.

Abstract

On the 14th September 2015 the Advanced Laser Interferometer Gravitational-wave Observatory (LIGO) made the first direct detection of gravitational waves from merging stellar mass binary black holes during its first observation run (O1). The signal, GW150914, originated from the merger of two $\sim 30M_{\odot}$ black holes over a billion light years from the Earth. GW150914 heralded the beginning of a new era of astronomy; gravitational wave astronomy. GW150914 was followed by a second confident detection of gravitational-waves from a lower mass merging binary black hole GW151226. Additionally, a statistically less significant binary black hole merger candidate LVT151012 was observed. A fourth likely binary black hole merger GW170104 was recently detected.

Gravitational-waves provide a unique probe of the stellar remnants—black holes and neutron stars—left behind at the end of massive stars lives. As LIGO and other ground based gravitational-wave detectors continue to observe the universe, they will begin to uncover a population of these binary black holes, which may have formed through the isolated evolution of two massive stars. Already, gravitational-waves have: demonstrated the existence of binary black holes which merge within the age of the universe; provided evidence for stellar mass black hole masses in the broad range $5\text{--}40M_{\odot}$; and have empirically constrained the merger rate to be $9\text{--}240\text{ Gpc}^{-3}\text{ yr}^{-1}$. These place significant constraints on population models.

Here we develop Compact Object Mergers: Population Astrophysics and Statistics (COMPAS). COMPAS is a platform incorporating astrophysical modelling tools and statistical analysis tools to extract information from the population of merging binary black holes we observe, and offer insights into binary black hole formation.

In this thesis we present the rapid population synthesis element of COMPAS. We use it to show that all three (assuming LVT151012 is real) presently observed binary black holes are consistent with formation through a single evolutionary channel – classical isolated binary evolution channel via a common-envelope. We show all three events could have formed in low-metallicity environments ($Z = 0.001$) from progenitor binaries with typical total masses $\gtrsim 160M_{\odot}$, $\gtrsim 60M_{\odot}$ and $\gtrsim 90M_{\odot}$, for

GW150914, GW151226, and LVT151012, respectively.

We also show how in principle the masses and rate of observed signals can be used to distinguish between a suite of such population synthesis models. Population synthesis models predict differing mass distributions and merger rates for different astrophysical assumptions about the evolution of massive binary stars, many of which are highly uncertain. These include effects such as supernova kick velocities, parameters governing the energetics of common envelope evolution and the strength of stellar winds. Using a suite of publicly available population synthesis models, we show that observing multiple binary black hole systems through gravitational waves will allow us to infer details of the astrophysical mechanisms that lead to their formation.

We then extend this to show how using measurements of the spin-orbit misalignments in binary black holes can yield information about their formation, whether it be through isolated binary evolution or through dynamical interactions in dense stellar environments. These formation channels leave imprints on the alignment of the black holes spins with respect to orbital angular momentum. Gravitational waves from these systems directly encode information about the spin-orbit misalignment angles, allowing them to be (weakly) constrained. Identifying sub-populations of spinning binary black holes will inform us about compact binary formation and evolution. We simulate a mixed population of binary black holes with spin-orbit misalignments modelled under a range of assumptions. We then develop a hierarchical analysis and apply it to mock gravitational-wave observations of these populations. Assuming a population with spins of $\chi \sim 0.7$, we show that with tens of observations it will be possible to distinguish the presence of subpopulations of coalescing binary black holes based on their spin orientations. With 100 observations it will be possible to infer the relative fraction of coalescing binary black holes with isotropic spin directions (corresponding to dynamical formation) with a fractional uncertainty of $\sim 40\%$. Meanwhile, only ~ 5 observations are sufficient to distinguish between extreme models—all binary black holes either having exactly aligned spins or isotropic spin directions.

Finally, we apply this methodology to the existing O1 observations of binary black hole mergers GW150914, LVT151012, GW151226 and GW170104. If binary black hole spin magnitudes extend to high values, as is suggested by observations of black hole X-ray binaries, we show that the data already exhibit a 2.4σ preference for an isotropic angular distribution. The existing preference for either an isotropic spin distribution or low spin magnitudes for the observed systems will be confirmed (or overturned) confidently in the near future by subsequent observations.

Contents

Abstract	i
List of Figures	v
List of Tables	viii
Acknowledgments	x
Declaration	xii
1 Introduction	1
1.1 Observation of gravitational-waves from a merging binary black hole	1
1.2 Isolated Binary Evolution	5
1.2.1 Initial distributions	5
1.3 (massive) Stellar evolution	7
1.4 Stellar winds	10
1.4.1 Luminous Blue Variables (LBVs)	11
1.4.2 Wolf Rayet	12
1.4.3 Magnetic fields and rotation	12
1.5 Supernovae	12
1.5.1 Observations	13
1.5.2 Initial-final mass relation	16
1.5.3 Pre-supernova orbital characteristics	18
1.5.4 Post-supernova orbital characteristics	21
1.5.5 Post-supernova semi-major axis	22
1.5.6 Post-supernova eccentricity	23
1.5.7 Post-supernova orbital tilt	24
1.6 Mass transfer	25
1.7 Common envelope	33
1.8 Post-Newtonian evolution	35

1.9	Alternate Formation Channels	42
1.9.1	Dynamical formation	42
1.9.2	(Quasi)-Chemically homogenous evolution	44
1.9.3	Population III binaries	44
1.9.4	Primordial black holes	45
1.9.5	Merger of a fragmented core inside a star	46
1.10	Thesis overview and key results	46
2	Formation of the first three gravitational-wave observations through isolated binary evolution	48
2.1	Introduction	50
2.2	Methods	51
2.2.1	COMPAS population synthesis code	51
2.3	Results	54
2.3.1	Forming GW151226 and LVT151012	54
2.3.2	Typical evolutionary pathway of GW151226	57
2.4	Discussion	58
3	Distinguishing compact binary population synthesis models using gravitational wave observations of coalescing binary black holes	65
3.1	Introduction	67
3.2	Compact binary formation and evolution	71
3.2.1	General overview	71
3.2.2	Detailed binary evolution models	73
3.3	Predicted observed distributions	77
3.3.1	Detectability	78
3.3.2	Cosmological effects	80
3.3.3	Detection rate and distance distribution	82
3.3.4	Estimating and Including Measurement Errors	85
3.4	Combining Measured Rates and Chirp Masses	88
3.5	Observing Scenarios	90
3.6	Results: Distinguishing binary black hole (BBH) Formation Models	92
3.6.1	First Advanced LIGO (aLIGO) observing run (O1)	92
3.6.2	Stellar winds	94
3.6.3	Second aLIGO observing run (O2)	94
3.7	Summary and future work	97

4	Hierarchical analysis of gravitational-wave measurements of binary black hole spin–orbit misalignments	105
4.1	Introduction	107
4.2	BH spin misalignment models	109
4.2.1	Mass and spin magnitude distribution	110
4.2.2	Models for spin–orbit misalignment distributions	112
4.2.3	Precession and spin–orbit resonances	116
4.3	Gravitational-wave parameter estimation	116
4.3.1	Signal analysis and inference	116
4.3.2	Previous studies	119
4.4	Hierarchical analysis for population inference	121
4.5	Results	123
4.5.1	Perfect measurement accuracy	123
4.5.2	Realistic measurement accuracy	125
4.5.3	Dependence on number of observations	128
4.6	Discussion and conclusions	133
5	Distinguishing Spin-Aligned and Isotropic Black Hole Populations With Gravitational Waves	136
5.1	Gravitational Wave Spin Measurements and Model Selection	138
5.1.1	Future Spin Measurements	142
5.2	Discussion	143
5.3	Effective Spin and Spin Magnitude Distributions	146
5.4	Mixture model	148
5.5	Hierarchical Modelling	149
5.5.1	Order of Magnitude Calculation	150
5.5.2	Accumulation of evidence	151
5.6	Effect of small spin magnitudes	152
5.7	Mass Ratio	152
5.8	Approximations in the Gravitational Waveform	154
5.9	Precision of χ_{eff} measurements	155
6	Conclusions, outstanding problems, avenues of future research.	157

List of Figures

1.1	Numerical relativity waveform for GW150914	2
1.2	LIGO sensitivity curves at the time of GW150914	3
1.3	The Initial Mass Function	6
1.4	Main-sequence lifetimes of massive stars	8
1.5	Radius as a function of time for a 15 solar mass star	9
1.6	Maxwellian natal kick distribution	15
1.7	COMPAS initial-final mass relation	17
1.8	Pair instability and pulsational pair instability core-remnant mass relations	18
1.9	Solving Kepler's equation	20
1.11	Supernova kick geometry	23
1.12	Orbital tilt as a function of dimensionless kick	26
1.13	Slice through the Roche potential	27
1.14	Contour plot for the Roche potential	28

1.15	Eggleton approximation to Roche lobe radius	29
1.16	Time until merger due to emission of gravitational waves	36
1.17	Geometry of binary black hole spins	37
1.18	Final distribution of $\Delta\Phi$ demonstrating post-Newtonian spin-orbit resonances	41
2.1	Masses of binary black holes observed by aLIGO and their progenitors.	55
2.2	Typical evolution of BBH progenitors.	59
2.3	Formation of GW151226	60
3.1	Horizon distance for early aLIGO	81
3.2	Detectable binaries in comoving distance	84
3.3	Measurement uncertainty on chirp mass for early aLIGO	87
3.4	Dominik <i>et al</i> 2012 chirp mass distributions	100
3.5	Posterior after O1	101
3.6	Posterior as a function of time	102
3.7	Combined posterior after O2	103
3.8	Rates and mass only posteriors after O2	104
4.1	Binary black hole spin–orbit misalignment model distributions . . .	114
4.2	Binary black hole spin–orbit misalignment model injections	115

4.3	Marginalised posterior for $\cos \theta_1, \cos \theta_2$	118
4.4	Dirichlet prior on hyperparameters	124
4.5	Triangle plot of posterior on hyperparameters assuming perfect measurement accuracy	126
4.6	Triangle plot of posterior on hyperparameters with realistic measurement accuracy	127
4.7	Example mock posterior distribution for $\cos \theta_1, \cos \theta_2$	129
4.8	Marginalised posterior on the fraction of dynamically formed binary black holes	130
4.9	Marginalised posterior on the combined aligned fraction of binary black holes	131
5.1	Approximate χ_{eff} posteriors from O1	139
5.2	χ_{eff} models	141
5.3	Model selection using χ_{eff}	142
5.4	Odds ratio predictions for O2	144
5.5	Spin magnitude distributions	147
5.6	Posterior on isotropic fraction	148
5.7	Effect of small spins	153
5.8	Effect of mass ratio on χ_{eff}	154
5.9	Precision of χ_{eff} measurements	156

List of Tables

1.1	Critical mass ratios from Claeys <i>et al</i> 2014	32
3.1	Summary of population synthesis models from Dominik <i>et al</i> 2012 .	74
3.2	Predicted merger and detection rates.	91
5.1	Accumulation of evidence for isotropic distribution	152

Acknowledgments

Thank you to everyone who has helped and guided me through my life so far. Whether academically or personally, without you I would not be where I am today, and would not get to go where I am going tomorrow. My achievements, and this thesis, are as much yours as they are mine.

Funding for my PhD studies comes from STFC and the University of Birmingham.

Mum, thank you for always supporting me in my everything I do. It means the world to me. Dad, thank you for loving science fiction, even if you don't understand my science fact. Also thanks for being my personal taxi driver/delivery man!

Nathan you are the best brother and friend I could ever ask for. Maybe when I'm done with this thesis, I will have time to finish a few more Final Fantasy games to catch up with you.

I owe special thanks to my late Nan for always believing in me, and encouraging me to go as far as I could.

Thank you to the rest of my family and friends.

I would like to thank the other academics and teachers who have guided me along the way, and hopefully will continue to guide me in the future. I'm sorry if I forgot your name. Selma de Mink, Will Farr, John Veitch, Alberto Vecchio, Conor Mow-Lowry, Andreas Freise, Steve Fairhurst, Frank Ohme, Patrick Sutton, Christopher Berry, Ben Farr; thank you all.

Ilya Mandel, my supervisor, mentor, fellow scientist, therapist, friend. Thank you for being an incredible supervisor; you always have the answer (to within an order of magnitude), and it always fits on the back of an envelope.

To my fellow University of Birmingham PhD students—Alejandro Vigna-Gómez, Jim Barrett, Coenraad Neijssel, Serena Vinciguerra, Sebastian Gaebel, Hanah Middleton, Daniel Töyrä, Anna Green, Sam Cooper, Ben Bradnick, Janna Goldstein, Siyuan Chen—I say thank you, and wish you all good luck.

To those who paved the way ahead of me—Carl Johan-Haster, Maggie Lieu, Sarah Mulroy, Kat Grover—thank you for your guidance and your friendship.

Thank you to Jo Cox for organising a bunch of disorganised physicists. To David Stops, thank you for all of your work, help and patience ensuring our computers do what they're supposed to do most of the time.

Thank you to Lewis Powell for accepting me, and for putting on headphones when playing on the PlayStation whilst I was writing this thesis.

Lastly, the love of my life, my wife, Jade Powell. You are my best friend, I have been so much happier as a person since we have been together. Jade, thank you, I love you.

Declaration

I, Simon Stevenson, confirm that the work in this thesis is my own. Chapter 1 gives an introduction to binary black hole formation. Appropriate references have been given for figures and information from other sources.

Chapter 2 reproduces the text of Stevenson *et al.* [1], published in Nature Communications, with permission from the journal. It introduces the rapid population synthesis element of COMPAS. This work was conducted in collaboration with Alejandro Vigna-Gómez, Ilya Mandel, Jim W. Barrett, Coenraad J. Neijssel, David Perkins and Selma E. de Mink. The code, analysis and text were written by Simon Stevenson. The text was edited by all authors. Figure 2.1 was made by Simon Stevenson. Figure 2.2 was made by Alejandro Vigna-Gómez. Figure 2.3 was made by Coenraad J. Neijssel.

Chapter 3 reproduces the text of Stevenson *et al.* [2], published in ApJ, with permission of the journal. This work was conducted in collaboration with Frank Ohme and Stephen Fairhurst. Simon Stevenson performed the analysis, made the figures and wrote the text. Frank Ohme performed the horizon distance and fisher matrix calculations, and made Figures 3.1, 3.2 & 3.3. All authors edited the text.

Chapter 4 introduces an hierarchical analysis for gravitational-wave measurements of binary black hole spin-orbit misalignments. It reproduces the text of Stevenson *et al.* [3], submitted to the Monthly Notices of the Royal Astronomical Society. This paper may undergo additional editing before publication. This paper is the result of collaboration with Christopher Berry and Ilya Mandel. The code, and text of the paper were written by Simon Stevenson. The analysis was performed by Simon Stevenson. All plots were made by Simon Stevenson. The text was edited by all authors.

Chapter 5 reproduces the text of Farr *et al.* [4], submitted to Nature. The work is the result of a collaboration with Will M. Farr, M. Coleman Miller, Ilya Mandel, Ben Farr and Alberto Vecchio. Simon Stevenson and Will M. Farr both performed the analysis. Simon Stevenson made preliminary versions of Figures 5.1, 5.2 and 5.3. Simon Stevenson wrote sections 5.4 and 5.6 and made Figures 5.6 and 5.7. Ben Farr wrote section 5.9 and made Figure 5.9. All other Figures made by Will M. Farr. The text of the paper was written by Will M. Farr. All Authors edited the text.

The conclusions in Chapter 6 are entirely my own. Any errors in the text are entirely my own.

Chapter 1

Introduction

1.1 Observation of gravitational-waves from a merging binary black hole

Gravitational waves were first predicted by Einstein [5, 6] as a prediction of his theory of General Relativity in 1916. One hundred years later, on the 14th September 2015 the Advanced Laser Interferometer Gravitational-wave Observatory (LIGO) made the first direct detection of gravitational waves from merging stellar mass binary black holes during its first observation run (O1) [7, 8].

Advanced LIGO operates twin Michelson interferometers at Hanford, Washington (H1) and Livingston, Louisiana (L1), each with $L = 4$ km arms. These interferometers measure the dimensionless gravitational-wave strain $h = \Delta L/L$, projected onto the detector, as a change in the arm length ΔL .

The peak dimensionless gravitational-wave strain for GW150914 was $\sim 1 \times 10^{-21}$. The signal, GW150914 [7], originated from the merger of two $\sim 30M_{\odot}$ black holes at a distance of ~ 500 Mpc from the Earth [7, 9, 10], and was detected by both Advanced LIGO detectors at high confidence $> 5\sigma$. A numerical relativity calculation of the gravitational-waveform for GW150914 is shown in Figure 1.1 for illustration. One can see the three stages of the signal; the inspiral, merger and ringdown.

The signal is referred to as GW150914; in this thesis we often use the event name to refer to progenitors of the event, as well as the event itself. The observation of GW150914 heralded the beginning of a new era of astronomy; gravitational wave astronomy.

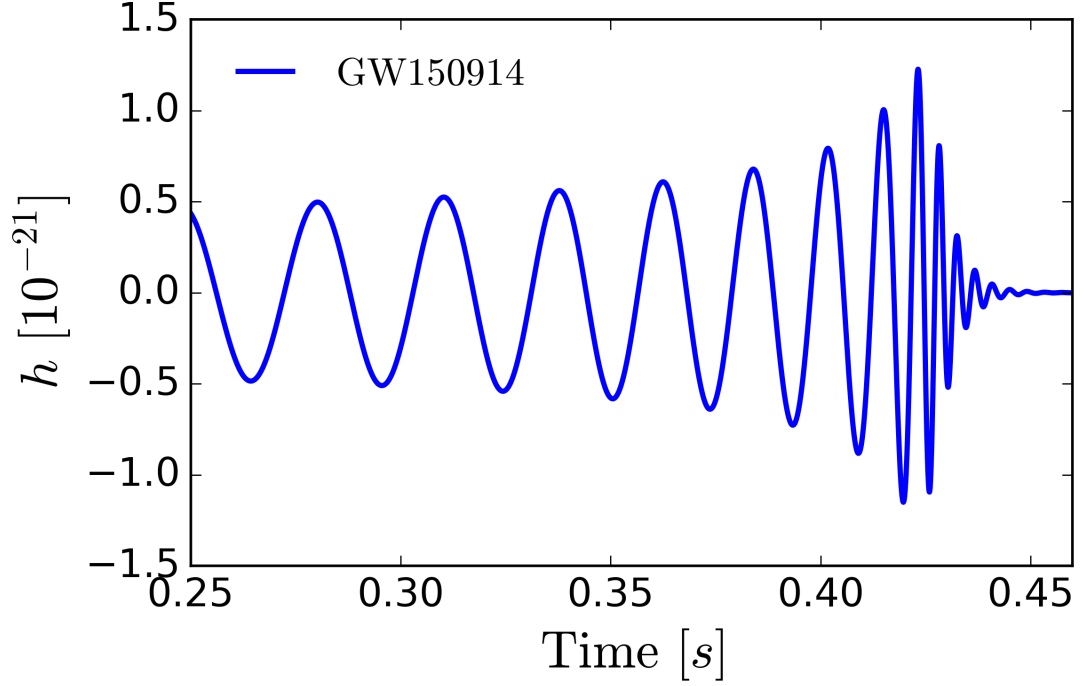


Figure 1.1: Best fitting unwhitened numerical relativity waveform for GW150914 [7] projected onto the LIGO Hanford detector (H1). The y-axis shows the dimensionless strain h as a function of time. Times are shown relative to September 14, 2015 at 09:50:45 UTC. Data downloaded from the LIGO Open Science Center (LOSC) at <https://losc.ligo.org/events/GW150914/>

The sensitivity of the LIGO detectors at the time GW150914 was observed is shown in Figure 1.2. There is also a British-German run GEO detector [11, 12]. The Italian-French Virgo [13] will soon join the LIGO detectors beginning the start of a global network of gravitational-wave observatories [14]. In the future, additional detectors will join this network, including a LIGO detector in India [15], the Japanese KAGRA [16] and eventually the Einstein Telescope [17, 18].

Although ground-based gravitational-wave observatories may detect gravitational-waves from many different astrophysical sources, here we focus on binary black holes due to the existing observations.

GW150914 was followed by a second confident detection of gravitational-waves

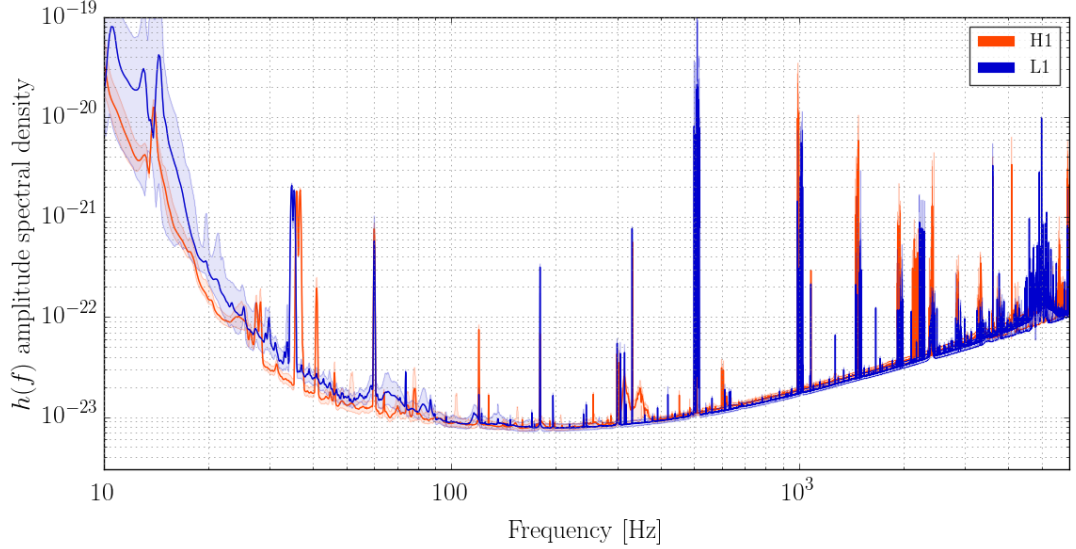


Figure 1.2: The amplitude spectral density for LIGO Hanford (H1) in red and LIGO Livingston (L1) in blue at the time of GW150914 [7]. The solid traces represent the median sensitivity and the shaded regions indicate the 5th and 95th percentile over the analysis period. The narrowband features in the spectra are due to known mechanical resonances, mains power harmonics, and injected signals used for calibration. Data downloaded from the LIGO Open Science Center (LOSC) at <https://losc.ligo.org/events/GW150914/>

from a lower mass merging binary black hole GW151226 [19] on the 26th December 2015 (Boxing Day). The chirp mass—a well measured combination of the component black hole masses m_1 and m_2 —is given by

$$\mathcal{M} = \frac{(m_1 m_2)^{3/5}}{(m_1 + m_2)^{1/5}}. \quad (1.1)$$

GW151226 has a chirp mass of $\sim 9M_\odot$ [19, 8].

A black holes' spin angular momentum \mathbf{S} is characterised by its dimensionless *spin* a as

$$a = \frac{c}{Gm^2} |\mathbf{S}|, \quad (1.2)$$

bounded by $0 \leq a < 1$ for a black hole of mass m . One of the black hole spins in GW151226 was determined to be > 0.2 at 99% confidence [19].

GW170104 [20] was the third confident binary black hole merger observed by the Advanced LIGO detectors, demonstrating the existence of a population of merging binary black holes in nature with a broad range of masses.

Additionally, a statistically less significant binary black hole merger candidate

LVT151012 was observed [21, 8] with an $\sim 86\%$ probability of astrophysical origin [8].

Gravitational-waves provide a unique probe of the stellar remnants—black holes and neutron stars—left behind at the end of massive stars lives. As LIGO and other ground based gravitational-wave detectors continue to observe the universe, they will begin to uncover a population of these binary black holes, which may have formed through the isolated evolution of two massive stars. Already, gravitational-waves have: demonstrated the existence of binary black holes which merge within the age of the universe; provided evidence for stellar mass black hole masses in the broad range $5\text{--}40M_{\odot}$; and have empirically constrained the merger rate to be $9\text{--}240\text{ Gpc}^{-3}\text{ yr}^{-1}$ [22, 23, 8]. These place significant constraints on population models.

In this thesis we present methods for using the measured masses and spins of binary black holes, along with their merger rate, to constrain models of their formation. We give an overview of this work in the next section. Since the work we present here appeared, there has been further work extending some of the studies we carry out. Zevin *et al.* [24] use a hierarchical modelling approach to show that one can infer the fraction of binary black holes forming through isolated binary evolution from the chirp mass distribution alone, improving on the study we present in Chapter 3. Talbot & Thrane [25] expand on the work we present here in Chapter 4 in determining the population of binary black hole spins using gravitational waves.

We have restricted our focus to the near future, and the insights that can be gained from the current generation of ground-based gravitational-wave detectors. The binary black hole masses and merger rates implied by the detection of GW150914 [7, 22] suggest some binary black holes will be detectable with (e)LISA [26] years before coalescing in the frequency band of ground based detectors. At these frequencies, binary black holes may retain residual eccentricity. Since different formation scenarios (above) predict different eccentricity distributions, this may provide an additional parameter with which to distinguish between formation scenarios [27, 28, 29].

1.2 Isolated Binary Evolution

Isolated binaries—systems containing two stars in a bound orbit—are those binaries which don’t interact with any other stars in their lifetimes. Isolated binary evolution describes the co-evolution of the two stars from birth (section 1.2.1) to death and beyond. Isolated binary evolution has been discussed as a promising channel for the formation of binary black holes for over 40 years [30, 31, 32, 33, 34, 35, 36, 1]. In the following sections we review some of the key processes involved in isolated binary evolution required for the formation of a binary black hole, and discuss the current major uncertainties. This is not meant to be an exhaustive discussion of the impacts of the uncertainties in each ingredient on predictions for binary black holes (which are discussed in greater detail in the later chapters). Instead, here we introduce each ingredient, and give some basic background that is omitted in the later chapters.

1.2.1 Initial distributions

The fate of an individual isolated binary is approximately determined by its initial conditions, such as the masses of the stars, the orbital period (or equivalently semi-major axis) and the orbital eccentricity, along with additional parameters such as the strength of the magnetic field and the stellar rotation rate. The distributions of these quantities therefore affects the resulting distribution of binary black holes [37]. It has often been assumed (for simplicity) that these distributions are separable, but recent observations have shown that they are correlated [38].

Stars are thought to form with the distribution of their masses given according to the initial-mass-function (IMF) [39]:

$$\frac{dN}{dM} = M^{-\alpha}, \quad (1.3)$$

where N is the number of stars, M is the mass of a star in solar masses and α is the

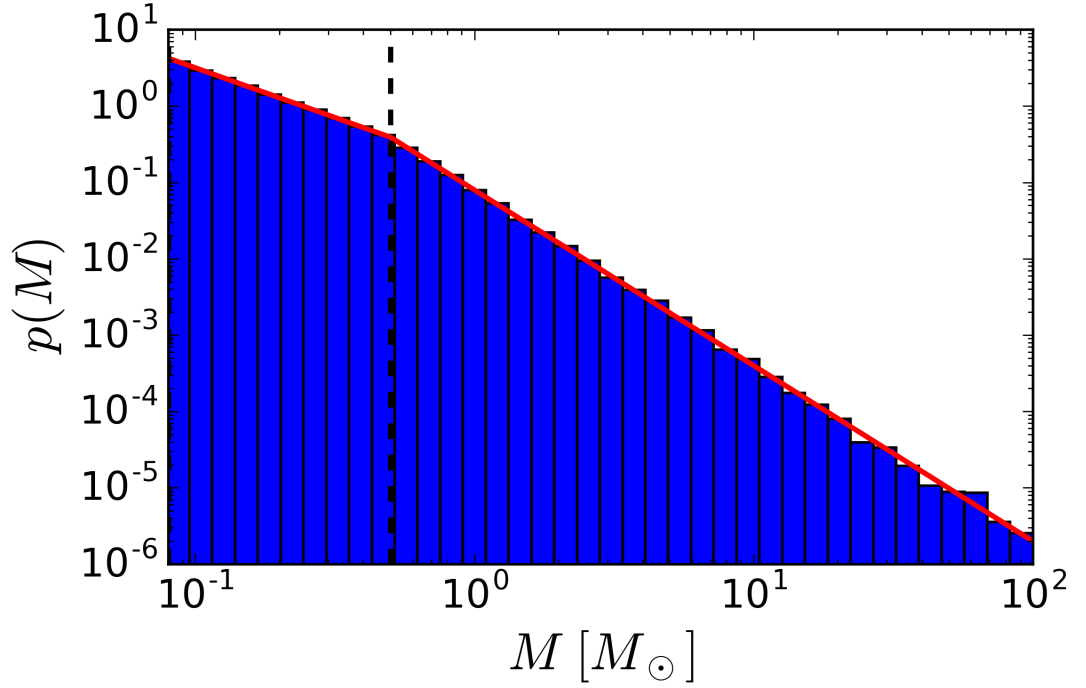


Figure 1.3: The red line shows the probability density function of the Kroupa [40] IMF. The blue histogram shows Monte Carlo samples from this distribution. The dashed vertical black line shows the break in the power law at $0.5M_\odot$ as given in Equation 1.4

power law slope. In this thesis we use the apparently universal Kroupa [40] IMF

$$\alpha = \begin{cases} 0.3, & \text{for } M < 0.08 \\ 1.3, & \text{for } M \in [0.08, 0.5] \\ 2.3, & \text{for } M > 0.5 \end{cases} \quad (1.4)$$

The mass ratio distribution in binaries is typically assumed to be flat [41, 37] i.e.

$$p(q) = 1, \text{ for } q \in [0, 1]. \quad (1.5)$$

Orbital separations a are typically assumed to be drawn from a distribution that is flat in the log [42], i.e.

$$p(a) \propto \frac{1}{a}. \quad (1.6)$$

Binaries with orbital periods less than about 10 years will interact and exchange mass during their lives. Sana *et al.* [41] find a preference for close interacting massive binaries, with around 70% of massive binaries exchanging mass with a companion.

The thermal eccentricity distribution, expected for a thermalised system [43], is given by

$$p(e) = 2e. \quad (1.7)$$

Sana *et al.* [41] instead find an eccentricity distribution for massive stars which heavily favours circular systems.

The overall fraction of stars in binaries (the *binary fraction*) determines the importance of binary interactions for stellar populations. The fraction of stars in binaries (or higher multiples, multiplicity) appears to be a function of the mass of the primary [42, 44, 41, 45, 46]. For massive O-type binaries Sana *et al.* [41] find a binary fraction of around 70%.

All of these observations are made locally, either of stars within our own Galaxy, or of stars in the nearby Magellanic clouds. These environments cover a relatively small range of metallicities from solar [47] down to one quarter of solar. Many predictions of binary black hole formation find the need for formation in much lower metallicity environments than this [e.g., 1]. This means that all simulations are assuming that the initial distributions observed locally can be extrapolated to much lower metallicities.

1.3 (massive) Stellar evolution

Stars support themselves against gravitational collapse by fusing elements in their core, primarily hydrogen to helium on the main sequence. For a review of massive stellar evolution see Woosley *et al.* [48]. In this thesis we are mostly interested in massive stars, those with zero-age main-sequence masses $\gtrsim 8M_{\odot}$ that will end their lives as compact objects—neutron stars and black holes. Massive stars live fast and die young; the lifetime of massive stars asymptotes to ~ 3 million years for masses above $\sim 30M_{\odot}$. We show the main-sequence lifetimes for massive stars with zero-age main-sequence masses $0.1\text{--}300M_{\odot}$ at solar metallicity calculated using MIST [49] in Figure 1.4. Stellar models are often computed using 1D stellar evolution codes [e.g., MESA 50, 51, 52]. These models often neglect potentially important effects such as magnetic fields and rotation. Recently stellar models have begun to include the effects of moderate rotations [53, 54, 49].

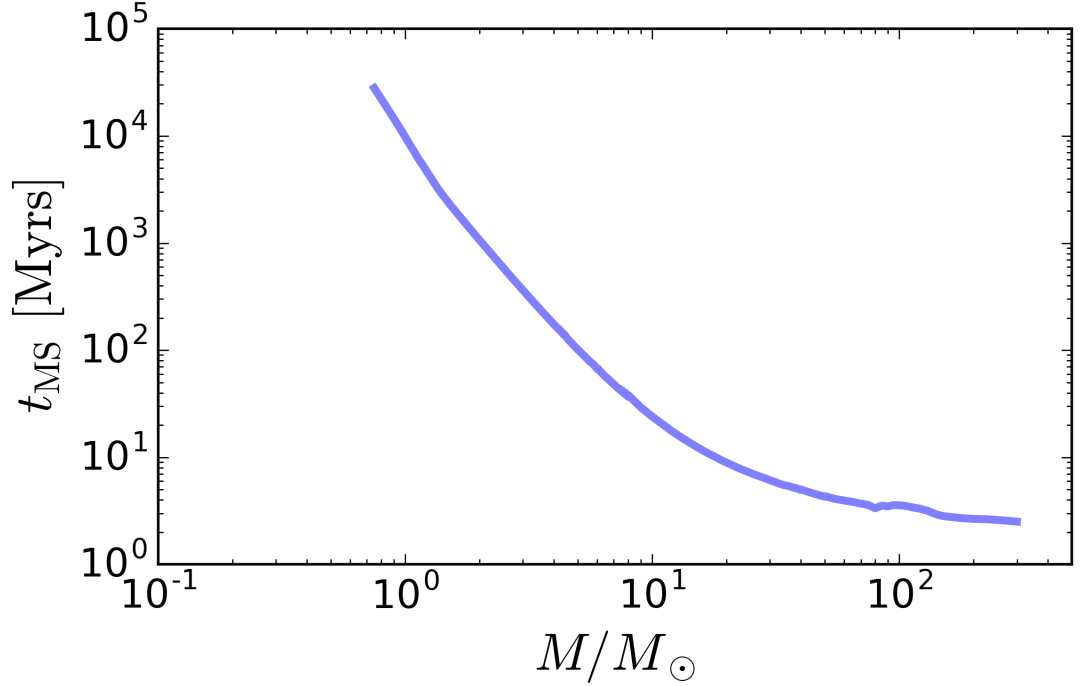


Figure 1.4: Main-sequence lifetimes t_{MS} in Myrs of massive stars with zero-age main-sequence masses M in the range $1 - 300M_{\odot}$ at solar metallicity ($Z = 0.014$ [47]) calculated using the 1D stellar evolution code MESA [50, 51, 52] and interpolated with MIST [49].

In Figure 1.5 we show the evolution of a typical slowly rotating $15M_{\odot}$ star from Choi *et al.* [49] at two representative metallicities Z_{\odot} and $0.1Z_{\odot}$. We see that the radius of stars can increase by up to two orders of magnitude over their lifetimes as they evolve off of the main sequence. It is also important to realise that lower metallicity stars are more compact (i.e. have a smaller radius for a given mass). This has important effects in binary evolution that we discuss further in Chapter 2.

To be used in a rapid binary evolution population synthesis code such as COMPAS, one must be able to evolve each star accurately and efficiently, since large populations of millions of binaries are typically evolved. This makes solving actual stellar evolution in this context prohibitively computationally expensive, and one must use a grid of pre-computed models (as a function of initial parameters such as zero-age main-sequence mass and metallicity). In COMPAS we employ the interpolated models of non-rotating single stellar evolution as a function of mass and metallicity from Hurley *et al.* [55] based on the original models of Pols *et al.* [56]. We note that the original grid of single star models extends only to 50 solar masses. We extrapolate above this limit to 100 solar masses, as described in Hurley *et al.*

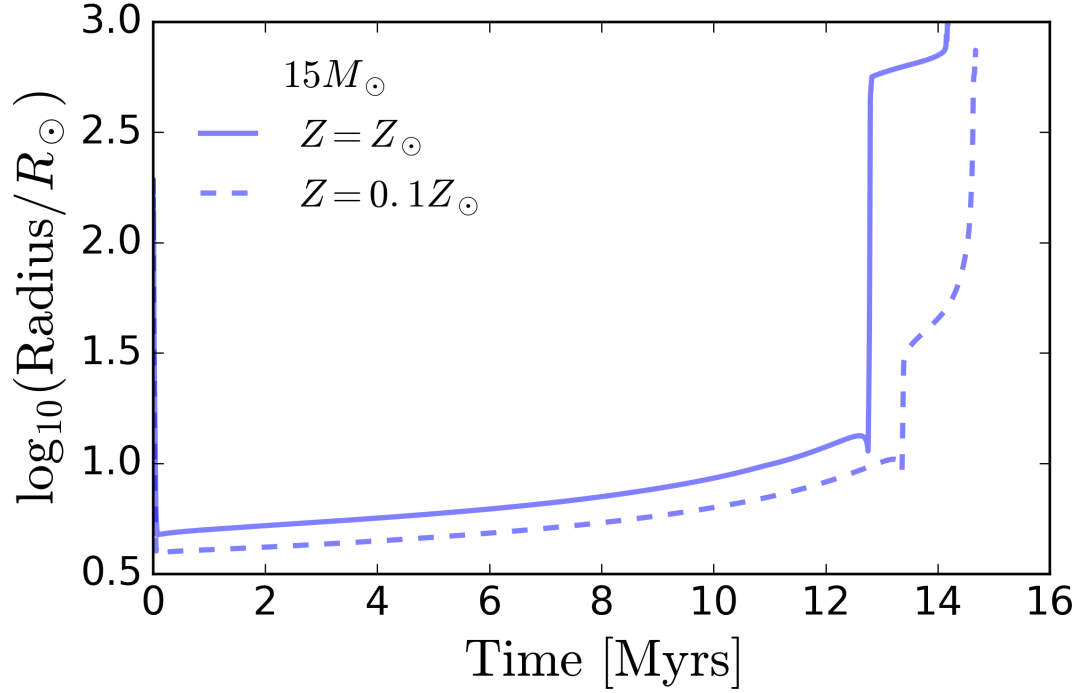


Figure 1.5: Radius as a function of time for a $15 M_{\odot}$ star at Z_{\odot} and $0.1Z_{\odot}$. Stars calculated using the 1D stellar evolution code MESA [50, 51, 52] and interpolated with MIST [49]

[55].

We note that these models used solar scaled abundances; i.e. $Z = fZ_{\odot}$ where f is some multiplicative constant. This need not be the case in reality.

There are additional uncertainties regarding convective overshooting, semiconvection, the duration of the main sequence, the presence or absence of blue loops, and the existence of luminous red supergiants [see 49, for a more detailed discussion]. We do not attempt to deal with these uncertainties further in this thesis.

In the next section (1.4) we describe stellar wind mass loss and the prescriptions used for it in COMPAS.

1.4 Stellar winds

Stars lose mass through their lives through stellar winds [57]. This mass loss is one of the most important processes determining the masses of compact remnants - neutron stars and black holes [e.g. 58, 59]. Stellar winds set the initial-final mass relation (for single stars, see section 1.5.2) and are important for determining final core masses (and thus remnant masses) for stars in binaries. For hot massive stars on the main sequence, stellar winds are primarily radiatively (line) driven [e.g., 60, 61]. Models for stellar wind mass loss rates are calibrated to a variety of observations and simulations. Wind mass loss changes as a function of stellar parameters (such as luminosity, mass and temperature) and depend crucially on the composition (i.e. metallicity) of the star [62]. Here we reproduce the wind mass loss prescriptions employed in COMPAS for the various phases of stellar evolution.

Vink *et al.*

Vink *et al.* [62] calculate mass loss rates for hot massive OB stars as a function of metallicity using Monte Carlo simulations of photon transport in the stellar atmosphere. They provide two formulae for mass loss, one either side of the iron bi-stability jump at effective temperatures of around $T_{\text{eff}} \sim 25000$ K. Typically, mass loss increases with effective temperature (as radiation pressure scales with T_{eff}^4). However, below this temperature, Fe IV ions recombine to Fe III [62, 63, 59], which has a large cross section, increasing the mass loss.

For stars with effective temperatures $12500 \leq T_{\text{eff}}/K \leq 22500$ we use:

$$\begin{aligned} \log(dM/dt)_{\text{OB}} = & -6.688 + 2.210 \log(L/10^5 L_{\odot}) \\ & -1.339 \log(M/30 M_{\odot}) - 1.601 \log(V/2.0) \\ & + 0.85 \log(Z/Z_{\odot}) + 1.07 \log(T_{\text{eff}}/20000 K), \end{aligned} \quad (1.8)$$

with the ratio of wind velocity at infinity to escape velocity $V = v_{\infty}/v_{\text{esc}} = 1.3$ [63].

For stars with $12500 \leq T \leq 25000\text{K}$; and

$$\begin{aligned} \log(dM/dt)_{\text{OB}} = & -6.697 + 2.194 \log(L/10^5 L_{\odot}) \\ & -1.313 \log(M/30 M_{\odot}) - 1.226 \log(V/2.0) \\ & +0.85 \log(Z/Z_{\odot}) + 0.933 \log(T_{\text{eff}}/40000) \\ & -10.92[\log(T_{\text{eff}}/40000)]^2, \end{aligned} \quad (1.9)$$

with $V = 2.6$ for stars with $25000 \leq T \leq 50000\text{K}$.

1.4.1 Luminous Blue Variables (LBVs)

Luminous Blue Variables (LBVs) are massive, luminous stars, which can experience extremely high mass loss rates. In COMPAS we follow Hurley *et al.* [55] in defining an LBV as an evolved star beyond the Humphreys & Davidson [64] limit with luminosity $L/L_{\odot} > 6 \times 10^5$ and $10^5(R/R_{\odot})(L/L_{\odot})^{0.5} > 1.0$. An example of an LBV is Eta Carinae (η Car), which may have lost up to a 10 solar masses in a single eruption [see for e.g., 65].

For these stars the mass loss rate is given as [55]:

$$\left(\frac{dM}{dt}\right)_{\text{LBV1}} = 0.1 \left(10^{-5} \frac{R}{R_{\odot}}\right) \left(\frac{L}{L_{\odot}}^{0.5} - 1\right)^3 \left(\frac{L}{6 \times 10^5 L_{\odot}} - 1\right) M_{\odot} \text{yr}^{-1}. \quad (1.10)$$

Alternatively, following Belczynski *et al.* [63] we use:

$$\left(\frac{dM}{dt}\right)_{\text{LBV2}} = f_{\text{LBV}} \times 10^{-4} M_{\odot} \text{yr}^{-1}, \quad (1.11)$$

with the default value $f_{\text{LBV}} = 1.5$ calibrated to reproduce the most massive known black holes in the galaxy.

Mass loss in the LBV stage may lead to a lack of Red Supergiants (RSG), resolving the so called RSG problem [see 34, and references within].

1.4.2 Wolf Rayet

Wolf-Rayet stars are massive stars which have lost their outer hydrogen envelopes, leaving behind a (naked) helium star. This can occur either through strong stellar winds causing a single star to strip itself, or through stripping in binary interactions. Wolf-Rayet stars are hot ($\log_{10}(T_{\text{eff}}/K) \sim 4$), luminous ($\log_{10}(L/L_{\odot}) \sim 5$) stars, and have high observed mass loss rates of order $10^{-5} M_{\odot} \text{ yr}^{-1}$; we calculate Wolf-Rayet mass loss rates following [66, 67, 68, 55, 69, 63], as:

$$(dM/dt)_{\text{WR}} = 10^{-13} (L/L_{\odot})^{1.5} (Z/Z_{\odot})^{0.86} M_{\odot} \text{ yr}^{-1}, \quad (1.12)$$

which includes the metallicity dependence determined by Vink & de Koter [70].

1.4.3 Magnetic fields and rotation

Along with a dependence on the stage of stellar evolution and the composition (i.e. metallicity) of a star, it seems reasonable that the wind mass loss rate may also depend on other stellar parameters such as the rate of rotation and the strength of the magnetic field. Recently, Petit *et al.* [71] have argued that strong magnetic fields may reduce wind mass loss in a comparable way to low metallicities, allowing for the production of higher mass black holes in solar type environments. It remains to be seen if a black hole exists with such a mass in the Milky Way.

1.5 Supernovae

Stars with zero-age main-sequence masses above $\sim 8M_{\odot}$ end their lives in supernovae [72, 48]. The stars leave behind compact remnants such as neutron stars and black holes.

1.5.1 Observations

Supernovae are classified observationally, primarily into types by their spectra, according to the presence (type II) or absence (type I) of hydrogen emission lines. Some types are further subclassified by features in their lightcurves. These observational types are associated with progenitors of the supernovae.

Type Ia

Supernova Type Ia are thought to involve the thermonuclear explosion of a white dwarf at the Chandrasekhar mass [73, 74], either in a single degenerate system (accreting WD) [75] or in a binary white dwarf merger [76, 77]. Due to their approximately constant mass, supernova type Ia are standard candles with a constant intrinsic luminosity, which has been exploited for cosmological measurements, demonstrating the acceleration in the expansion of the universe [78, 79]. The Type Ia rate can also inform some of the theoretical uncertainties in binary evolution [80]. Double white dwarfs are not binary black hole progenitors, and ground based gravitational wave detectors are not sensitive to gravitational waves from inspiralling double white dwarfs (they typically merge at $f_{\text{GW}} \sim 0.01$ Hz, below the low frequency sensitivity of LIGO) or Type Ia supernovae [although see 81]. We therefore do not consider these systems further in this thesis. However, double white dwarf will be an important gravitational-wave source for space based gravitational-wave detectors [e.g., 82, 83, 84].

Core-collapse supernovae

Here, we are interested in core-collapse supernovae, the violent explosions of massive stars [for a review see 85]. These stars burn up to iron in their cores. At this point, the pressure supporting the star is removed, causing it to collapse. The core of the star collapses to nuclear densities, where the equation of state stiffens. The outer layers then *bounce* off of the core, although this bounce is not sufficient to explode the star. The mechanism responsible for exploding the star is currently unclear (and may depend on the progenitor properties), but may be due to some of the energy in the neutrinos produced being deposited in the outer layers.

Type II-P supernovae are associated with the explosion of red supergiants, and are the most common supernovae [85].

Type Ib/c supernovae are associated with the explosion of Wolf-Rayet or stripped stars, with (Ib) or without (Ic) helium [85]. These stars have been stripped of their hydrogen envelopes through strong stellar winds (see section 1.4) or binary interactions such as mass transfer or common envelope. Type Ic supernovae may be so called “ultra-stripped” supernovae [86, 87, 88, 89], where a helium star (already stripped once through binary interaction) expands and engages in case BB mass transfer and is stripped again, removing most of the helium envelope, leaving behind a naked metal core. Ultra-stripped supernovae may lead to systematically smaller natal kicks.

Some stars which are only just massive enough to go supernova experience electron capture supernovae [90].

The galactic supernova rate is approximately 1 per century [e.g., 91]. This makes studying supernovae in the Milky Way impossible, except in the fortuitous event of a galactic supernova. Supernova surveys such as the Supernova Legacy Survey [92], the Sloan Digital Sky Survey [93] and the Palomar Transient Factory [94] therefore concentrate on other galaxies.

Core collapse supernovae are also bright in neutrinos and gravitational-waves. Neutrinos were observed from supernova 1987A [95]. Gravitational-wave observations of a potential galactic supernova will give us insights into the poorly understood physics of core-collapse supernovae [96, 97]. However, gravitational-waves from supernovae are only detectable at distances within the galaxy [98, 99].

The most massive stars may end their lives silently in failed supernovae; searches for failed supernovae are underway [e.g., 100] and will allow the fraction of massive stars collapsing this way to be constrained observationally.

Black holes may receive natal kicks at birth, in the same way as is determined empirically for neutron stars. Observations of galactic (single) radio pulsars show that the distribution is well described by a Maxwellian distribution [101]; see also earlier work [102, 103, 104].

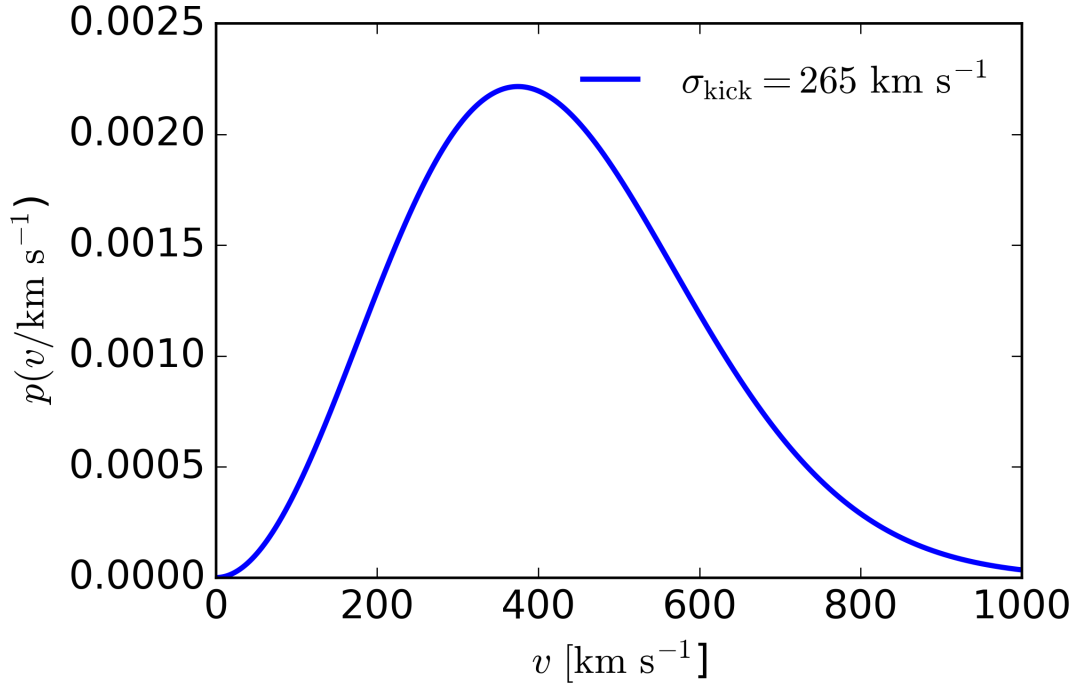


Figure 1.6: Maxwellian natal kick velocity distribution adopted in COMPAS [105].

The probability distribution adopted in COMPAS for the natal kick v is [105]:

$$p(v) = \sqrt{\frac{2}{\pi}} \frac{v^2}{\sigma_{\text{kick}}^3} \exp \frac{-v^2}{2\sigma_{\text{kick}}^2}. \quad (1.13)$$

We show this distribution in Figure 1.6.

Observations of galactic low mass X-ray binaries provides some evidence that some black holes receive kicks of a similar order to neutron stars [e.g., 106, 107, 108, 109, 110, 111].

The distribution of neutron star natal kicks inferred from isolated galactic pulsars is inconsistent with observations of the rates and orbits (periods, eccentricities) of galactic double neutron star systems [e.g., 112].

It is commonly assumed in binary evolution simulations that the angular distribution of supernova kicks is isotropic, i.e. the polar angle θ is given by:

$$p(|\cos(\theta)|) \sim U(-1, 1), \quad (1.14)$$

where $U()$ denotes a uniform distribution, and the final angle ϕ is uniform:

$$p(\phi) \sim U(0, 2\pi). \quad (1.15)$$

1.5.2 Initial-final mass relation

It is possible to relate the initial zero-age main-sequence mass to the final compact object mass for single stars [63, 113]. There is considerable uncertainty in this relation, which translates to uncertainty in the mass distribution of merging binary black holes. In binaries, a simple relation between initial stellar mass is unhelpful since stars can lose or gain mass through mass transfer (see section 1.6). It is therefore more useful to relate the presupernova core mass to any final remnant mass. Whether a star explodes successfully and forms a neutron star, or collapses to form a black hole may be a non-trivial function of initial mass and may depend sensitively on the *compactness* of the pre supernova stellar core [114, 115, 116, 117, 59]

Observationally, there is some evidence for a gap in compact remnant masses between the most massive observed neutron stars [around $2M_{\odot}$ 118, 119] and the lowest mass observed black holes [120, 121]. Gravitational-waves may provide a probe of such a mass gap [2, 122, 123, 124].

In COMPAS we apply the Fryer *et al.* [125] prescription to calculate remnant masses for compact objects from their presupernova core masses.

The COMPAS initial-final mass relation for single stars for metallicities $Z = 0.02$ and $Z = 0.005$ are shown in Figure 1.7.

The apparent dip in Figure 1.7 around a zero-age main sequence mass of $\sim 40M_{\odot}$ at $Z = 0.005$ occurs as single stars above this strip themselves of their hydrogen envelope, and subsequently experience stronger mass loss as a Wolf-Rayet star [63].

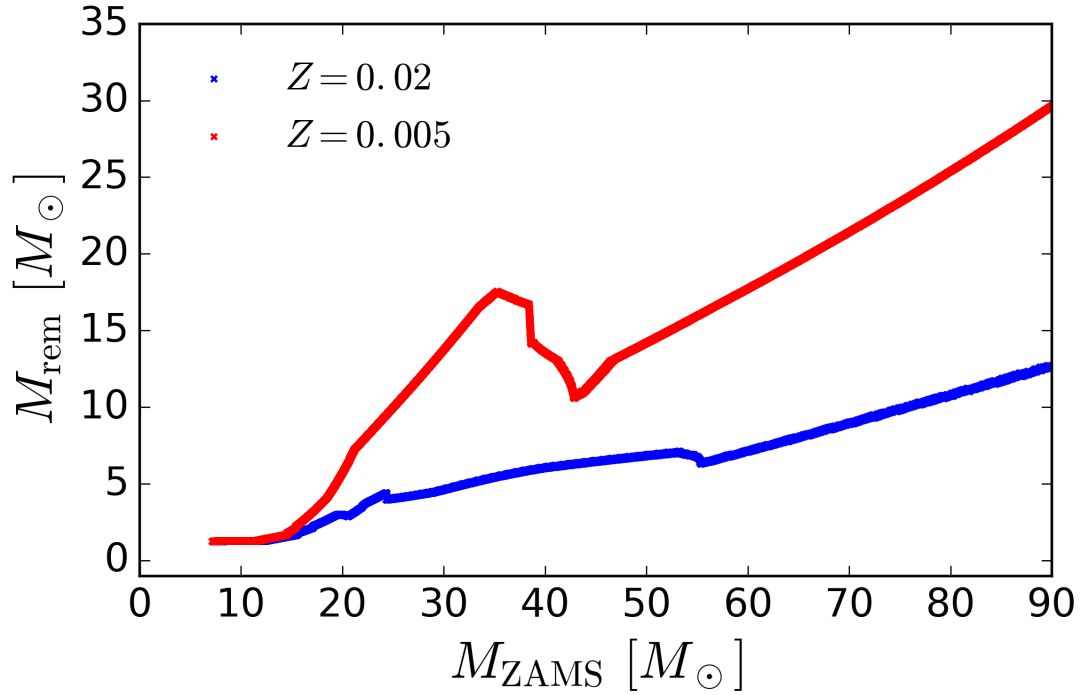


Figure 1.7: Final remnant (compact object) mass M_{rem} as a function of zero-age main-sequence (ZAMS) mass M_{ZAMS} for non-rotating single stars in COMPAS at metallicities $Z = 0.02$ and $Z = 0.005$. Models are calculated using the stellar models of Hurley *et al.* [55], the wind prescriptions of Belczynski *et al.* [63] and the *delayed* supernova prescription from Fryer *et al.* [125].

Pair instability supernovae

Stars with helium core masses in the range $30 - 130 M_{\odot}$ [corresponding to a more uncertain range of zero-age main-sequence masses of approximately $70 - 250 M_{\odot}$ [126]] may experience pair instability in their core, leading to electron-positron pair production towards the end of their lives if the central temperature is $> 7 \times 10^8$ K. This leads to a loss of pressure support for the star, causing it to begin to collapse. This can cause a dramatic increase in the central temperature, sufficient to explosively burn oxygen, releasing enough energy to unbind the entire star, leaving behind no remnant. A variant of this process is called pulsational pair instability [127, 126], and is not energetic enough to completely unbind a star. Instead pulsational pair instability leads to a series of pulses, most likely leading to the removal of any remaining hydrogen envelope. In COMPAS, for pair instability supernovae (and pulsational pair instability) we adopt fits to the data from Tables 1 and 2 of [126] as plotted in Figure 1.8: Pair instability may lead to a second mass gap in the masses of compact objects between $\sim 60 - 130 M_{\odot}$ [128, 129, 130]. As with the first mass gap (described in section 1.5.2), it may be possible to use gravitational-wave

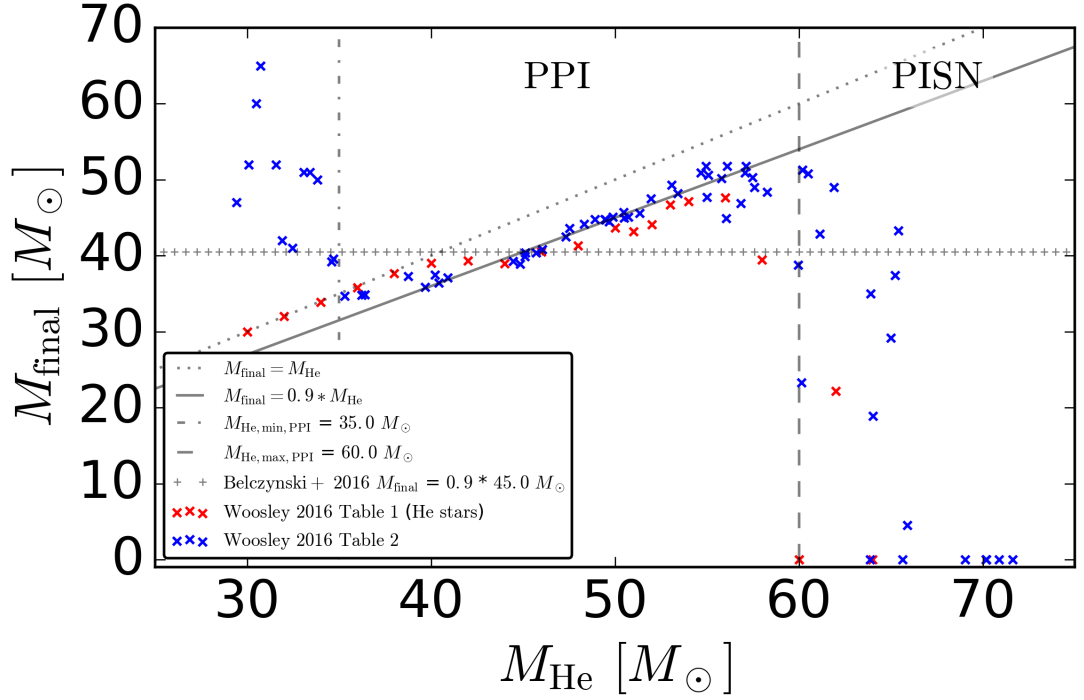


Figure 1.8: Relationship between the helium core mass M_{He} and the final stellar mass M_{Final} for stars experiencing pulsational pair instability and pair instability supernovae. Data taken from [126].

observations to detect the presence or absence of such a mass gap.

1.5.3 Pre-supernova orbital characteristics

This section contains some material from the mid-course assessment “Population synthesis for binary black holes”, Simon Stevenson, 2014.

Supernovae can affect the orbital characteristics (orbit period or equivalently semi-major axis and eccentricity) through natal kicks and mass loss. In a supernova with no kick imparted on the remnant, we recall the classic result [131] that if more than half of the total mass of the system is lost, it will become unbound. However, in addition to mass loss, it is expected that the compact remnant will be born with a kick, which can either act to disrupt the binary, or if directed appropriately, can harden the binary.

Kepler's equation

Here we define the orbit of a binary at the moment of a supernova explosion. Since supernovae occur on timescales much shorter than the orbital timescale (which we don't resolve in our simulations), we assume that supernovae are instantaneous. Since Kepler's 2nd law states *equal times sweep out equal areas of the orbit*, supernovae are more likely when the binary is at apoapsis. We determine the position of the binary in its orbit at random by solving Kepler's Equation. In this section, we denote the variable that describes the point at which the system is at during its orbit as the angle ψ , which is known as the *true anomaly*.

The mean anomaly M ranges from 0 (at periapsis) to 2π , and tells you the angle from periapsis to the position of an imaginary body moving along a circular orbit with the same orbital period P . The mean anomaly, is therefore given by:

$$M = \frac{2\pi t}{P}. \quad (1.16)$$

Since t is defined to be in the range $0 \leq t \leq P$, we draw a random number uniform in 0 to 1, and then multiply the result by 2π . However, what we want is the true anomaly. The mean anomaly is related to the *eccentric anomaly* E using the transcendental Kepler's Equation (not to be confused with Kepler's Laws):

$$M = E - e \sin(E), \quad (1.17)$$

for an ellipse with eccentricity e . The eccentric anomaly is defined as the angle of the point on the auxillary circle which has the same projection on the ellipses major axis as the point on the ellipse you are interested in. Equation 1.17 must be solved for E iteratively, using some root-finding method such as the Newton-Raphson method. I.e we can write:

$$f(E) = E - e \sin(E) - M = 0, \quad (1.18)$$

and then using the Newton-Raphson formula:

$$x_{i+1} = x_i - \frac{f(x_i)}{f'(x_i)}. \quad (1.19)$$

The iterative formula is thus:

$$E_{i+1} = E_i - \frac{E_i + e \sin(E_i) - M}{1 - e \cos(E_i)}. \quad (1.20)$$

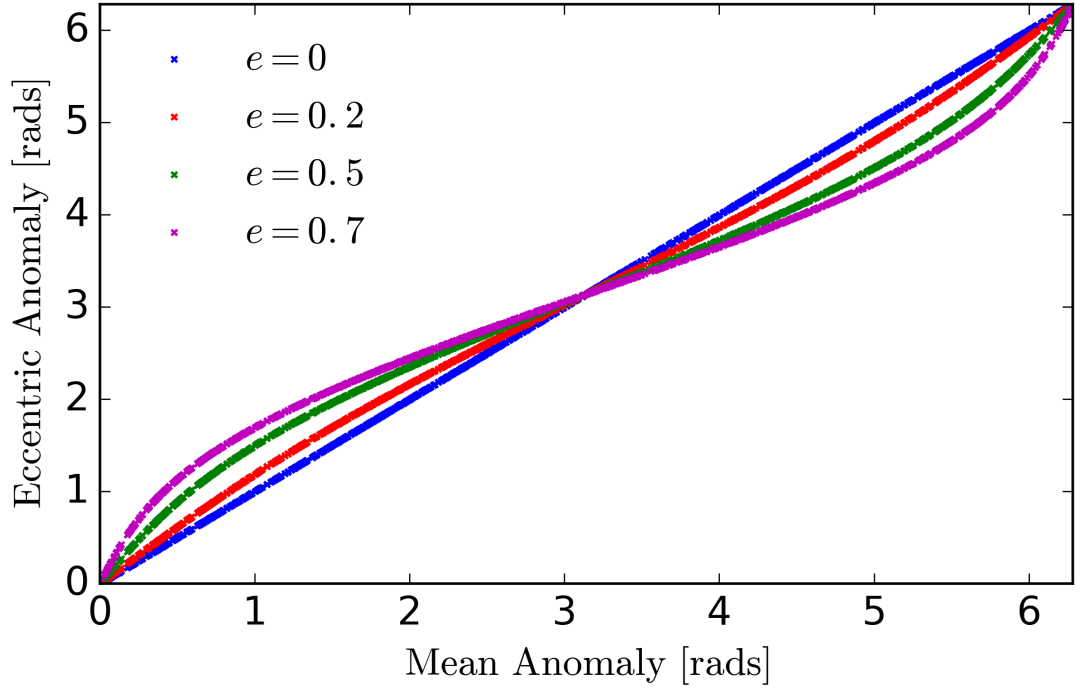


Figure 1.9: Plot showing relationship between the eccentric anomaly E and the mean anomaly M for 4 different eccentricities, $e = 0, 0.2, 0.5, 0.7$

We repeat this iterative process until $f(E) \leq \epsilon$, where ϵ is some accuracy tolerance. Using the Newton-Raphson method requires you to provide two inputs. The first is the initial ‘guess’ at E , E_0 . For a circular orbit, it is clear from Equation 1.17 that $E = M$, and so we will use this as our initial guess. You also need to specify a termination condition for the iteration, which here is the accuracy ϵ described above. Here we use $\epsilon = 1 \times 10^{-5}$. Once we have the eccentric anomaly E , we can calculate the true anomaly using:

$$\tan\left(\frac{\psi}{2}\right) = \sqrt{\frac{1+e}{1-e}} \cdot \tan\left(\frac{E}{2}\right) \quad (1.21)$$

This gives:

$$\psi = \begin{cases} 2 \tan^{-1} \left(\sqrt{\frac{1+e}{1-e}} \cdot \tan\left(\frac{E}{2}\right) \right) + 2\pi & \text{if } E \in (\pi, 2\pi) \\ 2 \tan^{-1} \left(\sqrt{\frac{1+e}{1-e}} \cdot \tan\left(\frac{E}{2}\right) \right) & \text{otherwise} \end{cases} \quad (1.22)$$

We show the relation between the mean anomaly and the eccentric anomaly for several illustrative eccentricities in Figure 1.9.

1.5.4 Post-supernova orbital characteristics

We have now determined the moment in which the supernova occurs. We now set up the orbit at the moment of the supernova. We denote pre-supernova variables without a prime, whilst post-supernova variables are denoted with a prime. For example, the total mass of the system prior to the supernova is M , whereas after the supernova it is M' . In general in an eccentric orbit, the pre-supernova orbital position vector \mathbf{r} and the orbital velocity vector \mathbf{v} are not perpendicular to one another as shown in Figure 1.10. The specific angular momentum at the moment

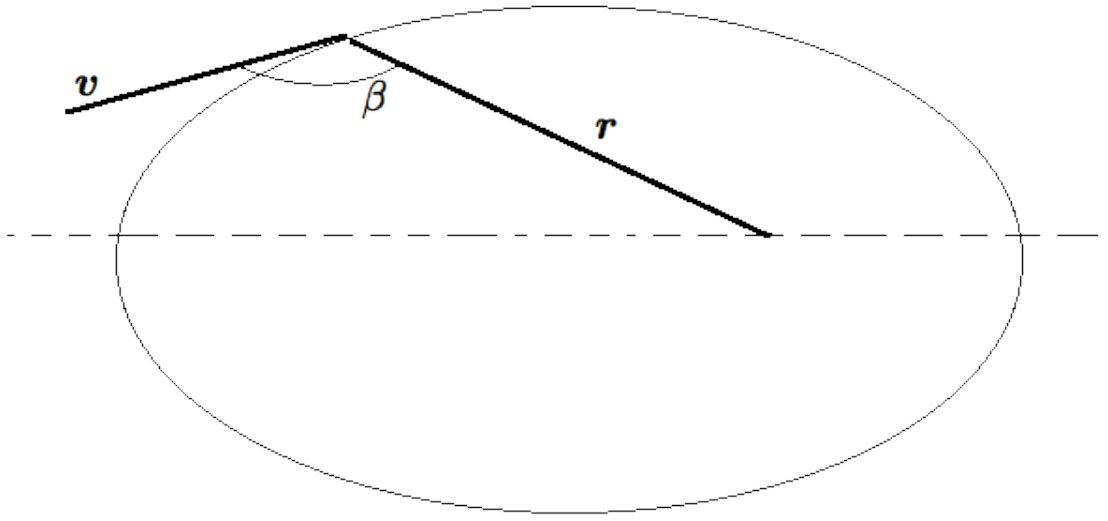


Figure 1.10: Angle β between the position vector \mathbf{r} and the velocity vector \mathbf{v} in an eccentric orbit.

of the supernova (assumed to be instantaneous) is given by:

$$|\mathbf{r} \times \mathbf{v}|^2 = r^2 v^2 \sin^2(\beta) = GMa(1 - e^2), \quad (1.23)$$

where we have used the definition of the cross product and defined β to be the angle between \mathbf{r} and \mathbf{v} . We can substitute in for v^2

$$v^2 = GM \left(\frac{2}{r} - \frac{1}{a} \right), \quad (1.24)$$

where G is the gravitational constant $G \approx 6.67 \times 10^{-11} \text{ Kg m}^2\text{s}^{-1}$ and $M = m_1 + m_2$. We can then rearrange to find

$$\sin^2(\beta) = \frac{a^2(1 - e^2)}{2ra - r^2}. \quad (1.25)$$

We can then write

$$\mathbf{r} = r \begin{pmatrix} \cos(\beta) \\ \sin(\beta) \\ 0 \end{pmatrix}, \quad (1.26)$$

and

$$\mathbf{v} = v \begin{pmatrix} 1 \\ 0 \\ 0 \end{pmatrix}, \quad (1.27)$$

where we have fixed the pre-supernova orbital velocity along the x axis. After the kick has been applied, the post-supernova velocity vector is given by

$$\mathbf{v}' = \begin{pmatrix} v_k \cos \theta \cos \phi + v \\ v_k \cos \theta \sin \phi \\ v_k \sin \theta \end{pmatrix}, \quad (1.28)$$

where θ and ϕ are the angles describing the kick direction, and v_k describes the kick magnitude, as shown in Figure 1.11.

1.5.5 Post-supernova semi-major axis

We can write down an expression for the post-supernova semi-major axis using the *vis-viva* equation for the total orbital energy after the supernova

$$E' = \frac{1}{2} \mu' v'^2 - \frac{G \mu' M'}{r} = -\frac{G \mu' M'}{2a'}, \quad (1.29)$$

where μ' is the post-supernova reduced mass and a' is the post-supernova semi-major axis. The magnitude of the post-supernova orbital velocity is given by

$$v'^2 = v_k^2 + v^2 + 2v_k v \cos \theta \cos \phi. \quad (1.30)$$

Substituting this into Equation 1.29 and rearranging for a' gives

$$a' = \frac{1}{2/r - M/M' (2/r - 1/a) (1 + 2u_k \cos \theta \cos \phi + u_k^2)}, \quad (1.31)$$

where we have defined the dimensionless kick velocity $u_k = v_k/v$. In the case of an initially circular orbit, $e = 0$ and $r = a$ this expression simplifies to the one given

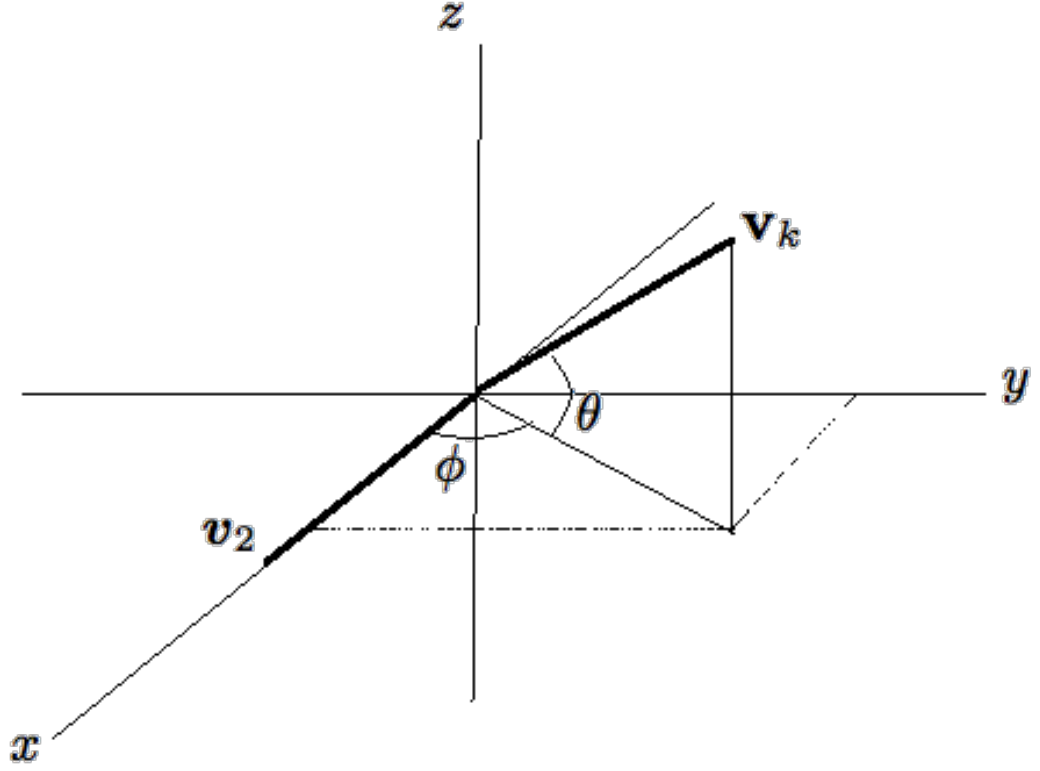


Figure 1.11: The supernova kick velocity has a magnitude v_k drawn from Maxwellian with $\sigma = 265 \text{ km s}^{-1}$, and its direction (parameterised by θ and ϕ) is drawn isotropically.

in [132]

$$a' = \frac{a}{2 - M/M' (1 + 2u_k \cos \theta \cos \phi + u_k^2)}. \quad (1.32)$$

1.5.6 Post-supernova eccentricity

We can now calculate the post-supernova eccentricity e' by equating the orbital angular momentum of instantaneously after the supernova to the angular momentum of the resulting elliptical orbit. We write this as

$$|\mathbf{r} \times \mathbf{v}'|^2 = r^2 \left[v_k^2 \sin^2 \theta + \left(v_k \cos \theta \sin \phi \cos \beta - (v_k \cos \theta \cos \phi + v) \sin \beta \right)^2 \right] = GM' a' (1 - e'^2). \quad (1.33)$$

We can rearrange this to find

$$(1-e'^2) = r^2 \frac{M}{M'} \left(\frac{2}{r} - \frac{1}{a} \right) \left[u_k \sin^2 \theta + [u_k \cos \theta \sin \phi \cos \beta - (u_k \cos \theta \cos \phi + 1) \sin \beta]^2 \right] \\ \left[\frac{2}{r} - \frac{M}{M'} \left(\frac{2}{r} - \frac{1}{a} \right) (1 + 2u_k \cos \theta \cos \phi + u_k^2) \right], \quad (1.34)$$

which again simplifies to the expression given in [132] when $e = 0$, $r = a$, $\beta = \pi/2$

$$(1-e'^2) = \frac{M}{M'} \left[2 - \frac{M}{M'} (1 + u_k^2 + 2u_k \cos \theta \cos \phi) \right] [u_k^2 \sin^2 \theta + (1 + u_k \cos \theta \cos \phi)^2]. \quad (1.35)$$

To determine if the binary remains bound, we define the dimensionless post-supernova orbital energy ϵ as the ratio of the post-supernova orbital energy E' to the pre-supernova orbital energy E

$$\epsilon \equiv -\frac{E'}{E} = \frac{a}{a'} \frac{\mu' M'}{\mu M}. \quad (1.36)$$

If $\epsilon < 0$, the system is bound, whereas if $\epsilon > 0$ the system becomes unbound. Equivalently, if $e' > 1$ the system becomes unbound as a result of the supernova kick.

1.5.7 Post-supernova orbital tilt

We also wish to know how the supernova kick tilts the binary orbit. We can calculate the inclination angle between the pre and post-supernova orbital planes, as defined by the orbital angular momentum vectors. These are given by

$$L = \mu \mathbf{r} \times \mathbf{v} = \mu \begin{pmatrix} 0 \\ 0 \\ -rv \sin \beta \end{pmatrix}, \quad (1.37)$$

and

$$L' = \mu' \mathbf{r} \times \mathbf{v}' = \mu' \begin{pmatrix} rv_k \sin \theta \sin \beta \\ -rv_k \sin \theta \cos \beta \\ rv_k \cos \theta \sin \phi \cos \beta - [r \sin \beta (v_k \cos \theta \cos \phi)] \end{pmatrix}. \quad (1.38)$$

The angle between these is given by

$$\cos i = \frac{\mathbf{L} \cdot \mathbf{L}'}{|\mathbf{L}||\mathbf{L}'|}, \quad (1.39)$$

which gives:

$$\cos i = \frac{\sin \beta (u_k \cos \theta \cos \phi + 1) - u_k \cos \beta \cos \theta \sin \phi}{[u_k^2 \sin^2 \theta + u_k^2 \cos^2 \theta \sin^2 \phi \cos^2 \beta + \sin^2 \beta (u_k \cos \theta \cos \phi + 1)^2 - 2 \cos \theta \sin \phi \cos \beta \sin \beta (u_k \cos \theta \cos \phi + 1)]^{1/2}}. \quad (1.40)$$

. Once again, we can check that this simplifies to the correct formula in the limit of an initially circular ($\beta = \pi/2$) orbit

$$\cos(i) = \frac{1 + u_k \cos \theta \cos \phi}{[(u_k \sin \theta)^2 + (1 + u_k \cos \theta \cos \phi)^2]^{1/2}}, \quad (1.41)$$

as given by [132].

The post-supernova orbital tilt, given by Equation 1.40 is important for calculating the spin-orbit misalignment angles of binary black holes discussed in Chapter 4 of this thesis. In Figure 1.12 we show $\cos i$ as a function of u_k , Monte-Carlo averaged over the angles θ and ϕ for a circular orbit. Similar plots appear in O'Shaughnessy *et al.* [133].

Comparing population synthesis models for isolated binary evolution to the empirically determined binary black hole merger rate shows that large value of black hole natal kicks are disfavoured [35, 128]. Similar work has compared population synthesis models to the observed, apparently universal [134, 135] high-mass X-ray binary luminosity function [136].

1.6 Mass transfer

Whilst stars in a binary remain widely separated, their evolution is well approximated by that of single stars. When stars begin to interact, their evolution can differ wildly from that of a single star. One of the main ways the evolution of stars can differ from that of a single star is by losing or gaining mass through mass transfer.

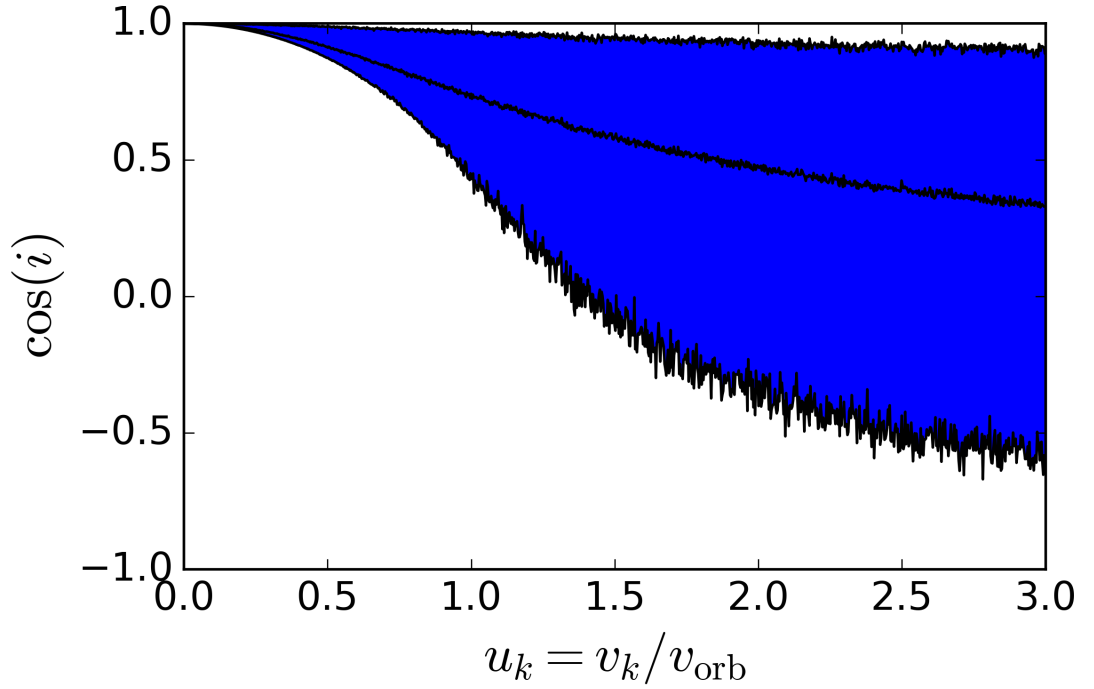


Figure 1.12: Post-supernova orbital tilt $\cos i$ as a function of the dimensionless kick $u_k = v_k/v_{\text{orb}}$ assuming the supernova kick velocity has a magnitude v_k drawn from Maxwellian with $\sigma = 265 \text{ km s}^{-1}$, and its direction (parameterised by θ and ϕ) is drawn isotropically. The blue region show the 90% contour for the tilt $\cos i$, with the median shown by the solid black line.

Roche lobe

Although this section is primarily a review, the work presented here was conducted along with Fabian Gittins, who wrote the code to produce some of the plots in this section.

In order to determine if stars engage in mass transfer, one must check if a star is contained within its Roche lobe. The outer layers of a star that fills its Roche lobe can be transferred from one star to another. The Roche lobe is the 3D equipotential surface passing through the inner Lagrange point L1. The Lagrange points are the Maxima/saddle points of the Roche potential. The Roche potential includes both gravitational and centripetal energy, and so is an effective potential. Following Mochnacki [137] the Roche potential is given by:

$$\Psi(x, y, z) = -\frac{G(M_1 + M_2)}{2a}C(x, y, z), \quad (1.42)$$

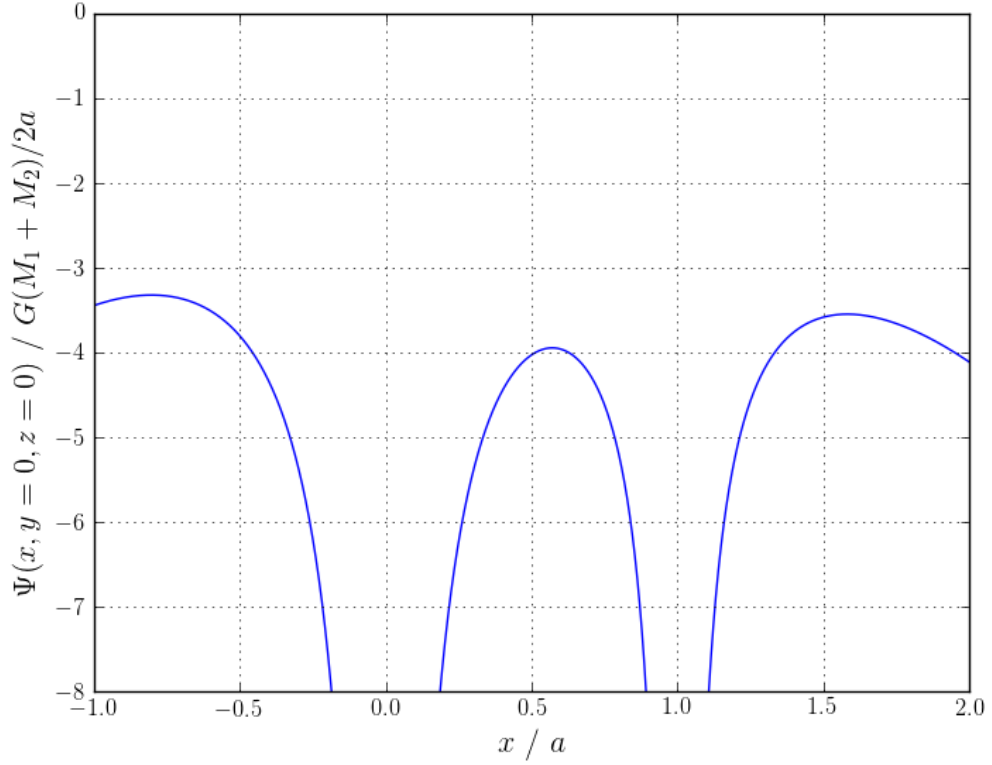


Figure 1.13: Total potential of a system with $q = 0.5$ plotted against the x -axis. The potential is taken at $y = z = 0$.

where

$$C(x, y, z) = \frac{2}{1+q} \frac{1}{(x^2 + y^2 + z^2)^{1/2}} + \frac{2q}{1+q} \frac{1}{[(x-1)^2 + y^2 + z^2]^{1/2}} + \left(x - \frac{q}{1+q}\right)^2 + y^2, \quad (1.43)$$

is the normalised potential and G is the gravitational constant. M_1 and M_2 are the masses of the two stars in the binary. The coordinates (x, y, z) in equation 1.43 are in units of the semi-major axis a , with the primary star located at the origin $(0, 0, 0)$ and the secondary at $(a, 0, 0)$. A 1D slice through the Roche potential is shown in Figure 1.13. A 2D contour plot of the Roche lobe for an equal mass system is shown in Figure 1.14.

Since stellar models are often calculated only in 1D, a 1D criterion is often used to determine if a binary fills its Roche lobe. The volume equivalent Roche lobe radius is the radius of a sphere with the same volume V_{RL} as that of the Roche lobe, i.e.

$$R_{\text{RL}} \equiv \left(\frac{3V_{\text{RL}}}{4\pi} \right)^{1/3}. \quad (1.44)$$

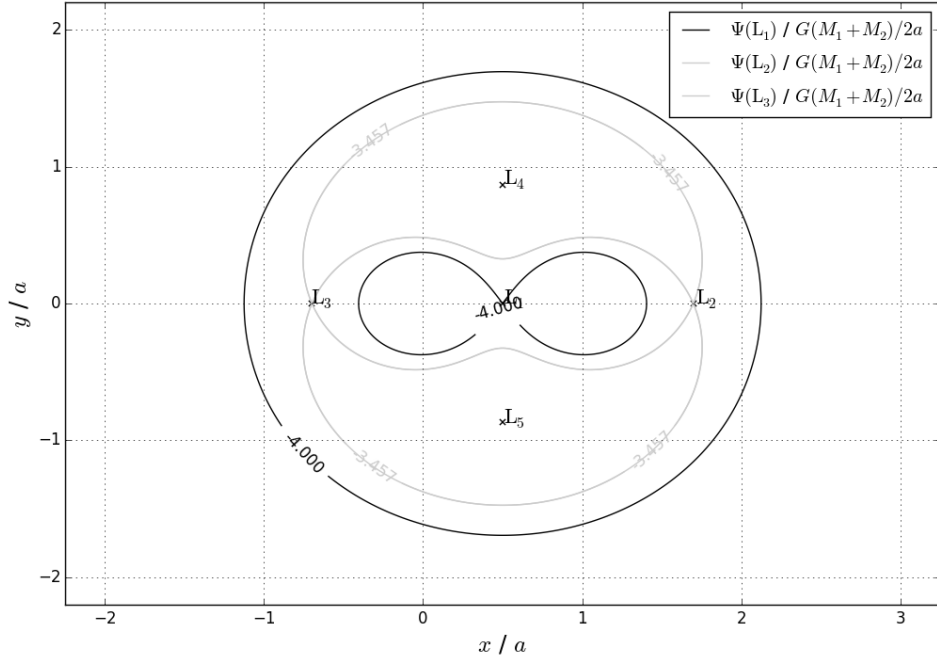


Figure 1.14: Contour plot of equipotential lines for the Roche potential for an equal mass binary. The plot shows a slice at $z = 0$. L_1 , L_2 , L_3 , L_4 and L_5 denote the Lagrangian points.

A star begins mass transfer when it fills its Roche lobe, i.e. when the radius of the star R is greater than the Roche lobe radius R_{RL} .

Equation 1.44 is often approximated, with the most commonly used fit given by Eggleton [138]. This fit assumes that the binary is in a circular orbit ($e = 0$), and approximates the stars as point masses which are rotating synchronously with the orbit. Under these assumptions the Roche lobe (in units of the semi-major axis) is simply a function of the binary mass ratio q , and is given by

$$\frac{R_{L1}}{a} = \frac{0.49q_1^{2/3}}{0.6q_1^{2/3} + \log(1 + q_1^{1/3})}. \quad (1.45)$$

This Equation is plotted in Figure 1.15.

The approximation of stars as point masses is typically valid since stars tend to engage in mass transfer as giants when they are highly centrally condensed, with most of their mass in a dense core surrounded by a large tenuous envelope. More detailed fits to the Roche lobe radius have been developed in [139, 140] which relax some of the simplifying assumptions commonly made.

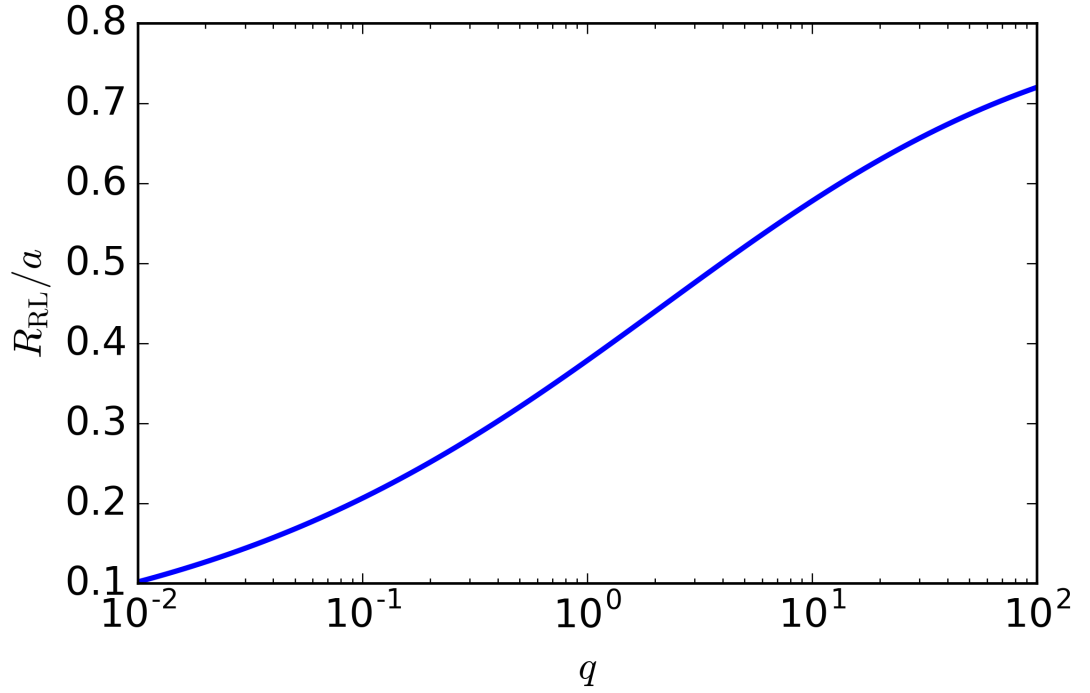


Figure 1.15: Eggleton [138] approximation to Roche lobe radius (in units of semi-major axis a) as a function of mass ratio q

Cases of mass transfer

We will refer to different cases of mass transfer, depending on the evolutionary phase of the donor star:

- Case A - Donor engaging in mass transfer as it expands on the Main Sequence (MS) during core hydrogen burning.
- Case B - Donor engaging in mass transfer as it expands after hydrogen exhaustion as it expands off of main sequence
- Case C - Donor engaging in mass transfer as it after helium exhaustion

Non-conservative mass transfer

In general, not all mass lost from a donor star \dot{M}_{don} will be accreted by the accreting star in the binary. The rate at which the accreting star can accept mass \dot{M}_{acc} will

depend upon the properties (mass, radius, luminosity) of the accreting star, along with its evolutionary phase. Sometimes the fraction of mass lost from the system in an episode of mass transfer β is parameterised as:

$$\beta = \frac{\dot{M}_{\text{acc}}}{\dot{M}_{\text{don}}} \leq 1.0. \quad (1.46)$$

Schneider *et al.* [141] show this parameter in their Figures 1, 17–20 as a function of initial mass ratio and orbital period. They find that case A mass transfer is typically conservative $\beta \sim 1$, case B mass transfer is conservative for nearly equal masses, and becomes completely non conservative for mass ratios $q < 0.5$ and case C mass transfer is typically highly non-conservative.

Accreting compact objects typically have their accretion limited by the Eddington luminosity. The accreting material has its gravitational potential energy converted into luminosity. The Eddington mass accretion rate is the limit when the radiation pressure balances the force due to gravity. The Eddington luminosity is¹[e.g., 142, 136]:

$$L_{\text{Edd}} = \frac{4\pi c G m_p}{\sigma_T} M = 3.3 \times 10^4 (M/M_\odot) L_\odot = 1.3 \times 10^{38} \text{ erg s}^{-1}, \quad (1.47)$$

where σ_T is the Thomson cross section of an electron, m_p is the proton mass, M is the mass of the compact object and c is the speed of light. The Eddington mass accretion rate is given by:

$$\dot{M}_{\text{Edd}} = \frac{L_{\text{Edd}}}{c^2} = \frac{4\pi G m_p}{c \sigma_T} M = 1.5 \times 10^{-8} \left(\frac{R}{10 \text{ km}} \right) M_\odot \text{ yr}^{-1}, \quad (1.48)$$

where R is the radius of the accreting compact object (in COMPAS, we follow Belczynski *et al.* [142] and Zuo *et al.* [136] in assuming R_{acc} to be the surface of a neutron star or white dwarf, and three Schwarzschild radii for a non-spinning black hole). Accretion onto a compact object is typically highly non-conservative. StarTrack assumes a constant $\beta = 0.5$ for all episodes of mass transfer [142, 35] where the accretor is not a degenerate compact object. When material cannot be accreted and is lost from the system, one key question is how is it lost, and the effect it has on the orbit of the binary.

¹see also Van de Sluys, <http://www.astro.ru.nl/~sluys/Teaching/files/BinaryEvolutionNutshell.pdf>

The rate of change of the semi-major axis \dot{a} is given by:

$$\frac{\dot{a}}{a} = -2 \frac{\dot{M}_d}{M_d} \left[1 - \beta \frac{M_d}{M_a} - (1 - \beta)(\gamma + 1/2) \frac{M_d}{M_d + M_a} \right], \quad (1.49)$$

where the angular momentum lost from the binary in non-conservative mass transfer is γ times the specific angular momentum of the binary.

In the so called “Jean’s Mode” of mass loss, mass is lost from the donor star (with its specific angular momentum) in a fast wind. This corresponds to $\gamma = \frac{M_a}{M_d}$. In the case of accretion onto a compact object, it might be that mass is transferred during Roche Lobe overflow, but then cannot be accreted, and is lost from the system in a wind or jets with the specific angular momentum of the accretor. This *isotropic re-emission* [143, 144] corresponds to $\gamma = \frac{M_d}{M_a}$. Finally, an extreme case would be if the mass is lost through a circumbinary disk with a radius a_{ring} of roughly twice the binary’s semi-major axis a . It may occur when mass is lost through the L_2/L_3 Lagrange points. This corresponds to²:

$$\gamma = \frac{(M_d + M_a)^2}{M_d M_a} \sqrt{\frac{a_{\text{ring}}}{a}}. \quad (1.50)$$

Stability

Stars at different stages of their lives respond to mass loss in different ways, and on different timescales. Whether mass transfer is stable or unstable depends on how the donor star responds to mass loss (whether it expands or contracts), and how the orbit (and the Roche lobe) responds to the mass transfer and mass loss (whether the orbit expands or shrinks). The response of the Roche lobe to mass loss is defined as:

$$\zeta_{\text{RL}} \equiv \frac{d \log R_{\text{RL}}}{dM}. \quad (1.51)$$

The response of a star to mass loss is defined as:

$$\zeta_* \equiv \frac{d \log R_*}{dM}. \quad (1.52)$$

Mass transfer is stable if $\zeta_* > \zeta_{\text{RL}}$.

²see Pols, http://www.astro.ru.nl/~onnop/education/binaries_utrecht_notes/Binaries_ch6-8.pdf

Mass loss/gain of mass will drive a star out of its equilibrium configuration. The star will then relax to a new equilibrium on a given timescale. The star returns to hydrostatic equilibrium on a dynamical timescale:

$$\tau_{\text{dynamical}} = \sqrt{\frac{R^3}{2GM}}, \quad (1.53)$$

where R is the radius of the star, and M is the mass. On this timescale there is no time for heat exchange, and the star responds adiabatically. Hjellming & Webbink [145] derived ζ_{ad} using condensed polytrope models, valid for giants.

The star then regains its thermal equilibrium on the longer thermal (Kelvin-Helmholtz) timescale:

$$\tau_{\text{KH}} = \frac{GM^2}{RL}, \quad (1.54)$$

where L is the luminosity. The response on this timescale is given by ζ_{eq} .

Mass transfer stability can be parametrised as a function of the binary's mass ratio, as well as the evolutionary phases of the donor and accretor. If the mass ratio of a binary $Q < Q_{\text{crit}}$, where Q_{crit} is the critical mass ratio for mass transfer to be stable, mass transfer is dynamically unstable and will lead to a common-envelope. In COMPAS we adapt the values of Q_{crit} from Claeys *et al.* [80] and de Mink *et al.* [146], shown in Table 1.1.

Donor type	Non-degenerate accretor	Degenerate accretor
Main Sequence $M < 0.7M_{\odot}$	0.625	— ^a
Main Sequence $M > 0.7M_{\odot}$	1.44	1.0
Hertzsprung Gap	0.25	0.21
Giant Branch		
/Asymptotic Giant Branch	— ^a	0.87
Helium Hertzsprung gap	0.25	0.21
Helium Giant Branch	1.28	0.87
White Dwarf	— ^a	1.6

Table 1.1: Critical mass ratios Q_{crit} with $Q \equiv M_{\text{a}}/M_{\text{d}}$. Table reproduced from Claeys *et al.* [80].

^a “—” means no critical value is available

1.7 Common envelope

A common envelope is a dynamical timescale event that occurs when a binary experiences dynamically unstable mass transfer. More correctly, the *plunge in* phase of a common-envelope event occurs on a dynamical timescale. There are also stages prior to this (such as the *loss of corotation*) and after this (such as a *self regulated spiral-in*) which occur on longer timescales than the dynamical one (potentially thermal). The dynamical timescale plunge in phase is the best studied with simulations [e.g., 147]. For more detail on the stages of a common-envelope event see the review by Ivanova *et al.* [148].

The binary becomes enveloped in a common-envelope, and the resulting drag then drains energy from the orbit, dramatically reducing the orbital separation. In some cases the envelope will be successfully ejected, whilst in others it will lead to a stellar merger. Common envelope evolution is the classical solution to the *separation* problem for forming binary black holes; how to form two black holes separated by $\mathcal{O}(10)R_{\odot}$ when the progenitor stars can grow to be more than 100 times this size during their lives.

In the α -formalism [149, 150, 151, 152, 153, 148] it is assumed that the orbital energy is used to unbind and eject envelope. The difference in the initial and final orbital energies is given by:

$$\Delta E_{\text{orb}} = E_{\text{initial}} - E_{\text{final}} = \left(-\frac{GM_1M_2}{2a_{\text{initial}}} + \frac{GM_{1,c}M_2}{2a_{\text{final}}} \right), \quad (1.55)$$

where a_{initial} and a_{final} are the initial and final orbital separations respectively, M_1 and M_2 are the initial masses of the two stars and $M_{1,c}$ is the core mass of the primary after ejecting its envelope. The parameter α is the common envelope efficiency, and is introduced to characterise the efficiency with which the orbital energy can be used to eject the envelope:

$$\alpha \Delta E_{\text{orb}} = E_{\text{bind}}. \quad (1.56)$$

Conservation of energy would argue that $0 \leq \alpha \leq 1$, but there are additional possible energy source not taken into account in the classical definition such as recombination energy [154] (although this is unlikely to be important for the massive stars we consider as black hole progenitors [155]) or enthalpy [156]. We therefore

allow $\alpha > 1$ in COMPAS.

The binding energy of the stellar envelope E_{bind} can be calculated by detailed stellar models as [e.g. 157, 158, 159, 160, 161, 155]:

$$E_{\text{bind}} = - \int_{\text{core}}^{\text{surface}} (\Psi(m) + \epsilon(m)) dm = \frac{GM_1 M_{1,e}}{\lambda R_{\text{initial}}}, \quad (1.57)$$

where $\Psi(m) = -Gm/r(m)$ is the gravitational potential, $\epsilon(m)$ is the specific internal energy, $M_{1,e}$ is the mass of the ejected envelope, R_{initial} is the radius of the star at the onset of the common envelope. The main source of uncertainty in calculating the binding energy is in determining the core-envelope boundary [162, 148]. The parameter λ is introduced (by de Kool *et al.* [163]) as a fitting parameter, useable with the quantities available in a rapid binary evolution population synthesis code such as COMPAS.

Note that as formulated above, the energy formalism for common-envelope ejection assumes that the kinetic energy of ejected material at infinity is zero [160].

An alternate common-envelope prescription has been proposed by Nelemans *et al.* [164], Nelemans & Tout [165] based on the conservation of angular momentum:

$$\frac{\Delta J_{\text{orb}}}{J_i} = \frac{J_i - J_f}{J_i} = \gamma \frac{M_{1,e}}{M_1 + M_2}, \quad (1.58)$$

where J_i and J_f are the angular momenta of the initial and final binaries. This prescription was required to explain observations of double white dwarf systems, in which envelope loss without significant spiral-in was required. In these systems, the γ formalism corresponded to energy generation, i.e. a *negative* α parameter. Woods *et al.* [166] argue that the γ formalism is not applicable to arbitrary common-envelope events; we choose not to use it as the default in COMPAS, and instead opt for the $\alpha\lambda$ -formalism.

Due to their dynamical nature, observations of common-envelope events are difficult. Systems such as double white dwarfs and sdB stars are likely post-common envelope binaries, allowing their orbital properties to be used to constrain the common-envelope event. Common-envelope events may also produce electromagnetic transients.

Luminous Red Novae (LRN) such as V1309 Sco have been associated with common-envelope events [167, 168, 169, 170]. Up to thousands of these events may be observed in the near future with the Large Synoptic Survey Telescope [LSST, 171, 94]. More speculatively, the infrared SPRITES (eSPecially Red Intermediate-luminosity Transient Events) observed by Spitzer may also be common-envelope events [170].

1.8 Post-Newtonian evolution

After the formation of a binary black hole, its evolution is dominated by post-Newtonian effects. These can be accurately approximated whilst the binary is at large orbital separations and the orbital speeds are much less than the speed of light. This is the weak-field approximation. When the binary nears merger, these approximations break down and one must resort to solving the Einstein equations numerically, known as numerical relativity.

In this section we use geometric units $G = c = 1$.

Inspiral and circularisation

Gravitational radiation emitted from a binary carries energy and angular momentum, causing a decrease in the semi-major axis a and eccentricity e of the orbit, as first derived by [172, 173]. To leading order, the average decay of the orbit is given by:

$$\frac{da}{dt} = -\frac{64m_1m_2(m_1+m_2)}{a^3(1-e^2)^{7/2}} \left(1 + \frac{73}{24}e^2 + \frac{37}{96}e^4\right), \quad (1.59)$$

and

$$\frac{de}{dt} = -\frac{304}{15} \frac{m_1m_2(m_1+m_2)e}{a^4(1-e^2)^{5/2}} \left(1 + \frac{121}{304}e^2\right). \quad (1.60)$$

The lifetime of an orbit can be found by integrating Equation 1.59. For a circular orbit the lifetime is

$$t_c = \frac{5a_0^4}{256m_1m_2(m_1+m_2)}. \quad (1.61)$$

The binary may have picked up significant eccentricity during its formation. The ratio of the lifetime of an eccentric orbit t to that of a circular one t_c is given by

$$\frac{t}{t_c} = \frac{48}{19} \frac{(1 - e_0^2)^4}{e_0^{48/19}} \left[1 + \frac{121}{304} e_0^2 \right]^{-3480/2299} \int_0^{e_0} \frac{e^{29/19}}{(1 - e^2)^{3/2}} \left[1 + \frac{121}{304} e^2 \right]^{1181/2299} de. \quad (1.62)$$

which is independent of the initial semi-major axis, and masses. This is plotted in Figure 1.16. Eccentricity is radiated quickly enough that all merging binaries are expected to be essentially perfectly circular. We count a binary as a gravitational-wave driven merging binary if the time to merger is less than a Hubble time.

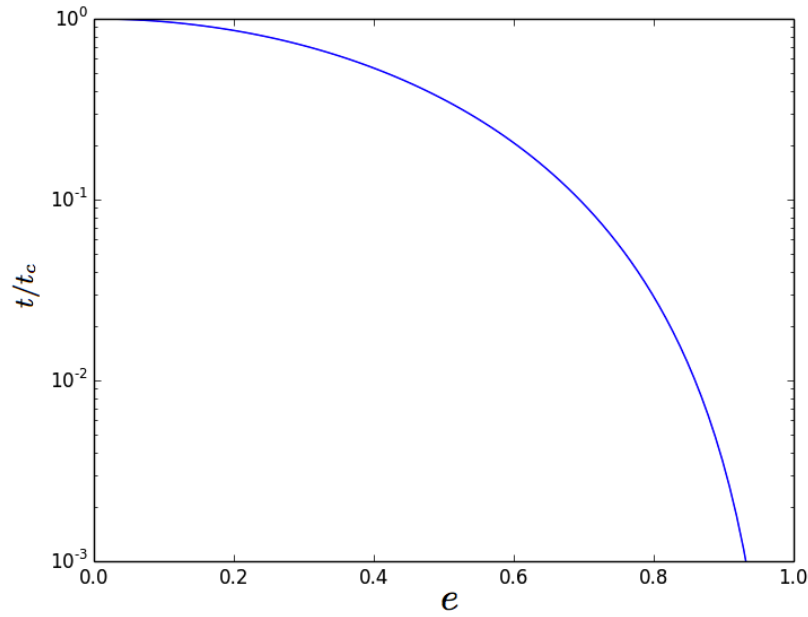


Figure 1.16: Time until merger due to emission in gravitational waves for an eccentric binary with initial eccentricity e in units of the lifetime of an initially circular binary, t_c . Eccentric binaries merge much quicker than an initially circular binary. This plot is formatted to be comparable to Figure 2 in [173].

Precession and resonances

Following the second supernova, our system consists of two black holes, with spin vectors \mathbf{S}_1 and \mathbf{S}_2 in general not aligned with the orbital angular momentum vector \mathbf{L} (shown in Figure 1.17). This causes the spins to precess around the total angular momentum vector $\mathbf{J} = \mathbf{L} + \mathbf{S}_1 + \mathbf{S}_2$. The spins are given as

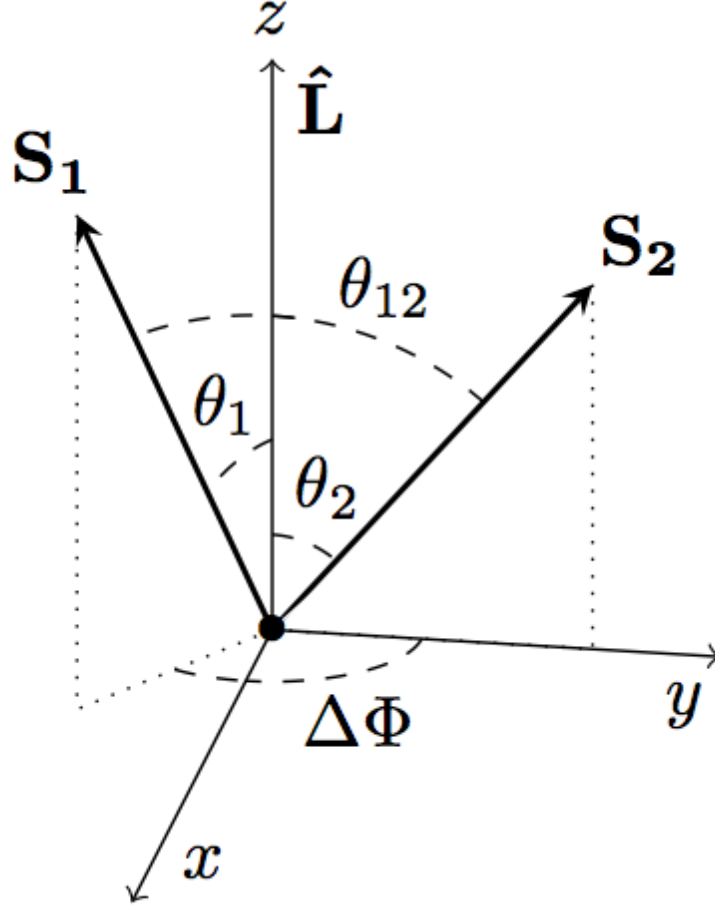


Figure 1.17: Geometry of the spins and orbital angular momentum. Figure reproduced from [174].

$$\mathbf{S}_i = \chi_i m_i^2 \hat{\mathbf{S}}_i, \quad (1.63)$$

where $\chi_i \in [0, 1]$ is the dimensionless spin of the black hole, $\hat{\mathbf{S}}_i$ denotes the spin unit vector and m_i is its mass. We choose the spin of the secondary to lie in the y-z plane such that we can write the spins as

$$\hat{\mathbf{S}}_1 = \begin{pmatrix} \sin \theta_1 \sin \Delta\Phi \\ \sin \theta_1 \cos \Delta\Phi \\ \cos \theta_1 \end{pmatrix} \quad \text{and} \quad \hat{\mathbf{S}}_2 = \begin{pmatrix} 0 \\ \sin \theta_2 \\ \cos \theta_2 \end{pmatrix}, \quad (1.64)$$

where θ_i is the angle between \mathbf{S}_i and the orbital angular momentum vector \mathbf{L} and $\Delta\Phi$ is the angle between the projections of the two spins onto the orbital plane. These are in turn given by

$$\cos \theta_1 = \hat{\mathbf{S}}_1 \cdot \hat{\mathbf{L}}, \quad (1.65)$$

$$\cos \theta_2 = \hat{\mathbf{S}}_2 \cdot \hat{\mathbf{L}}, \quad (1.66)$$

and

$$\cos \Delta\Phi = \frac{\hat{\mathbf{S}}_1 \times \hat{\mathbf{L}}}{|\hat{\mathbf{S}}_1 \times \hat{\mathbf{L}}|} \cdot \frac{\hat{\mathbf{S}}_2 \times \hat{\mathbf{L}}}{|\hat{\mathbf{S}}_2 \times \hat{\mathbf{L}}|}. \quad (1.67)$$

We define the angle between the two spins, denoted θ_{12} , as

$$\cos \theta_{12} = \hat{\mathbf{S}}_1 \cdot \hat{\mathbf{S}}_2. \quad (1.68)$$

Segregation of timescales

This problem has three distinct timescales into which the various processes segregate [175, 176]. The shortest timescale is the orbital timescale

$$t_{\text{orb}} \approx \frac{2\pi}{\omega} \approx \left(\frac{a^3}{M}\right)^{1/2} \approx a^{3/2}. \quad (1.69)$$

The component spins precess on the longer precessional timescale

$$t_{\text{precession}} \approx 0.5 \left(\frac{M}{M_\odot}\right)^{3/2} \left(\frac{a}{R_\odot}\right)^{5/2} \text{ years}. \quad (1.70)$$

The semi-major axis a , eccentricity e and the magnitude of the orbit angular momentum L_N decay on the radiation reaction timescale t_{rad} which from Peter's equations (Equation 1.61) goes like

$$t_{\text{rad}} \approx a^4, \quad (1.71)$$

with $t_{\text{orb}} \ll t_{\text{precession}} \ll t_{\text{rad}}$. This allows us to only follow the magnitude of the orbital angular momentum L_N on the radiation reaction timescale, whilst orbit averaging the spin precession equations since the spins will evolve on the precessional timescale.

Integrating the equations of motion

The evolution of the angular momentum and spin vectors with time can be obtained by integrating the PN equations of motion [e.g., 177, 174]

$$\frac{d\hat{\mathbf{L}}}{dt} = \frac{-\nu}{\eta M^2} \left[\frac{d\mathbf{S}_1}{dt} + \frac{d\mathbf{S}_2}{dt} \right], \quad (1.72)$$

$$\frac{d\mathbf{S}_1}{dt} = \boldsymbol{\Omega}_1 \times \mathbf{S}_1, \quad (1.73)$$

and

$$\frac{d\mathbf{S}_2}{dt} = \boldsymbol{\Omega}_2 \times \mathbf{S}_2. \quad (1.74)$$

$\boldsymbol{\Omega}_1$ and $\boldsymbol{\Omega}_2$ are the orbit averaged precession vectors (since precession occurs on a timescale longer than the orbital timescale) given by

$$M\boldsymbol{\Omega}_1 = \eta\nu^5 \left(2 + \frac{3q}{2}\right) \hat{\mathbf{L}} + \frac{\nu^6}{2M^2} \left[\mathbf{S}_2 - 3 \left(\hat{\mathbf{L}} \cdot \mathbf{S}_2 \right) \cdot \hat{\mathbf{L}} - 3q \left(\hat{\mathbf{L}} \cdot \mathbf{S}_1 \right) \cdot \hat{\mathbf{L}} \right], \quad (1.75)$$

and

$$M\boldsymbol{\Omega}_2 = \eta\nu^5 \left(2 + \frac{3}{2q}\right) \hat{\mathbf{L}} + \frac{\nu^6}{2M^2} \left[\mathbf{S}_1 - 3 \left(\hat{\mathbf{L}} \cdot \mathbf{S}_1 \right) \cdot \hat{\mathbf{L}} - \frac{3}{q} \left(\hat{\mathbf{L}} \cdot \mathbf{S}_2 \right) \cdot \hat{\mathbf{L}} \right], \quad (1.76)$$

Here we have defined some combinations of the component masses m_1 and m_2 as $\delta m = m_1 - m_2$ and $M = m_1 + m_2$. The rate of change of orbital velocity with time is given by

$$\begin{aligned} \frac{d\nu}{dt} = & \frac{32}{5} \frac{\eta}{M} \nu^9 \left\{ 1 - \nu^2 \frac{743 + 924\eta}{336} + \nu^3 \left[4\pi - \sum_{i=1,2} \chi_i \left(\hat{\mathbf{S}}_i \cdot \hat{\mathbf{L}} \right) \left(\frac{113}{12} \frac{m_i^2}{M^2} + \frac{25}{4} \eta \right) \right] \right. \\ & + \nu^4 \left[\frac{34103}{18144} + \frac{13661}{2016} \eta + \frac{59}{18} \eta^2 + \frac{\eta \chi_1 \chi_2}{48} \left(721 \left(\hat{\mathbf{S}}_1 \cdot \hat{\mathbf{L}} \right) \left(\hat{\mathbf{S}}_2 \cdot \hat{\mathbf{L}} \right) - 247 \left(\hat{\mathbf{S}}_1 \cdot \hat{\mathbf{S}}_2 \right) \right) \right. \\ & \quad \left. \left. + \frac{1}{96} \sum_{i=1,2} \left(\frac{m_i \chi_i}{M} \right)^2 \left(719 \left(\hat{\mathbf{S}}_i \cdot \hat{\mathbf{L}} \right)^2 - 233 \right) \right] - \nu^5 \pi \frac{4159 + 15876\eta}{672} \right. \\ & + \nu^6 \left[\frac{16447322263}{139708800} + \frac{16}{3} \pi^2 - \frac{1712}{105} (\gamma_E + \ln 4\nu) + \left(\frac{451}{48} \pi^2 - \frac{56198689}{217728} \right) \eta + \frac{541}{896} \eta^2 - \frac{5605}{2592} \eta^3 \right] \\ & \left. \left. + \nu^7 \pi \left[\frac{-4415}{4032} + \frac{358675}{6048} \eta + \frac{91495}{1512} \eta^2 \right] + \mathcal{O}(\nu^8) \right\}, \quad (1.77) \end{aligned}$$

where $\gamma_E \approx 0.577$ is the Euler-Mascheroni constant and the orbital velocity ν is

$$\nu^2 = \frac{M}{a}. \quad (1.78)$$

This last equation is sometimes equivalently written in terms of the orbital frequency $\omega = \nu^3/M$. That these equations are expansions – valid at large orbital separations when $\nu/c \ll 1$ – is clear from the structure. Terms of order ν^{2n} are said to be of n^{th} post-Newtonian order.

The equations of motion are integrated using a 5th order Dormand–Prince [178] algorithm with an adaptive timestep. Since this is computationally expensive, we begin integrating not at the orbital separation after the second supernova, but when $a = 1000M$. We can do this since to a good approximation the misalignments between the BH spins and the orbital angular momentum will not have evolved by this point.

We cease our integrations when the orbital separation is such that the gravitational-wave frequency of the binary – $f_{\text{GW}} = 2f$ where f is the orbital frequency – is greater than the frequency it enters the Advanced LIGO band, which we take to be 10 Hz.

Spin-orbit resonances

Schnittman [179] discovered a set of PN spin-orbit resonances that black hole spins can be attracted to, depending on the initial misalignments of the spins θ_i . These are resonant configurations in which the spins and orbital angular momentum precess in a common plane around the total angular momentum vector, known as *resonant plane locking*. This can cause the two component spins to become aligned or anti-aligned with one another.

Kesden *et al.* [180] have shown that resonances are effective at capturing binaries with mass ratios $0.4 \lesssim q < 1$. They do not act in equal mass binaries since symmetry would mean the two black holes are exchangeable. However, it is unlikely for astrophysical formation scenarios to produce exactly equal mass binaries. They are also effective when spins $\chi_i \gtrsim 0.5$, which seems likely for astrophysical black holes. These resonances do not act in the case of equal misalignments. It is well known in the literature that an initially isotropic distribution of spins will remain isotropic.

To demonstrate the effects of these resonances in a controlled experiment, we evolve 1000 binaries with mass ratio $q = 0.8$ where each spin $\chi_i = 0.7$ was randomly misaligned (at an orbital separation of $a = 1000M$) less than about 18 degrees. In Figure 1.18, binaries in which the more massive primary is more aligned than the secondary ($\theta_1 < \theta_2$) are coloured red, whilst binaries in which the primary is more misaligned ($\theta_1 > \theta_2$) are coloured blue. The top panel shows the initial distribution of spins in the $\cos\theta_{12}, \Delta\Phi$ plane (at an initial separation $a = 1000M$) whereas the

bottom panel shows the distribution when the binary enters the LIGO frequency band.

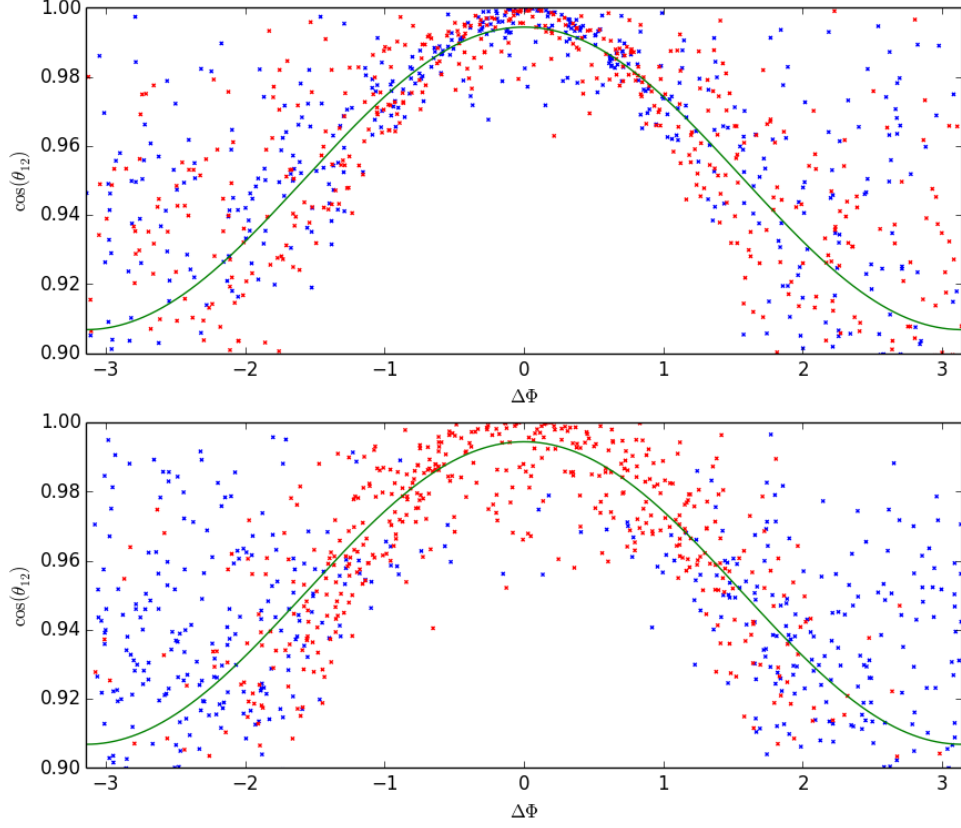


Figure 1.18: Plot showing the initial (top) and final ($f_{\text{GW}} = 10$ Hz, bottom) distributions of $\Delta\Phi$ and $\cos\theta_{12}$ for binaries with both spins initially preferentially aligned (misalignment less than about 18 degrees) in the $\cos\theta_{12}$, $\Delta\Phi$ plane. Those binaries which initially have $\cos\theta_1 < \cos\theta_2$ (coloured blue) are attracted to the $\Delta\Phi = \pm\pi$ resonances whilst those with $\cos\theta_1 > \cos\theta_2$ (coloured red) are attracted to the $\Delta\Phi = 0$ resonance. The green line shows the expected correlation between $\cos\theta_{12}$ and $\Delta\Phi$.

We see that binaries with $\theta_1 < \theta_2$ are attracted to the $\Delta\Phi = 0$ resonance, which tends to align the two spins such that $\cos\theta_{12} \approx 1$. Binaries with $\theta_1 > \theta_2$ are attracted to the $\Delta\Phi = \pm\pi$ resonances which tend to anti-align the two spins.

It has been suggested that we can use the clustering of binaries in different regions of parameter space to diagnose how they formed, if formation mechanisms lead to one spin being more misaligned than the other and we are able to measure accurately the angles between the spins in merging binaries [174, 181, 182]. We return to this issue in Chapter 4.

1.9 Alternate Formation Channels

In this thesis we restrict our focus to the formation of binary black holes through the classical isolated binary evolution channel via a common envelope described above in Section 1.7. In this Section, we briefly summarise other proposed mechanisms for forming merging binary black holes.

1.9.1 Dynamical formation

One of the most robust alternative formation channels for binary black holes is in dense stellar environments such as globular clusters through dynamical (gravitational) interactions. These systems have a high enough number density of stars that assuming stars form following the IMF, there will be many stars massive enough to form black holes. The number density of black holes can be 10^5 – 10^6 per pc^3 in globular clusters [e.g., 183].

Since black holes are thought to receive small to zero kicks when they form (see section 1.5 and [125]) these black holes are expected to be retained in the cluster, unlike neutron stars, the large majority of which are expected to be kicked out (although not all since we see (millisecond)-pulsars in galactic globular clusters³). Several black holes are observed in both galactic and extragalactic globular clusters [185, 186, 187], although some of these may potentially be intermediate-mass black holes. For a review of dynamical binary black hole formation see [e.g., 188, 189, 190] on which the present discussion was based.

These black holes then sink towards the center of the cluster, where they form binaries [191, 192, 193]. Heavier black holes sink to the center of the cluster faster than lighter ones (a process known as *mass segregation* [194, 195, 188, 189, 190]).

Soft binaries are defined as those binaries which have a binding energy less than the typical kinetic energy of a cluster member (i.e. wide binaries). As these binaries are wide, they have a large cross section for interaction (which scales as the semi-major axis for binaries), meaning they have a high rate of three body

³A list updated in 2012 is available at <http://www.naic.edu/~pfreire/GCpsr.html> [184]

interactions. The semi major axis of a soft binary typically increases in such an interaction, increasing the rate of encounters they experience. This is a run away process, eventually leading to them being unbound. *Hard* binaries, those with binding energy greater than the typical kinetic energy of a cluster member, typically have their semi-major axis reduced in a three body interaction, with the interloper carrying away the excess energy. Therefore soft binaries get softer and hard binaries get harder. Since this reduces the cross section for interaction, this is not a run away process. Eventually binaries become hard enough that they no longer experience interactions and merge due to the emission of gravitational radiation, or are ejected from the cluster due to the recoil kick they receive [196, 43]. For galactic globular clusters, the velocity dispersion is of order $\sim 10 \text{ km s}^{-1}$ [197, 192] and the typical escape velocity is around $\sim 30 \text{ km s}^{-1}$ [187].

Single black holes can also substitute into binaries in binary single interactions, where the lightest of the three stars is typically ejected [190]. In addition, unbound black holes can be captured in two body interactions if they pass close enough to one another and release enough energy in a burst of gravitational waves to leave the black holes in a bound orbit [190].

N-body simulations have studied the rates and properties of binary black holes formed in globular clusters [198, 199, 200, 201, 183, 202, 203, 204]. The rate of merging binary black holes forming in old globular clusters is $\sim 5 \text{ Gpc}^{-3} \text{ yr}^{-1}$ [202]. Globular clusters are therefore “dynamical factories for binary black holes” [200], and dynamical formation is therefore much more efficient at producing binary black holes than isolated binary evolution in the field, since only 10^{-4} of stars in the galaxy are in globular and nuclear clusters [190].

Since black holes form in isolation and form binaries only after stellar evolution, many of the theoretical uncertainties associated with isolated binary evolution are avoided by this formation scenario. Nonetheless, there remain significant uncertainties regarding stellar wind mass loss rates, supernova physics and the initial conditions of the globular clusters we see today [204].

In addition to globular clusters, binary black holes may also form through dynamics in other dense stellar environments such as in galactic nuclei [196, 205, 206].

Since the black holes do not form together, binary black holes in globular clusters are expected to have an isotropic distribution of spins [e.g., 207], which may be one way to distinguish systems formed this way. In Chapter 4 we develop a method to distinguish binary black holes formed dynamically from those formed through isolated binary evolution, and we apply it to the existing O1 LIGO observations in Chapter 5.

1.9.2 (Quasi)-Chemically homogenous evolution

Some massive stars may be rapidly rotating, and interactions can spin them up [208]. This can lead to strong rotational mixing within a star, allowing them to evolve chemically homogeneously [209, 210, 211]. Stars evolving chemically homogeneously evolve at approximately constant radius, avoiding the large radial expansion typical for non-rotating massive stars. This means that such stars can evolve without ever filling their Roche lobe. VFTS 352 is an overcontact binary consisting of two approximately $30 M_{\odot}$ stars in a 1.12 day orbit, and appears to be evolving at least partly chemically homogeneously [212]

Chemically homogeneous evolution may allow for black hole formation in situ without the need to invoke a common envelope phase [211]. Since stellar winds cause stars to spin down due to angular momentum loss, low metallicity is required in order to suppress wind mass loss and maintain chemically homogeneous evolution. This channel tends to form approximately equal mass high mass (total mass $M > 50M_{\odot}$), rapidly spinning binary black holes [213, 129, 130, 214].

1.9.3 Population III binaries

The formation scenarios above all involve the evolution of Population I or Population II stars with some non-zero metal content. The first generation of stars with zero metallicity, Population III stars, may also form massive black holes [215] since they may lose little mass through winds. These stars may contribute to the formation of merging binary black holes [216]. A lack of observational constraints on the initial properties of Population III stars make this channel even more uncertain than classical isolated binary evolution.

Some of these Population III stars may never develop convective envelopes as giants and may form binary black holes without a common envelope event [217]. The rates of merging binary black holes at redshifts observable by current ground based gravitational-wave detectors is highly uncertain, but may be as high as $\sim 25 \text{ Gpc}^{-3} \text{ yr}^{-1}$ at low redshifts [218, 219, 220, 217]. Belczynski *et al.* [221] find much lower merger rates of $\lesssim 0.1 \text{ Gpc}^{-3} \text{ yr}^{-1}$ at $z < 0.2$, in agreement with [222], but in disagreement with many of the above studies. This is due to uncertainties in a number of the evolutionary assumptions made in the models.

Interestingly, the typical mass of black holes formed from Population III stars predicted by Kinugawa *et al.* [219] is around $\sim 30M_{\odot}$. This was predicted prior to the observation of GW150914 which contains two $\sim 30M_{\odot}$ black holes.

1.9.4 Primordial black holes

The above channels are all different ways of forming a binary black holes from the evolution of massive stars. A theoretical alternative to this is to form primordial black holes in the early universe [223, 224, 225, 226, 227], which can then form binaries.

The mass range of primordial black holes is extremely broad, covering the mass range of black holes advanced ground based gravitational-wave detectors are sensitive to ($1 - 100M_{\odot}$) [21]. The rates of primordial binary black hole mergers is highly uncertain [224].

Very low spins are expected for primordial black holes since they form with very little angular momentum [228, 229]. Since the binaries are formed dynamically, the directions of the black hole spins are expected to be isotropic. This is consistent with the existing O1 measurements of spins in binary black holes.

Electromagnetic observations of the cosmic microwave background, cosmic infrared background and microlensing have the potential to rule out primordial black hole binaries in the mass range of interest to ground based gravitational-wave detectors [230, 231, 225, 232, 233, 234, 235].

1.9.5 Merger of a fragmented core inside a star

Following the detection of GW150914 [7] and the possible detection by Fermi GBM of an associated gamma ray afterglow [236] there was much theoretical speculation about the origin of binary black hole mergers. Loeb [237] suggested that GW150914 might have formed from the fragmented core of a massive star, which then merges very rapidly due to the emission of gravitational-waves. Drag from the gas causes the binary black hole to inspiral faster than in vacuum. Fedrow *et al.* [238] rule out this model, showing that for typical densities in the interiors of stars, the observed waveform does not match numerical predictions.

1.10 Thesis overview and key results

In this thesis we present Compact Object Mergers: Population Astrophysics and Statistics (COMPAS). COMPAS is a platform incorporating astrophysical modelling tools and statistical analysis tools to extract information from the population of merging binary black holes we observe, and offer insights into binary black hole formation.

In Chapter 2 we present the rapid population synthesis element of COMPAS. We use it to show that all three (assuming LVT151012 is real) presently observed binary black holes are consistent with formation through a single evolutionary channel – classical isolated binary evolution channel via a common-envelope. We show all three events could have formed in low-metallicity environments ($Z = 0.001$) from progenitor binaries with typical total masses $\gtrsim 160M_{\odot}$, $\gtrsim 60M_{\odot}$ and $\gtrsim 90M_{\odot}$, for GW150914, GW151226, and LVT151012, respectively.

In Chapter 3 we show how in principle the masses and rate of observed signals can be used to distinguish between a suite of such population synthesis models. We show that we will be able to distinguish between them with observations (or the lack of them) from the early runs of the advanced LIGO and Virgo detectors. This will allow us to narrow down the large parameter space for binary evolution models.

We then extend this in Chapter 4 to show how using measurements of the spin-orbit misalignments in binary black holes can yield information about their

formation, whether it be through isolated binary evolution or through dynamical interactions in dense stellar environments. Assuming a population with spins of $\chi \sim 0.7$, we show that with tens of observations it will be possible to distinguish the presence of subpopulations of coalescing binary black holes based on their spin orientations. With 100 observations it will be possible to infer the relative fraction of coalescing binary black holes with isotropic spin directions (corresponding to dynamical formation) with a fractional uncertainty of $\sim 40\%$. Meanwhile, only ~ 5 observations are sufficient to distinguish between extreme models—all binary black holes either having exactly aligned spins or isotropic spin directions.

We apply this methodology in Chapter 5 to the existing O1 observations of binary black hole mergers GW150914, GW151226 and LVT151012. If binary black hole spin magnitudes extend to high values, as is suggested by observations of black hole X-ray binaries, we show that the data already exhibit a 1.7σ preference for an isotropic angular distribution. The existing preference for either an isotropic spin distribution or low spin magnitudes for the observed systems will be confirmed (or overturned) confidently in the near future by subsequent observations.

We conclude in Chapter 6.

Chapter 2

Formation of the first three gravitational-wave observations through isolated binary evolution

Simon Stevenson,¹ Alejandro Vigna-Gómez,¹ Ilya Mandel,¹
Jim W. Barrett,¹ Coenraad J. Neijssel,¹ David Perkins,¹ Selma E. de Mink²

¹ School of Physics and Astronomy, University of Birmingham, Edgbaston, Birmingham
B15 2TT, United Kingdom

² Anton Pannekoek Institute for Astronomy, University of Amsterdam, 1090 GE Amsterdam,
The Netherlands

This Chapter introduces the rapid population synthesis element of COMPAS, and uses it to show that isolated binary evolution is capable of explaining all 3 currently observed gravitational-wave sources. It reproduces the text of Stevenson *et al.* [1], published in Nature Communications, with permission from the journal. There are some minor cosmetic changes compared to the published version, with regards to references and figure captions. The methods section has been moved from the appendix of the paper to the main body. The code, analysis and text were written by Simon Stevenson. The text was edited by all authors. Figure 2.1 was made by Simon Stevenson. Figure 2.2 was made by Alejandro Vigna-Gómez. Figure 2.3 was made by Coenraad J. Neijssel.

Abstract

During its first 4 months of taking data, Advanced LIGO has detected gravitational waves from two binary black hole mergers, GW150914 and GW151226, along with the statistically less significant binary black hole merger candidate LVT151012. We use our rapid binary population synthesis code COMPAS to show that all three events can be explained by a single evolutionary channel – classical isolated binary evolution via mass transfer including a common envelope phase. We show all three events could have formed in low-metallicity environments ($Z = 0.001$) from progenitor binaries with typical total masses $\gtrsim 160M_{\odot}$, $\gtrsim 60M_{\odot}$ and $\gtrsim 90M_{\odot}$, for GW150914, GW151226, and LVT151012, respectively.

2.1 Introduction

Advanced LIGO [239] has confidently observed gravitational-waves (GWs) from two BBH mergers, GW150914 [7] and GW151226 [19]. The BBH merger candidate LVT151012 is less statistically significant, but has a $> 86\%$ probability of being astrophysical in origin [21, 8].

GW150914 was a heavy BBH merger, with a well-measured total mass $M = m_1 + m_2 = 65.3 \pm_{3.4}^{4.1} M_\odot$ [9, 8], where $m_{1,2}$ are the component masses. Several formation scenarios could produce such heavy BBHs. These include: the classical isolated binary evolution channel we discuss in this paper [35, 213, 36], including formation from population III stars [217]; formation through chemically homogeneous evolution in very close tidally locked binaries [130, 129, 214]; dynamical formation in globular clusters [183, 240, 241], young stellar clusters [242], or galactic nuclei [205, 206]; or even mergers in a population of primordial binaries [224, 226]. One common feature of all GW150914 formation channels with stellar-origin black holes is the requirement that the stars are formed in sub-solar metallicity environments in order to avoid rapid wind-driven mass loss which would bring the remnant masses below $30M_\odot$ [243, 113]; see Results and Abbott *et al.* [189, 8] for further discussion.

We are developing a platform for the statistical analysis of observations of massive binary evolution, Compact Object Mergers: Population Astrophysics and Statistics (COMPAS). COMPAS is designed to address the key problem of GW astrophysics: how to go from a population of observed sources to understanding uncertainties about binary evolution. In addition to a rapid population synthesis code developed with model-assumption flexibility in mind, COMPAS also includes tools to interpolate model predictions under different astrophysical model assumptions, astrostatistics tools for population reconstruction and inference in the presence of selection effects and measurement certainty, and clustering tools for model-independent exploration.

Here, we attempt to answer the following question: can all three LIGO-observed BBHs have formed through a single evolutionary channel? We use the binary population synthesis element of COMPAS to explore the formation of the observed systems through the classical isolated binary evolution channel [244] via a Common-envelope (CE) phase [148]. We show that GW151226 and LVT151012 could have

formed through this channel in an environment at $Z = 10\%Z_{\odot}$ (with $Z_{\odot} \equiv 0.02$) from massive progenitor binaries with a total zero-age main-sequence (ZAMS) mass $\gtrsim 65M_{\odot}$ and $\gtrsim 95M_{\odot}$, respectively.

These BBHs could also originate from lower-mass progenitors with total masses $\gtrsim 60M_{\odot}$ and $\gtrsim 90M_{\odot}$, respectively, at metallicity $Z = 5\%Z_{\odot}$, where the same channel could have formed GW150914 from binaries with a total ZAMS mass $\gtrsim 160M_{\odot}$. At low metallicity, this channel can produce merging BBHs with significantly unequal mass ratios: more than 50% of BBHs have a mass ratio more extreme than 2 to 1 at $Z = 10\%Z_{\odot}$.

2.2 Methods

2.2.1 COMPAS population synthesis code

COMPAS includes a rapid Monte-Carlo binary population synthesis code to simulate the evolution of massive stellar binaries, the possible progenitors of merging compact binaries containing neutron stars (NSs) and black holes (BHs) which are potential GW sources. Our approach to population synthesis is broadly similar to BSE [245] and the codes derived from it, such as `binary_c` [246, 247, 248, 208] and `StarTrack` [249, 142].

COMPAS was developed to explore the many poorly constrained stages of binary evolution, such as mass transfer, CE evolution and natal supernova kicks imparted to NSs and BHs [244]. Here we provide a brief overview of our default assumptions.

For our `Fiducial` model, we simulate likely BBHs progenitor binaries with the primary mass m_1 drawn from the Kroupa IMF [40] up to $m_1 \leq 100M_{\odot}$ where the IMF has a power-law index of -2.3 . The mass of the secondary is then determined by the initial mass ratio $q \equiv m_2/m_1$, which we draw from a flat distribution between 0 and 1 [41].

The semimajor axis a is chosen from a flat-in-the-log distribution [250, 42] and restricted between $0.1 < a/\text{AU} < 1000$; the period distribution is therefore set

by the convolved semimajor axis and mass distributions. The boundaries on the component masses and separations are chosen to safely encompass all individual solutions yielding BBHs of interest, and so impact normalisation only. Binaries are assumed to have an initial eccentricity of zero; the initial semimajor axis distribution serves as a proxy for the periapsis distribution, which is the relevant parameter affecting binary evolution [37]. Stellar rotation and tides are not included in the **Fiducial** model.

We use the analytical fits of Hurley *et al.* [55] to the models of Pols *et al.* [56] for single stellar evolution. We note that the original grid of single star models extends only to 50 solar masses. We extrapolate above this limit, as described in Hurley *et al.* [55].

We include mass loss due to stellar winds for hot O stars following the Vink model [62, 243], with a Luminous Blue Variable (LBV) mass loss rate of $f_{\text{LBV}} \times 10^{-4} M_{\odot} \text{ yr}^{-1}$, independent of metallicity. In the **Fiducial** model $f_{\text{LBV}} = 1.5$ [243]. For Wolf-Rayet (WR) stars we use the formalism of Hamann & Koesterke [251], modified as in Belczynski *et al.* [243] to be metallicity dependent ($\propto Z^{0.85}$) based on Vink & de Koter [252]. We assume that all stellar winds are isotropic and remove the specific angular momentum of the mass losing object. We do not account for wind accretion by a companion.

Mass transfer occurs when the donor star fills its Roche lobe, whose radius is calculated according to Eggleton [138]. Although all of our binaries are initially circular, supernovae can lead to some eccentric systems. We use the periastron to check whether a star would fill its Roche lobe, whose radius is computed for a circular orbit with the periastron separation. We assume that mass transfer circularises the orbit.

In the absence of accurate stellar models spanning the full parameter space of interest, we use a simplified treatment of mass transfer. We assume that mass transfer from main-sequence, core-hydrogen-burning donors (case A) is dynamically stable for mass ratios $q \geq 0.65$. We follow de Mink *et al.* [208] and Claeys *et al.* [80] in assuming that case A systems with $q < 0.65$ will result in mergers as the accretor expands and brings the binary into contact [146]. Stable case A mass transfer is solved using an adaptive algorithm [141] which requires the radius of the donor to stay within its Roche lobe during the whole episode; when this is

impossible, we assume that any donor mass outside the Roche lobe is transferred on a thermal timescale until the donor is again contained within its Roche lobe. In our Fiducial model we first test whether mass transfer is stable; if it is, we treat stable mass transfer from all evolved stars (case B or case C) equally, without distinguishing between donors with radiative and convective envelopes: we remove the entire envelope of the donor on its thermal timescale [253]. We follow Tout *et al.* [254], Belczynski *et al.* [142] in our model for the rejuvenation of mass accreting stars.

The efficiency of mass transfer (i.e., how conservative it is) is set by the rate at which the accretor can accept material from the donor. For NS and BH accretors, the maximum rate of accretion is defined by the Eddington limit. We assume that a star can accrete at a rate $CM_{\text{acc}}/\tau_{\text{th}}$, with the Kelvin-Helmholtz thermal timescale $\tau_{\text{th}} = GMM_{\text{env}}/RL$, where G is the gravitational constant, M is the total mass of the star, M_{env} is the mass of the envelope, R is the radius of the star and L is its luminosity. The constant C is a free parameter in our model; we use $C = 10$ for all accretion episodes in the **Fiducial** model [245]. The material that fails to be accreted is removed from the system with the specific angular momentum of the accretor via isotropic re-emission.

We determine the onset of dynamically unstable mass transfer by comparing the response of the radius of the donor star to a small amount of mass loss against the response of the orbit to a small amount of mass transfer [143]. We use fits to condensed polytrope models [145, 143] to calculate the radius response of a giant to mass loss on a dynamical timescale. Dynamically unstable mass transfer leads to a CE. If the donor star is on the Hertzsprung-Gap (HG), we follow Belczynski *et al.* [255, 35] in assuming such systems cannot survive a CE. In fact, such systems may never enter CE at all. Pavlovskii *et al.* [256] have shown that in many cases mass transfer from HG donors will be stable and not lead to a CE.

All of our successful CE events therefore involve a donor star which has reached core helium-burning (CHeB). For CE events, the λ parameter, which characterizes the binding energy of the envelope [151], is set to $\lambda = 0.1$ [157, 159, 33, 35] while the α parameter, which characterizes the efficiency of converting orbital energy into CE ejection, is set to $\alpha = 1$. If one of the stars in the post-CE binary is filling its Roche lobe immediately after CE ejection, we assume that there is insufficient orbital energy available to eject the envelope and the binary evolution is terminated

in a merger. We assume that CE events with successful envelope ejections circularise orbits (see section 10.3.1 of Ivanova *et al.* [148].)

The relationship between the pre-supernova core mass and the compact remnant mass follows the ‘delayed’ model of Fryer *et al.* [125]. Supernova kicks are assumed to be isotropic and their magnitude is drawn from a Maxwellian distribution with a 1D velocity dispersion $\sigma = 250 \text{ km s}^{-1}$ [101], reduced by a factor of $(1 - f)$, where f is the fallback fraction, calculated according to Fryer *et al.* [125]. As in Belczynski *et al.* [35], we find that most of our heavy black holes form through complete fallback without a supernova or associated kick.

2.3 Results

2.3.1 Forming GW151226 and LVT151012

For relatively low-mass GW events the GW signal in the aLIGO sensitive frequency band is inspiral-dominated and the chirp mass $\mathcal{M} = Mq^{3/5}(1 + q)^{-6/5}$ is the most accurately measured mass parameter, while the mass ratio $q = m_2/m_1$ cannot be measured as accurately (see figure 4 of Abbott *et al.* [8]). The 90% credible intervals on these for GW151226 and LVT151012 are $8.6 \leq \mathcal{M}/M_\odot \leq 9.2$, $q \geq 0.28$; and $14.0 \leq \mathcal{M}/M_\odot \leq 16.5$, $q \geq 0.24$, respectively [8]. For more massive events, the ringdown phase of the GW waveform makes a significant contribution and the most accurately measured mass parameter is the total mass M . For GW150914, $M = 65.3 \pm_{3.4}^{4.1} M_\odot$ [9, 8], with mass ratio $q \geq 0.65$.

We simulate events at 10%-solar ($Z = 0.002$) and 5%-solar ($Z = 0.001$) metallicity using the **Fiducial** model assumptions (see Methods). We select binaries which fall within the 90% credible interval on total (chirp) BBH mass and with q above the 90% credible interval lower bound for GW150914 (GW151226 and LVT151012). In all cases, we select only BBHs that merge within the Hubble time. Systems satisfying these conditions are shown in Figure 2.1. The upper panel shows BBHs formed at 10%-solar metallicity whilst the lower panel shows those formed at 5%-solar metallicity. The black hole mass of the initially more massive star is labeled as M_1^{BH} and that of the initially less massive star as M_2^{BH} .

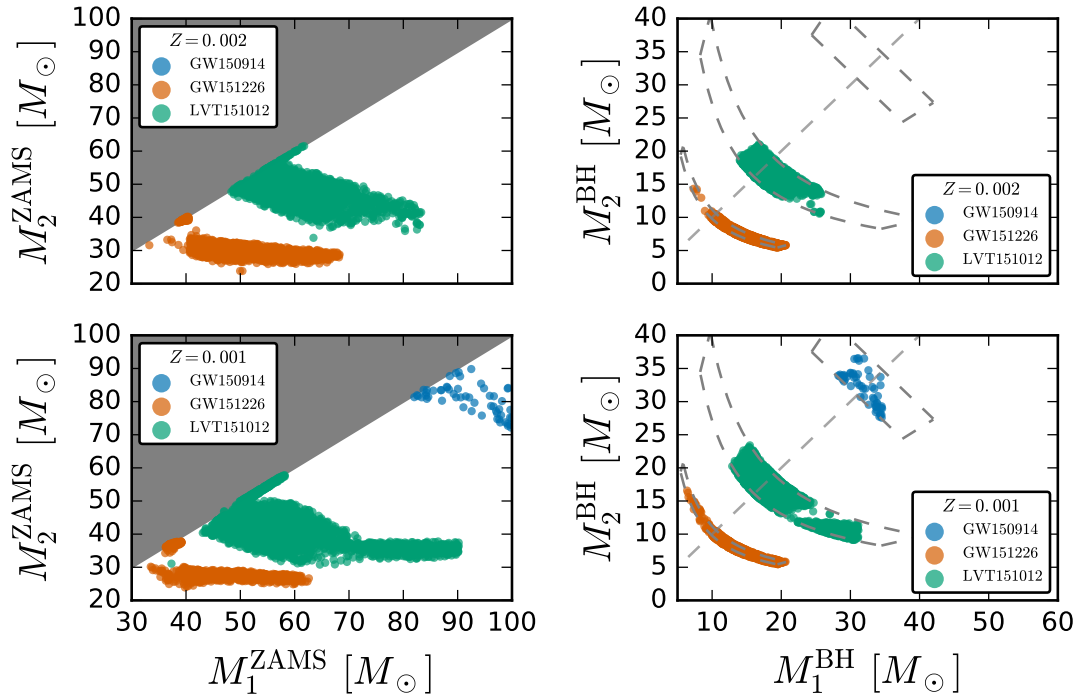


Figure 2.1: Each point in the plots represents one system in our simulations.

(a) ZAMS masses M_1^{ZAMS} and M_2^{ZAMS} for GW150914 (blue - no events), GW151226 (orange) and LVT151012 (green) progenitors at $Z = 10\%Z_\odot = 0.002$. We define $M_1^{\text{ZAMS}} > M_2^{\text{ZAMS}}$ and so shade the non-allowed region gray.

(b) Final black hole masses M_1^{BH} and M_2^{BH} for merging BBHs consistent with GW150914, GW151226 and LVT151012 formed at $Z = 10\%Z_\odot$. The grey diagonal dashed line shows $M_1^{\text{BH}} = M_2^{\text{BH}}$. The constraints we use to determine if a merging binary black hole is similar to one of the observed GW events are shown in grey and described in Results.

(c) ZAMS masses M_1^{ZAMS} and M_2^{ZAMS} for GW150914, GW151226 and LVT151012 progenitors at the lower metallicity $Z = 5\%Z_\odot = 0.001$. The progenitor masses required to produce GW151226 and LVT151012 decrease, and we are able to produce GW150914.

(d) Final black hole masses M_1^{BH} and M_2^{BH} for GW150914, GW151226 and LVT151012 BBHs formed from 5%-solar metallicity progenitors.

The panels of this figure are formatted to be comparable to Figure 4 in Abbott *et al.* [8].

Figure reproduced from Stevenson *et al.* [1].

In the left hand column of Figure 2.1 we show the ZAMS masses of possible progenitors of these events. Progenitors of the events are separated in ZAMS masses apart from rare systems that start on very wide orbits, avoiding mass transfer altogether, but are brought to merger by fortuitous supernova kicks. These systems do not lose mass through non-conservative mass transfer, and can therefore form more massive binaries from lower mass progenitors – the LVT151012 outlier progenitor in the lower left corner of the bottom left panel of Figure 2.1 was formed this way.

Massive stars have high mass loss rates; e.g., at solar metallicity, massive stars could lose tens of solar masses through winds even before interacting with their companion. We find, in agreement with Abbott *et al.* [189] and Belczynski *et al.* [35], that it is not possible to form GW150914 or LVT151012 through classical isolated binary evolution at solar metallicity. GW151226 lies at the high-mass boundary of BBHs that can be formed at solar metallicity.

GW151226 is consistent with being formed through classical isolated binary evolution at 10%-solar metallicity from a binary with total mass $65 \lesssim M/M_\odot \lesssim 100$ (see upper left panel of Figure 2.1). LVT151012 is also consistent with being formed at 10%-solar metallicity from binaries with initial total masses $95 \lesssim M/M_\odot \lesssim 125$. Typical progenitors have a mass ratio close to unity (median $q = 0.75$), with an initial orbital period of ~ 500 days.

GW150914 could have formed through isolated binary evolution at metallicities $Z \lesssim 5\%Z_\odot$ from binaries with initial total mass $\gtrsim 160M_\odot$ (see lower left panel of Figure 2.1). While this mass range is similar to that found by others who investigated the formation of GW150914 through isolated binary evolution at low metallicities [35, 36, 213], we note that, unlike Eldridge & Stanway [213], we do not require fortuitous supernova kicks resulting in high eccentricity to form this binary at $Z = 5\%Z_\odot$. We identify the same main evolutionary channel (see Figure 2.2) as Belczynski *et al.* [35]. We find that GW151226 and LVT151012 are also consistent with forming through this channel at lower metallicity, from initially lower mass binaries. For example, the total progenitor binary mass range for forming GW151226 reduces from $65 \lesssim M/M_\odot \lesssim 100$ at 10% solar metallicity to $60 \lesssim M/M_\odot \lesssim 90$ at 5%-solar metallicity, demonstrating a degeneracy in the ZAMS masses and metallicity inferred in our model due to the dependence of mass loss rates on metallicity.

We find that the chirp masses of GW151226 and LVT151012 lie near the peak

of the mass distribution of BBH mergers formed at 10%-solar metallicity which are observable by aLIGO. There remains significant support for both systems at 5%-solar metallicity. GW150914 cannot be formed at 10%-solar metallicity in our model, and remains in the tail of the total mass distribution at 5%-solar, which is the highest metallicity at which we form significant numbers of all three event types in the **Fiducial** model. Events like GW150914 are much more common at 1%-solar metallicity.

At $Z = 5\%Z_{\odot}$, the more massive black hole is formed from the initially more massive star in $\sim 90\%$ of systems.

Interestingly, low metallicities can produce significantly unequal mass ratios. For example, the median mass ratio of merging BBHs is ~ 0.5 at 10% solar metallicity. The high fraction of merging BBHs with low mass ratios at low metallicities is a general trend; this agrees with Figure 9 of Dominik *et al.* [33], who do not, however, discuss this effect. A GW detection of a heavy BBH with an accurately measured low mass ratio could indicate formation in a lower metallicity environment, and not necessarily dynamical formation as suggested in Abbott *et al.* [8].

The significant fraction of low mass-ratio mergers at low metallicity arises due to a combination of effects. The maximum BH mass for single stars is a function of metallicity (e.g., Figure 6 of Spera *et al.* [113]), with more massive BHs formed at lower metallicities due to reduced mass loss. Therefore, for a given observed chirp mass, more unequal BHs can be formed at low metallicity. A second effect comes from the difference in the onset of the first episode of mass transfer, which is key for determining the mass of the remnant. The dependence of stellar radius on metallicity [56] means that stars with lower metallicity experience their first episode of mass transfer in a more evolved phase of their evolution for a given initial orbital separation [257]. They thus lose less mass when the hydrogen envelope is stripped, again allowing for more unequal remnants.

2.3.2 Typical evolutionary pathway of GW151226

In Figure 2.2 we show the evolution in time of the masses, stellar types and orbital period of typical progenitors of all three observed GW events. Progenitors of all three systems follow the same typical channel. Here we describe the evolution

of a typical 10%-solar metallicity progenitor of GW151226 (solid orange line in Figure 2.2); it is shown graphically in Figure 2.3.

The binary initially has two high-mass main-sequence (MS) O stars, a primary of $\sim 64M_{\odot}$ and a $\sim 28M_{\odot}$ companion with an initial orbital period of ~ 300 days. The primary expands at the end of its main sequence evolution, fills its Roche lobe and initiates mass transfer as a $\sim 60M_{\odot}$ HG or CHeB star (case B or C mass transfer), donating its $\sim 36M_{\odot}$ hydrogen-rich envelope to the secondary, which accretes only $\sim 3M_{\odot}$ of it. This leaves the primary as a stripped naked helium star (HeMS) of $\sim 25M_{\odot}$. After evolving and losing a few solar masses through stellar winds, the primary collapses to a BH of $\sim 19M_{\odot}$ through almost complete fallback.

The secondary continues evolving and initiates mass transfer as a CHeB star of $\sim 30M_{\odot}$. This mass transfer is dynamically unstable and leads to the formation and subsequent ejection of a CE. The CE ejection draws energy from the orbit and results in significant orbital hardening: the orbital period is reduced by ~ 3 orders of magnitude as can be seen in the lower right panel of Figure 2.2. The secondary, which becomes a HeMS star of $\sim 11M_{\odot}$ after the ejection of the envelope, eventually collapses to a $\sim 6M_{\odot}$ BH. Finally, the binary merges through GW emission in ~ 100 Myrs.

A few percent of our BBH progenitors form through a variant of this channel involving a double CE. This variant involves two nearly equal mass ZAMS stars which first interact during the CHeB phase of their evolution, initiating a double CE which brings the cores close together. This is followed by both stars collapsing into BHs and merging through GW emission.

2.4 Discussion

We have explored whether all of the GW events observed to date could have been formed through classical isolated binary evolution via a CE phase. All three observed systems can be explained through this channel under our **Fiducial** model assumptions. Forming all observed GW events through a single formation channel avoids the need to fine tune the merger rates from the very different evolutionary channels discussed in the Introduction to be comparable. Other proposed formation

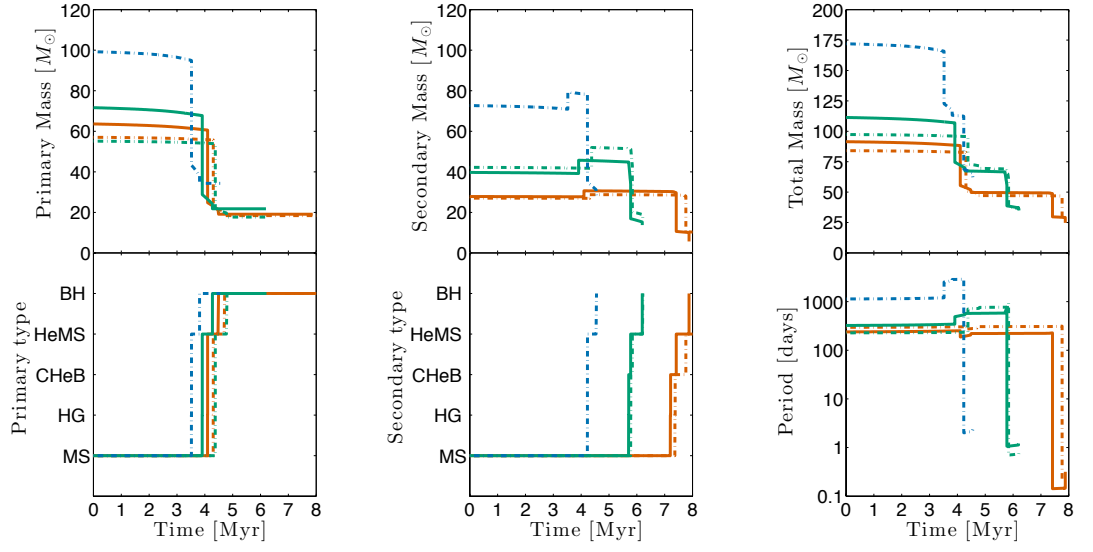


Figure 2.2: Evolution in time of representative GW150914 (blue), GW151226 (orange) and LVT151012 (green) progenitors at 10%-solar ($Z = 0.002$, solid lines) and 5%-solar metallicity ($Z = 0.001$, dashed lines). (a) The mass of the initially more massive star. The stars lose mass through stellar winds, mass transfer and supernovae. (b) The mass of the secondary star. The stars may accrete mass during mass transfer episodes. (c) The evolution of the total mass of the binary. (d) The evolutionary stage (stellar type) of the initially more massive star as given by Hurley *et al.* [55] (see Results for definitions). (e) The evolutionary stage (stellar type) of the secondary star. (f) The orbital period of the binary in days.

Figure reproduced from Stevenson *et al.* [1].

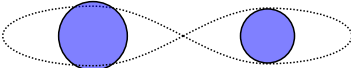
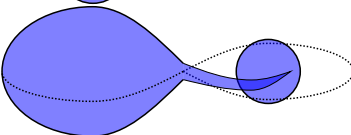
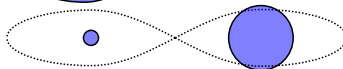
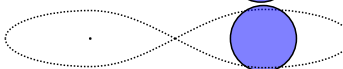
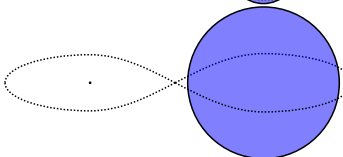
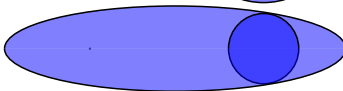


Time	M_1	ST_1		ST_2	M_2	a
[Myr]	$[M_\odot]$	–		–	$[M_\odot]$	$[R_\odot]$
0.0	63.6	MS		MS	27.8	729.93
4.1	60.4	HG		MS	27.7	757.5
4.12	24.6	HeMS		MS	30.6	622.07
4.49	19.1	BH		MS	30.6	692.7
7.21	19.1	BH		CHeB	30.3	697.48
7.42	19.1	BH		CHeB	29.7	706.33
7.42	19.1	BH		HeMS	10.6	5.18
7.88	19.1	BH		BH	5.7	8.82

Figure 2.3: Typical formation of GW151226 at 10%-solar metallicity in our model, as described in the Results. The columns show the time, the masses and stellar types of the primary and secondary, M_1 , ST_1 and M_2 , ST_2 respectively, and the semi-major axis a . Some intermediate stages of the evolution are omitted for clarity. Figure reproduced from Stevenson *et al.* [1].

scenarios struggle to produce at least one of the observed BBHs. For example, both chemically homogeneous evolution [130, 129, 214] and dynamical formation in old, low-metallicity globular clusters in the model of Rodriguez *et al.* [183] (see their figure 2) have little or no support for relatively low-mass BBHs such as GW151226, which has a total mass $M = 21.8 \pm_{1.7}^{5.9} M_{\odot}$ [8]. The ability of a single channel to explain all observed events will be tested with future GW observations [8, 14].

We form $\sim 2 \times 10^4$ BBHs that merge in a Hubble time per 1×10^9 solar masses of star formation at 10%-solar metallicity in our **Fiducial** model, using the Kroupa [40] IMF, a uniform mass ratio distribution and assuming that all stars are in binaries. This increases to $\sim 3 \times 10^4$ BBHs per 1×10^9 solar masses of star formation at $Z = 5\%Z_{\odot}$. Rescaling by the total star formation rate[258] at redshift $z = 0$, this would correspond to a BBH formation rate of $\sim 300 \text{ Gpc}^{-3} \text{ yr}^{-1}$ assuming all star formation happens at 10%-solar metallicity. This can be compared to the empirical LIGO BBH merger rate estimate[8] of $9 - 240 \text{ Gpc}^{-3} \text{ yr}^{-1}$. However, this comparison should be made with caution, because even local mergers can arise from binaries formed at a broad range of redshifts and metallicities. An accurate calculation of the merger rate requires the convolution of the metallicity-specific redshift-dependent star formation rate with the time delay distribution, integrated over a range of metallicities[259].

There are many uncertainties in the assumptions we make (see Methods for details of our default assumptions). The evolution of massive progenitor binaries is poorly constrained by observations, although there has been recent progress, such as with the VLT-FLAMES Tarantula Survey (VFTS) in the 30 Doradus region of the Large Magellanic Cloud[260].

In rapid population synthesis codes like COMPAS, these uncertainties are treated by parametrising complex physical processes into simple one or two parameter models, such as treating the CE with the α prescription [151], or scaling LBV mass loss rates with f_{LBV} . The multidimensional space of model parameters, including α and f_{LBV} , must then be explored in order to properly examine the model uncertainties.

We leave a full exploration of this parameter space for future studies with COMPAS; here we follow the common approach[33, 34, 37] of varying individual parameters independently and assessing their impact relative to the **Fiducial** model.

In the **Fiducial** model, we used the ‘delayed’ supernova model of Fryer *et al.* [125]. We have also checked that using the ‘rapid’ model of Fryer *et al.* [125] does not significantly alter the typical evolutionary pathways for forming heavy BBHs discussed here, since both models predict high-mass BH formation through almost complete fallback.

Mennekens & Vanbeveren [34] use a LBV mass loss rate of $10^{-3}M_{\odot} \text{ yr}^{-1}$. They find that such strong mass loss can shut off the typical channel for BBH formation. In COMPAS, we follow SSE [55] for identifying LBVs as massive stars with $L/L_{\odot} > 6 \times 10^5$ and $(R/R_{\odot})(L/L_{\odot})^{1/2} > 10^5$. We find that increasing the mass loss rate of LBVs from $1.5 \times 10^{-4}M_{\odot}$ to $10^{-3}M_{\odot} \text{ yr}^{-1}$ does not significantly change the total BBH merger rate; nevertheless, the number of BBH mergers similar to LVT151012 was reduced by a factor of ~ 10 for progenitors at 5%-solar metallicity.

In the **Fiducial** model we only permit evolved CHeB stars with a well defined core-envelope separation to survive CE events (see Methods). This model therefore corresponds to the pessimistic model of Dominik *et al.* [33], which is also the standard model (M1) of Belczynski *et al.* [35]. We also consider an alternate model where we allow HG donors to initiate and survive CE events, as in the optimistic model of Dominik *et al.* [33]. We find that the optimistic CE treatment predicts total BBHs merger rates which are ~ 3 times higher than the **Fiducial** model at $Z = 10\%Z_{\odot}$, and ~ 2 times higher at $Z = 5\%Z_{\odot}$. This optimistic variation also raises the total merging BBH mass that can be formed at a given metallicity; e.g., at $Z = 10\%Z_{\odot}$, the maximum total BBH mass rises from $\sim 50M_{\odot}$ for the pessimistic model to $\sim 60M_{\odot}$ for the optimistic model, as also noted by Dominik *et al.* [33]. The spread between these optimistic and pessimistic models also reflects the uncertainty in the radial evolution of very massive stars; the results of the pessimistic model could move toward those of the optimistic model if the radial expansion for the most massive stars predominantly happens during the CHeB phase rather than during the HG phase.

For a very small number of our simulated systems, immediately after the CE is ejected the binary is comprised of a BH and a HeMS secondary that is already overfilling its Roche lobe. In the **Fiducial** model we treat these systems as an unsuccessful CE event, leading to mergers. Similar studies [146, 261] have allowed only those systems which overfill the Roche lobe by no more than 10% at the end of the CE phase to survive. We also consider the extreme alternative of allowing all

such systems to survive. The HeMS stars lose a significant fraction of their mass through rapid but stable mass transfer onto the BH companion. Most of this mass is removed from the binary as the BH companion can only accrete at the Eddington limit, and the HeMS star leaves behind a relatively low mass BH. We verify that this has no impact on our conclusions.

We test the impact of the assumed CE ejection efficiency by changing the value of $\alpha\lambda$ from the fiducial 0.1 to 0.01. At 10%-solar metallicity we find the total BBH merger rate drops by a factor of ~ 2 . Dominik *et al.* [33] performed the same study, setting $\alpha\lambda = 0.1$ (model V2) and $\alpha\lambda = 0.01$ (model V1) and report the same decrease (see tables 1,2 and 3 in Dominik *et al.* [33]). At 5%-solar metallicity, the total BBH merger rate drops by a factor of ~ 4 , with the specific merger rates of binaries like GW151226, LVT151012, and GW150914 dropping by factor of ~ 25 , ~ 4 , and ~ 50 , respectively. The maximum BBH mass produced at 10%-solar metallicity increases from $\sim 50M_{\odot}$ in the `Fiducial` model to $\sim 60M_{\odot}$ under this variation. At 5%-solar metallicity we find that the maximum total BBH mass decreases from $\sim 75M_{\odot}$ to $\sim 65M_{\odot}$.

In conclusion, we have shown that GW150914, GW151226 and LVT151012 are all consistent with formation through the same classical isolated binary evolution channel via mass transfer and a common envelope. GW observations can place constraints on the uncertain astrophysics of binary evolution [262, 263, 2, 123, 124]. Although the focus of this paper has been on the constraints placed by the observed BBH masses, other observational signatures, including merger rates (and their variation with redshift) [264], BH spin magnitude and spin-orbit misalignment measurements [265, 266, 207], and possibly a GW stochastic background observation [267, 268], can all contribute additional information. COMPAS will provide a platform for exploring the full evolutionary model parameter space with future GW and electromagnetic observations.

Acknowledgments

We would like to thank Chris Belczynski, Christopher Berry, Natasha Ivanova, Stephen Justham, Vicky Kalogera, Gijs Nelemans, Philipp Podsiadlowski, David Stops and Alberto Vecchio for useful discussions and suggestions. IM acknowledges

support from STFC grant RRCM19068.GLGL; his work was performed in part at the Aspen Center for Physics, which is supported by National Science Foundation grant PHY-1066293. AVG acknowledges support from CONACYT. SS and IM are grateful to NOVA for partially funding their visit to Amsterdam to collaborate with SdM. SdM acknowledges support by a Marie Skłodowska-Curie Action (H2020 MSCA-IF-2014, project id 661502) and National Science Foundation under Grant No. NSF PHY11-25915.

Author contributions

All authors contributed to the analysis and writing of the paper.

Data Availability

We make the results of our simulations available at <http://www.sr.bham.ac.uk/compas/>.

Competing Financial Interests

The authors declare no competing financial interests.

Chapter 3

Distinguishing compact binary population synthesis models using gravitational wave observations of coalescing binary black holes

Simon Stevenson,^{1,2} Frank Ohme,² Stephen Fairhurst²

¹ School of Physics and Astronomy, University of Birmingham, Edgbaston, Birmingham B15 2TT, United Kingdom

² School of Physics and Astronomy, Cardiff University, The Parade, Cardiff, CF24 3AA, United Kingdom

This Chapter reproduces the text of Stevenson *et al.* [2], published in ApJ, with permission of the journal. Simon Stevenson performed the analysis, made the figures and wrote the text. Frank Ohme performed the horizon distance and fisher matrix calculations, and made Figures 3.1, 3.2 & 3.3. All authors edited the text.

This paper was written before the start of O1. As such, it does not discuss any of the detections.

Abstract

The coalescence of compact binaries containing neutron stars or black holes is one of the most promising signals for advanced ground-based laser interferometer gravitational-wave detectors, with the first direct detections expected over the next few years. The rate of binary coalescences and the distribution of component masses is highly uncertain, and population synthesis models predict a wide range of plausible values. Poorly constrained parameters in population synthesis models correspond to poorly understood astrophysics at various stages in the evolution of massive binary stars, the progenitors of binary neutron star and binary black hole systems. These include effects such as supernova kick velocities, parameters governing the energetics of common envelope evolution and the strength of stellar winds. Observing multiple binary black hole systems through gravitational waves will allow us to infer details of the astrophysical mechanisms that lead to their formation. Here we simulate gravitational-wave observations from a series of population synthesis models including the effects of known selection biases, measurement errors and cosmology. We compare the predictions arising from different models and show that we will be able to distinguish between them with observations (or the lack of them) from the early runs of the advanced LIGO and Virgo detectors. This will allow us to narrow down the large parameter space for binary evolution models.

3.1 Introduction

The aLIGO [239] and Advanced Virgo (AdV) [13] second generation, kilometre-scale ground based laser interferometers are currently being commissioned and should begin observing runs in 2015 [14] with the sensitivity increasing gradually over a number of years before reaching their design sensitivity near the end of the decade. These GW observatories will be an order of magnitude more sensitive than the first generation observatories and are expected to yield the first GW detections [269] and herald the beginning of GW astronomy. In GW astronomy we are interested in the emission of gravitational radiation from astrophysical sources. One of the primary sources of GWs for aLIGO is the coalescence of compact binaries – binary neutron star (BNS), neutron star-black hole (NSBH) and BBH systems.

The orbits of these systems decay due to radiation reaction [172, 173], causing the two objects to spiral in towards one another. During the final orbits and merger, these sources emit a large amount of gravitational radiation, and this will be observable by aLIGO and AdV. The gravitational waveform emitted by the binary can be modelled with great accuracy using the post-Newtonian formalism [270]. Closer to merger, full numerical simulations are required to track the binary evolution and calculate the waveform (see Hannam [271], Hinder [272], Sperhake *et al.* [273] for overviews). By combining the insights of post-Newtonian theory and numerical modelling, a large range of analytic/semi-analytic approximate waveform models have been developed over the past few years (see, e.g., Buonanno *et al.* [274] and Ohme [275] for an overview). These models now provide accurate waveforms over a large fraction of the parameter space of non-precessing BBHs. In particular, they provide accurate waveforms for signals with a range of mass ratios and also cover the space of aligned spins. There is ongoing work [276, 277] to extend these to the full parameter space that incorporates spin-induced precession of the binary orbit.

The availability of accurate waveform models makes a matched filter search of these signals feasible [278, 279] and allows us to extract the physical parameters of the binary system from the observed GW signal [280, 281]. The observed sky location and orientation of the binary system will be used to aid searches for electromagnetic counterparts of GW systems [282, 283, 284, 285]. Meanwhile, measurement of the masses and spins of the binary components will shed light upon

the formation and evolution of the binary by comparing the observations with predictions from stellar evolution models. We expect the majority of systems to be observed with relatively low signal-to-noise ratio (SNR) and consequently the parameters will not be measured with great accuracy [286, 287]. For an individual binary, the *chirp mass* of the system — a combination of the two masses that determines the rate at which the binary evolves — can be measured with good accuracy [288, 286], while the mass ratio and spins are unlikely to be well constrained.

In addition, there is significant uncertainty in the astrophysical mass and spin distributions of black hole binaries. Thus, it seems unlikely that the measurement of parameters from individual systems will significantly impact our understanding of black hole binary formation. Instead, it will require the measurement of parameters from a population of signals to significantly constrain compact binary formation and evolution models. In this paper, we consider how this might be done and what we expect to learn with the observations from the early aLIGO and AdV runs.

Compact binaries can be formed as a result of the evolution of isolated massive binaries (where the components have initial masses $\geq 8M_{\odot}$) or can be formed dynamically (i.e., in dense globular and nuclear star clusters) from binary-single star interactions between compact remnants and primordial binaries [264]. While the key stages of the binary evolution are well understood, there are significant uncertainties in the details of the process. Population synthesis codes attempt to model these uncertainties using empirical prescriptions. These models contain numerous parameters which are not well constrained relating to astrophysics such as stellar winds, supernova kicks imparted on black holes at birth and common envelope binding energy among others. Varying these parameters will have a significant impact on both the predicted rate of compact binary mergers, as well as the distribution of expected masses and spins of the compact remnants that comprise the binary [33].

In this paper, we introduce a straightforward model selection method to distinguish between various formation and evolution scenarios. We focus on the two parameters that will be best measured: the overall rate of binary mergers and the chirp masses of the observed binaries.

Furthermore, we restrict attention to BBHs as, based upon the recent population synthesis models, these are predicted to be the most numerous [32, 33]. We caution, however, that detection rates are highly uncertain and previous papers have argued

that there will be essentially no BBHs [255, 34]. This trivially means that any detections of merging BBHs will allow models predicting a dearth of such systems to be ruled out, shedding light on the astrophysical assumptions made therein. Beyond that, we show how, in addition to the merger rates, the broad range of BBH chirp masses predicted by population synthesis models encodes information about the BBH formation mechanisms.

There have been many studies performed over the last decade that have made use of either one or both of these pieces of information to distinguish between competing astrophysical models. Bulik & Belczyński [262] used a Kolmogorov-Smirnov test to compare simulated GW chirp mass measurements to a series of predicted observed distributions from population synthesis models. They find they can distinguish many models with ~ 100 observations, a finding we confirm in the present study. Kelley *et al.* [289] use a Bayesian approach introduced in Mandel [290] to show how one can use GW observations along with dark matter simulations to distinguish between different natal kick-velocity models, and again find they require $\mathcal{O}(100)$ observations to distinguish between models.

Belczynski *et al.* [291] discuss using upper limits on binary merger rates to distinguish between population synthesis models. Recently, Mandel *et al.* [123] have shown how one can use population synthesis models along with GW observations of binary mergers to measure the relative rate of BNS, NSBH and BBH mergers with $\mathcal{O}(10)$ observations. In addition, Messenger & Veitch [292] show how one should use all of the information available to avoid selection biases when attempting to make inferences about distributions of rates and parameters of merging binaries.

More sophisticated techniques have also been discussed in the literature. O’Shaughnessy [263] introduces a framework to incorporate measurements of both the merger rate and parameter distributions of GW observations, and compares these to a set of population models which sparsely sample the relevant parameter space. A similar technique is used in Mandel & O’Shaughnessy [264] (see also [293]).

Here, we introduce a fast, simple method to make inferences about astrophysical models using information from GW observations. The method is general, and could be applied to any set of binary evolution models. We illustrate its utility by evaluating the ability to distinguish between a suite of population synthesis models [33]. For concreteness, we restrict attention to the expected results from the early

observing runs of the advanced GW detector era [14].

Population synthesis models typically predict the galactic rate of binary mergers and the parameter distributions. From this, we model the observed distribution by accounting for observational bias: GW detectors are able to observe signals from higher mass systems to a greater distance. Additionally, we incorporate cosmological effects that lead to a red-shifting of both the observed masses and the observed merger rate. Finally, we model measurement errors and uncertainties inherent in the extraction of the signal from a noisy data stream. For each population synthesis model, we generate an expected observed rate and associated mass distribution.

Based on simulated observational results, we can use model selection to differentiate between the various models. To give a sense of what we can expect, we simulate results from the early aLIGO and AdV observational runs. To do this, we choose one of models from a suite of population synthesis models to play the role of the universe, and draw GW observations of BBHs from it, accounting for known observational biases and anticipated measurement errors. We then compare these observations to the full suite of population synthesis models and, starting with a uniform prior on the models, we compute the posterior probability for each model.

While the results that we present are limited to these specific scenarios, the method we introduce is general and could easily be applied to the predictions from any population synthesis model and the results (predicted or observed) from any detector network. We also caution the reader that the models of Dominik *et al.* [33] represent the most optimistic predictions of BBH merger rates, with all models predicting a detection within the first two aLIGO and AdV science runs. Lower merger rates would lead to observations of BBH mergers only in later runs at, or close to the design sensitivity of the detectors. For an overview of rate predictions for aLIGO and AdV see [269].

This paper is structured in the following way. In Section 3.2 we give a brief review of compact binary formation, and introduce the models we use in Section 3.2.2. In Section 3.3 we describe our algorithm for accounting for known selection biases, converting an intrinsic chirp mass distribution to a predicted observed distribution. Section 3.4 shows how to use information from the two well measured parameters — the chirp mass and the merger rate — to distinguish between population synthesis models. In Sections 3.5 & 4.5 we show what we may be able to learn about binary

evolution using GW observations of binary black holes from the first two aLIGO and AdV science runs. Finally in Section 3.7 we conclude and suggest areas which require further investigation.

3.2 Compact binary formation and evolution

In this section, we provide a brief review of isolated binary evolution, highlighting the poorly understood stages of the evolution, which lead to the uncertainties in the predicted merger rates and mass distributions of the binaries. For more information see a review such as Postnov & Yungelson [294].

3.2.1 General overview

For a single star, its evolution is solely determined by the zero-age main sequence (ZAMS) mass and composition. However, the majority of massive stars exist in binaries or multiple systems, with $\gtrsim 70\%$ of massive O-type stars exchanging mass with a companion during their lifetime [44, 41, 45]. In this case, the evolution is no longer straightforward, and can lead to a plethora of exotic systems. Here we give one possible evolutionary pathway for a massive binary; many alternative pathways also exist (see for example Tables 4 & 5 in Dominik *et al.* [33] for a summary).

Consider a binary in which both stars have ZAMS masses $\gtrsim 8M_{\odot}$. The initially more massive star (the primary) in the binary will evolve off of the main sequence first since it has the shorter lifetime. As it evolves, its radius expands until it fills its Roche Lobe as a giant and begins to transfer mass to the companion (the secondary) star, stripping the primary's hydrogen outer layers and leaving a He/Wolf-Rayet star. Already the evolution of the binary is different to that of single stars since the companion can change its mass considerably, leading in some cases to a reversal of the mass ratio. If the core is massive enough, the primary will then collapse in a supernova, and leave behind a compact remnant — either a neutron star or a black hole depending on the pre-supernova core mass.

In stellar evolution models, the distinction between collapse to a neutron star or

a black hole is made via mass alone, with the maximum allowed mass of a neutron star being one of the free parameters. In reality, the maximum neutron star mass is set by the unknown neutron star equation-of-state. The maximum observed neutron stars have masses around $2M_{\odot}$ [118, 119]. Causality and General relativity require the maximum neutron star mass to be $\leq 3.2M_{\odot}$ [295, 296].

The mechanism of the supernova itself is intensely studied but still not fully understood. If the supernova is asymmetric (due to asymmetric mass loss or neutrino emission) the resulting neutron star can be given a natal kick velocity due to the conservation of momentum, which is of the order 250 km s^{-1} for galactic neutron stars [101]. It is unclear whether black holes also receive a kick of this magnitude or whether mass falling back onto the black hole reduces the size of this kick significantly (see for e.g. [297, 107, 108]).

If the system survives the first kick, then the secondary will begin to evolve. The compact remnant accretes matter from the stellar wind of its companion, becoming a luminous X-ray source. At this stage, the binary may be observable electromagnetically as a high-mass X-ray binary. Although the theory of stellar winds is fairly robust [61], the strength of stellar winds in these systems remains uncertain [298].

As the secondary continues to evolve, it will continue to expand and fill its Roche Lobe. If the mass transfer through Roche Lobe Overflow is unstable, a common envelope phase [148, 299] can be initiated. This is where both the compact remnant and the core of the secondary orbit within the secondary's hydrogen outer layers. The common envelope is the least well understood phase in the evolution of binaries. The common envelope is usually parametrised in one of two fashions; the α prescription [151] focusing on conservation of energy, or the γ prescription [164] focusing on conservation of angular momentum. The core and compact object spiral in towards one another on a dynamical timescale due to drag, and orbital energy is used to eject the envelope. This stage is responsible for dramatically reducing the orbital separation in the binary.

If the binary survives the common envelope, the core of the secondary can then go supernova, potentially imparting a second kick on the system (although it is generally less likely to unbind the system since the orbital velocities are now much higher). Finally, a compact binary remains containing neutrons stars and/or black holes. It is these systems which then inspiral towards one another and merge due

to radiation reaction, and will be observed in GWs by aLIGO and AdV.

3.2.2 Detailed binary evolution models

Population synthesis codes are Monte-Carlo simulations that evolve large ensembles of primordial binaries via semi-analytical prescriptions, taking as input parameters corresponding to the poorly understood astrophysical stages outlined above. Binary population synthesis models can be used to try to understand the effects of these uncertainties on binary evolution, and on the resultant population of compact binaries. One way to exploit the information contained in GW observations of coalescing BBHs is therefore to compare the measured properties of a population to population synthesis model predictions.

For this study we use a set of publicly available¹ population synthesis models presented in Dominik *et al.* [33], produced using the **StarTrack** population synthesis code [142]. Predicted chirp mass distributions and merger rates of BNS, NSBH and BBH systems are provided for a range of input physics.

The relative rates of BNS, NSBH and BBH mergers are uncertain. Although BBH systems are more massive (and consequently detectable to a greater distance), much more massive stars are needed in order to form them, and the IMF falls off rapidly at high masses, meaning these stars are rarer. It is also worth noting that no BBH has ever been observed, although systems which may be progenitors for them such as Cyg X-3 [300], IC 10 X-1 [301] and NGC 300 X-1 [302, 301] have been studied and provide some limits on BBH merger rates. The population synthesis model we are utilising predicts that BBH detection rates will dominate over those for BNS and NSBH. Based on this, and to keep the analysis simple, we restrict our attention to BBH systems. It would be relatively straightforward to extend the framework we introduce to include *all* GW observations of binary mergers.

We use the set of 12 population synthesis models for which predicted rates and mass distributions are available. These models are summarised in Table 3.1. The standard model assumes a maximum neutron star mass of $2.5M_{\odot}$, uses the *rapid* supernova engine detailed in Fryer *et al.* [125], physically motivated common

¹<http://www.syntheticuniverse.org>

Model	Physical difference
Standard	Maximum neutron star mass = $2.5 M_{\odot}$, <i>rapid</i> supernova engine [125], physically motivated envelope binding energy [158], standard kicks $\sigma = 265 \text{ km s}^{-1}$
Variation 1	Very high, fixed envelope binding energy ^a
Variation 2	High, fixed envelope binding energy ^a
Variation 3	Low, fixed envelope binding energy ^a
Variation 4	Very low, fixed envelope binding energy ^a
Variation 5	Maximum neutron star mass = $3.0 M_{\odot}$
Variation 6	Maximum neutron mass = $2.0 M_{\odot}$
Variation 7	Reduced kicks $\sigma = 123.5 \text{ km s}^{-1}$
Variation 8	High black hole kicks, $f_b = 0$
Variation 9	No black hole kicks, $f_b = 1$
Variation 10	<i>Delayed</i> supernova engine [125]
Variation 11	Reduced stellar winds by factor of 2

Table 3.1: Summary of population synthesis models presented in Dominik *et al.* [33], with parameter variations indicated in the second column which broadly relate to the uncertainties in binary evolution discussed in the text. All other parameters retain their standard model value. Table reproduced from [2].

^a See Section 2.3 in Dominik *et al.* [33] for details

envelope binding energy [158], and kick velocities for supernova remnants drawn from a Maxwell distribution with a characteristic velocity of $\sigma = 265 \text{ km s}^{-1}$. There are then eleven variations, in each of which one of the above parameters is varied: the first four variations consider changes in the energetics of the common envelope phase, the next two vary the maximum mass of neutron stars, three more change the kick imparted on the components during collapse to a neutron star or black hole and the final two consider a delayed supernova engine and a change in the strength of stellar winds. The models are described in detail in section 2 of Dominik *et al.* [33].

We expect that in general, the true universe will not match one of a small set of models, but will lie in between these models (or potentially outside of them if additional unmodelled physics is required to accurately describe binary evolution). Assumptions that are not varied in these models, but which may have a large impact on the resultant BBH distribution include distributions of the parameters of primordial binaries (IMF, orbital elements [37]), tides, stellar rotation [208] and magnetic fields. Here we neglect these additional considerations and investigate how one can differentiate between a small suite of population synthesis models using GW observations of BBHs. A full treatment of these additional properties

has the potential to significantly impact stellar evolution models and may well lead to degeneracies whereby significantly different astrophysical models predict comparable populations of binaries.

Since calculating population synthesis models can be computationally expensive, the models are discretely sampled over a large range of parameter space (in some cases orders of magnitude) in an attempt to bracket the truth. Furthermore, each of the models used in this study varies only one parameter from its standard value at a time. It is quite likely that the true values of many of these parameters will differ from those presented in Dominik *et al.* [33], resulting in a population that does not match any of the ones included here. Varying combinations of parameters will also need to be studied, as this may lead to issues with degeneracies in which combinations of parameters can be determined from GW observations. To be able to reliably extract the details of stellar evolution from GW observations, one would require to have models calculated on a dense enough grid that one can perform interpolation between them [263, 303].

Metallicity

Each model is calculated at solar ($Z = 0.02 = Z_{\odot}$) and sub-solar ($Z = 0.002 = 0.1Z_{\odot}$) metallicities. In addition, there are two submodels that differ in the way binaries entering into a common envelope when one of the stars is on the Hertzsprung gap are handled (see section 3.2.2).

We choose to use a 50-50 mixture of the solar and sub-solar models as used in Belczynski *et al.* [243], motivated by results from the Sloan Digital Sky Survey (SDSS, [304]) showing that star formation is approximately bimodal with half of the stars forming with $Z \sim Z_{\odot}$ and the other half forming with $Z \sim 0.1Z_{\odot}$. For the future, it would be desirable to include a more thorough treatment of the metallicity distribution, including its evolution with cosmic star formation history as done in Dominik *et al.* [305, 259].

Although metallicity in the local universe may be bimodal, one still expects a smooth distribution of metallicities to exist. Using only a discrete mixture of solar and sub-solar metallicity predictions may give rise to non-physical peaks or sharp features in the chirp mass distributions which may artificially aid in distinguishing

between them [259]. However, in practise we find that these peaks are sufficiently smoothed out by measurement errors (see section 3.3.4).

Studies have shown that the majority of BBHs observable by aLIGO were formed within ~ 1 Gyr of the Big Bang [305, 259], when the metallicity of the universe was distinctly lower. This is due to a number of reasons (see for example [243]). It is easier for supernova progenitor stars to remain massive at lower metallicities due to weaker stellar winds compared to at solar metallicity. Also, many potential BBH progenitor systems merge prematurely at higher metallicities during the CE phase since the secondary is likely to be on the Hertzsprung Gap, whereas at lower metallicities the secondary does not expand enough to initiate a CE event until it is a core-helium burning star (see Hurley *et al.* [55] for the effect of metallicity on stellar radius). These BBHs are formed with long delay times such that they are only merging now. One therefore needs to include the time evolution of metallicity to accurately model the expected population of BBHs mergers [305].

Fate of Hertzsprung Gap donors

The Hertzsprung gap is a short lived (Kelvin-Helmholtz timescale) stage of stellar evolution where a star evolves at approximately constant luminosity across the Hertzsprung-Russell diagram after core hydrogen burning has been depleted but before hydrogen shell burning commences.

Whilst on the main sequence, stars are core burning hydrogen, and do not possess a core-envelope separation as the helium core is still being formed. Therefore, if a main sequence star enters into a common envelope, orbital energy is dissipated into the whole star, rather than just the envelope, making ejecting the envelope extremely difficult. It is therefore expected that any star entering into a common envelope phase whilst on the main sequence will result in the two stars merging prematurely in an event which is not interesting from a GW astronomy point of view.

For stars that are on the Hertzsprung gap, the situation is not so clear. The helium core begins contracting whilst the envelope of the star expands. It is unclear if there is sufficient core-envelope separation on the Hertzsprung gap for a star entering a common envelope phase to have its envelope ejected, or whether it would

suffer a similar fate to a main sequence star.

The fate of Hertzsprung Gap donors is another of the uncertainties that is investigated by Dominik *et al.* [33]. In the optimistic submodel (referred to as submodel A in Dominik *et al.* [33]), the authors ignore the issue and calculate the common envelope energetics as normal [151]. In the pessimistic submodel (referred to as submodel B), any binary in which the donor is on the Hertzsprung gap when the binary enters into a common envelope phase is assumed to merge. This tends to reduce the number of merging binaries (and thus the rates) compared to the optimistic model. It is unlikely that either of these models is accurate, as the fate of a Hertzsprung gap donor will depend on the internal structure of the star as it enters the common envelope phase. Nonetheless, submodels A and B provide upper and lower bounds, respectively, on the number of Hertzsprung gap donors forming BBH.

In this paper, we compare results for the twelve models listed above for *both* the optimistic (submodel A) and pessimistic (submodel B) Hertzsprung gap evolution.

3.3 Predicted observed distributions

For each of the models described above, we are given an expected rate of binary mergers per Milky Way Equivalent Galaxy (MWEG), as well as a distribution of binary parameters (notably the component masses). The population of BBHs observed by the advanced GW detectors will differ from this underlying intrinsic distribution due to the following observational effects.

- (a) The GW signal from binaries at large distances will be red-shifted due to the expansion of the universe which consequently leads to a shifted measurement of the binary's total mass.
- (b) The GW amplitude scales with the binary's total mass, thus binaries with heavier components will be observable to greater distances, provided their signal still lies in the sensitive frequency region of the detector, which leads to an increased number of observed high-mass systems.
- (c) Due to the presence of noise in the detector the best-measured parameters will differ from the binary's intrinsic parameters which effectively blurs the

observed distribution.

We take all three effects into account and calculate the distribution of parameter we expect to observe. Our approach is consistent with previous methods in the literature (e.g., Dominik *et al.* [259]), apart from how we account for measurement errors across the parameter space. For completeness, in the remainder of the section, we briefly recap how these effects are accounted for and the observed distribution obtained.

3.3.1 Detectability

We model the GW signals by the dominant harmonic only, which is sufficient for the majority of black hole systems we are considering [306, 307]. The signal observed in a GW detector can then be expressed as [308]

$$h(t) = \frac{1}{D_{\text{eff}}} [h_0(t) \cos \Phi + h_{\pi/2}(t) \sin \Phi], \quad (3.1)$$

where D_{eff} is called the effective distance, Φ is the coalescence phase as observed in the detector and $h_{0,\pi/2}$ are the two phases of the waveform which are offset by $\pi/2$ relative to each other [equivalently, their Fourier transforms obey $\tilde{h}_0(f) = i\tilde{h}_{\pi/2}(f)$]. The effective distance is defined as

$$D_{\text{eff}} = \frac{D_L}{\sqrt{F_+^2(1 + \cos^2 \iota)^2/4 + F_\times^2 \cos^2 \iota}}. \quad (3.2)$$

D_L is the luminosity distance to the binary, $F_{+,\times}$ are the detector response functions and ι is the binary inclination angle. The maximal (and circularly polarised) GW signal is obtained when the signal is directly overhead the detector $F_+ = 1$; $F_\times = 0$ and with $\iota = 0, \pi$ corresponding to a face on signal.

The effective distance is inversely proportional to the SNR, ρ , which is defined as [288, 309]:

$$\rho^2 = 4 \int_{f_{\text{low}}}^{\infty} \frac{|\tilde{h}(f)|^2}{S_n(f)} df, \quad (3.3)$$

where $\tilde{h}(f)$ is the frequency-domain gravitational waveform and the detector noise power spectral density is denoted by $S_n(f)$. We choose a lower cutoff frequency

of $f_{\text{low}} = 20 \text{ Hz}$, suitable for the early advanced detectors. The SNR at which a signal can be detected will depend upon the details of the detector network, including the sensitivities of the detectors as well as the character of the data — non-stationarities in the data make it more difficult to distinguish candidate signals from the background noise. However, for studies such as this, it is convenient to choose an approximate threshold. Experience has shown that a network SNR of 12 is approximately where we might expect to make a detection [310, 14]. This corresponds to an SNR of around 8 in each of the LIGO detectors in the early science runs². For the studies presented in this paper, we use this simple, single detector threshold to decide whether a signal would be observed by the detector network.

Given a model for the waveform, $h(t)$, we can calculate the maximum effective distance to which the signal could be detected. This is known as the *horizon distance*, D_H , and corresponds to the maximal distance at which the signal could be observed if it is optimally oriented and overhead. To calculate the horizon distance we use the phenomenological waveform model introduced by Santamaría *et al.* [311] that includes the inspiral, merger and ringdown sections of the waveform calibrated using numerical relativity. The model provides the waveform $\tilde{h}(f)$ in the frequency domain as a function of the binary's total mass M , its symmetric mass ratio η and an effective total spin parameter, χ .

The mass parameters of the binaries are characterized in terms of the best measured parameter combination, the so called *chirp mass* \mathcal{M} , which is a combination of the component masses m_1 and m_2 ,

$$\mathcal{M} = \frac{(m_1 m_2)^{3/5}}{(m_1 + m_2)^{1/5}} = M \eta^{3/5}, \quad (3.4)$$

where $M = m_1 + m_2$ is the total mass, and η is the symmetric mass ratio,

$$\eta = \frac{m_1 m_2}{(m_1 + m_2)^2} \leq 0.25. \quad (3.5)$$

For an equal mass binary $m_1 = m_2 = m$, the chirp mass $\mathcal{M} \approx 0.87m$. In the remainder of the paper, we will focus on the predicted and observed chirp mass

²For the early science runs, we expect the LIGO detectors to be about twice as sensitive as Virgo so, on average, one might expect a threshold event to have SNR of 8 in each of the LIGO detectors and 4 in Virgo

distributions, and not consider mass ratio or spin.

Our aim is to predict the observed chirp mass distribution given the intrinsic model prediction, and compare these with observations.

Throughout most of this paper, we assume the early aLIGO (circa 2015) noise spectrum [312, 14] representing the expected sensitivity of aLIGO during its first observing runs. A plot of the horizon distance as a function of the chirp mass and the symmetric mass ratio is given in Figure 3.1. It encodes the farthest distance to which a BBH with the given parameters can be seen. The horizon distance will also be a function of the black hole spins. Since Dominik *et al.* [33] do not provide individual spin information in their catalogues, we set the spin parameter to zero for simplicity when simulating signals in our synthetic universe. Our ignorance of the spins may lead to systematic biases, as high spins can noticeably affect the horizon distance [313] and could change the rate of observed signals by a factor of two or three [259]. One could incorporate this lack of knowledge by assuming a spin distribution for black holes and marginalizing the result over the spins. We defer this to a later study when more informed spin priors (observationally motivated or from population synthesis) can be incorporated.

Not every binary within the horizon will be detected, as D_{eff} is location and orientation dependent. Under the assumption of a uniform distribution over the sky and a uniform source orientation, however, we can numerically calculate the fraction $P(\xi)$ of systems with

$$\frac{D_L}{D_{\text{eff}}} = \sqrt{F_+^2(1 + \cos^2 \iota)^2/4 + F_\times^2 \cos^2 \iota} > \xi, \quad (3.6)$$

with $\xi \in [0, 1]$. Note that $P(\xi)$, which we can interpret as a cumulative distribution function, is independent of the binary's masses, and we will use it to determine what fraction of signals at a given luminosity distance is detectable, i.e., has an SNR larger than the detection threshold.

3.3.2 Cosmological effects

We simulate an expanding universe with sources distributed uniformly and isotropically in comoving volume, which on scales of hundreds of Mpc is a valid assumption.

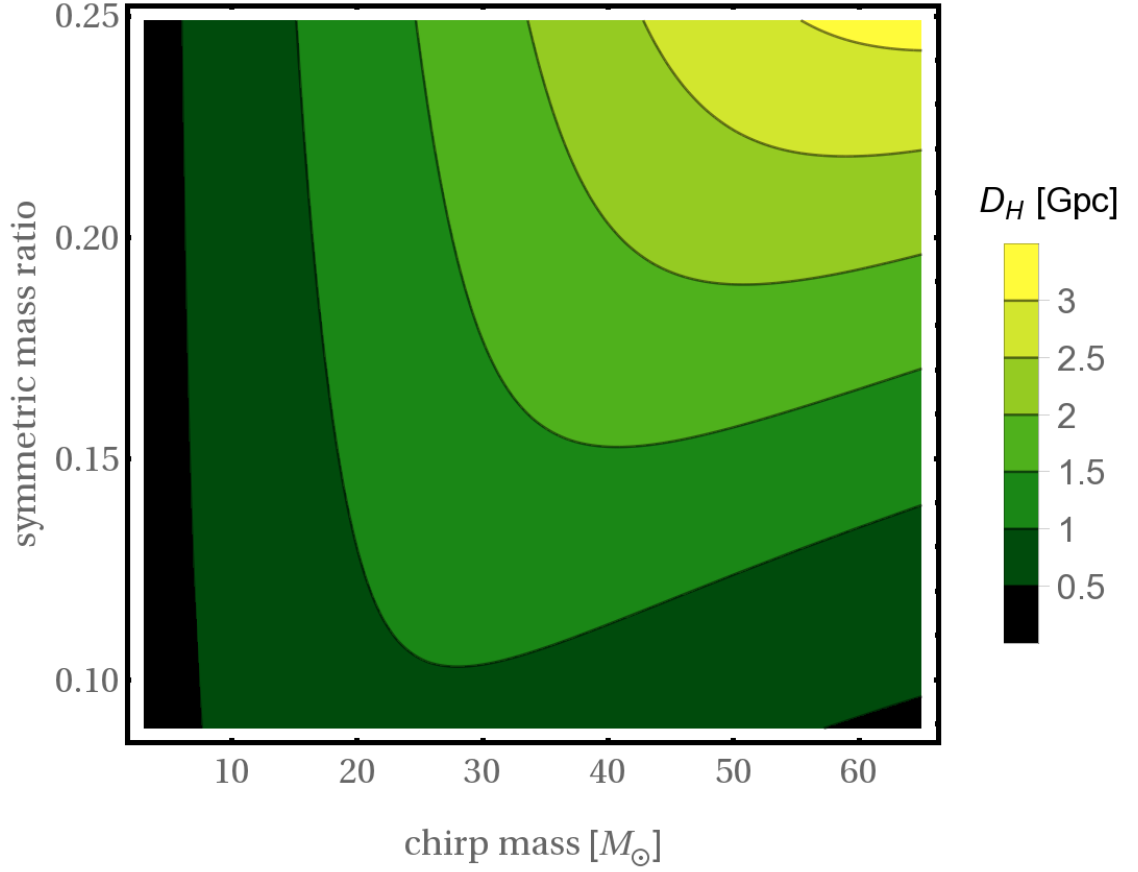


Figure 3.1: Horizon distance in Gpc for nonspinning BBHs as a function of chirp mass and symmetric mass ratio assuming a single detector with the early aLIGO noise spectrum. Figure reproduced from [2].

Since the frequencies of any signal become increasingly redshifted with growing distance between source and detector, the total chirp mass measured at the detector is shifted by

$$\mathcal{M}^* = \mathcal{M}(1 + z), \quad (3.7)$$

where z denotes the redshift. Assuming zero curvature and standard cosmological parameters [314]

$$\Omega_M = 0.286, \quad \Omega_\Lambda = 1 - \Omega_M, \quad H_0 = 69.6, \quad (3.8)$$

we calculate the comoving distance as a function of the redshift [315],

$$D_C(z) = \frac{c}{H_0} \int_0^z \frac{dz'}{\sqrt{\Omega_M(1+z')^3 + \Omega_\Lambda}}. \quad (3.9)$$

Here, c denotes the speed of light.

The catalogues by Dominik *et al.* [33] provide large sets of binaries characterized by their intrinsic chirp mass \mathcal{M} and symmetric mass ratio η . When we distribute them uniformly in comoving volume, the observed chirp masses \mathcal{M}^* are redshifted according to (3.7). This implies that the maximal distance to which they can be detected changes as it is the observed parameters, not the intrinsic parameters, that determines the appropriate horizon distance. Since

$$D_L = D_C(1+z), \quad (3.10)$$

the maximal observable comoving distance satisfies

$$D_C^{\max}(\mathcal{M}, \eta, z) (1+z) = D_H(\mathcal{M}^*, \eta), \quad (3.11)$$

which we solve numerically for z . Note that the leading-order inspiral horizon distance behaves as $D_H(\mathcal{M}^*) \sim (\mathcal{M}^*)^{5/6}$, hence

$$D_C^{\max}(\mathcal{M}) \sim \frac{\mathcal{M}^{5/6}}{(1+z)^{1/6}} < D_H(\mathcal{M}). \quad (3.12)$$

While the derivation of (3.12) is only valid for low-mass systems, we find that D_C^{\max} is generally less than the static, Euclidean universe equivalent D_H .

3.3.3 Detection rate and distance distribution

We now assume binaries of a fixed model, distributed isotropically and uniformly in comoving volume, that merge at a constant comoving merger rate density \mathcal{R} (in $\text{MWEG}^{-1} \text{Myr}^{-1}$) as given in the data sets by Dominik *et al.* [33]. To convert these numbers into a detection rate for aLIGO, we proceed as follows:

First, the comoving merger rate \mathcal{R} per MWEG has to be multiplied by an average galaxy density which we take as $\rho_G \approx 0.0116 \text{Mpc}^{-3}$ following Kopparapu *et al.* [316]. Next, we must calculate the effective volume in which each binary is observable, by integrating the number of observable binaries as a function of D_C . As the distance increases, the area of the corresponding sphere increases as D_C^2 but the fraction of binaries that are oriented such that their signal is sufficiently loud for detection (that is, $D_{\text{eff}} < D_H$) becomes smaller. Finally, due to the redshifted

time,

$$t_L = t_C(1 + z) \quad (3.13)$$

the observed merger rate for binaries at redshift $z > 0$ is less than the comoving merger rate. Thus, the effective volume for a binary with chirp mass \mathcal{M} is

$$V_{\text{eff}}(\mathcal{M}) = 4\pi \int_0^{D_C^{\text{max}}} \frac{D_C^2}{1+z} P\left(\frac{D_L}{D_H(\mathcal{M}^*, \eta)}\right) dD_C, \quad (3.14)$$

where D_C^{max} is defined by (3.11). The function P , introduced in Eq. (3.6), gives the fraction of suitably oriented binaries (i.e., those giving an SNR greater than 8) and $(1+z)^{-1}$ accounts for the difference between apparent and comoving merger rate density. We note that the integrand in (3.14) can be interpreted (up to a normalisation) as the observed distance distribution for binaries with fixed intrinsic parameters.

The average detection rate for each model is given by

$$\dot{N} = \mathcal{R} \times \rho_G \times \overline{V_{\text{eff}}}, \quad (3.15)$$

where $\overline{V_{\text{eff}}}$ denotes the average effective volume, with the average taken over all binaries in a given model. We take \mathcal{R} and ρ_G from Dominik *et al.* [33] and Kopparapu *et al.* [316], respectively.

Figure 3.2 shows this distribution for an equal-mass BBH with $m_1 = m_2 = 10M_\odot$. For comparison, we include the equivalent curve for a static, Euclidean universe, where $D_L \equiv D_C$ and (3.14) simplifies to the case $z = 0$. As expected, both curves agree for low redshift, but as we have noted above, there are fewer binaries seen at large comoving distances if the expansion of the universe is taken into account. This effect becomes increasingly important for larger distances, i.e., for high-mass binaries and more sensitive detector configurations.

The effective volume in which binaries with fixed parameters are detectable changes considerably across the parameter space. This leads to an observational bias in favour of systems with large volume reach. We incorporate this effect by re-weighting the chirp mass distribution of binaries according to their individual effective volumes. In practice, Dominik *et al.* [33] provide the data for each of their models in form of a discrete set of binary parameters. For each of those binaries, we calculate the integer part of $V_{\text{eff}}/V_{\text{eff}}^{\text{min}}$ and add that many copies of the binary

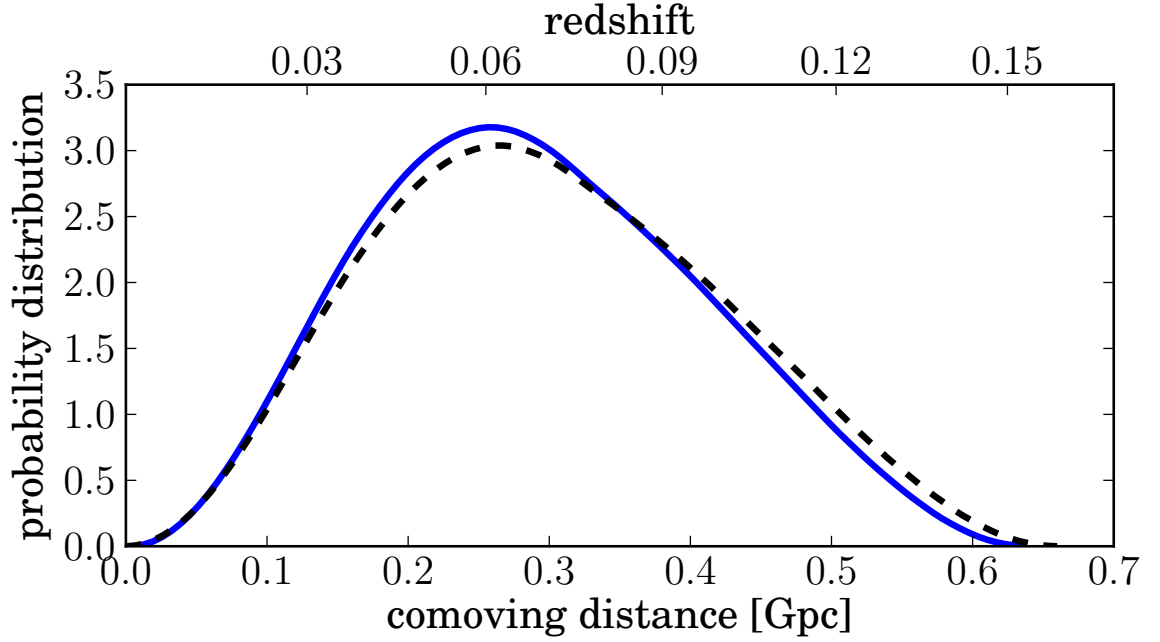


Figure 3.2: The probability distribution in comoving distance for detectable BBHs with $m_1 = m_2 = 10M_\odot$. The solid (blue online) curve takes cosmological effects into account (see text) while the dashed line assumes a static, Euclidean universe (i.e. local universe approximation). Figure reproduced from [2].

to our new set of observable parameters. Here, $V_{\text{eff}}^{\text{min}}$ denotes the smallest effective volume across all binaries in the set, and only one copy of the binary with this smallest effective volume is kept.³

Finally, for each binary in our new set, we draw a comoving distance from the distribution underlying V_{eff} . From this distance, we then infer the redshift and change from \mathcal{M} to the observable redshifted chirp mass \mathcal{M}^* according to (3.7). Our discrete representation of observable binaries then consists of multiple copies of the same intrinsic systems, each however with a unique redshifted chirp mass.

Note that an equivalent, but computationally more expensive, procedure would be to randomly draw binaries from the intrinsic distribution, then draw comoving distances and orientations for each binary within the total sensitive volume for the respective model and only keep those binaries with a detectable GW signal. Our method instead avoids disregarding any randomly drawn sources by drawing from the appropriate (distance/orientation) distribution of detectable signals.

³We could keep more copies of the binary with the smallest effective volume and multiply the number of every other binary in the set accordingly, but tests showed that this has no effect on our results.

3.3.4 Estimating and Including Measurement Errors

Including the observational bias discussed in Sec. 3.3.3 in the chirp mass distribution still does not yield the distribution that one would expect to observe, because there will be a measurement error associated with each of the observations. Previous publications have mainly discussed a full Bayesian framework to combine multiple observations including their measurement uncertainties [290, 264, 263]. We instead assume a statistical fluctuation of the measured parameter around its true value as detailed below.

The accuracy of the parameters recovered during GW searches is limited by two factors. First, since we match to templates of the signals, the accuracy of recovered parameters will be limited by the accuracy of the waveform models that used in the search. Second, the accuracy will be affected by statistical fluctuations of the noise in the measurement process. While we leave the former for dedicated studies such as Buonanno *et al.* [274] and Nitz *et al.* [317], we can estimate the uncertainty due to the latter using the well-known Fisher matrix estimate.

Fisher matrix analyses rely on a linear approximation of signal variations and are valid for large SNRs. Neither of the two assumptions is typically valid in realistic scenarios, and recent papers have discussed some implications of violating these assumptions [318, 319, 320]. Here, however, in order to demonstrate the basic efficacy of our method to distinguish BBH populations with GW observations, we take Fisher-matrix predictions as a proxy for the width of posterior distributions of parameters obtained via a fully Bayesian analysis of the kind that will be performed on actual GW events [281]. In performing a population study of the kind we perform here, one should include not only a point estimate for parameters such as the chirp mass, but the full posterior from these parameter estimation routines. These posteriors can then be combined in the correct way, as described in [290]. The method we use here is essentially the point estimate approximation to the full analysis.

We employ the same inspiral-merger-ringdown model [311] for our Fisher-matrix calculations as we used to simulate GW signals. We only consider variations of the intrinsic parameters: masses, time, phase and a model-specific single effective spin. We assume that these are also the parameters that are recovered, at least initially by the GW search algorithm (see, e.g., the recently proposed search algorithm for

nonprecessing, spinning binaries by Dal Canton *et al.* [321]). This assumption is likely to make our error estimates too large since actual GW events will be followed up by complex parameter estimation routines (see e.g., Veitch *et al.* [281]) exploring the full parameter space of precessing binaries [281, 322, 323]. However, since we only need an approximate error estimate that can be obtained in a fast and reliable way across the BBH parameter space, we choose to use the Fisher-matrix method here for nonprecessing binaries, and we neglect small correlations with extrinsic parameters such as sky location, orientation or distance.

The characteristic standard deviations in the measurement process are estimated by [309]

$$\Delta\theta^i = \sqrt{(\Gamma^{-1})_{ii}}, \quad (3.16)$$

$$\Gamma_{ij} = \left(\frac{\partial h}{\partial \theta^i}, \frac{\partial h}{\partial \theta^j} \right), \quad (3.17)$$

where Γ_{ij} is the Fisher information matrix and $h = h(\theta^i)$ is the waveform model. The inner product used in (3.17) is given by

$$(g|h) = 4 \operatorname{Re} \int_{f_{\text{low}}}^{\infty} \frac{\tilde{g}(f) \tilde{h}^*(f)}{S_n(f)} df \quad (3.18)$$

which is consistent with the SNR definition in (3.3). The form of the waveform model we use allows us to calculate the partial derivatives used in the definition of Γ_{ij} analytically, and we ensure numerical errors in the matrix inversion remain small.⁴

The only parameter we use to distinguish BBH populations in this study is the observable, redshifted chirp mass, \mathcal{M}^* . The data sets of expected observable chirp masses that we prepared following the algorithm introduced in Sec. 3.3.3 shall now be skewed further by adding measurement errors to each binary in the data set. We do so by assuming a Gaussian distribution centred around the chirp mass value of each binary with a standard deviation given by the Fisher matrix estimate (3.16). We evaluate the Fisher matrix at the appropriate observed chirp mass and mass ratio of the binary, setting the value of the black hole spins to zero (although we allow the spins to vary when calculating the Fisher matrix). This has a negligible effect on our results as the measurement accuracy for the chirp mass is only weakly dependent

⁴In fact, we find that no element of $\Gamma\Gamma^{-1}$ and $\Gamma^{-1}\Gamma$ deviates from the respective element of the identity matrix by more than 10^{-7} , in most cases the deviation is much less than this.

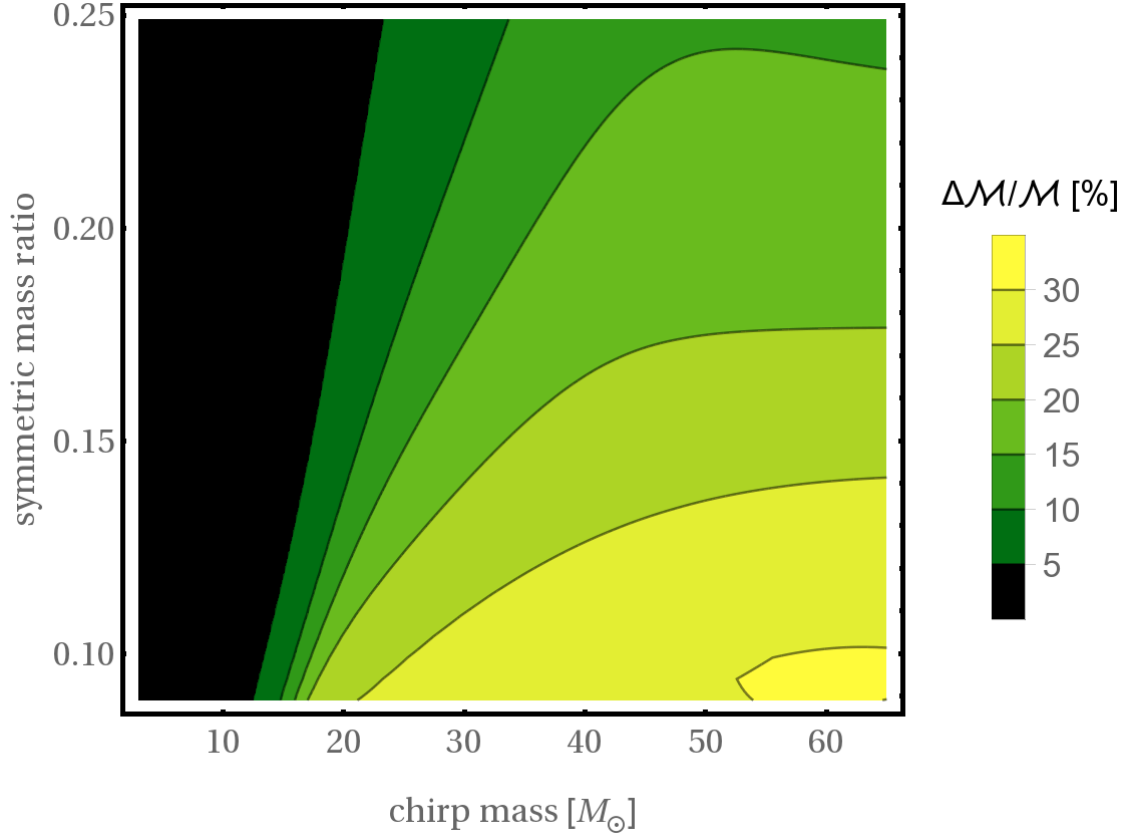


Figure 3.3: Expected relative measurement errors in the chirp mass for an early configuration of aLIGO, SNR 10, calculated using the PhenomC waveform model [311]. Figure reproduced from [2].

on the spins [287]. We randomly draw a sample from this distribution to re-define the measured chirp mass. Similarly, when we later simulate the universe with a particular model, each observation is drawn from the distribution that incorporates observational biases, but the actually measured chirp mass is additionally offset following the Gaussian distribution that simulates measurement errors.

The Fisher-matrix estimates scale inversely with the SNR, so we only calculate them once across the parameter space and scale them for each binary in the data set according to its SNR, which in turn is inferred from the distance and a randomly chosen orientation. Figure 3.3 shows the chirp mass uncertainty at a constant SNR of 10 across the parameter space for the early configuration of aLIGO.

Figure 3.4 illustrates the transition from the intrinsic BBH population, predicted by Dominik *et al.* [33] for each of their models, to the expected observed chirp mass distribution. The main effect of the observational bias detailed in Sec. 3.3.3 is that the distribution becomes skewed towards high-mass binaries, and its support ex-

tends to larger chirp masses due to the redshift of distant sources. The addition of measurement errors hardly affects the distribution at low chirp masses, simply because the errors are small compared to the typical variation of the distribution in this regime. For heavy systems, on the other hand, noise fluctuations introduce a non-vanishing chance of measuring chirp mass values greater than the largest (redshifted) chirp mass in each model. Hence, the main effect of introducing measurement errors is that the expected observed distributions show a characteristic tail at high chirp masses.

3.4 Combining Measured Rates and Chirp Masses

Given a set of BBH observations, for each model variation V_i , we wish to calculate the posterior probability for that being the correct model. The information we gather about the correct model is twofold. First, we obtain a set of observed chirp masses $\{\mathcal{M}\}$, and second, we measure the rate of BBH detections by observing n binaries in a given observation period. In reality each observation will include measurements of additional physical parameters of the system, such as the component spins (see [174, 181] for information on how measurements of spin misalignments can help to constrain astrophysical formation scenarios.) Including additional information from these other dimensions should help in distinguishing astrophysical formation scenarios.

We simulate the observed population by choosing one of the model variations, adjusted to account for selection effects as described above, to describe the universe. We then draw n individual chirp mass measurements from this model, which form the data $\{\mathcal{M}\}$. The number of observations we assume is itself drawn from a Poisson distribution with a mean value that is dictated by the observation time and the merger rate of the model variation we have selected to simulate the universe.

With these measurements, $\{\mathcal{M}\}$ and n , the posterior probability that model V_i is the correct model reads

$$P(V_i|\{\mathcal{M}\}, n) = \frac{P(\{\mathcal{M}\}, n|V_i)P(V_i)}{P(\{\mathcal{M}\}, n)}, \quad (3.19)$$

where we have used Bayes' Theorem. $P(V_i)$ is the prior probability on model V_i ,

$P(\{\mathcal{M}\}, n|V_i)$ is the likelihood of making these chirp mass measurements *and* measuring this detection rate given model variation V_i , and $P(\{\mathcal{M}\}, n)$ is a normalisation factor called the evidence.

Assuming that the number of observations n is independent from the chirp mass values we observe, we can rewrite this as

$$P(V_i|\{\mathcal{M}\}, n) = \frac{P(\{\mathcal{M}\}|n, V_i)P(n|V_i)P(V_i)}{P(\{\mathcal{M}\}, n)}. \quad (3.20)$$

We normalise by assuming that the discrete model variations we consider cover all possible states of the universe, which is an idealisation that we shall discuss in more detail later. However, this assumption allows us to define the normalisation factor by requiring the sum of the probabilities for each model to be unity, which leads to

$$P(V_i|\{M\}, n) = \frac{P(\{M\}|n, V_i)P(n|V_i)P(V_i)}{\sum_k P(\{M\}|n, V_k)P(n|V_k)P(V_k)}. \quad (3.21)$$

We assume a uniform prior on the models,

$$P(V_i) = \frac{1}{\mathcal{N}}, \quad (3.22)$$

where \mathcal{N} is the number of models we are considering. The prior then cancels out and we are left with

$$P(V_i|\{\mathcal{M}\}, n) = \frac{P(\{\mathcal{M}\}|n, V_i)P(n|V_i)}{\sum_k P(\{\mathcal{M}\}|n, V_k)P(n|V_k)}. \quad (3.23)$$

The likelihood of making n observations in a set time, given a model predicting mean number of observations, μ_i , is given by the Poisson distribution:

$$P(n|V_i) = P(n|\mu_i) = \frac{e^{-\mu_i} \mu_i^n}{n!}. \quad (3.24)$$

The likelihood terms of the form $P(\{\mathcal{M}\}|n, V_i)$ are calculated by binning the chirp mass distributions for each model into a histogram. We then calculate the likelihood of the observed samples being drawn from their bins using the multinomial

distribution

$$P(\{\mathcal{M}\}|n, V_i) = n! \prod_{k=1}^b \frac{p_{ik}^{x_k}}{x_k!}, \quad (3.25)$$

where n is the number of samples in the observations, b is the number of bins, p_{ik} is the probability in model i of drawing a sample from bin k and x_k is the number of observations that fall into bin k , with

$$\sum_k x_k = n \quad \text{and} \quad \sum_k p_{ik} = 1. \quad (3.26)$$

We calculate p_{ik} for each model and bin as the fraction of the total number of samples in the model which fall into that bin. The bin size we employ is motivated by Scott’s rule [324],

$$\Delta = \frac{3.5\sigma}{\sqrt[3]{N_m}}, \quad (3.27)$$

where Δ denotes the bin width, σ is the standard deviation of the model, and N_m is the total number of samples in model. To be able to consistently compare our simulated data with all models, we apply (3.27) to all models and then use the median bin width for the actual analysis. However, we find that changing this bin width by a factor of a few does not impact our results noticeably.

3.5 Observing Scenarios

The method we have developed transforms predicted binary distributions and merger rates into *observable* distributions and detection rates which in turn can be confronted with a set of observations in order to assign posterior probabilities to each model. As such, the method is generally applicable to any set of theoretical predictions and detector configuration.

In the following, however, we present results for specific choices of binary population models, detector sensitivity and observing time. As detailed Sec. 3.2.2 and summarised in Table 3.1, we consider 12 binary population models by Dominik *et al.* [33], each with both the “pessimistic” (submodel B) and “optimistic” (submodel A) assumption about the common envelope evolution. This leads to 24 distinct predictions of the BBH chirp mass distribution (see Figure 3.4), where each comes

with a distinct average merger rate density that we take from the arithmetic mean of the solar and subsolar metallicity predictions by Dominik *et al.* [33] (Tables 2 and 3 therein). The local merger rate densities for each model are given in Table 3.2. Interestingly, due to the mass-dependent observational bias, models with higher merger rate density do not necessarily exhibit a higher detection rate, see for instance models 9 and 10 in Table 3.2.

Recent calculations by Dominik *et al.* [305] that include the cosmological evolution of merger rates give lower rate densities than the ones we infer from earlier work of the same authors. Consequently, the detection rates we find are up to a factor of 2 larger than those recently predicted by Dominik *et al.* [259] (this is based on a direct comparison of our method with their otherwise equivalent approach using the same detector configuration). However, this neither affects the general proof of principle carried out here, nor do the conclusions we shall draw in the following section change qualitatively by varying the detection rate at this level.

V_i	\mathcal{R}^a		$\langle \mathcal{M} \rangle^b$		μ^c (O1)		μ^c (O2)	
	A	B	A	B	A	B	A	B
0	7.8	40.8	26.0	24.9	4.0	25.2	64	402
1	4.6	6.8	27.3	26.2	2.3	3.9	37	63
2	8.3	36.0	26.6	24.9	4.2	25.9	67	413
3	4.0	47.6	25.0	24.4	1.9	28.7	30	458
4	0.1	3.1	25.0	24.7	0.1	1.9	1	30
5	7.8	40.9	26.0	24.9	4.0	25.3	64	404
6	7.9	41.3	25.6	24.2	3.9	25.1	63	401
7	8.6	47.1	25.3	23.8	4.0	26.3	65	420
8	0.4	2.1	21.3	10.0	0.0	0.6	1	9
9	11.8	54.6	23.2	20.7	3.4	20.2	54	324
10	5.8	31.3	26.8	26.2	4.3	26.0	68	415
11	10.4	54.5	29.8	28.6	8.5	46.5	136	742

Table 3.2: Predicted merger and detection rates. The binary populations models, V_i , predicted by Dominik *et al.* [33] are summarised in Table 3.1 and the submodels B and A refer to pessimistic and optimistic assumptions about the common envelope evolution of Hertzsprung gap donors (Sec. 3.2.2). Table reproduced from [2].

^a Local merger rate density in $\text{MWEG}^{-1}\text{Myr}^{-1}$.

^b Average predicted observed chirp mass in M_\odot (see Sec. 3.3)

^c Mean number of detections predicted by each model for the early aLIGO observing runs O1 and O2 (see text for details).

We also have to specify in the sensitivity (i.e., noise spectral density) of our assumed GW detector and the observing time. Closely following Abbott *et al.* [14], we consider the first two aLIGO science runs dubbed O1 and O2, respectively. The first science run for aLIGO (O1) is planned to begin in autumn 2015. The duration

of O1 will be approximately 3 months for the two aLIGO detectors. We assume each detector has a duty cycle of 0.8 so that the total period of coincident observation during O1 will be about 0.16 years. The noise power spectral density we use is the “early aLIGO” configuration [325].

We further consider a second science run, O2. During O2, the detectors are planned to observe for approximately 6 months with a comparable duty cycle to O1. It is expected that, after further improvements of the instruments following O1, the aLIGO detectors during O2 will be approximately a factor of 2 more sensitive than the nominal early aLIGO noise curve we use for O1. While the evolution of the noise power spectral density is in general a function of the frequency, we find that, in practice, the difference between the predicted noise curves in Abbott *et al.* [14] results in improved horizon distances and error estimates that are well approximated by simply scaling the results we obtain for the early aLIGO configuration. Hence, we simulate O2 by multiplying the O1 horizon distance by 2. The Fisher-matrix errors change only due increased SNR at fixed distance. This increase in sensitivity leads to a factor of 8 increase in volume meaning that, in total, O2 surveys 16 times the time-volume of O1. We show in the following section that this is when we will begin to distinguish between astrophysical models.

3.6 Results: Distinguishing BBH Formation Models

3.6.1 First aLIGO observing run (O1)

We simulate the observed BBH systems, assuming the universe matches one of the models from Dominik *et al.* [33], and calculate the posterior probability for each model. We repeat the experiment 10000 times before turning to the next model to simulate the universe. Figure 3.5 gives the median posterior probability for each model.

In cases where one or few models have a high probability, these would be distinguishable from the other models. However, all models with a high probability would be consistent with the observations. We reiterate that here we restrict attention to

the models in [33]. Of course these do not cover the full space of binary merger predictions. If we were to include a broader range of models, it is likely that the conclusions we are able to draw would be weaker as various models would lead to comparable rates and mass distributions. Nonetheless, some of the conclusions we reach, such as excluding a number of models if there are no observations in O1, are robust.

We first observe that, for the most part, we would be able to distinguish between submodels A and B that correspond to different common envelope scenarios (see Sec. 3.2.2). This is unsurprising as the predicted rates for the majority of models are significantly higher for submodel A (cf. Table 3.2). Models which predict low detection rates for model A remain degenerate with those in model B. The mass distribution from such a small sample does not provide enough additional information to break these degeneracies in the rates. For example, model 1 A uses a very high, fixed envelope binding energy, meaning that most binaries entering a common envelope event fail to throw off the common envelope and merge, causing them to never form BBH systems (for a more detailed discussion of this, see Dominik *et al.* [33]). On the other hand, submodel B does not allow a binary to survive a common envelope event if the donor is on the Hertzsprung Gap, and so again, many binaries merge and never form BBHs. This generically lowers the merger rates and thus detection rates for submodel B models, leading to the degeneracy visible in the upper right quadrant of Fig. 3.5.

Another interesting example involves models 4 and 8 that, in the pessimistic submodel B, are consistent with no observations at all during O1. Hence, they cannot be distinguished from each other, or indeed model 8 A, although they are favoured over all other models if indeed no detection are made.

Within the two submodels, it is difficult to identify the correct model. Indeed, there are numerous variations which would be indistinguishable from the standard model. The only model which can be clearly identified is model 11, a model which reduces the strength of stellar winds by a factor of 2 over the standard model. We now discuss why we are able to distinguish this model from the others in such a short observational period.

3.6.2 Stellar winds

In massive O-type stars, stellar winds of high temperature charged gas are driven by radiation pressure. In Wolf–Rayet stars mass loss rates can be as high as $10^{-4}M_{\odot}\text{yr}^{-1}$ [69]. This can cause stars to lose a large amount of mass prior to the supernova. Theoretical uncertainties in modelling these mass loss rates therefore translate into uncertainties in the pre-supernova masses for massive stars. Dominik *et al.* [33] examine the effects of reducing the strength of stellar winds by a factor of 2 on the distribution of BBHs in their Variation 11. Firstly, reducing stellar winds results in stars having a higher mass prior to supernova than they would otherwise have. This in turn leads to more mass falling back onto the compact object during formation, which reduces the magnitude of natal kicks given to black holes. This results in more systems surviving the supernova (rather than being disrupted) and increases the merger rates. More massive pre-supernova stars also form more massive remnants, resulting in the most massive BBH having a chirp mass of $\sim 64M_{\odot}$ with reduced stellar winds compared to $\sim 37M_{\odot}$ using the standard prescription. Finally, reducing the strength of stellar winds allows stars with a lower zero age main sequence mass to form black holes due to more mass being retained. This can boost the BBH merger rate compared to the standard model.

All of these effects combined mean that Variation 11 predicts BBHs with characteristically higher chirp masses, as well as predicting a much higher merger rate than all other models (even for the pessimistic submodel B in O1, Variation 11 predicts $\mathcal{O}(10)$ observations). We therefore expect that we would be able to correctly distinguish a universe following Variation 11 from all other models with relatively few observations. In Figure 3.6 we show the median posterior probability for each model as a function of the observation time, based on 10000 redraws of the observations. We find that when drawing observations from a universe following Variation 11 we overwhelmingly favour it within the duration of O1, with $\mathcal{O}(10)$ observations.

3.6.3 Second aLIGO observing run (O2)

We now turn our attention to the second observing run, O2, and investigate which models can be distinguished using the much larger time-volume surveyed by O2. In Figure 3.7 we again show a matrix plot showing the (median) posterior probability

for each model after a period corresponding to the O2 run.

Figure 3.7 has a more diagonal form than Figure 3.5, meaning that in many cases the correct model is favoured and others are disfavoured within the O2 period. In particular, the optimistic and pessimistic submodels A and B become almost entirely distinct from each other. This is because most of the Dominik *et al.* [33] models predict $\mathcal{O}(100)$ ($\mathcal{O}(10)$) observations during the O2 period for the optimistic (pessimistic) submodels respectively (as shown in Table 3.2). Furthermore, the majority of variations in submodel A can be unambiguously identified; the exception being that the standard model which remains degenerate with models 5, 6 and 7, as we discuss in detail in Section 3.6.3. For the pessimistic submodel B, the standard model remains indistinguishable from a number of other variations. However, there are a few models which can be clearly distinguished, including models 4 and 8 (that predict significantly lower rates), and 9, 10 and 11. All of these models predict tens of observations and consequently, we are able to use information from both the chirp mass distribution and the detection rate to help distinguish models. Model 10 involves the variation of the supernova engine, which we elaborate on in Section 3.6.3.

Black hole kicks and maximum neutron star mass

Not all models are distinguishable, even with the $\mathcal{O}(100)$ observations predicted by the optimistic submodel A for O2. For example, in Figure 3.7 we see that the standard model is degenerate with Variations 5, 6 and 7. We now explain why this is so.

As already mentioned, it is unclear what the correct distribution of natal kicks given to black holes upon formation is. In order to investigate the possibilities, Dominik *et al.* [33] vary two parameters relating to the kicks imparted onto newly formed black holes; the characteristic velocity σ and the fraction of mass f_b which falls back onto the newly born black hole.

In their standard model, black holes receive a kick v_k whose magnitude v_{\max} is drawn from a Maxwellian distribution with $\sigma = 265 \text{ km s}^{-1}$, and reduced by the

fraction of mass falling back onto the black hole f_b as

$$v_k = v_{\max}(1 - f_b), \quad (3.28)$$

where f_b is calculated using the prescription given in [125].

In order to test the effects of smaller natal kicks, in Variation 7 Dominik *et al.* [33] reduce the magnitude of kicks given to neutron stars and black holes at birth by a factor of 2. They use a Maxwellian distribution with $\sigma = 132.5 \text{ km s}^{-1}$. For BBHs, this has very little effect on the chirp mass distribution, and so one cannot expect to be able to distinguish this model from one using full kicks.

The same holds true when the maximum neutron-star mass is increased (decreased) from its fiducial value in the standard model of $2.5 M_\odot$. This has very little impact on the BBH chirp mass distribution and so there is effectively a degeneracy between these models. This could be resolved by also including BNS observations in the comparison. We do not do this here as we concentrate on the BBH predictions, due to the prediction by Dominik *et al.* [33] that these will dominate the early aLIGO detections.

Supernova engine

In their standard model, Dominik *et al.* [33] employ the [125] prescription to calculate the fraction of mass falling back onto the black hole during formation, and thus the black hole masses. In particular, they use the *rapid* supernova engine. When employed in a compact binary population code such as **StarTrack**, the rapid supernova engine reproduces the observed mass gap [121, 120] in compact objects between the highest mass neutron stars and the lowest mass black holes (for a discussion of using GW observations to infer the presence or absence of a mass gap, see [286, 122, 123]).

In model 10 Dominik *et al.* [33] vary this prescription to use the *delayed* supernova engine from [125], which produces a continuous distribution of black hole masses (and thus BBH chirp masses). We therefore expect that the difference between these two models might be visible in the chirp mass distributions. We see however from Table 3.2 that these two models predict similar merger rates for BBH,

and so we do not expect to be able to distinguish them based on the detection rate. Nonetheless, we see from Figure 3.7 that this model can be distinguished from the others by the end of O2 and even, to a lesser degree, at the end of O1 (Figure 3.5)

To illustrate the importance of both the mass distribution and predicted rates, in Figure 3.8 we show the results that would be obtained using only one of these to separate the models. By comparing these results with Figure 3.7, it becomes clear that *both* the mass and rate measurements contribute significantly to our ability to distinguish between models. As expected, the delayed supernova engine (model 10) is distinguished from observed masses, but the rates are quite degenerate with other models. In contrast, models 4 and 8, are distinguished primarily by rate measurements, and not masses. As we have mentioned previously, the unknown spin distribution of black holes in binary systems can change the rate by a factor of two or three. Similarly, both the mass and rate distributions are subject to uncertainties due to additional physical effects which are not yet incorporated. Consequently, one might choose to incorporate an uncertainty in the rates or mass distributions. The results in Figure 3.8 illustrate the extreme scenario where one assumes knowledge of only the rate or mass distribution. Adding an uncertainty to the mass or rate distributions will lead to a result between those shown in Figure 3.7 and 3.8.

3.7 Summary and future work

In this paper we have outlined a method for comparing GW observations of BBH mergers to binary population synthesis predictions using a Bayesian model comparison framework. Starting from chirp mass distribution predicted by Dominik *et al.* [33], we produce predicted observed chirp mass distributions accounting for known observational effects. We incorporate

- (a) The redshifting of observed binary masses due to the cosmological distances out to which they will be observed.
- (b) The observational bias of GW detectors to detect more massive systems, since they can be seen to greater distances and thus in much larger volumes.
- (c) Fisher matrix estimates of measurement uncertainties in the recovery of the chirp mass of BBH.

We show that given the merger rates predicted by the models of Dominik *et al.* [33], we will begin to be able to distinguish between population synthesis models in the first two aLIGO science runs. Ruling out models in turn can help to constrain the value of unknown parameters, which relate to poorly understood astrophysics relating to binary evolution.

Of course, the set of models considered here by no means encompasses the full set of stellar evolution models available in the literature. We restricted attention to this subset of models as the data was publicly available in an easy to use form. It would be straightforward to include additional models into this analysis. Ideally, we would make use of a dense set of models, where numerous astrophysical parameters are jointly varied. This would allow us to interpolate between models, and extract best-fit parameters [263, 303]. Furthermore, we have restricted attention to the two best-measured quantities: the rate and chirp mass distribution of binaries, and only used point estimates of the masses. The inclusion of full parameter distributions can only enhance our ability to distinguish between models.

The method we have introduced allows us to distinguish between a given set of stellar evolution models. It will identify the model, or models, that best agree with the observed rate and mass distribution. It will not, however, indicate whether the best model is actually a good fit to the observations — only that it is better than the others. This could be remedied by introducing a simple, generic model. For example, the intrinsic mass distributions shown in Figure 3.4 are reasonably well described by a decaying power law with an upper and lower mass cutoff. One could then imagine extending the set of models to include this phenomenological mass distribution parametrized by three variables with an additional variable rate. To calculate the posterior for this distribution, we would then have to marginalize over four parameters. Thus, even if the generic model was a reasonable fit to the data, it would be penalized by the large initial parameter space. It is likely that the generic model would be preferred after a small number of observations. With a large number of observations, the rate and mass distributions would be reasonably well measured. Any specific model which matched the observations well would then be preferred to the generic model due to its broader support on the parameter space. It would be reasonably straightforward to extend our method to include a generic model, and this is something we plan to incorporate in the future.

In this study we concentrated on the information that could be gained from GW observations of BBH mergers. aLIGO and AdV are also expected to observe the inspiral, merger and ringdown of compact binaries including neutron stars (BNS and NSBH systems). One should include all GW observations of compact binaries in order to extract the maximum amount of information from the observations. In fact, as discussed above, we are unable to distinguish models which vary the maximum allowed neutron star mass since we ignore these events here. In this study we ignored these events since the predicted detection rates for BBH mergers dominated those of other compact binary mergers. The BBH mass distribution also spans a large range of masses, with structure encoding information about binary evolution. Ignoring other families of compact binaries also allowed us to avoid ambiguities in discerning the family of the source (BNS, NSBH or BBH) due to degeneracies which exist in measuring the mass ratio for these systems [286], although this can be dealt with in the future [326].

All these considerations have to be carefully taken into account in future studies. However, our results indicate that the upcoming generation of advanced GW detectors will soon start putting non-trivial bounds on current and future binary evolution models, and analyses like the one presented here will provide an important basis to link theoretical models with GW observations.

Acknowledgements

The authors would like to thank Mark Hannam, Ilya Mandel and Chris Messenger for useful discussions. SS would like to acknowledge support from the STFC, Cardiff University and the University of Birmingham. FO has been supported by the STFC grant ST/L000962/1. SF would like to acknowledge the support of the Royal Society and STFC grant ST/L000962/1.

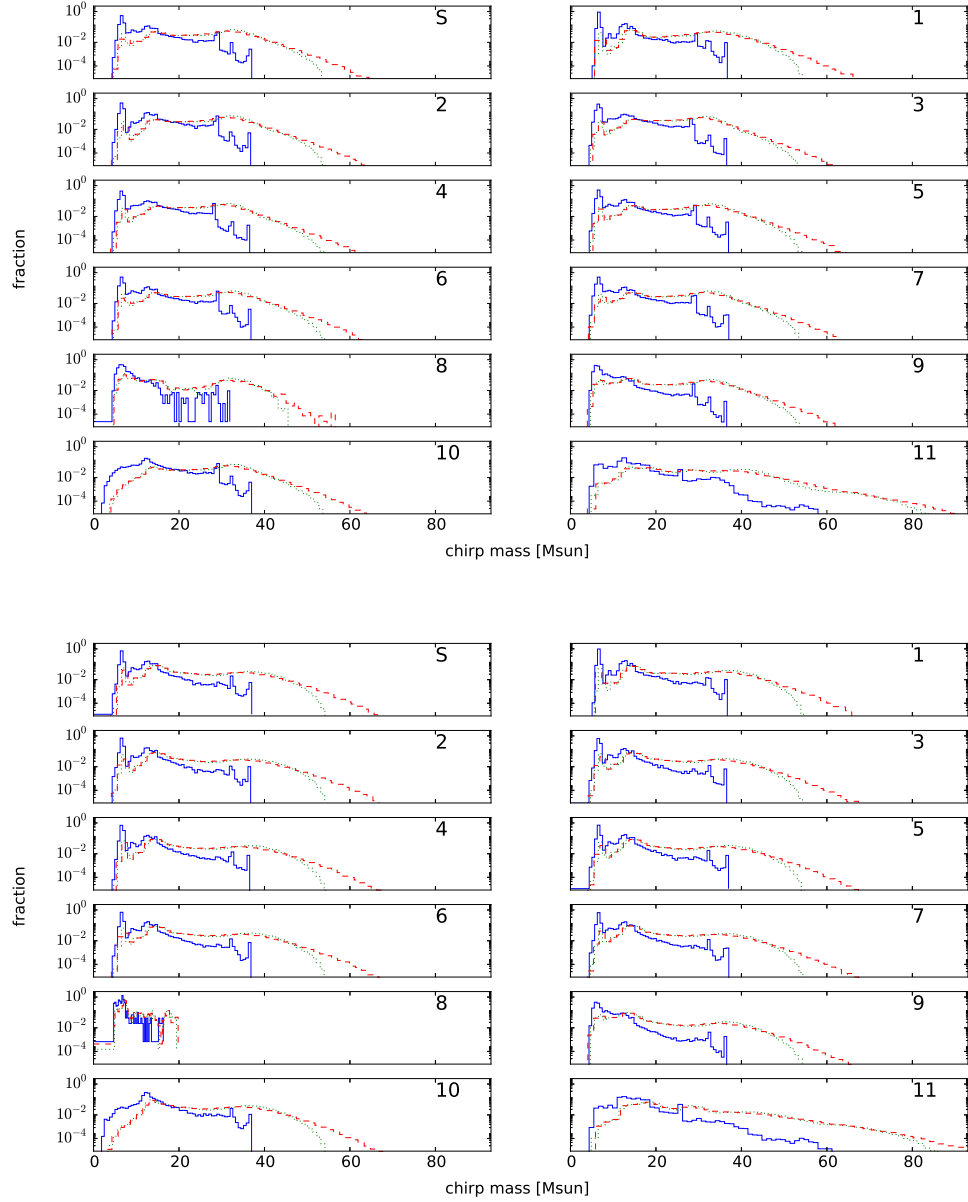


Figure 3.4: Chirp-mass distributions for each model in Dominik *et al.* [33] using either their optimistic (top panel) or pessimistic (bottom panel) submodel and a 50-50 split of solar and sub-solar metallicities. The solid (blue online) line shows the intrinsic distribution as given by Dominik *et al.* [33]. The dotted (green) line shows the same distribution when accounting for the observational biases introduced in Section 3.3.3 as predicted for the early configuration of aLIGO. Finally, the dashed (red) line with largest chirp-mass support shows the expected observed distribution that additionally folds in the errors in measuring the chirp masses through GW observations. Figure reproduced from [2].

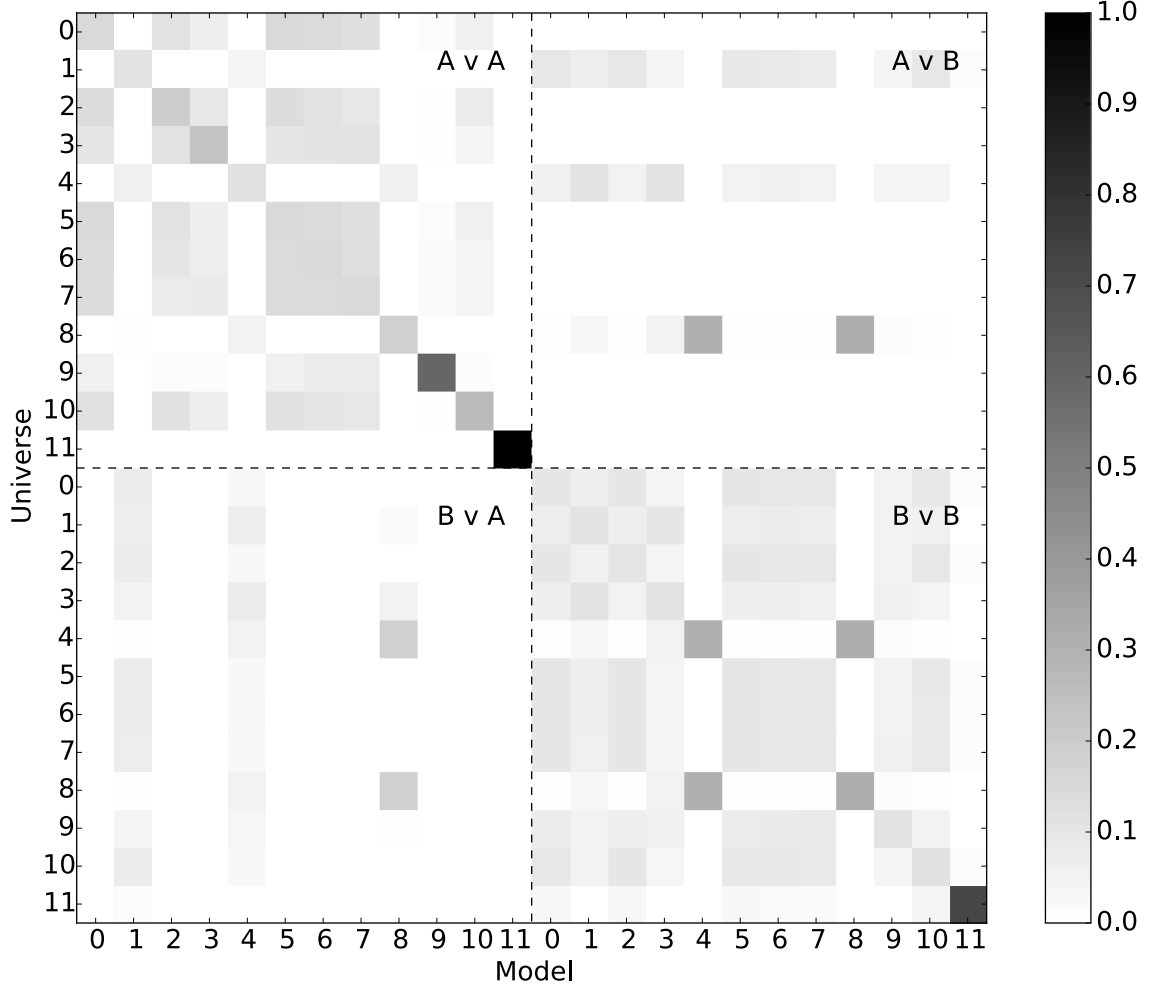


Figure 3.5: The median posterior probability for each model in the set of Dominik *et al.* [33] models after an O1 like observing period of 0.16 years, calculated from 10000 repeats. The model which observations were drawn from is shown on the axis labelled *Universe*. The models which these observations were then compared to is labelled *Model*, so that the probabilities in each row sum to one. Models 0-11 are described in Table 1. The two submodels, A and B, are described in Section 3.2.2. Figure reproduced from [2].

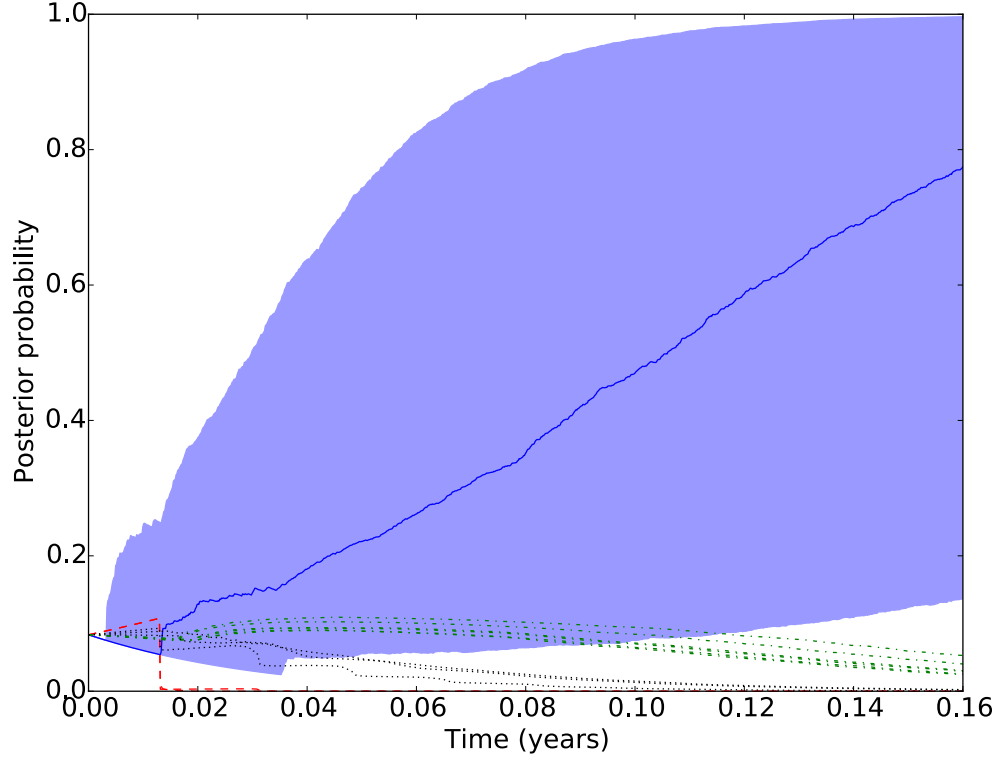


Figure 3.6: The median posterior probability for each of the models in the set as a function of observation time for a period of time corresponding to the aLIGO O1 run (0.16 years). GW observations are drawn from a universe following Variation 11, submodel B which reduces the strength of stellar winds by a factor of 2 compared to the standard model. The blue (solid) line shows the median posterior probability for Variation 11 taken from 10000 repeats, and the shaded error bar shows the 68% confidence interval. Variations 0,2,5,6,7 & 10 are plotted in green (dot-dash), while variations 1,3 & 9 are plotted in black (dotted). Variations 4 & 8 predicting ~ 0 observations in O1 are plotted in red (dashed). Figure reproduced from [2].

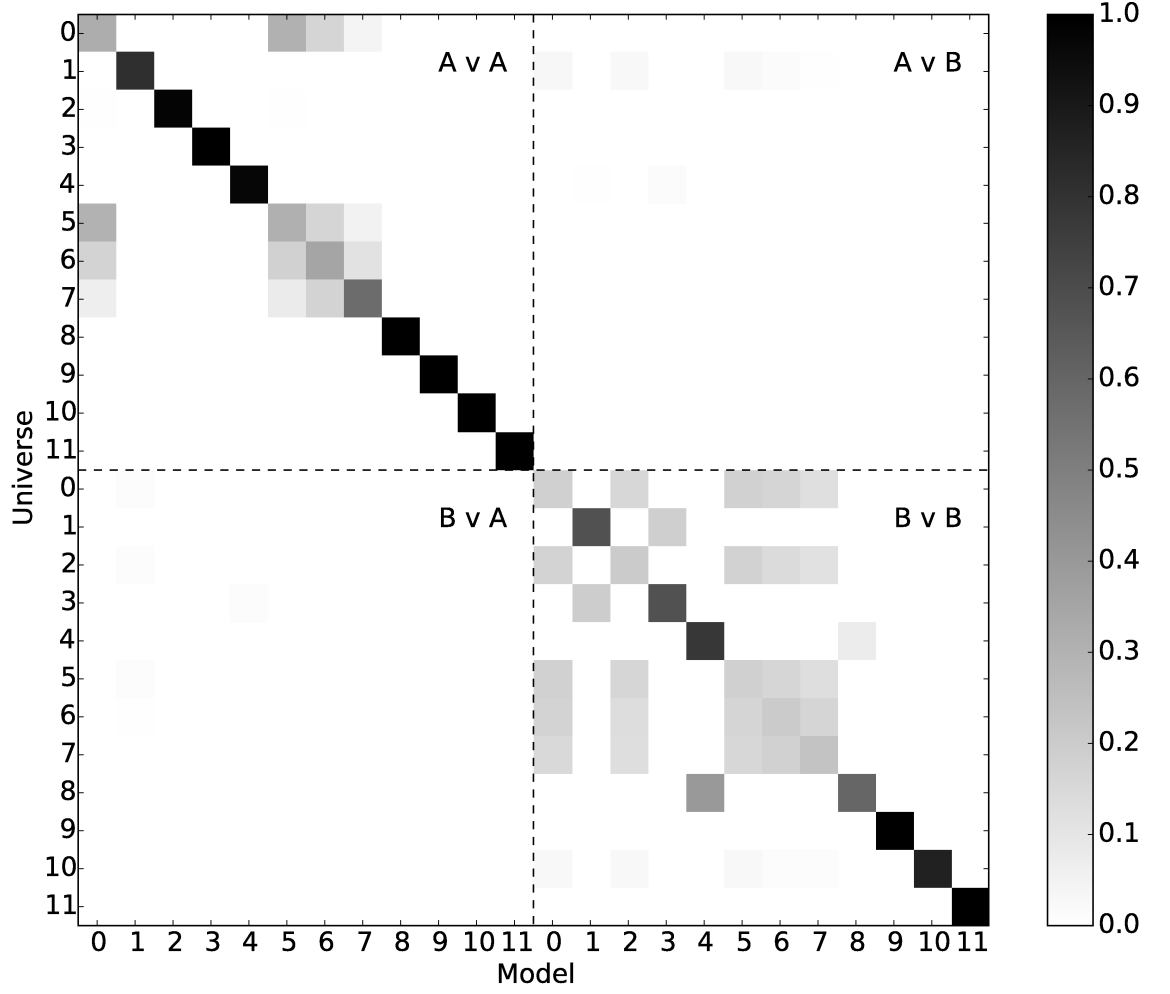


Figure 3.7: The median posterior probability for each model in the set of Dominik *et al.* [33] models after an O2 like observing period of 0.32 years with a detector more sensitive than the early aLIGO noise curve by a factor of 2. The median is calculated based on 10000 redraws of the observations. The model which observations were drawn from is shown on the axis labelled *Universe*. The model which these observations were then compared to is labelled *Model*. Models 0-11 are described in Table 3.1. The two submodels, A and B, are described in Section 3.2.2. Figure reproduced from [2].

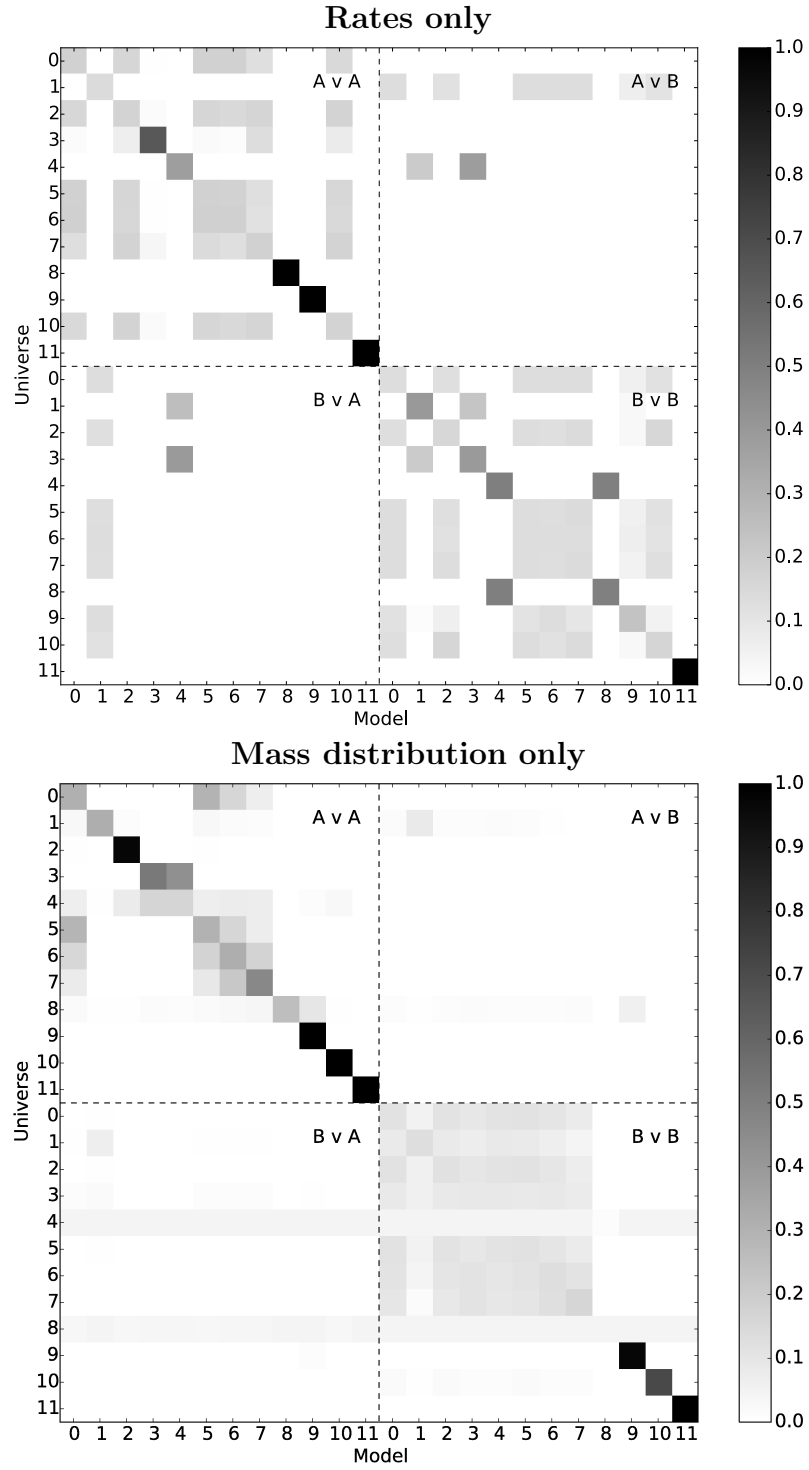


Figure 3.8: Probabilities for the scenario of Fig. 3.7, separated into contributions from the rates (top) and the mass distribution (bottom). Figure reproduced from [2].

Chapter 4

Hierarchical analysis of gravitational-wave measurements of binary black hole spin–orbit misalignments

Simon Stevenson,¹ Christopher P. L. Berry,¹ Ilya Mandel¹

¹ School of Physics and Astronomy, University of Birmingham, Edgbaston, Birmingham B15 2TT, United Kingdom

This Chapter introduces an hierarchical analysis for gravitational-wave measurements of binary black hole spin–orbit misalignments. It reproduces the text of Stevenson *et al.* [3], Submitted. This paper may undergo additional editing before publication. The code, and text of the paper were written by Simon Stevenson. The analysis was performed by Simon Stevenson. All plots were made by Simon Stevenson. The text was edited by all authors.

Abstract

Binary black holes may form both through isolated binary evolution and through dynamical interactions in dense stellar environments. These formation channels leave imprints on the alignment of the black holes spins with respect to orbital angular momentum. Gravitational waves from these systems directly encode information about the spin–orbit misalignment angles, allowing them to be (weakly) constrained. Identifying sub-populations of spinning binary black holes will inform us about compact binary formation and evolution. We simulate a mixed population of binary black holes with spin–orbit misalignments modelled under a range of assumptions. We then develop a hierarchical analysis and apply it to mock gravitational-wave observations of these populations. Assuming a population with spins of $\chi \sim 0.7$, we show that with tens of observations it will be possible to distinguish the presence of subpopulations of coalescing binary black holes based on their spin orientations. With 100 observations it will be possible to infer the relative fraction of coalescing binary black holes with isotropic spin directions (corresponding to dynamical formation) with a fractional uncertainty of $\sim 40\%$. Meanwhile, only ~ 5 observations are sufficient to distinguish between extreme models—all binary black holes either having exactly aligned spins or isotropic spin directions.

4.1 Introduction

Compact binaries containing two stellar-mass BHs can form as the end point of isolated binary evolution, or via dynamical interactions in dense stellar environments [see, e.g., 264, 189, for a review]. These BBHs are a promising source of GWs for ground-based detectors such as Advanced LIGO [aLIGO; 239], Advanced Virgo [AdV; 13] and KAGRA [16, 327]. Searches of data from the first observing run [O1; 8] of aLIGO yielded three likely BBH coalescences: GW150914 [7], GW151226 [19] and LVT151012 [21, 8]. GW observations give a unique insight into the properties of BBHs. We will examine one of the ways in which black hole spin measurements can be used to constrain formation mechanisms.

GW observations inform our understanding of BBH evolution in two ways: from the merger rate, and from the properties of the individual systems. The merger rate of BBHs is inferred from the number of detections; it is uncertain as a consequence of the small number of BBH observations so far. From O1, merger rates are estimated to be $9\text{--}240 \text{ Gpc}^{-3} \text{ yr}^{-1}$ [22, 8]. These rates are broadly consistent with predictions [269] from both population synthesis models of isolated binary evolution [e.g., 32, 328, 33, 329] and dynamical formation models [e.g., 330, 331, 200]. Possible progenitor systems of BBHs, including Cyg X-3 [300], IC 10 X-1 [301] and NGC 300 X-1 [302, 301] provide some additional limits on BBH merger rates, but extrapolation is hindered by current observational uncertainties.

The parameters of individual systems can be estimated by comparing the measured GW signal with template waveforms [9]. The masses and spins of the BHs can be measured through their influence on the inspiral, merger and ringdown of the system [288, 332, 333]. The distribution of parameters observed by aLIGO will encode information about the population of BBHs, and may also help to shed light on their formation channels [303, 289, 174, 181, 182, 123, 2, 334, 265]

Stellar-mass BHs are expected to be born spinning, with observations suggesting their dimensionless spin parameters χ take the full range of allowed values between 0 and 1 [335, 336, 337]. Stars formed in binaries are expected to have their rotational axis aligned with the orbital angular momentum [e.g., 338, 339], although there is observational evidence this is not always the case [e.g., 340]. Even if binaries are born with misaligned spins, there are many processes in binary evolution which can

act to align the spin of stars, such as realignment during a stable mass accretion phase [341, 342, 343], accretion onto a BH passing through a CE event [148], and realignment through tidal interactions in close binaries [e.g., 344, 345].

On the other hand, asymmetric mass loss during supernova explosions can tilt the orbital plane in binaries [132, 342], leading to BH spins being misaligned with respect to the orbital angular momentum vector. Population synthesis studies of BH X-ray binaries predict that these misalignments are generally small [342], with Fragos *et al.* [346] finding that the primary BH is typically misaligned by $\lesssim 10^\circ$. However, electromagnetic observations of high mass X-ray binaries containing BHs have hinted that the BHs may be more significantly misaligned. One such system is the microquasar V4641 Sgr [347, 348] where the primary BH is thought to be misaligned by $> 55^\circ$.

Alternatively, BBHs can form dynamically in dense stellar environments such as globular clusters. In these environments, it is expected that the distribution of BBH spin–orbit misalignment angles is isotropic [e.g., 207]. The distribution of BBH spin–orbit misalignments therefore contains information about their formation mechanisms.

Constraints on spin alignment from GW observations so far are weak [9, 10, 8]. Some configurations, such as anti-aligned spins for GW151226 [19], are disfavoured; however, there is considerable uncertainty in the spin magnitude and orientation. Determining the spins precisely is difficult because their effects on the waveform can be intrinsically small (especially if the source is viewed face on), and because of degeneracies between the spin and mass parameters [309, 349, 350]. Although the spins of individual systems are difficult to measure, here we show it is possible to use inferences from multiple systems to build a statistical model for the population [cf. 265].

This paper describes how to combine posterior probability density functions on spin–orbit misalignment angles from multiple GW events to explore the underlying population.

We develop a hierarchical analysis in order to combine multiple GW observations of BBH spin–orbit misalignments to give constraints on the fractions of BBHs forming through different channels. We consider different populations of poten-

tial spin–orbit misalignments, each representing different assumptions about binary formation, and use the GW observations to infer the fraction of binaries from each population. In the field of exoplanets, similar hierarchical analyses have been used to make inference on the frequency of Earth-like exoplanets from measurements of the period and radius of individual exoplanet candidates [e.g., 351, 352]. Other examples of the use of hierarchical analyses in astrophysics include modelling a population of trans-Neptunian objects [353], measurements of spin–orbit misalignments in exoplanets [354], measurements of the eccentricity distribution of exoplanets [355] and the measurement of the mass distribution of galaxy clusters [356].

In Section 4.2 we introduce our simplified population synthesis models for BBHs, paying special attention to the BH spins. We briefly describe in Section 4.3 the parameter estimation (PE) pipeline that will be employed to infer the properties (such as misalignment angles) of real GW events, and discuss previous spin-misalignment studies in the literature. We introduce a framework for combining posterior probability density functions on spin–orbit misalignment angles from multiple GW events to explore the underlying population in Section 5.5. We demonstrate the method using a set of mock GW events in Section 4.5, and show that tens of observations will be sufficient to distinguish subpopulations of coalescing binary black holes, assuming spin magnitudes of ~ 0.7 . We also show that more extreme models, such as the hypothesis that all BBHs have their spins exactly aligned with the orbital angular momentum, can be ruled out at a 5σ confidence level with only $\mathcal{O}(5)$ observations of rapidly spinning BBHs. Finally, we conclude and suggest areas which require further study in Section 4.6.

4.2 BH spin misalignment models

Owing to the many uncertainties pertaining to stellar spins and their evolution in a binary, and the fact that keeping track of stellar spin vectors can be computationally intensive, many population synthesis models choose not to include spin evolution. However, the distribution of spins of the final merging BHs is one of the observables that can be measured with the advanced GW detectors. In this section, we therefore implement a simplified population synthesis model to evolve an ensemble of binaries that will be detectable with aLIGO and AdV and predict their distributions of spin–orbit misalignments. We describe the assumed mass distribution, spin distribution,

and spin evolution below.

4.2.1 Mass and spin magnitude distribution

We assume the same simplified mass distribution for all of our models, so that any differences in the final spin distributions are purely due to our assumptions about the spin-orbit misalignments described in the next section. There are many uncertainties in the evolution of isolated massive binaries, including (but not limited to) uncertainties in the initial distributions of the orbital elements [37], the strength of stellar winds in massive stars [63], the effect of rotation of massive stars on stellar evolution [208, 357], the natal kicks (if any) given to BHs [107, 110, 358, 111] and the efficiency of the CE [148, 155]. Population synthesis methods are large Monte-Carlo simulations using semi-analytic prescriptions in order to explore the effect these uncertainties have on the predicted distributions of compact binaries. Instead, we adopt a number of simplifications that allow us to produce an astrophysically plausible distribution which should not, however, be considered representative of the actual mass distribution of BBHs.

We simulate massive binaries with semimajor axis a drawn from a distribution uniform in $\ln a$ [42]. The components of the binary are a massive primary BH with mass m_1 and a secondary star at the end of its main sequence lifetime.

The primary BH was formed from a massive star with ZAMS mass m_1^{ZAMS} drawn from the IMF with a power law index of -2.35 [39, 40]. The mass ratio of the binary at ZAMS q^{ZAMS} is drawn from a flat distribution $[0, 1]$. The mass of the secondary star is given by $m_2^{\text{ZAMS}} = q^{\text{ZAMS}} m_1^{\text{ZAMS}}$.

We calculate the final remnant mass m_i as a function of the ZAMS mass m_i^{ZAMS} for each star using a fit to Figure 12 in Woosley *et al.* [48]. For stars with $30 < m_i^{\text{ZAMS}}/M_\odot < 50$, in which range BHs are formed after some delay by fall-back of ejecta, we use

$$m_i = 30 \left(\frac{m_i^{\text{ZAMS}}}{50M_\odot} \right)^\alpha M_\odot, \quad (4.1)$$

with $\alpha = 3.9$. For more massive stars with $m_i^{\text{ZAMS}} > 50M_\odot$, which are massive

enough to directly collapse during the iron-core collapse to form BHs, we use

$$m_i = 0.6m_i^{\text{ZAMS}}. \quad (4.2)$$

We only consider BBHs with component masses above $10M_\odot$ below, consistent with aLIGO detections to date [8], and hence omit stars with ZAMS masses below $30M_\odot$ from our population.

We assume that the binary has negligible eccentricity $e = 0$, appropriate for post-CE systems. In all models we have assumed that both main-sequence stars in the binary are born with their rotation axis aligned with the orbital angular momentum axis. In general, the first supernova will misalign the spins due to any natal kick imparted on the remnant. There are expected to be mass-transfer phases between the first and second supernovae which may realign both the spins of the primary BH and the secondary BH progenitor; we vary the assumed degree of realignment in our models.

We assume that BHs receive natal kicks comparable to those received by neutron stars [101], namely drawn from a Maxwellian with a root-mean-square velocity of $\sim 250 \text{ km s}^{-1}$. This assumption will lead to the maximum amount of spin misalignment, and may be consistent with neutrino-driven kicks; if the natal kicks are due to asymmetric ejection of baryonic matter, then any fall-back [125] onto BHs during formation will reduce the kick magnitude and thus the spin misalignment.

BH spins magnitudes can take any value $0 \leq \chi_i < 1$, but we set $\chi_i = 0.7$ for all our BHs. High spin magnitudes are consistent with measurements from X-ray observations [cf. 337], and lie toward the upper end of the range allowed by current GW observations [8]. Such spins are large enough to ensure spin effects on the gravitational waveform are significant, providing an opportunity for us to demonstrate our hierarchical approach, but small enough that we do not have to worry about the validity of the model gravitational waveform. Uncertainties in the relationship between pre-supernova stellar spins and BH spins mean it is not currently possible to produce a realistic distribution of spins from first principles, although a direct translation is often assumed, e.g., by Kushnir *et al.* [266]. If the distribution of BH spin magnitudes in nature favours smaller values, then more observations will be required to draw the conclusions we find here. The methodology we use here can be extended to models including BH spin magnitudes, which could

potentially give us further information regarding formation mechanisms.

After a supernova, we establish whether the binary remains bound and, for those that do, find the new orbital elements [131, 132, 359]. Of the remaining bound systems, we are only interested in those binaries which merge due to the emission of gravitational radiation within a Hubble time, as these are the binaries that are potentially observable with GW detectors.

4.2.2 Models for spin–orbit misalignment distributions

We model the overall population of BBHs as a mixture of 4 subpopulations, each of which makes differing assumptions leading to distinct spin–orbit misalignment distributions.

We define the spin–orbit misalignment angle as the angle between the spin vector $\hat{\mathbf{S}}_i$ of binary component $i \in 1, 2$ and the (Newtonian) orbital angular momentum vector $\hat{\mathbf{L}}$,

$$\cos \theta_i = \hat{\mathbf{S}}_i \cdot \hat{\mathbf{L}}, \quad (4.3)$$

where

$$\mathbf{S}_i = \chi_i m_i^2 \hat{\mathbf{S}}_i, \quad (4.4)$$

and m_i is the component mass ($m_1 \geq m_2$).¹ We will consider how a set of spin–misalignment measurements could be used to infer BBH formation mechanisms.

Subpopulation 1: Exactly aligned We assume that irrespective of all prior processes, both BHs have their spins aligned with the orbital angular momentum vector after the second supernova, such that $\cos \theta_1 = \cos \theta_2 = 1$. This may be the case if BHs receive no kicks. GW searches often assume BBHs have aligned spins as this simplification makes the search less computationally demanding [21].

Subpopulation 2: Isotropic/dynamical formation We assume that BBHs are formed dynamically, such that the distribution of spin angles is isotropic. Initially isotropic distributions of spins remain isotropic [179]. We still generate

¹Throughout this paper we use geometric units $G = c = 1$ unless otherwise stated.

the binary mass distribution with our standard approach, so that the only difference in BBHs between this model and the others is the spin distribution.

Subpopulation 3: Alignment before second SN Motivated by Kalogera [342], we assume that the spins of both components are aligned with the orbital angular momentum after a CE event and prior to the second supernova. The tilt of the orbital plane caused by the second supernova is then taken to be the spin misalignment angle of *both* components, i.e. $\cos\theta_1 = \cos\theta_2$. As we discuss in Section 4.2.3, these spins freely precess from the time of the second supernova up until merger. This precession somewhat scatters these angles, but leaves them with generally similar values, as seen in Figure 4.1.

Subpopulation 4: Alignment of secondary We follow the standard mass-ratio model with effective tides presented in Gerosa *et al.* [174], which assumes that after the first supernova, the secondary is realigned via tides or the CE prior to the second supernova. However, the primary BH is not realigned. Because the binary’s orbit shrinks during CE ejection, the kick velocity of the secondary is small relative to its pre-supernova velocity, causing the secondary to be only mildly misaligned (in general $\theta_1 > \theta_2$).

We generate several thousand samples from each of these models. We plot samples from the four subpopulations in the $\{\cos\theta_1, \cos\theta_2\}$ plane of the misalignment angles in Figure 4.1. From each of these models we randomly select 20 mock detected systems (for a total of $N = 80$) with component masses between $10M_\odot$ and $40M_\odot$ [cf. 8]; we describe the analysis of these mock GW signals in Section 4.3. We show the true values of the spin misalignment angles for the mock detected systems in Figure 4.2.

We use an astrophysical distribution of systems with sky positions and inclinations randomly chosen, and distances D_L distributed uniformly in volume, $p(D_L) \propto D_L^2$, such that the distribution of SNR ρ is $p(\rho) \propto \rho^{-4}$ [360]. We use a detection threshold (minimum network SNR) of $\rho_{\min} = 12$ [14, 361].

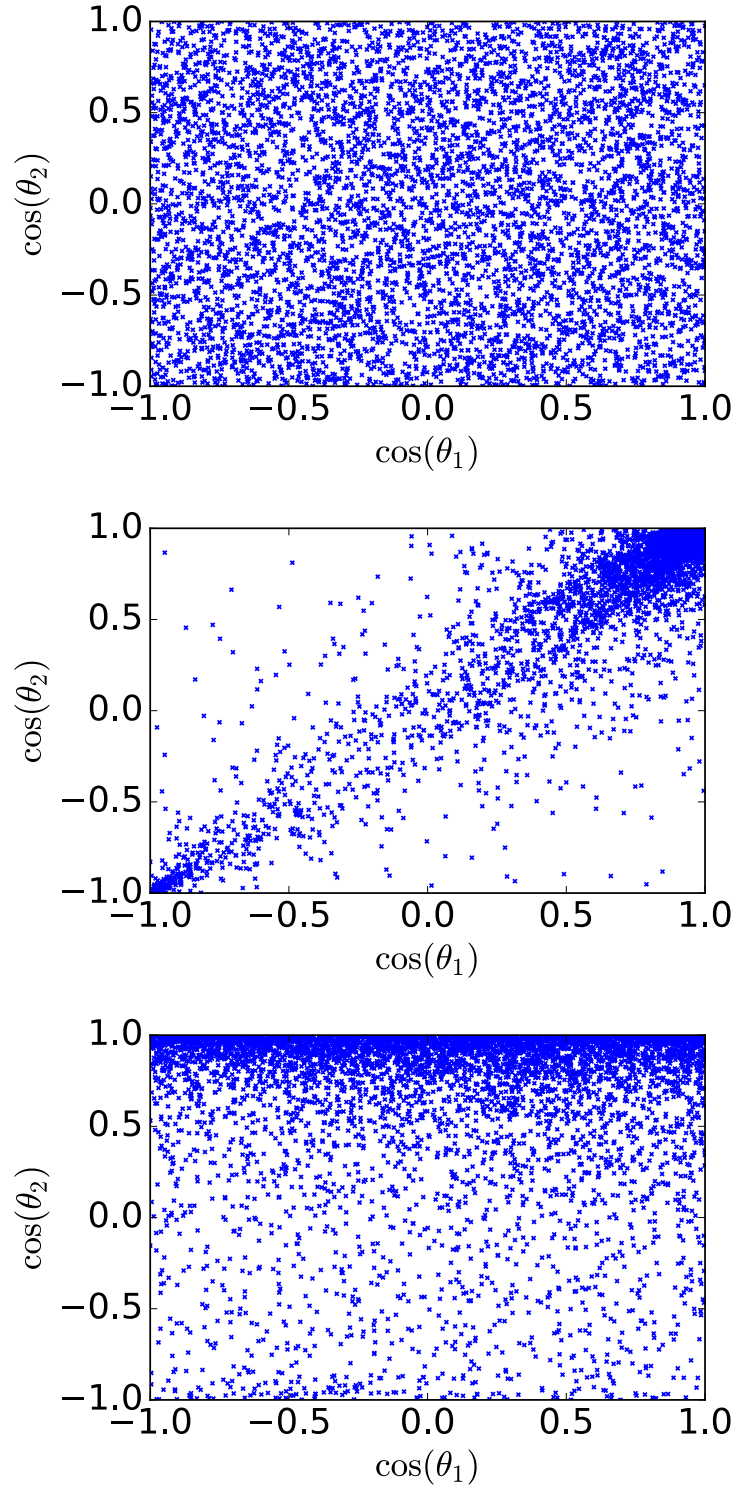


Figure 4.1: Three of the four astrophysically motivated subpopulations making up our mixture model for BBH spin misalignment angles θ_1 and θ_2 described in Section 4.2. Subpopulation 1 (not shown) has both spins perfectly aligned ($\cos\theta_1 = \cos\theta_2 = 1$), so all points would lie in the top right corner. In subpopulation 2 (top), both spins are drawn from an isotropic distribution, and so the samples are distributed uniformly in the plane. In subpopulation 3 (middle) BH spins are aligned with the orbital angular momentum just prior to the second supernova. In subpopulation 4 (bottom), the secondary BH has its spin aligned with the orbital angular momentum prior to the second supernova, whilst the primary is misaligned. See Section 4.2 for more details. Spins are quoted at a GW frequency of $f_{\text{ref}} = 10$ Hz. Figure reproduced from [3].

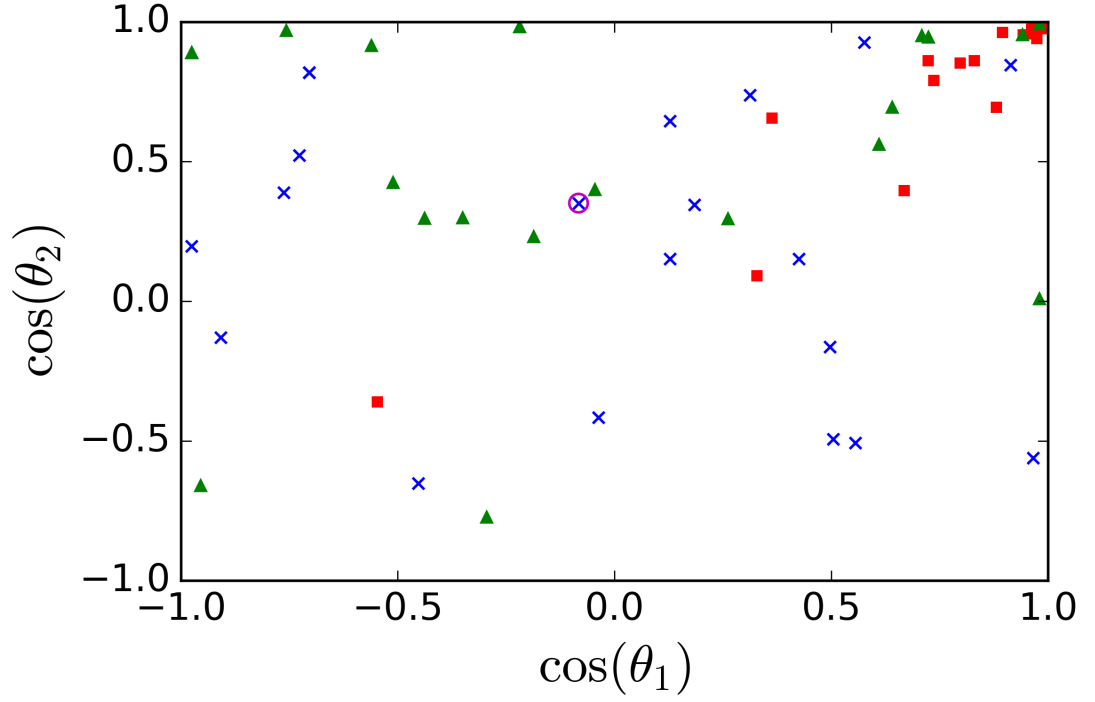


Figure 4.2: True values of BH spin–orbit misalignment angles $\cos \theta_1$ and $\cos \theta_2$ for a mixture of 20 draws from each of our four subpopulations. Exactly aligned systems from subpopulation 1 sit in the upper right corner of this diagram and thus are not shown. Systems drawn from subpopulation 2 are shown as blue crosses, those from subpopulation 3 as red squares and those from subpopulation 4 as green triangles. The injection plotted in Figures 4.3 and 4.7 is circled in magenta. Figure reproduced from [3]

4.2.3 Precession and spin–orbit resonances

After the second supernova, the evolution of the BBH is purely driven by relativistic effects and the orbit decays due to the emission of gravitational radiation [172, 173]. As the BHs orbit, their spins precess around the total angular momentum [362, 270]. In order to predict the spin misalignment angles when the frequency of GWs emitted by the binary are high enough (or equivalently when the orbital separation of the binary is sufficiently small) to be in the aLIGO band ($f_{\text{GW}} > 10$ Hz), we take into account the post-Newtonian (PN) evolution of the spins by evolving the ten coupled differential equations given by Equations (14)–(17) in Gerosa *et al.* [174]. We begin our integrations at an orbital separation $a = 1000M$, and integrate up until $f_{\text{GW}} = 10$ Hz.²

Some of these binaries are attracted to spin–orbit resonances [179]. In particular, the binaries from subpopulation 4 are attracted to the $\Delta\Phi = \pm 180^\circ$ resonance, where $\Delta\Phi$ is the angle between the projection of the two spins on the orbital plane. The current generation of ground-based GW observations are generally insensitive to this angle for binary black holes [363, 10], and the waveform model we use does not include it, so we focus on distinguishing subpopulations through the better-measured θ_1 and θ_2 angles.

4.3 Gravitational-wave parameter estimation

4.3.1 Signal analysis and inference

The strain measured by a GW detector is a combination of detector noise and (possibly) a GW signal $h(\Theta, t)$,

$$d(t) = n(t) + h(\Theta, t). \quad (4.5)$$

²A more efficient method of evolving binaries from wide orbital separations to the frequencies where they enter the aLIGO band was recently introduced [175, 176]. This exploits the hierarchy of timescales in the problem and integrates precession averaged equations of motion on the radiation reaction timescale, rather than integrating the orbit-averaged equations we use here.

Here Θ is the vector of parameters describing the GW signal; for a general spinning circular BBH, there are 15 parameters.³ Given a data stream, we want to infer the most probable set of parameters for that data. To estimate the properties of the signal, waveform templates are matched to the data [288, 281, 9]

The posterior probability for the parameters is given by Bayes' theorem,

$$p(\Theta|d) = \frac{p(d|\Theta)p(\Theta)}{p(d)}, \quad (4.6)$$

where $p(d|\Theta)$ is the likelihood of observing the data given a choice of parameters, $p(\Theta)$ is the prior on those parameters, and the evidence $p(d)$ is a normalisation constant for the purposes of PE. The prior encodes our belief about the parameters before we considered the data: we assume that sources are uniformly distributed across the sky and in volume; that spin magnitudes are uniformly distributed between 0 and 1; that spin orientations and the binary orientation are uniformly distributed across the surface of the sphere, and that component masses are uniformly distributed up to a maximum of $150M_\odot$ [cf. 9]. The likelihood is calculated from the residuals between the data and the signal template, assuming that the noise is Gaussian [288]:

$$p(d|\Theta) \propto \exp \left\{ -\frac{1}{2} (d - h(\Theta)|d - h(\Theta)) \right\}, \quad (4.7)$$

where the inner product $(g|h)$ is given by [364]

$$(g|h) = 4 \operatorname{Re} \int_{f_{\text{low}}}^{\infty} \frac{\tilde{g}(f)\tilde{h}^*(f)}{S_n(f)} df, \quad (4.8)$$

and $S_n(f)$ is the (one-sided) noise power spectral density [365], which we take to be the design sensitivities for aLIGO and AdV respectively, with $f_{\text{low}} = 10$ Hz as is appropriate for the advanced detectors.

We sample the posterior distribution using the publicly available, Bayesian PE code **LALInference** [281].⁴ For each event we obtain $\nu \sim 5000$ independent posterior samples. We show an example of the marginalised posterior distribution in

³These parameters are [e.g., 281]: two component masses $\{m_i\}$; six spin parameters describing $\{\mathbf{S}_i\}$; two sky coordinates; distance D_L ; inclination and polarization angles; a reference time, and the orbital phase at this time.

⁴Available as part of the LIGO Scientific Collaboration Algorithm Library (LAL) <https://wiki.ligo.org/DASWG/LALSuite>.

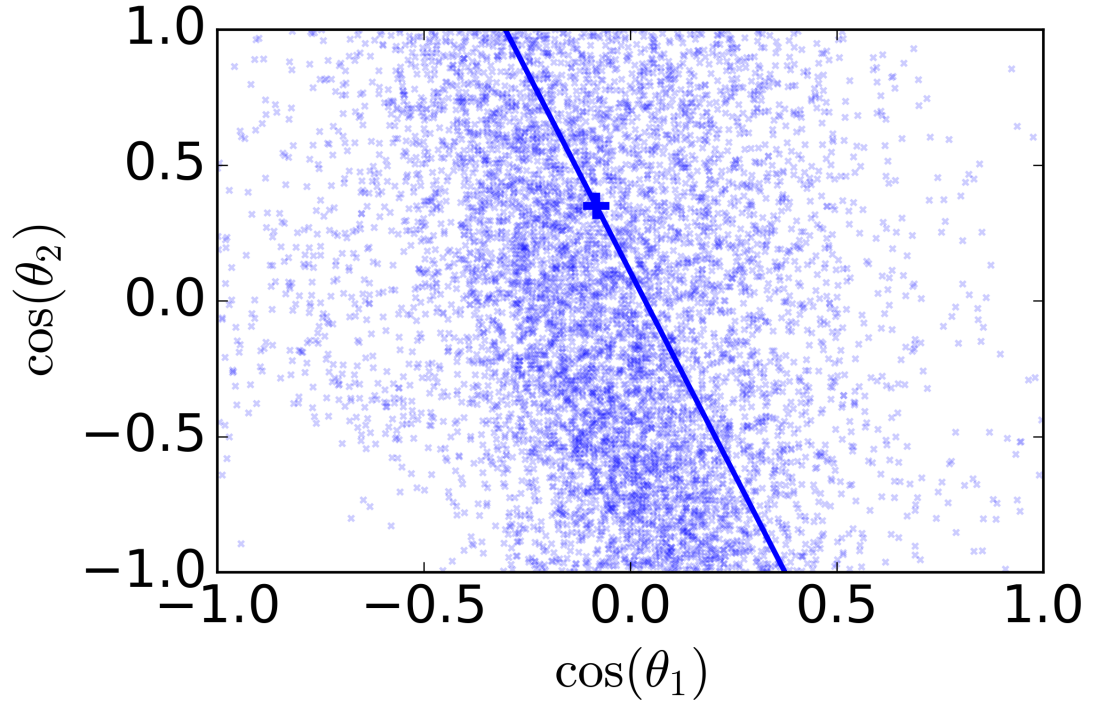


Figure 4.3: Marginalised posterior samples for one of the 80 events shown in Figure 4.2, generated by analysing mock GW data using **LALInference**. The true spin-orbit misalignments (thick blue plus) for this event were $\cos\theta_1 = -0.08$ and $\cos\theta_2 = 0.35$, with a network SNR of 15.35. The solid diagonal line shows the line of constant χ_{eff} . Figure reproduced from [3].

$\{\cos \theta_1, \cos \theta_2\}$ space for one of our 80 events in Figure 4.3. Unless otherwise stated, we quote all parameters at a reference frequency $f_{\text{ref}} = 10$ Hz.

We sample in the system frame [366], where the binary is parametrised by the masses and spin magnitudes of the two component BHs $\{m_i\}$ and $\{\chi_i\}$, the spin misalignment angles $\{\theta_i\}$, the angle $\Delta\Phi$ between the projections of the two spins on the orbital plane, and the angle β between the total and orbital angular momentum vectors. We find, in agreement with similar studies such as Littenberg *et al.* [122] and Miller *et al.* [367], that there is a strong preference for detecting GWs from nearly face-on binaries, since GW emission is strongest perpendicular to the orbital plane.

Following common practice in PE studies, we use a special realisation of Gaussian noise which is exactly zero in each frequency bin [368, 182]. Real GW detector noise will be non-Gaussian and non-stationary, and events will be recovered with non-zero noise.⁵ Non-zero noise-realisation will mean that in general the maximum likelihood parameters do not match the injection parameters; in the Gaussian limit, however, using a zero noise realisation is equivalent to averaging over a large number of random noise realisations, such that these offsets approximately cancel out [cf. 369]. This assumption makes it straightforward to compare the posterior distributions, as differences only arise from the input parameters and not any the specific noise realisation.

4.3.2 Previous studies

Vitale *et al.* [265] study GW measurements of BH spin misalignments in compact binaries containing at least one BH. They consider both BBHs (using `IMRPhenomPv2` waveforms as we do here) and NSBH binaries (using inspiral-only `SpinTaylorT4` waveforms). They fit a mixture model allowing for both a preferentially aligned/anti-aligned component and an isotropically misaligned component, excluding aligned/anti-aligned systems. They find that ~ 100 detections yield a $\sim 10\%$ precision for the measured aligned fraction. One of the main limitations of the analysis performed by Vitale *et al.* [265] is that they only consider models which are mutually exclu-

⁵Non-stationary, non-Gaussian noise has been shown not to affect average PE performance for binary neutron stars [361]; however, these noise features could be more significant in analysing the shorter duration BBH signals.

sive, although this should not affect their results since the excluded region for their nonaligned model is negligible. Here, all of our formation models overlap in the parameter space of spin–orbit misalignment angles. Therefore, we cannot directly apply the formalism of Vitale *et al.* [265]. The framework we develop here is able to correctly determine the relative contributions of multiple models, even when those models overlap in parameter space significantly, as expected in practice.

There have also been significant advances in the past few years in the understanding of PN spin–orbit resonances. These resonances occur when BH spins become aligned or anti-aligned with one another and precess in a common plane around the total angular momentum [179]. This causes binaries to be attracted to different points in parameter space identified by $\Delta\Phi$, the angle between the projections of the two BH spins onto the orbital plane. Kesden *et al.* [180] have shown that these resonances are effective at capturing binaries with mass ratios $0.4 < q < 1$ and spins $\chi_i > 0.5$. For equal-mass binaries, spin morphologies remain locked with binaries trapped in or out of resonance [370]; however, it is unlikely for astrophysical formation scenarios to produce exactly equal mass binaries, although Marchant *et al.* [129] predict nearly equal masses for the chemically homogeneous evolution channel.

Gerosa *et al.* [174] show how the family of resonances that BBHs are attracted to can act as a diagnostic of the formation scenario for those binaries. Trifirò *et al.* [182] demonstrate that GW measurements of spin misalignments can be used to distinguish between the two resonant families of $\Delta\Phi = 0^\circ$ and $\Delta\Phi = \pm 180^\circ$. They use a full PE study to show that they can distinguish two families of PN resonances. However, they only consider a small corner of parameter space which contains binaries which will become locked in these PN resonances.

Our study extends on those discussed in several ways:

1. Rather than focusing on specific systems preferred in previous studies, we use injections from an astrophysically motivated population. Our injections have total masses $M = m_1 + m_2$ in the range $10\text{--}40M_\odot$ and an astrophysical distribution of SNRs.
2. The misalignment angles of our BHs are given by simple but astrophysically motivated models introduced in Section 4.2.

3. For performing PE on individual GW events, we use the inspiral-merger-ringdown gravitational waveform `IMRPhenomPv2` model, rather than the inspiral-only waveforms used in some of the earlier studies.
4. Most importantly, we perform a hierarchical Bayesian analysis on the posterior probability density functions of a mock catalog of detected events in order to make inferences about the underlying population.

4.4 Hierarchical analysis for population inference

PE on individual GW events yields samples from the posterior distributions for parameters under astrophysical prior constraints. We now wish to combine these individual measurements of BH spin misalignment angles in order to learn about the underlying population, which may act as a diagnostic for binary formation channels and binary evolution scenarios. Importantly, we are able to do this without reanalysing the data for the individual events.

Given a set of reasonable population synthesis model predictions for BBH spin misalignment angles, we would like to learn what mixture of those subpopulations best explains the observed data. Here we assume that the subpopulation distributions representing different formation channels are known perfectly, and use the same subpopulations that we drew our injections from to set these distributions. Thus, each subpopulation model Λ_ℓ ($\ell \in 1 \dots 4$) corresponds to a known distribution of source parameters $p(\Theta|\Lambda_\ell)$. In practice, the uncertainty in the subpopulation models will be one of the challenges in carrying out accurate hierarchical inference⁶.

The overall mixture model is described by hyperparameters λ_ℓ , corresponding to the fraction of each of the four subpopulations, such that

$$p(\Theta|\lambda) = \sum_{\ell=1}^4 \lambda_\ell p(\Theta|\Lambda_\ell). \quad (4.9)$$

⁶The clustering approach of Mandel *et al.* [123, 334], which eschews assumptions about the subpopulation distributions, could provide an alternative pathway for robust but less informative inference on the data alone.

We assume that each event comes from one of these subpopulations:

$$\sum_{\ell=1}^4 \lambda_{\ell} = 1, \quad (4.10)$$

i.e., $\boldsymbol{\lambda}$ is a unit simplex.

For any individual event α ($\alpha = 1, \dots, N$) we have the posterior on $\boldsymbol{\Theta}$ given by

$$p(\boldsymbol{\Theta}|d_{\alpha}) = \frac{p(d_{\alpha}|\boldsymbol{\Theta})p(\boldsymbol{\Theta})}{p(d_{\alpha})}, \quad (4.11)$$

where $p(\boldsymbol{\Theta})$ is the prior used by `LALInference`, $p(d_{\alpha})$ is the evidence (which is only a normalising factor in our analysis), and we represent $p(\boldsymbol{\Theta}|d_{\alpha})$ by a set of discrete samples $\{\boldsymbol{\Theta}_i^k\}$ where $k = 1, \dots, \nu_{\alpha}$.

We can write the likelihood for obtaining all of the events as the product over the individual likelihoods [290, 355],

$$p\left(\{d_{\alpha}\}_{\alpha=1}^N \middle| \boldsymbol{\lambda}\right) = \prod_{\alpha=1}^N p(d_{\alpha}|\boldsymbol{\lambda}) \quad (4.12)$$

$$= \prod_{\alpha=1}^N \int d\boldsymbol{\Theta}_{\alpha} p(d_{\alpha}|\boldsymbol{\Theta}_{\alpha}) p(\boldsymbol{\Theta}_{\alpha}|\boldsymbol{\lambda}) \quad (4.13)$$

$$= \prod_{\alpha=1}^N p(d_{\alpha}) \int d\boldsymbol{\Theta}_{\alpha} \frac{p(\boldsymbol{\Theta}_{\alpha}|d_{\alpha})}{p(\boldsymbol{\Theta}_{\alpha})} p(\boldsymbol{\Theta}_{\alpha}|\boldsymbol{\lambda}), \quad (4.14)$$

where we have marginalised over the physical parameters of the individual events, and used Bayes' theorem to obtain the final line. Since we have samples drawn from the posterior $p(\boldsymbol{\Theta}_{\alpha}|d_{\alpha})$, we can approximate posterior-weighted integrals (posterior averages) as a sum over samples [371, chapter 29],

$$\int d\boldsymbol{\Theta}_{\alpha} p(\boldsymbol{\Theta}_{\alpha}|d_{\alpha}) f(\boldsymbol{\Theta}_{\alpha}) = \frac{1}{\nu_{\alpha}} \sum_{k=1}^{\nu_{\alpha}} f(\boldsymbol{\Theta}_{\alpha}^k), \quad (4.15)$$

where $f(\boldsymbol{\Theta})$ is some general function. Thus, we can rewrite Equation (4.14) as

$$p\left(\{d_{\alpha}\}_{\alpha=1}^N \middle| \boldsymbol{\lambda}\right) = \prod_{\alpha=1}^N \frac{p(d_{\alpha})}{\nu_{\alpha}} \sum_{k=1}^{\nu_{\alpha}} \frac{p(\boldsymbol{\Theta}_{\alpha}^k|\boldsymbol{\lambda})}{p(\boldsymbol{\Theta}_{\alpha}^k)}. \quad (4.16)$$

In effect, for each event we reweigh the evidence calculated using our general PE

prior to what it would have been using a prior for the model of interest, and then combine these probabilities together to form a likelihood.

The posterior for $\boldsymbol{\lambda}$ is then

$$p\left(\boldsymbol{\lambda} \middle| \{d_\alpha\}_{\alpha=1}^N\right) \propto p\left(\{d_\alpha\}_{\alpha=1}^N \middle| \boldsymbol{\lambda}\right) p(\boldsymbol{\lambda}), \quad (4.17)$$

for a choice of prior $p(\boldsymbol{\lambda})$. We assume a flat Dirichlet prior as shown in Figure 4.4. We sample from this posterior on $\boldsymbol{\lambda}$ using `emcee` [372], an affine-invariant ensemble sampler [373].⁷

4.5 Results

To gain a qualitative understanding of hierarchical modelling on the spin–orbit misalignment angles, we first consider inference under the assumption of perfect measurement accuracy for individual observations, and then introduce realistic measurement uncertainties. We then analyse the scaling of the inference accuracy with the number of observations.

4.5.1 Perfect measurement accuracy

Here, we assume that aLIGO–AdV GW observations could perfectly measure the spin–orbit misalignment angles of merging BBHs. In this case, the posterior is simply a delta function centered at the true value. Since our underlying astrophysical models have significant overlap in the $\{\cos(\theta_1), \cos(\theta_2)\}$ plane, as shown in Figure 4.1, there is still ambiguity about which model a given event comes from.

We sample Equation (4.17), where our data consist of 80 events with perfectly measured spin–orbit misalignments (as seen in Figure 4.2). This number of detections could be available by the end of the O3 observing run under optimistic assumptions about detector sensitivity improvements [8]. The results of this analysis are shown in Figure 4.5.

⁷Available from <http://dan.iel.fm/emcee/>.

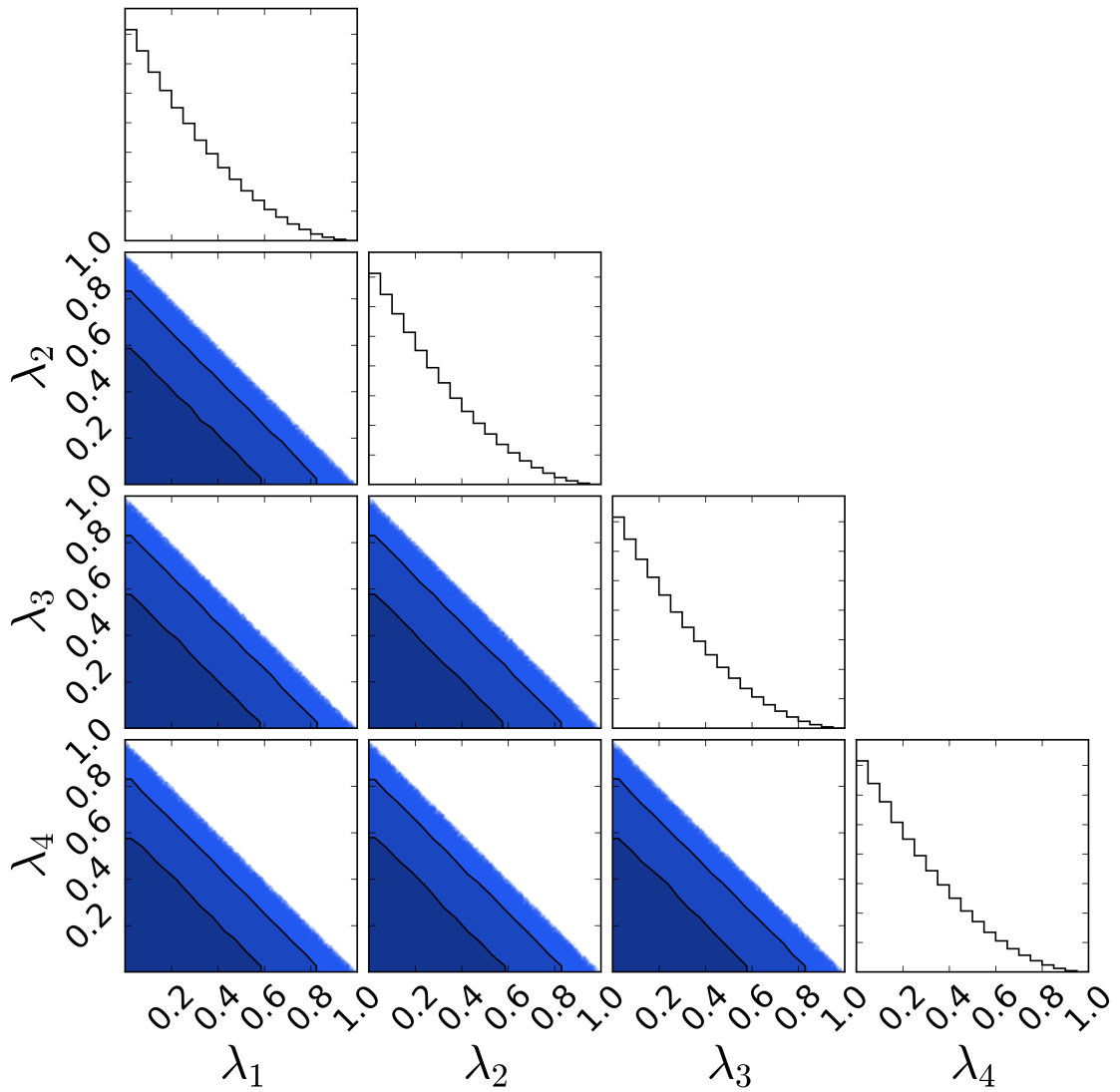


Figure 4.4: Marginalised 1D and 2D probability density functions for the Dirichlet prior used for the analysis of the λ parameters, which describe the fractional contribution of each of the four subpopulations introduced in Section 4.2. The constraint $\lambda_1 + \lambda_2 + \lambda_3 + \lambda_4 \equiv 1$ introduces correlations between parameters. The shaded regions show the 68% (darkest blue) and 95% (middle blue) confidence regions, with the individual posterior samples outside these regions plotted as scatter points (lightest blue). Figure reproduced from [3].

We find that after 80 BBH observations with perfect measurement accuracy, we would be able to confidently establish the presence of all four subpopulations. From this analysis, we can already understand some of the features of the posterior on the hyperparameters. For example, we see that there is a strong degeneracy between λ_1 and λ_3 , since both of these models predict a large (nearly) aligned ($\theta_1 = \theta_2 = 0$) population. There is a similar degeneracy between λ_2 and λ_4 . We can also see that the fraction of exactly aligned systems (λ_1) and the fraction of systems with isotropically distributed spin-orbit misalignments (λ_2) are not strongly correlated. Both fractions are measured with to be between ~ 0.15 and ~ 0.45 at the 90% credible level with 80 BBH observations, corresponding to a fractional uncertainty of $\sim 50\%$.

4.5.2 Realistic measurement accuracy

We know that in practice GW detectors will not perfectly measure the spin-orbit misalignments of merging BBHs (see Figure 4.3 for a typical marginalised posterior). We now use the full set of 80 **LALInference** posteriors, each containing ~ 5000 posterior samples as our input data, when sampling Equations (4.16) and (4.17).

We show the results of this analysis in Figure 4.6. Many of the features seen in the posteriors on the hyperparameters are the same as those seen in Figure 4.5, such as the strong anti-correlation between λ_1 and λ_3 . We see that the posterior is not perfectly centred on the true λ values, though the true values do have posterior support. While the hierarchical modelling unambiguously points to the presence of multiple subpopulations, with no single subpopulation able to explain the full set of observations, the data no longer require all four subpopulations to be present.

We have checked that the structure of this posterior is typical given the limited number of observations and the large measurement uncertainties. In the next section we show that our posteriors converge to the true values in the limit of a large number of detections.

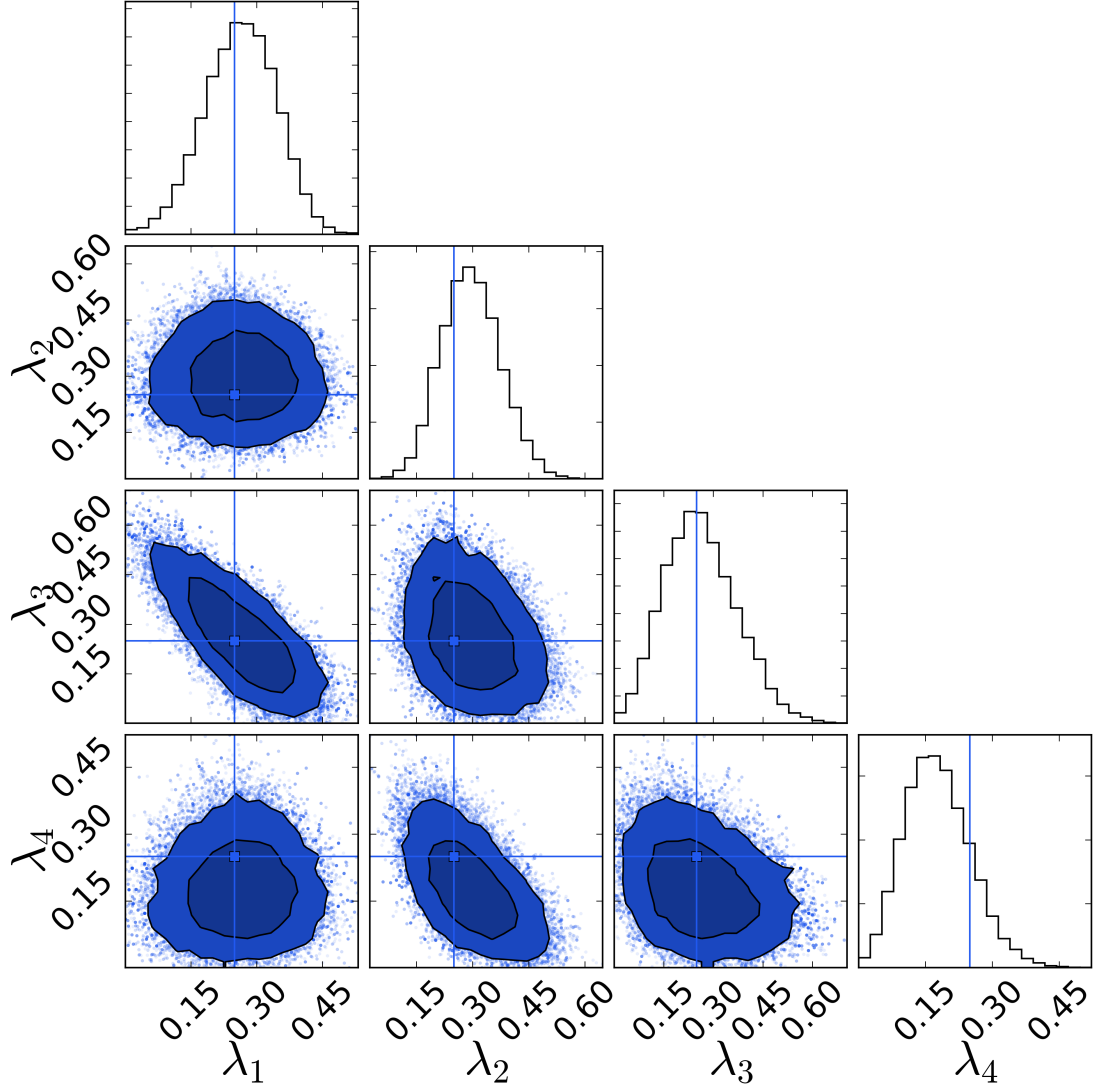


Figure 4.5: Marginalised 1D and 2D probability density functions for the λ parameters describing the fractional contribution of each of the four subpopulations introduced in Section 4.2. The thin blue lines indicate the true injection fraction from each model, which is 0.25 for all models. The data used were the 80 mock GW events shown in Figure 4.2, assumed to have perfect measurements of the spin-orbit misalignment angles $\cos \theta_1$ and $\cos \theta_2$. Colours are the same as Figure 4.4. Figure reproduced from [3].

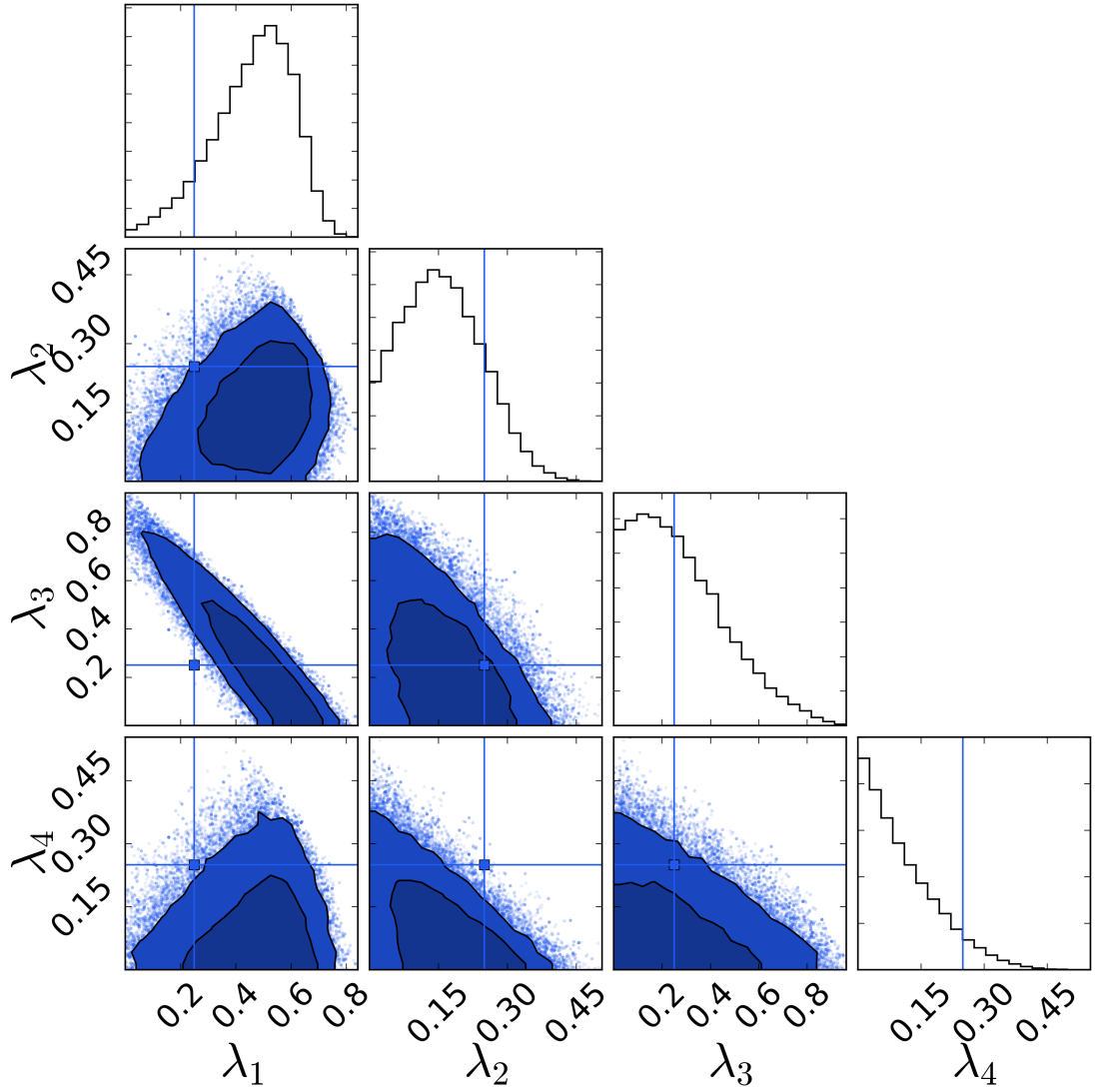


Figure 4.6: Marginalised 1D and 2D probability density functions for the λ parameters describing the fractional contribution of each of the four subpopulations introduced in Section 4.2. The thin blue lines indicate the true injection fraction from each model, which is 0.25 for all models. The data used were the full `LALInference` posteriors of the 80 mock GW events shown in Figure 4.2. Colours are the same as Figure 4.4. Figure reproduced from [3].

4.5.3 Dependence on number of observations

The `LALInference` PE pipeline used to compute the posterior distributions for our 80 injections in Section 4.3 is computationally expensive. However, we would like to generate a larger catalogue of mock observations. First, this allows us to check that our analysis is self consistent by running many tests, such as confirming that the true result lies within the $P\%$ credible interval in $P\%$ of trials. Second, it allows us to predict how the accuracy of the inferred fractions of the subpopulations evolves as a function of the number of GW observations.

We develop approximations to these posteriors, similar to Mandel *et al.* [334], based on the 80 posterior distributions generated in Section 4.3. The best measured spin parameter is a combination of the two component spins called the effective inspiral spin $\chi_{\text{eff}} \in [-1, 1]$ [313, 9, 374]:

$$\chi_{\text{eff}} = \frac{\chi_1 \cos \theta_1 + q \chi_2 \cos \theta_2}{(1 + q)}. \quad (4.18)$$

Having information about a single spin parameter makes it challenging to extract information about the spin distribution, but not impossible; for example, GW151226's positive χ_{eff} means that at least one spin must have non-zero magnitude and $\theta_i < 90^\circ$ [19].

To compute the approximate posteriors, we represent each observation with true parameter values $\chi_{\text{eff}}^{\text{true}}$ and $\cos \theta_1^{\text{true}}$ by data which are maximum-likelihood estimates in a random noise realization:

$$\chi_{\text{eff}}^{\text{data}} \sim N(\chi_{\text{eff}}^{\text{true}}, \sigma_{\chi_{\text{eff}}}^2(\chi_{\text{eff}}^{\text{true}})), \quad (4.19)$$

$$\cos \theta_1^{\text{data}} \sim N(\cos \theta_1^{\text{true}}, \sigma_{\cos \theta_1}^2(\cos \theta_1^{\text{true}})), \quad (4.20)$$

where $N(\mu, \sigma^2)$ indicates a normal distribution. Posterior samples are then drawn using the same likelihood functions, centred on the maximum-likelihood data value,

$$\chi_{\text{eff}}^{\text{sample}} \sim N(\chi_{\text{eff}}^{\text{data}}, \sigma_{\chi_{\text{eff}}}^2(\chi_{\text{eff}}^{\text{sample}})), \quad (4.21)$$

$$\cos \theta_1^{\text{sample}} \sim N(\cos \theta_1^{\text{data}}, \sigma_{\cos \theta_1}^2(\cos \theta_1^{\text{sample}})). \quad (4.22)$$

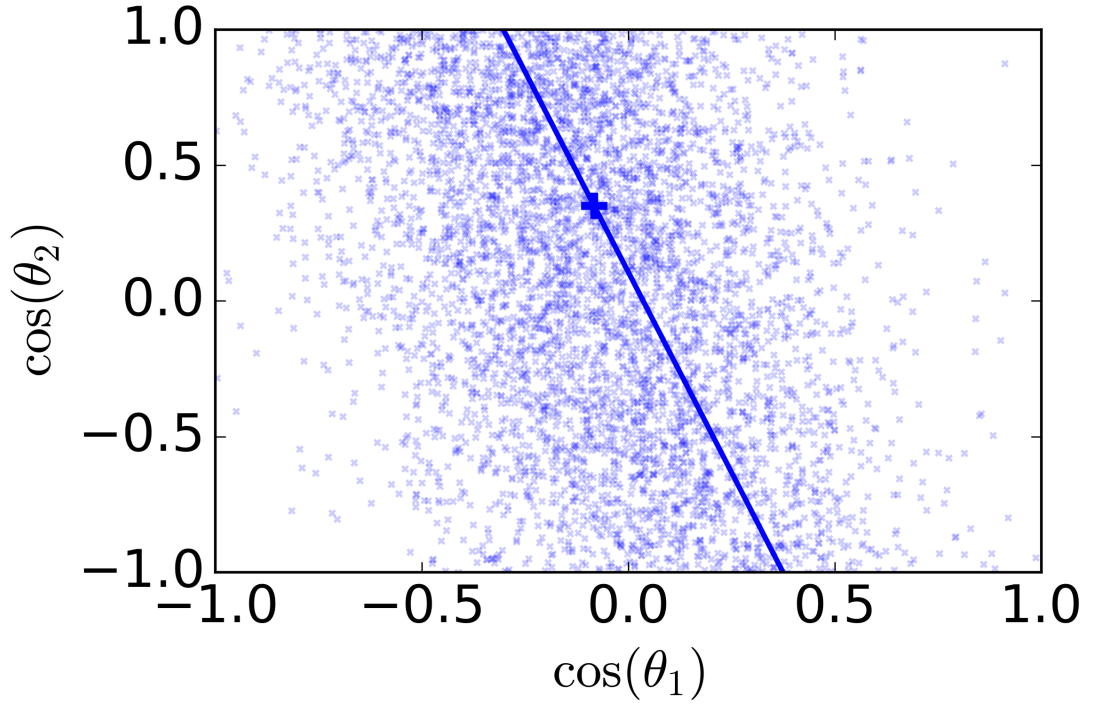


Figure 4.7: Marginalised posterior samples for the same event as shown in Figure 4.3, with the same notation. This posterior distribution was approximated using the model described in section 4.5.3. Figure reproduced from [3].

Here

$$\sigma_{\cos \theta_1} = \frac{12}{\rho}(A \cos \theta_1 + B), \quad (4.23)$$

$$\sigma_{\chi_{\text{eff}}} = \frac{12}{\rho}C, \quad (4.24)$$

with $A = -0.2$, $B = 0.3$ and $C = 0.2$ based on a fit to our 80 posteriors; the measurement uncertainty scales inversely with the signal-to-noise ratio ρ [288]. In all cases, we only consider $\cos \theta_1$, $\cos \theta_2$ and χ_{eff} in the permitted range of $[-1, 1]$.

We draw $\nu = 5000$ posterior samples of χ_{eff} and $\cos \theta_1$ independently, and calculate the values of $\cos \theta_2$ using Equation (4.18), fixing the mass ratio q and spin magnitudes χ_i to their true values. This builds the correct degeneracies between $\cos \theta_1$ and $\cos \theta_2$ into the mock posteriors. We show an example of a posterior distribution generated this way in Figure 4.7.

Using this method, we generate spin–orbit misalignment posteriors for 400 BBHs drawn in equal fractions ($\lambda_i = 0.25$) from the four subpopulation models introduced

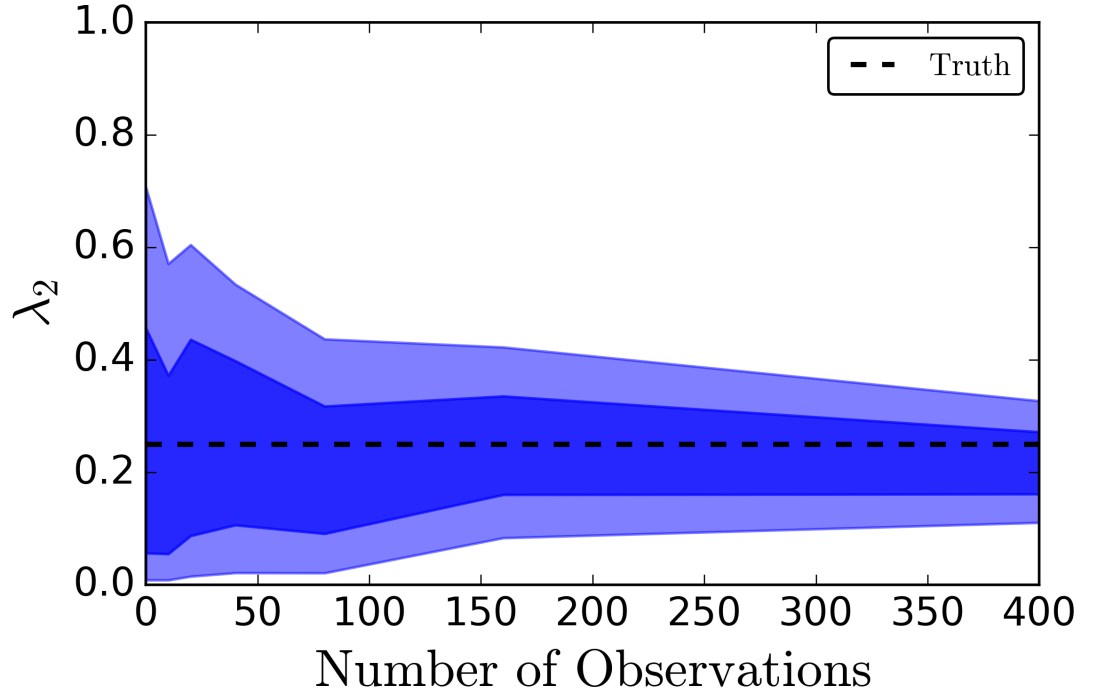


Figure 4.8: Marginalised posterior on λ_2 , the fraction of BBHs from the subpopulation with isotropic spin distribution (representing dynamical formation), as a function of the number of GW observations. The posterior converges to the injected value of $\lambda_2 = 0.25$ (dashed black horizontal line) after ~ 100 observations. The coloured bands show the 68% (darkest) and 95% (lightest) credible intervals. Figure reproduced from [3].

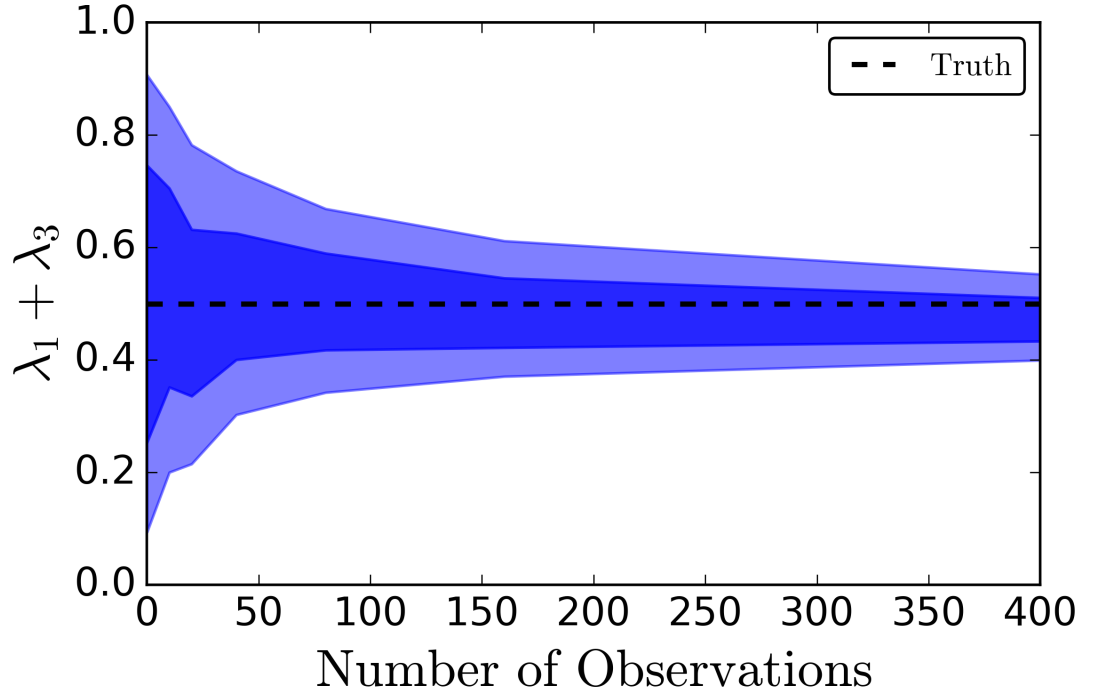


Figure 4.9: Marginalised posterior on $\lambda_1 + \lambda_3$, the combined fraction of BBHs formed through subpopulations 1 and 3, as a function of the number of GW observations. These subpopulations correspond to spins preferentially aligned with the orbital angular momentum. The posterior converges to the injected value of $\lambda_1 + \lambda_3 = 0.5$ (dashed black horizontal line) after ~ 20 observations. The coloured bands show the 68% (darkest) and 95% (lightest) credible intervals. Figure reproduced from [3].

in Section 4.2. Using the method introduced in Section 5.5, we calculate the posteriors on the λ parameters after 0 (prior), 10, 20, 40, 80, 160 and 400 observations, similar to Mandel *et al.* [334]. In Figure 4.8 we show the 68% and 95% credible intervals for the fraction λ_2 of observed BBHs coming from an isotropic distribution (subpopulation 2) corresponding to dynamically formed binaries. Given our models and incorporating realistic measurement uncertainties, we find that this fraction can be measured with a $\sim 40\%$ fractional uncertainty after 100 observations. Since subpopulation 1 and 3 are somewhat degenerate in our model, we find that the combined fraction $\lambda_1 + \lambda_3$ is a well measured parameter (as shown in Figure 4.9), whilst the individual components are measured less well. For $N \gtrsim 100$ observations the uncertainties in the λ_ℓ scale as the inverse square root of the number of observations; e.g., $\sigma_{\lambda_1+\lambda_3} \approx 0.8 N^{-1/2}$.

Although $\gtrsim 100$ observations are required to accurately measure the contribution of each of the four subpopulations, it is possible to test for more extreme models with fewer observations. For example, ~ 20 observations are sufficient to demonstrate the presence of an isotropic subpopulation at the 95% credible level.

Even fewer observations are needed to confidently rule out the hypothesis that all observations come from the exactly aligned or isotropic subpopulations. We draw observations from the isotropic subpopulation and calculate the ratio of the evidence (Bayes factor) Z_{aligned} for the model under which all BBH spins are exactly aligned ($\lambda_1 = 1$) to the evidence $Z_{\text{isotropic}}$ for the model under which all BBH spins are isotropically distributed ($\lambda_2 = 1$):

$$\frac{Z_{\text{aligned}}}{Z_{\text{isotropic}}} = \frac{p\left(\{d_\alpha\}_{\alpha=1}^N \middle| \lambda_1 = 1\right)}{p\left(\{d_\alpha\}_{\alpha=1}^N \middle| \lambda_2 = 1\right)}. \quad (4.25)$$

We repeat this test 100 times to account for the random nature of the mock catalog. In all cases, we find that with only 5 observations of BBHs with component spin magnitudes $\chi = 0.7$, the exactly aligned model $\lambda_1 = 1$ can be ruled out at more than 5σ confidence. Similarly, when drawing from the exactly aligned model, we find that the hypothesis that all events come from an isotropic population $\lambda_2 = 1$ can be ruled out at more than 5σ confidence in all tests with 5 observations.

4.6 Discussion and conclusions

With the first direct observations of GWs from merging BBHs, the era of GW astronomy has begun. GW observations provide a new and unique insight into the properties of BBHs and their progenitors. For individual systems, we can infer the masses and spins of the component BHs; combining these measurements we can learn about the population, and place constraints on the formation mechanisms for these systems, whether as the end point of isolated binary evolution or as the results of dynamical interactions.

In this work, we investigated how measurements of BBH spin-orbit misalignments could inform our understanding of the BBH population. We chose the properties of our sources to match those we hope to observe with aLIGO and AdV (at design sensitivity), using four different astrophysically motivated subpopulations for the distribution of spin-orbit misalignment angles, each reflecting a different formation scenario. We performed a Bayesian analysis of GW signals (using full inspiral-merger-ringdown waveforms) for a population of BBHs. We assumed a mixture model for the overall population of BBH spin-orbit misalignments and combined the full PE results from our GW analysis in a hierarchical framework to infer the fraction of the population coming from each subpopulation. A similar analysis could be performed following the detection of real signals.

Adopting a population with spins of $\chi = 0.7$, we demonstrate that the fraction of BBHs with spins preferentially aligned with the orbital angular momentum ($\lambda_1 + \lambda_3$) is well measured and can be measured with an uncertainty of $\sim 10\%$ with 100 observations, scaling as the inverse square root of the number of observations. We also show that after 100 observations, we can measure the fraction λ_2 of the subpopulation with isotropic spins (assumed to correspond to dynamical formation) with a fractional uncertainty of $\sim 40\%$. Extreme hypotheses can be tested and ruled out with even fewer observations. For example, with just 5 observations we can rule out the hypothesis that all BBHs have their spins exactly aligned with high confidence ($> 5\sigma$) if the true population has isotropically distributed spins, and vice versa. This number of observations may be reached by the end of the second aLIGO observing run.

One limitation of the current approach is the assumption that the subpopulation

distributions are known perfectly. This will not be the case in practice, but the simplified models considered here are still relevant as parametrizable proxies for astrophysical scenarios. Hierarchical modelling with strong population assumptions could lead to systematic biases in the interpretation of the observations if those assumptions are not representative of the true populations; this can be mitigated by coupling such analysis with weakly modelled approaches, such as observation-based clustering [123, 334].

In this work we have not taken into account observational selection effects, such as the impact of the effective spin parameter on the SNR [375], for the different subpopulations. These must be incorporated in the analysis to correctly infer the intrinsic subpopulation fractions [326]. Care must also be taken to avoid biases when performing an hierarchical analysis with real observations, since the observations will not be drawn from the same distribution as the priors used for the analysis of individual events. Our framework accounts for the differences in the priors on the parameters of interest (spin–orbit misalignment angles) between the original PE and model predictions, but not for any discrepancy in the priors of the parameters we marginalize over (e.g., masses); this is likely a second-order effect.

Neither theoretical models nor observations can currently place tight constraints on the spin magnitudes of BHs. We therefore chose to give all BHs a spin magnitude of 0.7 in this study. This choice is clearly *ad hoc*; we expect a distribution of BH spin magnitudes in nature. Since GW events with BHs with low spin will not constrain the spin–orbit misalignment angles well, a distribution of spin magnitudes containing lower BH spins will act to increase the requirements for the numbers of observations quoted here.

Here we have assumed that BHs receive large natal kicks, comparable to neutron stars, leading to relatively large spin–orbit misalignments even for isolated binary evolution. We further assume that the effect of the kick is simply to tilt the orbital plane, but not the BH spin. There is, however, evidence from the Galactic double pulsar PSR J0737–3039 that the second born pulsar received a spin tilt at birth [376]. If such spin tilts are also possible in BH formation, then any link between measured BBH spin–orbit misalignments and formation history could be erased.

Optimal hierarchical modelling should fold in all available information, including component masses [cf. 207] and spin magnitudes [cf. 377, 378], into a single analysis.

Complementary electromagnetic observations of high-mass X-ray binaries, Galactic radio pulsars, short gamma ray bursts, supernovae and luminous red novae will contribute to a concordance model of massive binary formation and evolution.

Acknowledgements

This work was supported in part by the Science and Technology Facilities Council. IM acknowledges support from the Leverhulme Trust. We are grateful for computational resources provided by Cardiff University, and funded by an STFC grant supporting UK Involvement in the Operation of Advanced LIGO. SS and IM acknowledge partial support by the National Science Foundation under Grant No. NSF PHY11-25915. We are grateful to colleagues from the Institute of Gravitational-wave Astronomy at the University of Birmingham, as well as M. Coleman Miller, Chris Pankow and Salvatore Vitale for fruitful discussions. We thank Davide Gerosa and the anonymous referee for comments on the paper. Corner plots were made using `triangle.py` available from <https://github.com/dfm/triangle.py>. This is LIGO Document P1700007.

Chapter 5

Distinguishing Spin-Aligned and Isotropic Black Hole Populations With Gravitational Waves

Will M. Farr,¹ Simon Stevenson,^{1,2} M. Coleman Miller,³ Ilya Mandel,^{1,2} Ben Farr,⁴ Alberto Vecchio¹

¹ School of Physics and Astronomy, University of Birmingham, Edgbaston, Birmingham B15 2TT, United Kingdom

² Kavli Institute for Theoretical Physics, Santa Barbara, CA 93106

³ Department of Astronomy and Joint Space-Science Institute, University of Maryland, College Park, MD 20742–2421, United States

⁴ Enrico Fermi Institute and Kavli Institute for Cosmological Physics, University of Chicago, Chicago, IL 60637, United States

This Chapter reproduces the text of Farr *et al.* [4], accepted in Nature. The work is the result of a collaboration with Will M. Farr, M. Coleman Miller, Ilya Mandel, Ben Farr and Alberto Vecchio. Simon Stevenson and Will M. Farr both performed the analysis. Simon Stevenson made preliminary versions of Figures 5.1, 5.2 and 5.3. Simon Stevenson wrote sections 5.4 and 5.6 and made Figures 5.6 and 5.7. Ben Farr wrote section 5.9 and made Figure 5.9. All other Figures made by Will M. Farr. The text of the paper was written by Will M. Farr. All Authors edited the text.

Abstract

The first direct detections of GWs [7, 19, 20, 8] from merging binary black holes open a unique window into the binary black hole formation environment. One promising environmental signature is the angular distribution of the black hole spins; systems formed through dynamical interactions among already-compact objects are expected to have isotropic spin orientations [192, 191, 193, 200, 206, 207] whereas binaries formed from pairs of stars born together are more likely to have spins preferentially aligned with the binary orbital angular momentum [30, 31, 379, 35, 1, 130, 129]. We consider existing gravitational wave measurements of the binary effective spin, the best-measured combination of spin parameters [9, 8], in the four likely binary black hole detections GW150914, LVT151012, GW151226 and GW170104. If binary black hole spin magnitudes extend to high values, as is suggested by observations of black hole X-ray binaries [337], we show that the data already exhibit a 2.4σ (0.015 odds ratio¹) preference for an isotropic angular distribution. By considering the effect of 10 additional detections [22] drawn from the various models in the suite we show that if all observations come from a single population such an augmented data set would enable at least a 2.4σ (0.016 odds ratio) distinction between the isotropic and aligned models for the assumed spin magnitude distributions, and in most cases better than 5σ (2.9×10^{-7} odds ratio). The existing preference for either an isotropic spin distribution or low spin magnitudes for the observed systems will be confirmed (or overturned) confidently in the near future by subsequent observations.

¹An odds ratio of r with $r \ll 1$ is equivalent to $x\sigma$ with $x = \Phi^{-1}(1 - r/2)$, where Φ is the unit normal CDF.

5.1 Gravitational Wave Spin Measurements and Model Selection

Following the detection of a merging binary black hole system, parameter estimation tools [281] compare model gravitational waveforms [e.g. 277, 380, 276] against the observed data to obtain a posterior distribution on the parameters that describe the compact binary source.

The spin parameter with the largest effect on waveforms, and a correspondingly tight constraint from the data[8], is a mass-weighted, combination of the components of the dimensionless spin vectors of the two black holes that are aligned with the orbital axis, the “effective spin,” $-1 < \chi_{\text{eff}} < 1$ (see Methods Section 5.3).

Figure 5.1 shows an approximation to the posterior inferred on χ_{eff} for the four likely GW detections GW150914, GW151226, GW170104, and LVT151012 from Advanced LIGO’s first and second observing runs (O1 and O2)[8, 20]. Because samples drawn from the posterior on χ_{eff} are not publicly released at this time, we have approximated the posterior as a Gaussian distribution with the same mean and 90% credible interval, truncated to $-1 < \chi_{\text{eff}} < 1$. None of the χ_{eff} posteriors are consistent with two black holes with large aligned spins, $\chi_{1,2} \gtrsim 0.5$; this contrasts with the large spins inferred for the majority of black holes in X-ray binaries with claimed spin measurements (see Section 5.2). The analysis here is relatively insensitive to the precise details of the posterior distributions; other conclusions are more sensitive. In particular, our Gaussian approximation does permit $\chi_{\text{eff}} = 0$ for GW151226 while the true posterior rules this out at high confidence [19, 8].

Small values of χ_{eff} as exhibited in these systems can result from either intrinsically small spins or larger spins whose direction is mis-aligned with the orbital angular momentum of the binary (i.e. spin vectors with small z -components). Mis-alignment is capable of producing *negative* values of χ_{eff} , however, whereas aligned spins will always have $\chi_{\text{eff}} \geq 0$. This difference provides strong discriminating power between the two angular distributions, even without good information about the magnitude distribution; to the extent that data favour negative χ_{eff} they weigh heavily against aligned models. To quantify the degree of support for these two alternate explanations of small χ_{eff} values in the merging BBH population, we compared the Bayesian evidence for various simple models of the spin population using

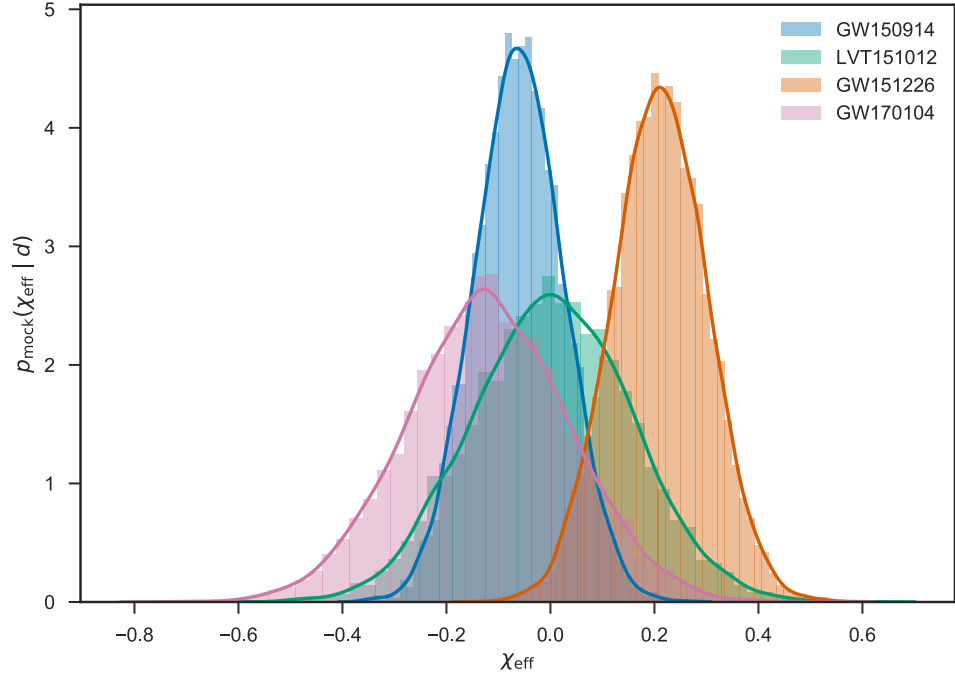


Figure 5.1: Approximate posteriors on χ_{eff} from the Advanced LIGO O1 and GW170104 observations Abbott *et al.* [8], Abbott *et al.* [20]. We approximate the posteriors reported using Gaussians with the same median and 90% credible interval as reported in Abbott *et al.* [8]. It is notable that none of the χ_{eff} posteriors support high BH spin magnitudes with aligned spins, suggested by observations of stellar-mass black holes in X-ray binaries (see Miller & Miller [337] for a summary of such measurements). Figure reproduced from [4].

the GW data set.

Each of our models for the merging binary black hole spin population assumes that the merging black holes are of equal mass (this is marginally consistent with the observations[8, 20], and the χ_{eff} distribution is not sensitive to the mass ratio—see Methods Section 5.7). We assume that the population spin distribution factorises into a distribution for the spin magnitude a and a distribution for the spin angles. Finally, we assume that the distribution of spins is common to each component in a merging binary (the distributions of spin for each component in the binary could differ systematically due to different formation histories). Choosing one of three magnitude distributions (see Methods Section 5.3), “low” (mean $a = 0.33$, standard deviation 0.24), “flat” (mean $a = 0.5$, standard deviation 0.29), “high” (mean $a = 0.67$, standard deviation 0.24) and pairing with an isotropic angular distribution or a distribution that generates perfect alignment yields six different models for the χ_{eff} distribution. These models are shown in Figure 5.2.

These magnitude distributions are not meant to represent any particular physical model, but rather to capture our uncertainty about the spin magnitude distribution; neither observations nor population synthesis codes can at this point authoritatively suggest *any* particular spin distribution[337]. Our models, however, allow us to see how sensitive the χ_{eff} distribution is to spin alignment given uncertainties about the spin magnitudes.

We fit hierarchical models of the three existing LIGO O1 and GW170104 observations using these six different, zero-parameter population distributions (see Methods Section 5.5). We also fit three mixture models for the population, where the angular distribution is a weighted sum of the isotropic and aligned distributions. The evidence, or marginal likelihood, for each of the models is shown in Figure 5.3. For all three magnitude distributions, the mixture models’ posterior on the mixing fraction peaks at 100% isotropic, which explains why the zero-parameter, pure-isotropic models are preferred over the single-parameter mixture models for every magnitude distribution with this data set. Not surprisingly, given the small χ_{eff} values in the three detected systems, the most-favoured model among those with an isotropic angular distribution has the “low” magnitude distribution; the most favoured model among those with an aligned distribution also has the “low” magnitude distribution. The odds ratio between the “low” aligned and “low” isotropic models is 0.015, or 2.4σ ; thus the data favour isotropic spins among our suite of

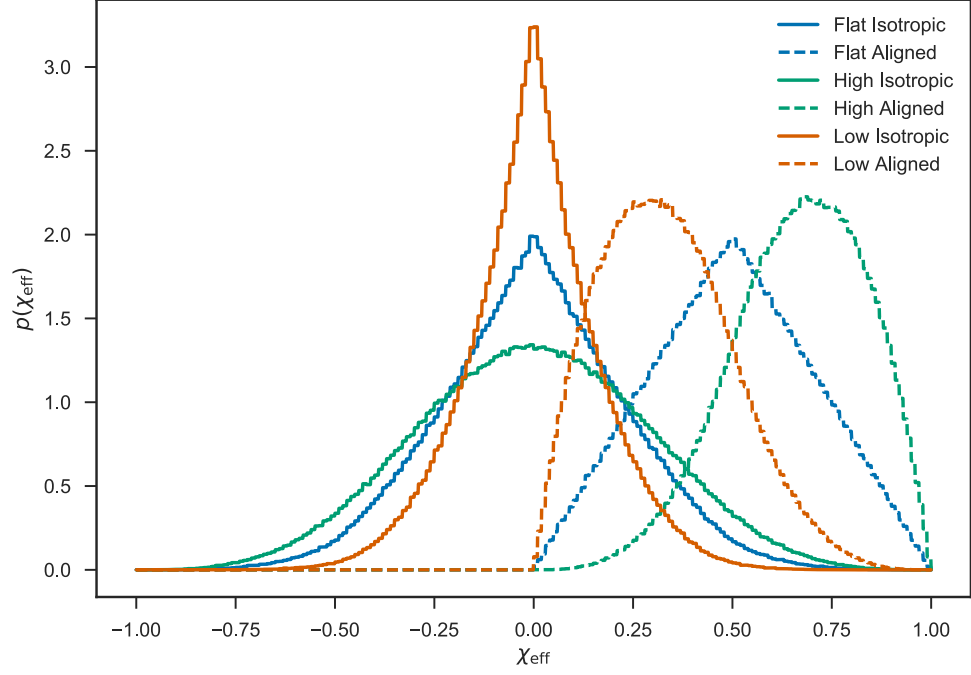


Figure 5.2: The models for the distribution of χ_{eff} considered in this paper. In all models we assume that the binary mass ratio $q \equiv m_1/m_2 = 1$ and that the distribution of spin vectors is the same for each component. The “flat” (blue lines), “high,” (green lines), and “low” (red lines) magnitude distributions are defined in Eq. (5.3). Solid lines give the χ_{eff} distribution under the assumption that the orientations of the spins are isotropic; dashed lines give the distribution under the assumption that both objects’ spins are aligned with the orbital angular momentum. The isotropic distributions are readily distinguished from the aligned distributions by the production of negative χ_{eff} values, while the distinction between the three models for the spin magnitude distribution is less sharp. Figure reproduced from [4].

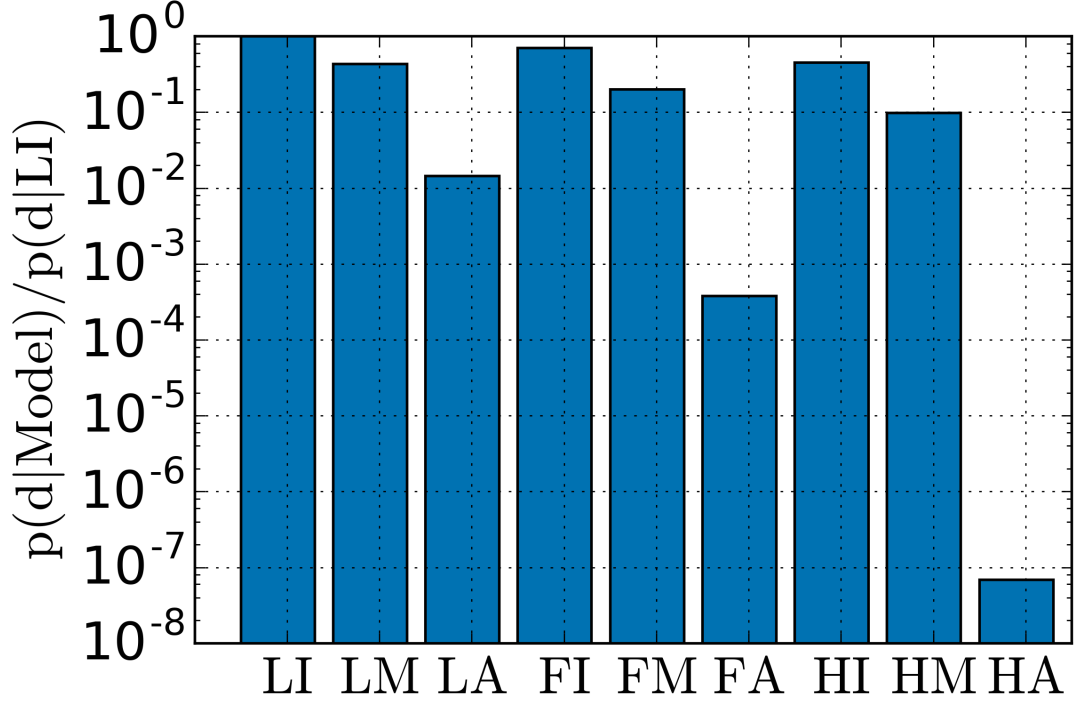


Figure 5.3: Odds ratios among our models using the approximations to the posteriors on χ_{eff} from the O1 and GW170104 observations shown in Figure 5.1. The flat (“F”), high (“H”), and low (“L”) spin magnitude distributions (see Eq. (5.3)) are paired with isotropic (“I”) and aligned (“A”) angular distributions, as well as a mixture model of the two (“M”). The most-favoured models have the “low” distribution of spin magnitudes. The odds ratio between the best aligned and best isotropic models is 0.015, or 2.4σ . For all magnitude distributions the pure-isotropic models are preferred over the mixture models; correspondingly, the posterior on the mixture fraction peaks at 100% isotropic. Figure reproduced from [4].

models. While the data favour spin amplitude distributions with small spin magnitudes, note that a model with all binary black hole systems having zero spin is ruled out by the GW151226 measurements, which bound at least one black hole to have spin magnitude ≥ 0.2 at 99% credibility[19].

5.1.1 Future Spin Measurements

Estimates of the rate of binary black hole coalescences give a reasonable chance of 10 additional binary black hole detections in the next three years [8, 22, 23]. Assuming 10 additional detections drawn from each of our six zero-parameter models for the spin distribution in addition to the three existing detections from O1, with observational uncertainties drawn randomly from the three Gaussian widths used

to approximate the χ_{eff} posteriors in Figure 5.1², we find the odds ratios shown in Figure 5.4. We find that most scenarios with an additional 10 detections allow the simulated angular distribution to be inferred with greater than 5σ (2.9×10^{-7} odds) credibility; and in the most pessimistic case the distinction is typically 2.4σ (0.016 odds ratio). While such future detections should permit a confident distinction between *angular* distributions, we would remain much less certain about the *magnitude* distribution among the three options considered here until we have a larger number of observations. In Figure 5.4, the odds ratio between different magnitude distributions with the same angular distribution is much closer to unity than the odds ratio between angular distributions.

5.2 Discussion

Most of our resolving power for the spin angular distribution is a result of the fact that our “aligned” models cannot produce $\chi_{\text{eff}} < 0$ (see Figure 5.2). If spins are intrinsically very small, with $a \lesssim 0.2$, then it is no longer possible to resolve the negative effective spin with a small number of observations (see Methods Section 5.6). As noted below, however, spins observed in X-ray binaries are typically large. Additionally, models which do not permit *some* spins with $\chi_{\text{eff}} \gtrsim 0.1$ are ruled out by the GW151226 observations[19]. An “aligned” model with spin magnitudes from our “flat” distribution but permitting spin vectors oriented anti-parallel to the orbital angular momentum (leading to the possibility of positive *or* negative χ_{eff}) can only be distinguished from an isotropic true population at $\sim 3\sigma$ after 10–20 observations[265]; our flat aligned model can be distinguished from such a population at better than 5σ (odds $< 10^{-8}$) after 10 observations, emphasizing the information content of the bound $\chi_{\text{eff}} > 0$ for our aligned models.

Observational data on spin magnitudes in black hole systems is sparse[337]. Most of the systems studied are low-mass X-ray binaries rather than the high-mass X-ray binaries that are likely to be the progenitors of double black hole binaries. In addition, there are substantial systematic errors that can complicate these analyses[337]

²The measurement uncertainty in χ_{eff} depends on the other parameters of the merging BBH system, particularly on the mass ratio. Our assumption about future observational uncertainties is appropriate if the parameters of the three detected events are representative of the parameters of future detections. See Methods Section 5.9 for further discussion.

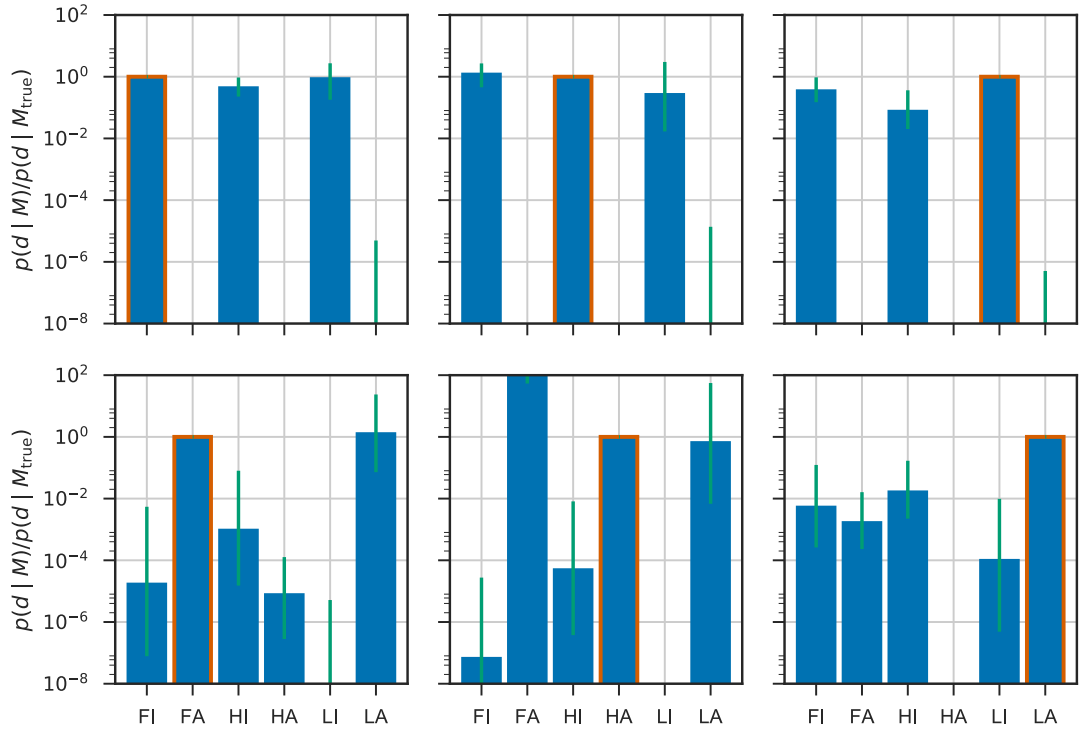


Figure 5.4: Distribution of odds ratios predicted with 10 additional observations above the three discussed in Section 5.1. Each panel corresponds to additional observations drawn from one of the χ_{eff} distribution models. The model from which the additional observations are drawn is outlined in red. The height of the blue bar gives the median odds ratio relative to the model from which the additional observations are drawn; the green line gives the 68% (1σ) symmetric interval of odds ratios over 1000 separate draws from the model distribution. The closest median ratio between the most-favoured isotropic model and the most-favoured aligned model is 0.016, corresponding to 2.4σ preference for the correct angular distribution; most models result in more than 5σ preference for the correct angular distribution. Because the three observations from Section 5.1 are included in each data set the “correct” model is not necessarily preferred over the others, particularly when that model uses the “high” magnitude distribution, which is strongly dis-favoured from the O1 observations alone. Figure reproduced from [4].

and selection effects could yield a biased distribution. Nonetheless, if we take the reported spin magnitudes as representative then we find that there is a preference for high spins; for example, 14 of the 19 systems with reported spins have dimensionless spin parameters in excess of 0.5. It is usually argued that the masses and spin parameters of stellar-mass black holes are unlikely to be altered significantly by accretion[381], but this may not be true for all systems[382, 336]. Thus the current spin parameters are probably close to their values upon core collapse, at least in high-mass X-ray binaries. However, the specific processes involved in the production of black hole binaries from isolated binaries could alter the spin magnitude distribution of those holes relative to the X-ray binary systems; for example, close tidal interactions could spin up the core, or stripping of the envelope could reduce the available angular momentum[266, 383, 384].

The spin directions in isolated binaries, whether evolving via the classical channel through a common-envelope phase [30, 31, 379, 35, 1] or through chemically homogeneous evolution [130, 129] are usually expected to be preferentially aligned. Despite observed spin-orbit misalignments in both massive stellar binaries [340, 386] and BH X-ray binaries [347, 348, 387, 388], mass accretion and tidal interactions will tend to realign the binary. On the other hand, a supernova natal kick (if any) can change the orbital plane and misalign the binary [342, 174]; the supernova can also tilt the spin angle, as in the double pulsar J0737-3039 [389]; and a variety of uncertain processes, such as wind-driven mass loss and post-collapse fallback, can couple the spin magnitude and direction distributions, contrary to our simplified assumptions. A small misalignment at wide separation can also evolve to a more significant misalignment in component spins as the binary spirals in through GW emission [176], but χ_{eff} is approximately conserved through this evolution.

The spin directions of binary black holes formed dynamically through interactions in dense stellar environments [192, 191, 193, 200, 206] are expected to be isotropic given the absence of a preferred direction [e.g., 207] and the persistence of an isotropic distribution through post-Newtonian evolution [179, 385].

Acknowledgements

Supplementary Information is linked to the online version of the paper at <http://www.nature.com/nature>.

We thank Richard O’Shaughnessy, Christopher Berry, Davide Gerosa and Salvatore Vitale for discussions and comments on this work. WF, SS, IM and AV were supported in part by the STFC. MCM acknowledges support of the University of Birmingham Institute for Advanced Study Distinguished Visiting Fellows program. SS and IM acknowledge support from the National Science Foundation under Grant No. NSF PHY11-25915.

All authors contributed to the work presented in this paper.

Reprints and permissions information is available at <http://www.nature.com/reprints>.

The authors declare no competing financial interests.

Correspondence and requests for materials should be addressed to w.farr@bham.ac.uk.

5.3 Effective Spin and Spin Magnitude Distributions

The effective spin is defined by[9]

$$\chi_{\text{eff}} = \frac{c}{GM} \left(\frac{\vec{S}_1}{m_1} + \frac{\vec{S}_2}{m_2} \right) \cdot \frac{\vec{L}}{|\vec{L}|} \equiv \frac{1}{M} (m_1 \chi_1 + m_2 \chi_2), \quad (5.1)$$

where $m_{1,2}$ are the gravitational masses of the more-massive (1) and less-massive (2) components, $M = m_1 + m_2$ is the total mass, $\vec{S}_{1,2}$ are the spin angular momentum vectors of the black holes in the binary, \vec{L} is the orbital angular momentum vector, assumed to point in the \hat{z} direction, and $\chi_{1,2}$ are the corresponding dimensionless

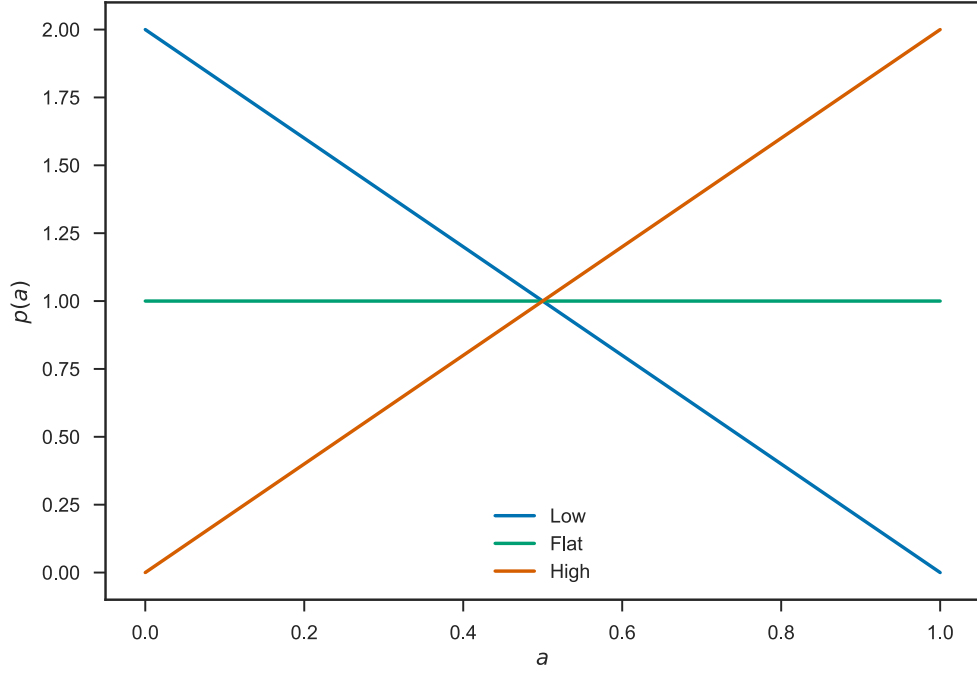


Figure 5.5: Distributions of spin magnitudes. See Eq. (5.3) for the definition of the low (blue line), flat (green line), and high (red line) magnitude distributions used here. The distributions have mean spin 0.33, 0.5, and 0.67 and standard deviations 0.24, 0.29, and 0.24.

projections of the individual BH spins. Because the dimensionless spin parameter,

$$a_{1,2} = \frac{c}{Gm_{1,2}^2} \left| \vec{S}_{1,2} \right|, \quad (5.2)$$

of each black hole is bounded by $0 \leq a_{1,2} < 1$, the projections along the orbital axis are bounded by $-1 < \chi_{1,2} < 1$, and $-1 < \chi_{\text{eff}} < 1$.

We form the population distributions of χ_{eff} shown in Figure 5.2 by assuming that each black hole in a binary has a dimensionless spin magnitude drawn from one of three distributions,

$$p(a) = \begin{cases} 2(1-a) & \text{“low”} \\ 1 & \text{“flat”} \\ 2a & \text{“high”} \end{cases}, \quad (5.3)$$

referred to as “low,” “flat,” and “high” in the text above. These distributions are shown in Extended Data Figure 5.5.

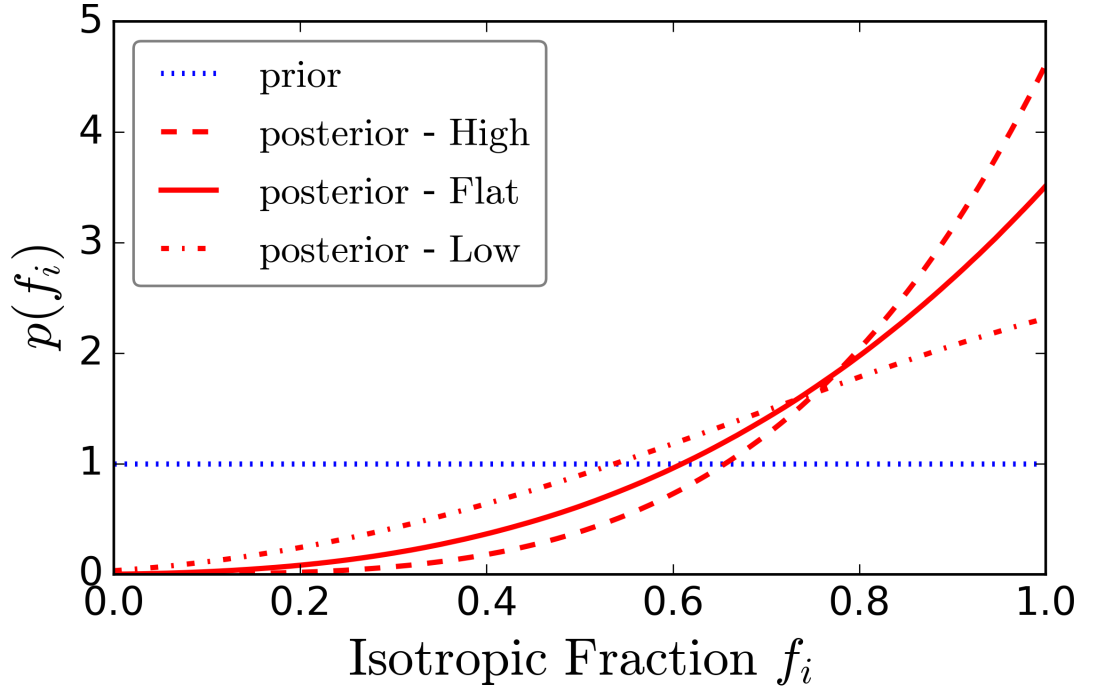


Figure 5.6: Fraction of the BBH population coming from an isotropic distribution under a mixture model. The dotted line shows the flat prior on the fraction of BBHs coming from an isotropic distribution, f_i , under the mixture model. The 3 red lines show the posterior on f_i after O1 and GW170104 with our various assumptions regarding BH spin magnitudes. The solid line shows the posterior assuming that all BHs have their spin magnitude drawn from the “flat” distribution. The dashed line assumes the “high” BH spin magnitude distribution $p(a) = 2a$. The dot-dash line assumes the “low” distribution $p(a) = 2(1 - a)$. We see that for a wide range of assumptions regarding BH spin magnitudes, the fraction coming from an isotropic distribution f_i peaks at 1. Figure reproduced from [4].

5.4 Mixture model

While we carried out Bayesian comparisons between isotropic and aligned spin distributions under various assumptions, a preference for one of the considered models over the others does not necessarily indicate that it is the correct model. All of the considered models could be inaccurate for the actual distribution, especially since all of the considered models are based on a number of additional assumptions, such as decoupled spin magnitude and spin misalignment angle distributions and identical distributions for primary and secondary spins.

We now partly relax the simplified assumptions made earlier by considering the possibility that the true distribution of BBH spin-orbit misalignments observed by LIGO is a mixture of binaries with aligned spins and binaries with isotropic spins.

We fit a mixture model[3] (labelled model 'M' in Figure 5.3) where a fraction f_i of BBHs have spins drawn from an isotropic distribution, whilst a fraction $1 - f_i$ have their spins aligned with the orbital angular momentum. We assume a flat prior on the fraction f_i . To test the robustness of our result, we vary the distribution we assume for BH spin magnitude distributions as with the aligned and isotropic models. We use the “flat”, “high” and “low” distributions (Equation 5.3), assuming all BHs have their spin magnitude drawn from the same distribution for both the aligned and isotropic populations. We calculate and plot the posterior on f_i given by Equation 5.6 ($f_i = \lambda$ in the derivation) in Extended Data Figure 5.6. We find the mean fraction of BBHs coming from an isotropic distribution is 0.70, 0.77 and 0.81 assuming the “low”, “flat” and “high” distributions for spin magnitudes respectively, compared to the prior mean of 0.5. The lower 90% limits are 0.38, 0.51 and 0.60 respectively, compared to the prior of 0.1. In all cases, the posterior peaks at $f_i = 1$. Thus, for these spin magnitude distributions we find that the current O1 and GW170104 LIGO observations constrain the majority of BBHs to have their spins drawn from an isotropic distribution. The evidence ratios of these mixture models to the isotropic distribution with “low” spin magnitudes are 0.43, 0.20 and 0.10 for the “low”, “flat” and “high” spin magnitude models. Thus we cannot rule out a mixture with the current data. If several different components contribute significantly to the true spin distribution it may take tens to hundreds of detections to accurately determined the mixing fraction, depending on the distribution of spin magnitudes[265, 3].

5.5 Hierarchical Modelling

LIGO measures χ_{eff} better than any other spin parameter, but still with significant uncertainty, so we need to properly incorporate measurement uncertainty in our analysis; thus our analysis must be *hierarchical* [355, 290]. In a hierarchical analysis, we assume that each event has a true, but unknown, value of the effective spin, drawn from the population distribution, which may have some parameters λ ; then the system is observed, represented by the likelihood function, which results in a distribution for the true effective spin (and all other parameters describing the system) consistent with the data. Combining, the joint posterior on each system's χ_{eff}^i parameters and the population parameters λ implied by a set of observations

each with data d^i , is

$$p(\{\chi_{\text{eff}}^i\}, \lambda \mid \{d^i\}) \propto \left[\prod_{i=1}^{N_{\text{obs}}} p(d^i \mid \chi_{\text{eff}}^i) p(\chi_{\text{eff}}^i \mid \lambda) \right] p(\lambda). \quad (5.4)$$

The components of this formula are

- The GW (marginal) likelihood, $p(d \mid \chi_{\text{eff}})$. Here we use “marginal” because we are (implicitly) integrating over all parameters of the signal but χ_{eff} . Note that it is the likelihood rather than the posterior that matters for the hierarchical analysis; if we are given posterior distributions or posterior samples, we need to re-weight to “remove” the prior and obtain the likelihood.
- The population distribution for χ_{eff} , $p(\chi_{\text{eff}} \mid \lambda)$. This function can be parameterised by population-level parameters, λ . (In the cases discussed above, there are no parameters for the population.)
- The prior on the population-level parameters, $p(\lambda)$.

If we do not care about the individual event χ_{eff} parameters, we can integrate them out, obtaining

$$p(\lambda \mid \{d^i\}) \propto \left[\prod_{i=1}^{N_{\text{obs}}} \int d\chi_{\text{eff}}^i p(d^i \mid \chi_{\text{eff}}^i) p(\chi_{\text{eff}}^i \mid \lambda) \right] p(\lambda). \quad (5.5)$$

If we are given posterior samples of χ_{eff}^{ij} (i labels the event, j labels the particular posterior sample) drawn from an analysis using a prior $p(\chi_{\text{eff}})$, then we can approximate the integral by a re-weighted average of the population distribution over the samples (here $p(\chi_{\text{eff}}^{ij})$ is the prior used to produce the posterior samples):

$$p(\lambda \mid \{d^i\}) \propto \left[\prod_{i=1}^{N_{\text{obs}}} \frac{1}{N_i} \sum_{j=1}^{N_i} \frac{p(\chi_{\text{eff}}^{ij} \mid \lambda)}{p(\chi_{\text{eff}}^{ij})} \right] p(\lambda). \quad (5.6)$$

5.5.1 Order of Magnitude Calculation

It is possible to estimate at an order-of-magnitude level the rate at which evidence accumulates in favour of or against the isotropic models as more systems are de-

tected. Based on Figure 5.2, approximate the isotropic population χ_{eff} distribution as uniform on $\chi_{\text{eff}} \in [-0.25, 0.25]$ and the aligned population χ_{eff} distribution as uniform on $\chi_{\text{eff}} \in [0, 0.5]$. Then the odds ratio between the isotropic and aligned models for each event is approximately

$$\frac{p(d | I)}{p(d | A)} \simeq \frac{P(-0.25 \leq \chi_{\text{eff}} \leq 0.25)}{P(0 \leq \chi_{\text{eff}} \leq 0.5)}, \quad (5.7)$$

where $P(A \leq \chi_{\text{eff}} \leq B)$ is the posterior probability (here used to approximate the likelihood) that χ_{eff} is between A and B . Using our approximations to the χ_{eff} posteriors described above, this gives an odds ratio of 5 in favour of the isotropic models, which is about a factor of two smaller than the ratio in the more careful calculation described in Section 5.1. This is a satisfactory answer at an order-of-magnitude level.

If the true distribution is isotropic and follows this simple model, and our measurement uncertainties on χ_{eff} are $\simeq 0.1$, then the geometric mean of each subsequent measurement's contribution to the overall odds is ~ 3 . After ten additional events, then, the odds ratio becomes $5 \times 3^{10} \simeq 3 \times 10^5$, or 4.6σ , consistent with the results of the more detailed calculation described above. If the true distribution of spins becomes half as wide ($\chi_{\text{eff}} \in [-0.125, 0.125]$ for isotropic and $\chi_{\text{eff}} \in [0, 0.25]$ for aligned spins), with the same uncertainties, then the existing odds ratio becomes 1.08, and each subsequent event drawn from the isotropic distribution contributes on average a factor of 1.6. In this case, after 10 additional events, the odds ratio becomes 150, or 2.7σ . With small spin magnitudes, our angular resolving power vanishes, as discussed in more detail in Section 5.6.

5.5.2 Accumulation of evidence

In Extended Data Table 5.1 we show how the evidence for an isotropic distribution increases when including: only the 2 confirmed events—GW150914 and GW151226—from O1; all O1 events (including LVT151012); and all 4 likely binary black hole mergers, including GW170104.

Events	$\sigma_{I/A}$ “Low”	$\sigma_{I/A}$ “Flat”	$\sigma_{I/A}$ “High”
GW150914 and GW151226	1.3	2.2	3.7
All O1 events	1.7	2.7	4.4
All O1 events and GW170104	2.4	3.5	5.4

Table 5.1: Significance $\sigma_{I/A}$ of the odds ratio between the isotropic and aligned models. The odds ratio is computed using just GW150914 and GW151226, all 3 O1 events, and all 4 currently observed events (including GW170104). The number in bold is the result we quote in the main text.

5.6 Effect of small spin magnitudes

In the main text we considered three models for BH spin magnitudes: “low”, “flat” and “high”. These were intended to capture some of the uncertainty regarding the BH spin magnitude distribution.

Here we extend the “low” model as:

$$p(a) \propto (1 - a)^\alpha \quad (5.8)$$

When $\alpha = 0$, this recovers the “flat” distribution, whilst $\alpha = 1$ recovers the “low” distribution. For higher values of α , this distribution becomes more peaked towards $a = 0$.

In Figure 5.7 we plot the evidence ratio of aligned to isotropic distributions (plotted as the equivalent sigma) with spin magnitudes given by this model with α in the range 0 – 6. The top axis shows the mean spin magnitude that value of α corresponds to (e.g., for the “flat” distribution $\alpha = 0$, the mean spin magnitude is 0.5). We see that if typical BH spins are $\lesssim 0.2$ we have no evidence for one model over the other.

5.7 Mass Ratio

Figure 5.8 shows the distributions of χ_{eff} that would obtain with a mass ratio $q = m_2/m_1 = 0.5$ compared to the distributions with $q = 1$ used above. The details

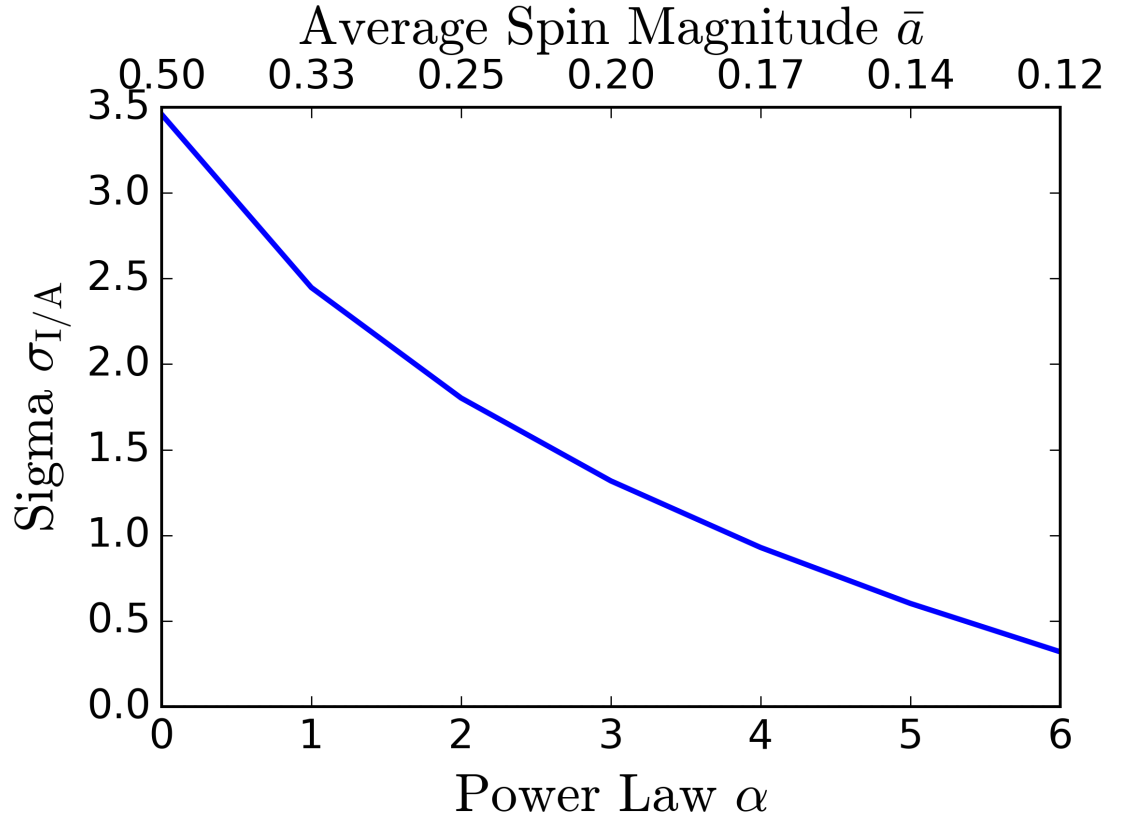


Figure 5.7: Effect of small spins on evidence ratio of aligned against isotropic models. The blue line shows the evidence ratio (plotted as the equivalent sigma) between a model where all systems are aligned, versus one where all systems are from an isotropic distribution as a function of the power law α corresponding to Equation 5.8. The top axis shows the mean spin magnitude \bar{a} which this α corresponds to. We see that for mean spin magnitudes $\lesssim 0.2$ we find no evidence for either distribution over the other. Figure reproduced from [4].

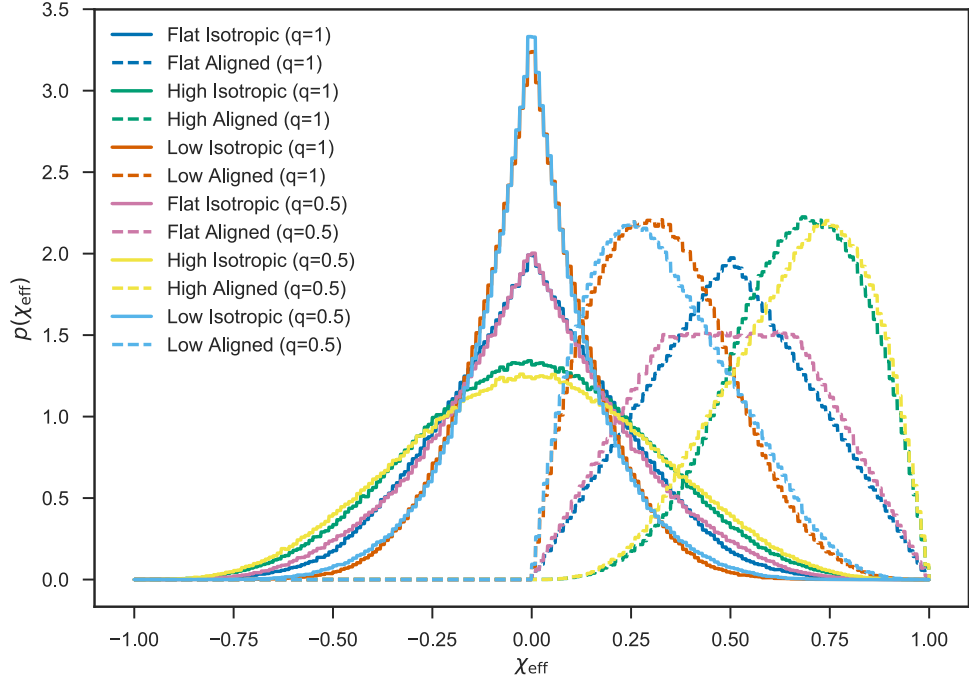


Figure 5.8: Distributions of χ_{eff} assuming all merging black holes have equal masses ($q = 1$) or a 2:1 mass ratio ($q = 0.5$). The details of the distribution are sensitive to the mass ratio, but in our analysis we are primarily sensitive to the changing *sign* of χ_{eff} under the isotropic models. This latter property is unchanged under changing mass ratio. Figure reproduced from [4].

of the distribution are sensitive to the mass ratio, but in our analysis we are primarily sensitive to the changing *sign* of χ_{eff} under the isotropic models. This latter property is insensitive to mass ratio. As an example, the distinction between the three different spin amplitude distributions after ten additional detections is quite weak compared to the aligned/isotropic distinction in Figure 5.4. The differences in the χ_{eff} distribution between $q = 1$ and $q = 0.5$ are even smaller than the differences between the different magnitude distributions.

5.8 Approximations in the Gravitational Waveform

While the Advanced LIGO searches use spin-aligned templates they are efficient in detecting misaligned binary black hole systems[21]; we assume here that the χ_{eff} distribution of observed sources follows the true population.

The model waveforms used to infer the χ_{eff} of the three LIGO events incorporate approximations to the true behaviour of the merging systems that are expected to break down for sufficiently high mis-aligned spins. The effect of these approximations on inference on the parameters describing GW150914 has been investigated in detail [390]. For this source, statistical uncertainties dominate over any waveform systematics. Detailed comparisons with numerical relativity computations using no approximations to the dynamics [391] also suggest that statistical uncertainties dominate the systematics for this system. Abbott *et al.* [390] suggests that systematics may dominate for signals with this large SNR ($\simeq 23$) when the source is edge-on or has high spins. The other two events discussed in this paper are at much lower SNR, with correspondingly larger statistical uncertainties, and are probably similarly oriented and with similarly small spins, so we do not expect systematic uncertainties to dominate.

We assume here that measurements made in the future are not dominated by systematic errors, but this assumption would need to be revisited for high-SNR, edge-on, or high-spin sources detected in the future.

5.9 Precision of χ_{eff} measurements

Throughout this work we have made the simplifying assumption that the precision to which χ_{eff} can be constrained for individual binaries is independent of the binary’s properties. In practice, our ability to constrain χ_{eff} *is* dependent on the system’s properties, in particular its true χ_{eff} and mass ratio, which we illustrate in figure 5.9.

For this figure a detected population³ of 500 binaries was selected from a population with component masses distributed uniformly between 1 and 30 M_{\odot} with $m_1 + m_2 < 30 M_{\odot}$, locations distributed uniformly in volume, and orientations distributed isotropically. Data were simulated for each binary, and posteriors were estimated using the LIGO-Virgo parameter estimation library `LALInference` [281] using inspiral-only waveform models (merger and ringdown effects can provide additional information for some binaries, but we ignore those effects here). χ_{eff} is better

³We qualify a system as “detected” if it produces a SNR above 8 in the second-loudest detector to select only coincident events.

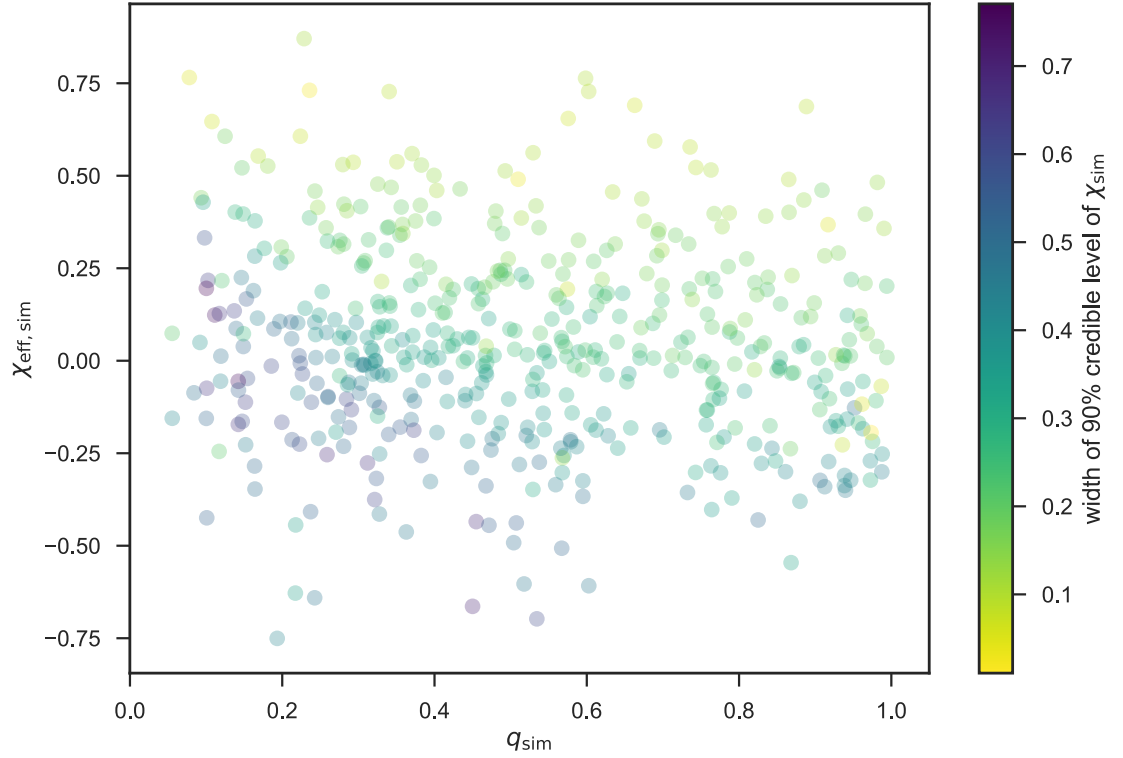


Figure 5.9: Widths of the 90% credible intervals for χ_{eff} for 500 binaries in a simulated detected population. χ_{eff} is better constrained for systems with low χ_{eff} and low mass ratio. Figure reproduced from [4].

constrained for binaries with low (negative) effective spins and low mass ratios.

By neglecting these effects, We do not expect to qualitatively affect our conclusions, though they could affect predictions for the total number of detections necessary to constrain the population. For example, if the universe preferentially forms asymmetric binaries with low mass ratios, individual χ_{eff} constraints will be systematically better, reducing the number of binaries needed to infer the properties of the population.

Chapter 6

Conclusions, outstanding problems, avenues of future research.

On the 14th September 2015 the Advanced Laser Interferometer Gravitational-wave Observatory (LIGO) made the first direct detection of gravitational waves from merging stellar mass binary black holes during its first observation run (O1). The signal, GW150914, originated from the merger of two $\sim 30M_{\odot}$ black holes over a billion light years from the Earth. GW150914 heralded the beginning of a new era of astronomy; gravitational wave astronomy. GW150914 was followed by a second confident detection of gravitational-waves from a lower mass merging binary black hole GW151226. Additionally, a statistically less significant binary black hole merger candidate LVT151012 was observed. The second Advanced LIGO observing run (O2) began on 30th November 2016, continuing until summer 2017, and will hopefully make more observations.

Gravitational-waves provide a unique probe of the stellar remnants—black holes and neutron stars—left behind at the end of massive stars lives. As LIGO and other ground based gravitational-wave detectors continue to observe the universe, they will begin to uncover a population of these binary black holes, which may have formed through the isolated evolution of two massive stars. Already, gravitational-waves have: demonstrated the existence of binary black holes which merge within the age of the universe; provided evidence for stellar mass black hole masses in

the broad range $5\text{--}40M_{\odot}$; and have empirically constrained the merger rate to be $9\text{--}240\text{ Gpc}^{-3}\text{ yr}^{-1}$. These place significant constraints on population models.

In this thesis we have presented Compact Object Mergers: Population Astrophysics and Statistics (COMPAS). COMPAS is a platform incorporating astrophysical modelling tools and statistical analysis tools to extract information from the population of merging binary black holes we observe, and offer insights into binary black hole formation.

In Chapter 2 we presented the rapid population synthesis element of COMPAS. We use it to show that all three (assuming LVT151012 is real) presently observed binary black holes are consistent with formation through a single evolutionary channel – classical isolated binary evolution channel via a common-envelope. We show all three events could have formed in low-metallicity environments ($Z = 0.001$) from progenitor binaries with typical total masses $\gtrsim 160M_{\odot}$, $\gtrsim 60M_{\odot}$ and $\gtrsim 90M_{\odot}$, for GW150914, GW151226, and LVT151012, respectively. In this work we assumed a fiducial model, with several highly uncertain parameters relating to evolutionary stages such as supernovae and common envelopes fixed to fiducial values taken from the literature. We assumed a constant λ for the common envelope. We have since implemented fits for λ [158, 159] which we will use in future studies. We also aim to incorporate more up to date stellar models (such as those provided by MIST [49]) and physics within COMPAS.

In the future, we plan to allow these uncertain parameters to be free, and build a fast COMPAS emulator which spans the large multi-dimensional parameter space [105].

In Chapter 3 we show how one can use the measured masses and rates of binary black hole mergers to distinguish between a suite of population synthesis models. The variations from the standard model used in this study only consider varying one parameter at a time. It is likely that the effects on the mass distributions and rates parameters have will be correlated or degenerate, and should be explored together. We will use our emulated COMPAS model [105] to explore this large parameter space and solve the inverse problem, constraining the population hyperparameters using binary black hole masses and merger rates. To do this, we will also need to properly integrate over cosmological history, as in Dominik *et al.* [305]. This introduces new uncertainties in things such as the metallicity specific star formation

history of the universe.

In Chapter 4 we develop an hierarchical model to show how gravitational-wave measurements of binary black hole spin-orbit misalignments can be used to measure the mixture fraction of systems forming through isolated binary evolution and dynamical interactions in dense stellar environments under a set of astrophysically motivated models. Assuming a population with spins of $\chi \sim 0.7$, we showed that with tens of observations it will be possible to distinguish the presence of subpopulations of coalescing binary black holes based on their spin orientations. With 100 observations it will be possible to infer the relative fraction of coalescing binary black holes with isotropic spin directions (corresponding to dynamical formation) with a fractional uncertainty of $\sim 40\%$. Meanwhile, only ~ 5 observations are sufficient to distinguish between extreme models—all binary black holes either having exactly aligned spins or isotropic spin directions.

In Chapter 5 we applied this methodology to the existing O1 observations of binary black hole mergers GW150914, GW151226 and LVT151012. If binary black hole spin magnitudes extend to high values, as is suggested by observations of black hole X-ray binaries, we show that the data already exhibit a 1.7σ preference for an isotropic angular distribution. The existing preference for either an isotropic spin distribution or low spin magnitudes for the observed systems will be confirmed (or overturned) confidently in the near future by subsequent observations.

COMPAS will branch out from gravitational-waves in the future, and use the methodology developed here to incorporate constraints from other astrophysical sources such as galactic double neutron star systems, Be/X-ray binaries and Luminous Red Novae. In doing so, we aim to develop a “concordance” model for binary evolution.

Bibliography

- [1] Stevenson, S. *et al.* Formation of the first three gravitational-wave observations through isolated binary evolution. *Nature Communications* **8**, 14906 (2017).
- [2] Stevenson, S., Ohme, F. & Fairhurst, S. Distinguishing Compact Binary Population Synthesis Models Using Gravitational Wave Observations of Coalescing Binary Black Holes. *Astrophys. J.* **810**, 58 (2015).
- [3] Stevenson, S., Berry, C. P. L. & Mandel, I. Hierarchical analysis of gravitational-wave measurements of binary black hole spin-orbit misalignments. *ArXiv e-prints* (2017).
- [4] Farr, W. M. *et al.* Distinguishing spin-aligned and isotropic black hole populations with gravitational waves (2017).
- [5] Einstein, A. Approximative Integration of the Field Equations of Gravitation. *Preuss. Akad. Weiss. Berlin* 688 (1916).
- [6] Einstein, A. Über Gravitationswellen. *Sitzungsberichte der Königlich Preussischen Akademie der Wissenschaften (Berlin), Seite 154-167*. 154–167 (1918).
- [7] Abbott, B. P. *et al.* Observation of Gravitational Waves from a Binary Black Hole Merger. *Phys. Rev. Lett.* **116**, 061102 (2016).
- [8] Abbott, B. P. *et al.* (LIGO Scientific Collaboration and Virgo Collaboration). Binary Black Hole Mergers in the First Advanced LIGO Observing Run. *Phys. Rev. X* **6**, 041015 (2016).
- [9] Abbott, B. P. *et al.* Properties of the Binary Black Hole Merger GW150914. *Phys. Rev. Lett.* **116**, 241102 (2016).
- [10] Abbott, B. P. *et al.* Improved Analysis of GW150914 Using a Fully Spin-Precessing Waveform Model. *Phys. Rev. X* **6**, 041014 (2016).

- [11] Grote, H. & the LIGO Scientific Collaboration. The status of GEO 600. *Class. Quantum Grav* **25**, 114043 (2008).
- [12] Grote, H. & LIGO Scientific Collaboration. The GEO 600 status. *Class. Quantum Grav* **27**, 084003 (2010).
- [13] Acernese, F. *et al.* (VIRGO). Advanced Virgo: a second-generation interferometric gravitational wave detector. *Class. Quant. Grav.* **32**, 024001 (2015).
- [14] Abbott, B. P. *et al.* Prospects for Observing and Localizing Gravitational-Wave Transients with Advanced LIGO and Advanced Virgo. *Living Reviews in Relativity* **19** (2016).
- [15] Iyer, B. *et al.* LIGO India. Technical report (2011). <https://dcc.ligo.org/cgi-bin/DocDB/ShowDocument?docid=75988>.
- [16] Somiya, K. Detector configuration of KAGRA-the Japanese cryogenic gravitational-wave detector. *Class. Quantum Grav* **29**, 124007 (2012).
- [17] Punturo, M. *et al.* The third generation of gravitational wave observatories and their science reach. *Class. Quantum Grav* **27**, 084007 (2010).
- [18] Hild, S. *et al.* Sensitivity studies for third-generation gravitational wave observatories. *Class. Quantum Grav* **28**, 094013 (2011).
- [19] Abbott, B. P. *et al.* GW151226: Observation of Gravitational Waves from a 22-Solar-Mass Binary Black Hole Coalescence. *Phys. Rev. Lett.* **116**, 241103 (2016).
- [20] Abbott, B. P. *et al.* (VIRGO, LIGO Scientific). GW170104: Observation of a 50-Solar-Mass Binary Black Hole Coalescence at Redshift 0.2. *Phys. Rev. Lett.* **118**, 221101 (2017).
- [21] Abbott, B. P. *et al.* GW150914: First results from the search for binary black hole coalescence with Advanced LIGO. *Phys. Rev. D* **93**, 122003 (2016).
- [22] Abbott, B. P. *et al.* The Rate of Binary Black Hole Mergers Inferred from Advanced LIGO Observations Surrounding GW150914. *Astrophys. J. Lett.* **833**, L1 (2016).
- [23] Abbott, B. P. *et al.* Supplement: The Rate of Binary Black Hole Mergers Inferred from Advanced LIGO Observations Surrounding GW150914 (2016, ApJL, 833, L1). *Astrophys. J. Supp. Ser.* **227**, 14 (2016).

- [24] Zevin, M. *et al.* Constraining Models of Binary Black Hole Formation with Gravitational-Wave Observations (2017).
- [25] Talbot, C. & Thrane, E. Determining the population properties of spinning black holes (2017).
- [26] Sesana, A. Prospects for Multiband Gravitational-Wave Astronomy after GW150914. *Phys. Rev. Lett.* **116**, 231102 (2016).
- [27] Breivik, K. *et al.* Distinguishing Between Formation Channels for Binary Black Holes with LISA. *Astrophys. J.* **830**, L18 (2016).
- [28] Nishizawa, A., Sesana, A., Berti, E. & Klein, A. Constraining stellar binary black hole formation scenarios with eLISA eccentricity measurements (2016).
- [29] Nishizawa, A., Berti, E., Klein, A. & Sesana, A. eLISA eccentricity measurements as tracers of binary black hole formation. *Phys. Rev.* **D94**, 064020 (2016).
- [30] Tutukov, A. & Yungelson, L. Evolution of massive close binaries. *Nauchnye Informatsii* **27**, 70 (1973).
- [31] Tutukov, A. V. & Yungelson, L. R. The merger rate of neutron star and black hole binaries. *Mon. Not. R. Astron. Soc.* **260**, 675–678 (1993).
- [32] Voss, R. & Tauris, T. M. Galactic distribution of merging neutron stars and black holes - prospects for short gamma-ray burst progenitors and LIGO/virgo. *Monthly Notices of the Royal Astronomical Society* **342**, 1169–1184 (2003). URL http://adsabs.harvard.edu/cgi-bin/nph-bib_query?bibcode=2003MNRAS.342.1169V&db_key=AST&high=432eb689bf01702.
- [33] Dominik, M. *et al.* Double Compact Objects. I. The Significance of the Common Envelope on Merger Rates. *Astrophys. J.* **759**, 52 (2012).
- [34] Mennekens, N. & Vanbeveren, D. Massive double compact object mergers: gravitational wave sources and r-process element production sites. *Astron. Astrophys.* **564**, A134 (2014).
- [35] Belczynski, K., Holz, D. E., Bulik, T. & O’Shaughnessy, R. The first gravitational-wave source from the isolated evolution of two stars in the 40–100 solar mass range. *Nature* **534**, 512–515 (2016).

- [36] Lipunov, V. M. *et al.* First Gravitational-Wave Burst GW150914, as predicted by the scenario machine. *New Astronomy* **51**, 122 – 127 (2017).
- [37] de Mink, S. E. & Belczynski, K. Merger Rates of Double Neutron Stars and Stellar Origin Black Holes: The Impact of Initial Conditions on Binary Evolution Predictions. *Astrophys. J.* **814**, 58 (2015).
- [38] Moe, M. & Di Stefano, R. Mind your Ps and Qs: the Interrelation between Period (P) and Mass-ratio (Q) Distributions of Binary Stars. *ArXiv e-prints* (2016).
- [39] Salpeter, E. E. The Luminosity Function and Stellar Evolution. *Astrophys. J.* **121**, 161 (1955).
- [40] Kroupa, P. On the variation of the initial mass function. *Mon. Not. R. Astron. Soc.* **322**, 231–246 (2001).
- [41] Sana, H. *et al.* Binary Interaction Dominates the Evolution of Massive Stars. *Science* **337**, 444– (2012).
- [42] Abt, H. A. Normal and abnormal binary frequencies. *Annu. Rev. Astron. Astrophys* **21**, 343–372 (1983).
- [43] Heggie, D. C. Binary evolution in stellar dynamics. *Mon. Not. Roy. Astron. Soc.* **173**, 729–787 (1975).
- [44] Duquennoy, A. & Mayor, M. Multiplicity among solar-type stars in the solar neighbourhood. II - Distribution of the orbital elements in an unbiased sample. *Astron. Astrophys.* **248**, 485–524 (1991).
- [45] Sana, H. *et al.* The VLT-FLAMES Tarantula Survey. VIII. Multiplicity properties of the O-type star population. *Astron. Astrophys.* **550**, A107 (2013).
- [46] Duchêne, G. & Kraus, A. Stellar Multiplicity. *Ann. Rev. Astron. Astroph.* **51**, 269–310 (2013).
- [47] Asplund, M., Grevesse, N., Sauval, A. J. & Scott, P. The Chemical Composition of the Sun. *Annu. Rev. Astron. Astrophys* **47**, 481–522 (2009).
- [48] Woosley, S. E., Heger, A. & Weaver, T. A. The evolution and explosion of massive stars. *Rev. Mod. Phys.* **74**, 1015–1071 (2002). URL <http://link.aps.org/doi/10.1103/RevModPhys.74.1015>.

- [49] Choi, J. *et al.* Mesa Isochrones and Stellar Tracks (MIST). I. Solar-scaled Models. *Astrophys. J.* **823**, 102 (2016).
- [50] Paxton, B. *et al.* Modules for Experiments in Stellar Astrophysics (MESA). *Astrophys. J. Suppl.* **192**, 3 (2011).
- [51] Paxton, B. *et al.* Modules for Experiments in Stellar Astrophysics (MESA): Planets, Oscillations, Rotation, and Massive Stars. *Astrophys. J. Suppl.* **208**, 4 (2013).
- [52] Paxton, B. *et al.* Modules for Experiments in Stellar Astrophysics (MESA): Binaries, Pulsations, and Explosions. *Astrophys. J. Suppl.* **220**, 15 (2015).
- [53] Maeder, A. & Meynet, G. The evolution of rotating stars. *Ann. Rev. Astron. Astrophys.* **38**, 143–190 (2000).
- [54] Brott, I. *et al.* Rotating massive main-sequence stars - i. grids of evolutionary models and isochrones. *Astronomy and Astrophysics* **530**, A115 (2011). URL <https://doi.org/10.1051/0004-6361/201016113>.
- [55] Hurley, J. R., Pols, O. R. & Tout, C. A. Comprehensive analytic formulae for stellar evolution as a function of mass and metallicity. *Mon. Not. R. Astron. Soc.* **315**, 543–569 (2000).
- [56] Pols, O. R. *et al.* Stellar evolution models for $Z = 0.0001$ to 0.03 . *Mon. Not. R. Astron. Soc.* **298**, 525–536 (1998).
- [57] Vink, J. S. Mass loss and the evolution of massive stars. *New Astron. Rev.* **52**, 419–422 (2008).
- [58] Smith, N. Mass Loss: Its Effect on the Evolution and Fate of High-Mass Stars. *Ann. Rev. Astron. Astroph.* **52**, 487–528 (2014).
- [59] Renzo, M., Ott, C. D., Shore, S. N. & de Mink, S. E. A Systematic Survey of the Effects of Wind Mass Loss Algorithms on the Evolution of Single Massive Stars. *ArXiv e-prints* (2017).
- [60] Puls, J., Vink, J. S. & Najarro, F. Mass loss from hot massive stars. *Astron. Astrophys. Rev.* **16**, 209–325 (2008).
- [61] Castor, J. I., Abbott, D. C. & Klein, R. I. Radiation-driven winds in Of stars. *The Astrophysical Journal* **195**, 157–174 (1975).

- [62] Vink, J. S., de Koter, A. & Lamers, H. J. G. L. M. Mass-loss predictions for O and B stars as a function of metallicity. *Astron. Astrophys.* **369**, 574–588 (2001).
- [63] Belczynski, K. *et al.* On The Maximum Mass of Stellar Black Holes. *ArXiv e-prints* (2009). 0904.2784.
- [64] Humphreys, R. M. & Davidson, K. The luminous blue variables: Astrophysical geysers. *Publications of the Astronomical Society of the Pacific* **106**, 1025–1051 (1994).
- [65] Smith, N. Eruptive Mass Loss in Very Massive Stars and Population III Stars. In *Astronomical Telescopes and Instrumentation 2006 Orlando, Florida, May 24-31, 2006* (2006).
- [66] Hamann, W.-R., Koesterke, L. & Wessolowski, U. Spectral analyses of the Galactic Wolf-Rayet stars: hydrogen-helium abundances and improved stellar parameters for the WN class. *Astron. Astrophys.* **299**, 151 (1995).
- [67] Hamann, W.-R. & Koesterke, L. Spectrum formation in clumped stellar winds: consequences for the analyses of Wolf-Rayet spectra. *Astron. Astrophys.* **335**, 1003–1008 (1998).
- [68] Nelemans, G. & van den Heuvel, E. P. J. The formation of black hole low-mass X-ray binaries: Through case B or case C mass transfer? *Astron. Astrophys.* **376**, 950–954 (2001).
- [69] Nugis, T. & Lamers, H. J. G. L. M. The mass-loss rates of Wolf-Rayet stars explained by optically thick radiation driven wind models. *Astron. Astrophys.* **389**, 162–179 (2002).
- [70] Vink, J. S. & de Koter, A. On the metallicity dependence of Wolf-Rayet winds. *Astron. Astrophys.* (2005). [Astron. Astrophys.442,587(2005)].
- [71] Petit, V. *et al.* Magnetic massive stars as progenitors of "heavy" stellar-mass black holes. *Mon. Not. Roy. Astron. Soc.* **466**, 1052–1060 (2017).
- [72] Baade, W. & Zwicky, F. On Super-novae. *Proceedings of the National Academy of Science* **20**, 254–259 (1934).
- [73] Chandrasekhar, S. The Maximum Mass of Ideal White Dwarfs. *Astrophys. J.* **74**, 81 (1931).

- [74] Mazzali, P. A., Ropke, F. K., Benetti, S. & Hillebrandt, W. A Common Explosion Mechanism for Type Ia Supernovae. *Science* **315**, 825 (2007).
- [75] Whelan, J. & Iben, I., Jr. Binaries and Supernovae of Type I. *Astrophys. J.* **186**, 1007–1014 (1973).
- [76] Webbink, R. F. Double white dwarfs as progenitors of R Coronae Borealis stars and Type I supernovae. *Astrophys. J.* **277**, 355–360 (1984).
- [77] Iben, I., Jr. & Tutukov, A. V. Supernovae of type I as end products of the evolution of binaries with components of moderate initial mass (M not greater than about 9 solar masses). *Astrophys. J. Supp. Ser.* **54**, 335–372 (1984).
- [78] Riess, A. G. *et al.* (Supernova Search Team). Observational evidence from supernovae for an accelerating universe and a cosmological constant. *Astron. J.* **116**, 1009–1038 (1998).
- [79] Perlmutter, S. *et al.* (Supernova Cosmology Project). Measurements of Omega and Lambda from 42 high redshift supernovae. *Astrophys. J.* **517**, 565–586 (1999).
- [80] Claeys, J. S. W. *et al.* Theoretical uncertainties of the Type Ia supernova rate. *Astron. Astrophys.* **563**, A83 (2014).
- [81] Lipunov, V. M. Double O-Ne-Mg white dwarfs merging as the source of the Powerfull Gravitational Waves for LIGO/VIRGO type interferometers (2017).
- [82] Nelemans, G., Yungelson, L. R. & Portegies Zwart, S. F. The gravitational wave signal from the Galactic disk population of binaries containing two compact objects. *Astron. Astrophys.* **375**, 890–898 (2001).
- [83] Nelemans, G., Yungelson, L. R., Portegies Zwart, S. F. & Verbunt, F. Population synthesis for double white dwarfs . I. Close detached systems. *Astron. Astrophys.* **365**, 491–507 (2001).
- [84] Seitenzahl, I. R. *et al.* Neutrino and gravitational wave signal of a delayed-detonation model of Type Ia supernovae. *Phys. Rev.* **D92**, 124013 (2015).
- [85] Smartt, S. J. Progenitors of Core-Collapse Supernovae. *Ann. Rev. Astron. Astroph.* **47**, 63–106 (2009).
- [86] Tauris, T. M. *et al.* Ultra-stripped Type Ic Supernovae from Close Binary Evolution. *Astrophys. J.* **778**, L23 (2013).

- [87] Tauris, T., Langer, N. & Podsiadlowski, P. Progenitors of ultra-stripped supernovae (2015). URL <https://inspirehep.net/record/1400980/files/arXiv:1510.07874.pdf>.
- [88] Tauris, T. Ultra-stripped supernovae and double neutron star systems (2015). URL <https://inspirehep.net/record/1400981/files/arXiv:1510.07875.pdf>.
- [89] Tauris, T. M., Langer, N. & Podsiadlowski, P. Ultra-stripped supernovae: progenitors and fate. *Mon. Not. Roy. Astron. Soc.* **451**, 2123–2144 (2015).
- [90] Nomoto, K. Evolution of 8-10 solar mass stars toward electron capture supernovae. I - Formation of electron-degenerate O + Ne + Mg cores. *Astrophys. J.* **277**, 791–805 (1984).
- [91] Diehl, R. *et al.* Radioactive Al-26 and massive stars in the galaxy. *Nature* **439**, 45–47 (2006).
- [92] Guy, J. *et al.* The Supernova Legacy Survey 3-year sample: Type Ia supernovae photometric distances and cosmological constraints. *Astron. Astrophys.* **523**, A7 (2010).
- [93] Sako, M. *et al.* (SDSS). The Data Release of the Sloan Digital Sky Survey-II Supernova Survey (2014).
- [94] Rau, A. *et al.* Exploring the Optical Transient Sky with the Palomar Transient Factory. *Publications of the Astronomical Society of the Pacific* **121**, 1334 (2009).
- [95] Hirata, K. *et al.* Observation of a neutrino burst from the supernova SN1987A. *Physical Review Letters* **58**, 1490–1493 (1987).
- [96] Logue, J. *et al.* Inferring Core-Collapse Supernova Physics with Gravitational Waves. *Phys. Rev.* **D86**, 044023 (2012).
- [97] Powell, J., Gossan, S. E., Logue, J. & Heng, I. S. Inferring the core-collapse supernova explosion mechanism with gravitational waves. *Phys. Rev.* **D94**, 123012 (2016).
- [98] Gossan, S. E. *et al.* Observing Gravitational Waves from Core-Collapse Supernovae in the Advanced Detector Era. *Phys. Rev.* **D93**, 042002 (2016).

- [99] Abbott, B. P. *et al.* (Virgo, LIGO Scientific). A First Targeted Search for Gravitational-Wave Bursts from Core-Collapse Supernovae in Data of First-Generation Laser Interferometer Detectors. *Phys. Rev.* **D94**, 102001 (2016).
- [100] Adams, S. M. *et al.* The search for failed supernovae with the Large Binocular Telescope: confirmation of a disappearing star (2016).
- [101] Hobbs, G., Lorimer, D. R., Lyne, A. G. & Kramer, M. A statistical study of 233 pulsar proper motions. *Mon. Not. R. Astron. Soc.* **360**, 974–992 (2005).
- [102] Lyne, A. G. & Lorimer, D. R. High birth velocities of radio pulsars. *Nature* **369**, 127–129 (1994).
- [103] Hansen, B. M. S. & Phinney, E. S. The Pulsar kick velocity distribution. *Mon. Not. Roy. Astron. Soc.* **291**, 569 (1997).
- [104] Arzoumanian, Z., Chernoffs, D. F. & Cordes, J. M. The Velocity distribution of isolated radio pulsars. *Astrophys. J.* **568**, 289–301 (2002).
- [105] Barrett, J. W. *et al.* Exploring the Parameter Space of Compact Binary Population Synthesis (2017). URL <https://inspirehep.net/record/1591308/files/arXiv:1704.03781.pdf>.
- [106] Mirabel, I. F. *et al.* A high-velocity black hole on a Galactic-halo orbit in the solar neighbourhood. *Nature* **413**, 139–141 (2001).
- [107] Repetto, S., Davies, M. B. & Sigurdsson, S. Investigating stellar-mass black hole kicks. *Mon. Not. R. Astron. Soc.* **425**, 2799–2809 (2012).
- [108] Janka, H.-T. Natal kicks of stellar mass black holes by asymmetric mass ejection in fallback supernovae. *Mon. Not. R. Astron. Soc.* **434**, 1355–1361 (2013).
- [109] Repetto, S. & Nelemans, G. Constraining the formation of black holes in short-period black hole low-mass X-ray binaries. *Mon. Not. R. Astron. Soc.* **453**, 3341–3355 (2015).
- [110] Mandel, I. Estimates of black hole natal kick velocities from observations of low-mass X-ray binaries. *Mon. Not. R. Astron. Soc.* **456**, 578–581 (2016).
- [111] Repetto, S., Igoshev, A. P. & Nelemans, G. The Galactic distribution of X-ray binaries and its implications for compact object formation and natal kicks. *Mon. Not. Roy. Astron. Soc.* (2017).

- [112] Chruslinska, M., Belczynski, K., Bulik, T. & Gladysz, W. Constraints on the Formation of Double Neutron Stars from the Observed Eccentricities and Current Limits on Merger Rates. *Acta Astronomica* **67**, 37–50 (2017).
- [113] Spera, M., Mapelli, M. & Bressan, A. The mass spectrum of compact remnants from the PARSEC stellar evolution tracks. *Mon. Not. R. Astron. Soc.* **451**, 4086–4103 (2015).
- [114] O'Connor, E. & Ott, C. D. Black Hole Formation in Failing Core-Collapse Supernovae. *Astrophys. J.* **730**, 70 (2011).
- [115] Ugliano, M., Janka, H.-T., Marek, A. & Arcones, A. Progenitor-explosion Connection and Remnant Birth Masses for Neutrino-driven Supernovae of Iron-core Progenitors. *Astrophys. J.* **757**, 69 (2012).
- [116] O'Connor, E. & Ott, C. D. The Progenitor Dependence of the Pre-explosion Neutrino Emission in Core-collapse Supernovae. *Astrophys. J.* **762**, 126 (2013).
- [117] Sukhbold, T. *et al.* Core-Collapse Supernovae from 9 to 120 Solar Masses Based on Neutrino-powered Explosions. *Astrophys. J.* **821**, 38 (2016).
- [118] Demorest, P. B. *et al.* A two-solar-mass neutron star measured using shapiro delay. *Nature* **467** (2010). URL <http://www.nature.com/nature/journal/v467/n7319/abs/nature09466.html>.
- [119] Antoniadis, J. *et al.* A Massive Pulsar in a Compact Relativistic Binary. *Science* **340**, 448 (2013).
- [120] Farr, W. M. *et al.* The Mass Distribution of Stellar-mass Black Holes. *Astrophys. J.* **741**, 103 (2011).
- [121] Özel, F., Psaltis, D., Narayan, R. & McClintock, J. E. The Black Hole Mass Distribution in the Galaxy. *Astrophys. J.* **725**, 1918–1927 (2010).
- [122] Littenberg, T. B. *et al.* Neutron Stars versus Black Holes: Probing the Mass Gap with LIGO/Virgo. *Astrophys. J. Lett.* **807**, L24 (2015).
- [123] Mandel, I., Haster, C.-J., Dominik, M. & Belczynski, K. Distinguishing types of compact-object binaries using the gravitational-wave signatures of their mergers. *Mon. Not. R. Astron. Soc.* **450**, L85–L89 (2015).

- [124] Mandel, I. *et al.* Model-independent inference on compact-binary observations. *Mon. Not. R. Astron. Soc.* **465**, 3254 (2017).
- [125] Fryer, C. L. *et al.* Compact Remnant Mass Function: Dependence on the Explosion Mechanism and Metallicity. *Astrophys. J.* **749**, 91 (2012).
- [126] Woosley, S. E. Pulsational Pair-Instability Supernovae. *Astrophys. J.* **836**, 244 (2017).
- [127] Woosley, S. E., Blinnikov, S. & Heger, A. Pulsational pair instability as an explanation for the most luminous supernovae. *Nature* **450**, 390 (2007).
- [128] Belczynski, K. *et al.* The Effect of Pair-Instability Mass Loss on Black Hole Mergers. *Astron. Astrophys.* **594**, A97 (2016).
- [129] Marchant, P. *et al.* A new route towards merging massive black holes. *Astron. Astrophys.* **588**, A50 (2016).
- [130] Mandel, I. & de Mink, S. E. Merging binary black holes formed through chemically homogeneous evolution in short-period stellar binaries. *Mon. Not. R. Astron. Soc.* **458**, 2634–2647 (2016).
- [131] Blaauw, A. On the origin of the O- and B-type stars with high velocities (the "run-away" stars), and some related problems. *Bull. Astron. Inst. Netherlands* **15**, 265 (1961).
- [132] Brandt, N. & Podsiadlowski, P. The effects of high-velocity supernova kicks on the orbital properties and sky distributions of neutron-star binaries. *Mon. Not. Roy. Astron. Soc.* **274**, 461–484 (1995).
- [133] O’Shaughnessy, R., Gerosa, D. & Wysocki, D. Inferences about supernova physics from gravitational-wave measurements: GW151226 spin misalignment as an indicator of strong black-hole natal kicks (2017).
- [134] Grimm, H. J., Gilfanov, M. & Sunyaev, R. High mass x-ray binaries as a star formation rate indicator in distant galaxies. *Mon. Not. Roy. Astron. Soc.* **339**, 793 (2003).
- [135] Mineo, S., Gilfanov, M. & Sunyaev, R. X-ray emission from star-forming galaxies - I. High-mass X-ray binaries. *Mon. Not. Roy. Astron. Soc.* **419**, 2095–2115 (2012).

- [136] Zuo, Z.-Y., Li, X.-D. & Gu, Q.-S. Population synthesis on high-mass X-ray binaries: prospects and constraints from the universal X-ray luminosity function. *Mon. Not. Roy. Astron. Soc.* **437**, 1187–1198 (2014).
- [137] Mochnacki, S. W. Accurate integrations of the Roche model. *Astrophys. J. Supp. Ser.* **55**, 551–561 (1984).
- [138] Eggleton, P. P. Approximations to the radii of Roche lobes. *Astrophys. J.* **268**, 368 (1983).
- [139] Sepinsky, J. F., Willems, B. & Kalogera, V. Equipotential Surfaces and Lagrangian points in Non-synchronous, Eccentric Binary and Planetary Systems. *Astrophys. J.* **660**, 1624–1635 (2007).
- [140] Leahy, D. A. & Leahy, J. C. A calculator for Roche lobe properties. *Computational Astrophysics and Cosmology* **2**, 4 (2015).
- [141] Schneider, F. R. N., Izzard, R. G., Langer, N. & de Mink, S. E. Evolution of Mass Functions of Coeval Stars through Wind Mass Loss and Binary Interactions. *Astrophys. J.* **805**, 20 (2015).
- [142] Belczynski, K. *et al.* Compact Object Modeling with the StarTrack Population Synthesis Code. *Astrophys. J. Supplement* **174**, 223–260 (2008).
- [143] Soberman, G. E., Phinney, E. S. & Heuvel, E. P. J. v. d. Stability criteria for mass transfer in binary stellar evolution. *Astron. Astrophys.* **327**, 620 (1997).
- [144] Heuvel, E. P. J. v. d., Portegies Zwart, S. F. & de Mink, S. E. Forming short-period Wolf-Rayet/X-ray binaries and double black holes through stable mass transfer (2017).
- [145] Hjellming, M. S. & Webbink, R. F. Thresholds for rapid mass transfer in binary systems. I - Polytropic models. *Astrophys. J.* **318**, 794–808 (1987).
- [146] de Mink, S. E., Pols, O. R. & Hilditch, R. W. Efficiency of mass transfer in massive close binaries. Tests from double-lined eclipsing binaries in the SMC. *Astron. Astrophys.* **467**, 1181–1196 (2007).
- [147] Passy, J.-C. *et al.* Simulating the Common Envelope Phase of a Red Giant Using Smoothed-particle Hydrodynamics and Uniform-grid Codes. *Astrophys. J.* **744**, 52 (2012).

- [148] Ivanova, N. *et al.* Common envelope evolution: where we stand and how we can move forward. *Astron. Astrophys. Rev.* **21**, 59 (2013).
- [149] Tutukov, A. & Yungelson, L. Evolution of massive common envelope binaries and mass loss. In Conti, P. S. & De Loore, C. W. H., editors, *Mass Loss and Evolution of O-Type Stars*, volume 83 of *IAU Symposium*, 401–406 (1979).
- [150] Iben, I., Jr. & Tutukov, A. V. Supernovae of type I as end products of the evolution of binaries with components of moderate initial mass (M not greater than about 9 solar masses). *Astrophys. J. Suppl.* **54**, 335–372 (1984).
- [151] Webbink, R. F. Double white dwarfs as progenitors of R Coronae Borealis stars and Type I supernovae. *Astrophys. J.* **277**, 355–360 (1984).
- [152] De Marco, O. *et al.* On the α formalism for the common envelope interaction. *Mon. Not. Roy. Astron. Soc.* **411**, 2277–2292 (2011).
- [153] Webbink, R. F. Common Envelope Evolution Redux. In Milone, E. F., Leahy, D. A. & Hobill, D. W., editors, *Astrophysics and Space Science Library*, volume 352 of *Astrophysics and Space Science Library*, 233 (2008).
- [154] Nandez, J. L. A. & Ivanova, N. Common envelope events with low-mass giants: understanding the energy budget. *Mon. Not. Roy. Astron. Soc.* **460**, 3992–4002 (2016).
- [155] Kruckow, M. U. *et al.* Common-envelope ejection in massive binary stars. Implications for the progenitors of GW150914 and GW151226. *Astron. Astrophys.* **596**, A58 (2016).
- [156] Ivanova, N. & Chaichenets, S. Common Envelope: Enthalpy Consideration. *Astrophys. J. Lett.* **731**, L36 (2011).
- [157] Dewi, J. D. M. & Tauris, T. M. On the energy equation and efficiency parameter of the common envelope evolution. *Astron. Astrophys.* **360**, 1043–1051 (2000).
- [158] Xu, X.-J. & Li, X.-D. On the Binding Energy Parameter λ of Common Envelope Evolution. *Astrophys. J.* **716**, 114–121 (2010).
- [159] Loveridge, A. J., van der Sluys, M. V. & Kalogera, V. Analytical Expressions for the Envelope Binding Energy of Giants as a Function of Basic Stellar Parameters. *Astrophys. J.* **743**, 49 (2011).

- [160] Ivanova, N. Common Envelope: The Progress and the Pitfalls. In Schmid-tobreick, L., Schreiber, M. R. & Tappert, C., editors, *Evolution of Compact Binaries*, volume 447 of *Astronomical Society of the Pacific Conference Series*, 91 (2011).
- [161] Wang, C., Jia, K. & Li, X.-D. The binding energy parameter for common envelope evolution. *Research in Astronomy and Astrophysics* **16**, 126 (2016).
- [162] Tauris, T. M. & Dewi, J. D. M. On the binding energy parameter of common envelope evolution. dependency on the definition of the stellar core boundary during spiral-in. *Astron. Astrophys.* **369**, 170 (2001).
- [163] de Kool, M., van den Heuvel, E. P. J. & Pylyser, E. An evolutionary scenario for the black hole binary A0620-00. *Astron. Astrophys.* **183**, 47–52 (1987).
- [164] Nelemans, G., Verbunt, F., Yungelson, L. R. & Portegies Zwart, S. F. Reconstructing the evolution of double helium white dwarfs: envelope loss without spiral-in. *Astron. Astrophys* **360**, 1011–1018 (2000).
- [165] Nelemans, G. & Tout, C. A. Reconstructing the evolution of white dwarf binaries: further evidence for an alternative algorithm for the outcome of the common-envelope phase in close binaries. *Mon. Not. Roy. Astron. Soc.* **356**, 753–764 (2005).
- [166] Woods, T. E., Ivanova, N., van der Sluys, M. V. & Chaichenets, S. On the Formation of Double White Dwarfs through Stable Mass Transfer and a Common Envelope. *Astrophys. J.* **744**, 12 (2012).
- [167] Kulkarni, S. R. *et al.* An unusually brilliant transient in the galaxy Messier 85. *Nature* **447**, 458–460 (2007).
- [168] Tytenda, R. *et al.* V1309 Scorpii: merger of a contact binary. *Astron. Astrophys.* **528**, A114 (2011).
- [169] Ivanova, N., Justham, S., Nandez, J. L. A. & Lombardi, J. C., Jr. Identification of the Long-Sought Common-Envelope Events. *Science* **339**, 433 (2013).
- [170] Metzger, B. D. & Pejcha, O. Shock-powered light curves of luminous red novae as signatures of pre-dynamical mass loss in stellar mergers (2017).
- [171] Ofek, E. O. *et al.* The Environment of M85 optical transient 2006-1: Constraints on the progenitor age and mass. *Astrophys. J.* **674**, 447 (2008).

- [172] Peters, P. C. & Mathews, J. Gravitational Radiation from Point Masses in a Keplerian Orbit. *Physical Review* **131**, 435–440 (1963).
- [173] Peters, P. C. Gravitational Radiation and the Motion of Two Point Masses. *Physical Review* **136**, 1224–1232 (1964).
- [174] Gerosa, D. *et al.* Resonant-plane locking and spin alignment in stellar-mass black-hole binaries: A diagnostic of compact-binary formation. *Phys. Rev. D* **87**, 104028 (2013).
- [175] Kesden, M. *et al.* Effective Potentials and Morphological Transitions for Binary Black Hole Spin Precession. *Phys. Rev. Lett.* **114**, 081103 (2015).
- [176] Gerosa, D. *et al.* Multi-timescale analysis of phase transitions in precessing black-hole binaries. *Phys. Rev. D* **92**, 064016 (2015).
- [177] Apostolatos, T. A., Cutler, C., Sussman, G. J. & Thorne, K. S. Spin-induced orbital precession and its modulation of the gravitational waveforms from merging binaries. *Phys. Rev. D* **49**, 6274 (1994).
- [178] Dormand, J. & Prince, P. A family of embedded runge-kutta formulae. *Journal of Computational and Applied Mathematics* **6**, 19 – 26 (1980). URL <http://www.sciencedirect.com/science/article/pii/0771050X80900133>.
- [179] Schnittman, J. D. Spin-orbit resonance and the evolution of compact binary systems. *Phys. Rev. D* **70**, 124020 (2004).
- [180] Kesden, M., Sperhake, U. & Berti, E. Final spins from the merger of precessing binary black holes. *Phys. Rev. D* **81**, 084054 (2010).
- [181] Gerosa, D. *et al.* Distinguishing black-hole spin-orbit resonances by their gravitational-wave signatures. *Phys. Rev. D* **89**, 124025 (2014).
- [182] Trifirò, D. *et al.* Distinguishing black-hole spin-orbit resonances by their gravitational wave signatures. II. Full parameter estimation. *Phys. Rev. D* **93**, 044071 (2016).
- [183] Rodriguez, C. L. *et al.* Dynamical Formation of the GW150914 Binary Black Hole. *Astrophys. J. Lett.* **824**, L8 (2016).
- [184] Freire, P. C. C. The pulsar population in Globular Clusters and in the Galaxy. In van Leeuwen, J., editor, *Neutron Stars and Pulsars: Challenges and Opportunities after 80 years*, volume 291 of *IAU Symposium*, 243–250 (2013).

- [185] Portegies Zwart, S. F. *et al.* The Formation of massive black holes through collision runaway in dense young star clusters. *Nature* **428**, 724 (2004).
- [186] Maccarone, T. J., Kundu, A., Zepf, S. E. & Rhode, K. L. A black hole in a globular cluster. *Nature* **445**, 183–185 (2007).
- [187] Strader, J. *et al.* Two stellar-mass black holes in the globular cluster M22. *Nature* **490**, 71–73 (2012).
- [188] Benacquista, M. J. & Downing, J. M. B. Relativistic binaries in globular clusters. *Living Reviews in Relativity* **16**, 4 (2013). URL <http://dx.doi.org/10.12942/lrr-2013-4>.
- [189] Abbott, B. P. *et al.* Astrophysical Implications of the Binary Black Hole Merger GW150914. *Astrophys. J. Lett.* **818**, L22 (2016).
- [190] Coleman Miller, M. Implications of the gravitational wave event GW150914. *Gen. Rel. Grav.* **48**, 95 (2016).
- [191] Kulkarni, S. R., Hut, P. & McMillan, S. Stellar black holes in globular clusters. *Nature* **364**, 421–423 (1993).
- [192] Sigurdsson, S. & Hernquist, L. Primordial black holes in globular clusters. *Nature* **364**, 423–425 (1993).
- [193] Portegies Zwart, S. F. & McMillan, S. L. W. Black hole mergers in the universe. *Astrophys. J.* **528**, L17 (2000).
- [194] Spitzer, L., Jr. Equipartition and the Formation of Compact Nuclei in Spherical Stellar Systems. *Astrophys. J. Lett.* **158**, L139 (1969).
- [195] Spitzer, L. *Dynamical evolution of globular clusters* (1987).
- [196] Antonini, F. & Rasio, F. A. Merging black hole binaries in galactic nuclei: implications for advanced-LIGO detections. *Astrophys. J.* **831**, 187 (2016).
- [197] Harris, W. E. A Catalog of Parameters for Globular Clusters in the Milky Way. *Astron. J.* **112**, 1487 (1996).
- [198] Downing, J. M. B., Benacquista, M. J., Giersz, M. & Spurzem, R. Compact binaries in star clusters - II. Escapers and detection rates. *Mon. Not. R. Astron. Soc.* **416**, 133–147 (2011).

- [199] Ziosi, B. M., Mapelli, M., Branchesi, M. & Tormen, G. Dynamics of stellar black holes in young star clusters with different metallicities - II. Black hole-black hole binaries. *Mon. Not. R. Astron. Soc.* **441**, 3703–3717 (2014).
- [200] Rodriguez, C. L. *et al.* Binary Black Hole Mergers from Globular Clusters: Implications for Advanced LIGO. *Phys. Rev. Lett.* **115**, 051101 (2015).
- [201] Morscher, M. *et al.* The Dynamical Evolution of Stellar Black Holes in Globular Clusters. *Astrophys. J.* **800**, 9 (2015).
- [202] Rodriguez, C. L., Chatterjee, S. & Rasio, F. A. Binary black hole mergers from globular clusters: Masses, merger rates, and the impact of stellar evolution. *Phys. Rev. D* **93**, 084029 (2016).
- [203] Chatterjee, S., Rodriguez, C. L., Kalogera, V. & Rasio, F. A. Dynamical Formation of Low-Mass Merging Black Hole Binaries like GW151226. *Astrophys. J.* **836**, L26 (2017).
- [204] Chatterjee, S., Rodriguez, C. L. & Rasio, F. A. Binary Black Holes in Dense Star Clusters: Exploring the Theoretical Uncertainties. *Astrophys. J.* **834**, 68 (2017).
- [205] Bartos, I., Kocsis, B., Haiman, Z. & Mrka, S. Rapid and Bright Stellar-mass Binary Black Hole Mergers in Active Galactic Nuclei. *Astrophys. J.* **835**, 165 (2017).
- [206] Stone, N. C., Metzger, B. D. & Haiman, Z. Assisted Inspirals of Stellar Mass Black Holes Embedded in AGN Discs: solving the 'final au problem'. *Mon. Not. R. Astron. Soc.* **464**, 946–954 (2017).
- [207] Rodriguez, C. L. *et al.* Illuminating Black Hole Binary Formation Channels with Spins in Advanced LIGO. *Astrophys. J.* **832**, L2 (2016).
- [208] de Mink, S. E. *et al.* The Rotation Rates of Massive Stars: The Role of Binary Interaction through Tides, Mass Transfer, and Mergers. *Astrophys. J.* **764**, 166 (2013).
- [209] de Mink, S. E. *et al.* Rotational mixing in close binaries. In Deng, L. & Chan, K. L., editors, *IAU Symposium*, volume 252 of *IAU Symposium*, 365–370 (2008).
- [210] de Mink, S. E. *et al.* Rotational mixing in massive binaries. Detached short-period systems. *Astron. Astrophys.* **497**, 243–253 (2009).

- [211] de Mink, S. E. *et al.* A New Evolutionary Scenario for the Formation of Massive Black-Hole Binaries such as M33 X-7 and IC 10 X-1. In Prša, A. & Zejda, M., editors, *Binaries - Key to Comprehension of the Universe*, volume 435 of *Astronomical Society of the Pacific Conference Series*, 179 (2010).
- [212] Almeida, L. A. *et al.* Discovery of the Massive Overcontact Binary VFTS352: Evidence for Enhanced Internal Mixing. *Astrophys. J.* **812**, 102 (2015).
- [213] Eldridge, J. J. & Stanway, E. R. BPASS predictions for Binary Black-Hole Mergers. *Mon. Not. R. Astron. Soc.* **462**, 3302–3313 (2016).
- [214] de Mink, S. E. & Mandel, I. The chemically homogeneous evolutionary channel for binary black hole mergers: Rates and Properties of gravitational-wave events detectable by advanced LIGO. *Mon. Not. R. Astron. Soc.* (2016).
- [215] Madau, P. & Rees, M. J. Massive Black Holes as Population III Remnants. *Astrophys. J. Lett.* **551**, L27–L30 (2001).
- [216] Bond, J. R. & Carr, B. J. Gravitational waves from a population of binary black holes. *Mon. Not. Roy. Astron. Soc.* **207**, 585–609 (1984).
- [217] Inayoshi, K., Kashiyama, K., Visbal, E. & Haiman, Z. Gravitational wave background from population iii binary black holes consistent with cosmic reionization. *Mon. Not. R. Astron. Soc.* **461**, 2722–2727 (2016).
- [218] Belczynski, K., Bulik, T. & Rudak, B. The First Stellar Binary Black Holes: The Strongest Gravitational Wave Burst Sources. *Astrophys. J. Lett.* **608**, L45–L48 (2004).
- [219] Kinugawa, T. *et al.* Possible indirect confirmation of the existence of Pop III massive stars by gravitational wave. *Mon. Not. R. Astron. Soc.* **442**, 2963–2992 (2014).
- [220] Kinugawa, T., Miyamoto, A., Kanda, N. & Nakamura, T. The detection rate of inspiral and quasi-normal modes of Population III binary black holes which can confirm or refute the general relativity in the strong gravity region. *Mon. Not. R. Astron. Soc.* **456**, 1093–1114 (2016).
- [221] Belczynski, K. *et al.* On the likelihood of detecting gravitational waves from Population III compact object binaries (2016).
- [222] Hartwig, T. *et al.* Gravitational Waves from the Remnants of the First Stars. *Mon. Not. Roy. Astron. Soc.* **460**, L74–L78 (2016).

- [223] Carr, B. J. & Hawking, S. W. Black holes in the early Universe. *Mon. Not. R. Astron. Soc.* **168**, 399–416 (1974).
- [224] Bird, S. *et al.* Did LIGO Detect Dark Matter? *Phys. Rev. Lett.* **116**, 201301 (2016).
- [225] Clesse, S. & García-Bellido, J. The clustering of massive Primordial Black Holes as Dark Matter: measuring their mass distribution with Advanced LIGO. *Phys. Dark Univ.* **10**, 002 (2016).
- [226] Sasaki, M., Suyama, T., Tanaka, T. & Yokoyama, S. Primordial Black Hole Scenario for the Gravitational-Wave Event GW150914. *Phys. Rev. Lett.* **117**, 061101 (2016).
- [227] Carr, B., Kuhnel, F. & Sandstad, M. Primordial Black Holes as Dark Matter. *Phys. Rev. D* **94**, 083504 (2016).
- [228] Blinnikov, S., Dolgov, A., Porayko, N. K. & Postnov, K. Solving puzzles of GW150914 by primordial black holes. *JCAP* **1611**, 036 (2016).
- [229] Chiba, T. & Yokoyama, S. Spin Distribution of Primordial Black Holes (2017).
- [230] Ricotti, M., Ostriker, J. P. & Mack, K. J. Effect of Primordial Black Holes on the Cosmic Microwave Background and Cosmological Parameter Estimates. *Astrophys. J.* **680**, 829 (2008).
- [231] Clesse, S. & García-Bellido, J. Massive Primordial Black Holes from Hybrid Inflation as Dark Matter and the seeds of Galaxies. *Phys. Rev. D* **92**, 023524 (2015).
- [232] Kashlinsky, A. LIGO gravitational wave detection, primordial black holes and the near-IR cosmic infrared background anisotropies. *Astrophys. J. Lett.* **823**, L25 (2016).
- [233] Green, A. M. Microlensing and dynamical constraints on primordial black hole dark matter with an extended mass function. *Phys. Rev. D* **94**, 063530 (2016).
- [234] Mediavilla, E. *et al.* Limits on the Mass and Abundance of Primordial Black Holes from Quasar Gravitational Microlensing. *Astrophys. J. Lett.* **836**, L18 (2017).

- [235] Carr, B. *et al.* Primordial black hole constraints for extended mass functions (2017).
- [236] Connaughton, V. *et al.* Fermi GBM Observations of LIGO Gravitational Wave event GW150914. *ArXiv e-prints* (2016).
- [237] Loeb, A. Electromagnetic Counterparts to Black Hole Mergers Detected by LIGO. *Astrophys. J.* **819**, L21 (2016).
- [238] Fedrow, J. M. *et al.* Gravitational Waves from Binary Black Hole Mergers Inside of Stars (2017).
- [239] Aasi, J. *et al.* Advanced LIGO. *Class. Quantum Grav* **32**, 074001 (2015).
- [240] O’Leary, R. M., Meiron, Y. & Kocsis, B. Dynamical formation signatures of black hole binaries in the first detected mergers by LIGO. *Astrophys. J.* **824**, L12 (2016).
- [241] Askar, A. *et al.* MOCCA-SURVEY Database I: Coalescing Binary Black Holes Originating From Globular Clusters. *Mon. Not. R. Astron. Soc. Lett.* **464**, L36–L40 (2017).
- [242] Mapelli, M. Massive black hole binaries from runaway collisions: the impact of metallicity. *Mon. Not. R. Astron. Soc.* (2016).
- [243] Belczynski, K. *et al.* The Effect of Metallicity on the Detection Prospects for Gravitational Waves. *Astrophys. J. Lett.* **715**, L138–L141 (2010).
- [244] Postnov, K. A. & Yungelson, L. R. The Evolution of Compact Binary Star Systems. *Living Reviews in Relativity* **17**, 3 (2014).
- [245] Hurley, J. R., Tout, C. A. & Pols, O. R. Evolution of binary stars and the effect of tides on binary populations. *Mon. Not. R. Astron. Soc.* **329**, 897–928 (2002).
- [246] Izzard, R. G., Tout, C. A., Karakas, A. I. & Pols, O. R. A new synthetic model for asymptotic giant branch stars. *Mon. Not. R. Astron. Soc.* **350**, 407–426 (2004).
- [247] Izzard, R. G. *et al.* Population nucleosynthesis in single and binary stars. *Astron. Astrophys.* **460**, 565–572 (2006).

- [248] Izzard, R. G., Glebbeek, E., Stancliffe, R. J. & Pols, O. R. Population synthesis of binary carbon-enhanced metal-poor stars. *Astron. Astrophys.* **508**, 1359–1374 (2009).
- [249] Belczynski, K., Kalogera, V. & Bulik, T. A comprehensive study of binary compact objects as gravitational wave sources: Evolutionary channels, rates, and physical properties. *Astrophys. J.* **572**, 407 (2002).
- [250] Öpik, E. Statistical Studies of Double Stars: On the Distribution of Relative Luminosities and Distances of Double Stars in the Harvard Revised Photometry North of Declination -31 degrees. *Publications of the Tartu Astrofizika Observatory* **25**, 1 (1924).
- [251] Hamann, W.-R. & Koesterke, L. Spectrum formation in clumped stellar winds: consequences for the analyses of Wolf-Rayet spectra. *Astron. Astrophys.* **335**, 1003–1008 (1998).
- [252] Vink, J. S. & de Koter, A. On the metallicity dependence of Wolf-Rayet winds. *Astron. Astrophys.* **442**, 587–596 (2005).
- [253] Kippenhahn, R. & Weigert, A. Entwicklung in engen Doppelsternsystemen I. Massenaustausch vor und nach Beendigung des zentralen Wasserstoff-Brennens. *Zeitschrift für Astrophysik* **65**, 251 (1967).
- [254] Tout, C. A., Aarseth, S. J., Pols, O. R. & Eggleton, P. P. Rapid binary star evolution for N-body simulations and population synthesis. *Mon. Not. R. Astron. Soc.* **291**, 732 (1997).
- [255] Belczynski, K. *et al.* On the Rarity of Double Black Hole Binaries: Consequences for Gravitational Wave Detection. *Astrophys. J.* **662**, 504–511 (2007).
- [256] Pavlovskii, K., Ivanova, N., Belczynski, K. & Van, K. X. Stability of mass transfer from massive giants: double black-hole binary formation and ultra-luminous X-ray sources. Preprint at <https://arxiv.org/abs/1606.04921> (2016).
- [257] de Mink, S. E., Pols, O. R. & Yoon, S. C. Binaries at Low Metallicity: ranges for case A, B and C mass transfer. *AIP Conf. Proc.* **990**, 230–232 (2008).
- [258] Madau, P. & Dickinson, M. Cosmic Star-Formation History. *Annu. Rev. Astron. Astrophys.* **52**, 415–486 (2014).

- [259] Dominik, M. *et al.* Double Compact Objects III: Gravitational-wave Detection Rates. *Astrophys. J.* **806**, 263 (2015).
- [260] Sana, H. & the VLT-Flames Tarantula consortium. The vlt-flames tarantula survey: an overview of the vfts results so far. *EAS Publications Series* **64**, 147–154 (2013). URL <https://doi.org/10.1051/eas/1364021>.
- [261] Podsiadlowski, P., Ivanova, N., Justham, S. & Rappaport, S. Explosive common-envelope ejection: implications for gamma-ray bursts and low-mass black-hole binaries. *Mon. Not. R. Astron. Soc.* **406**, 840–847 (2010).
- [262] Bulik, T. & Belczyński, K. Constraints on the Binary Evolution from Chirp Mass Measurements. *Astrophys. J. Lett.* **589**, L37–L40 (2003).
- [263] O’Shaughnessy, R. Data-driven methods to explore a large space of computationally costly compact binary progenitor models. *Phys. Rev. D* **88**, 084061 (2013).
- [264] Mandel, I. & O’Shaughnessy, R. Compact binary coalescences in the band of ground-based gravitational-wave detectors. *Class. Quantum Grav* **27**, 114007–+ (2010).
- [265] Vitale, S., Lynch, R., Sturani, R. & Graff, P. Use of gravitational waves to probe the formation channels of compact binaries. *Class. Quant. Grav.* **34**, 03LT01 (2017).
- [266] Kushnir, D., Zaldarriaga, M., Kollmeier, J. A. & Waldman, R. GW150914: spin-based constraints on the merger time of the progenitor system. *Mon. Not. R. Astron. Soc.* **462**, 844–849 (2016).
- [267] Abbott, B. P. *et al.* GW150914: Implications for the Stochastic Gravitational-Wave Background from Binary Black Holes. *Phys. Rev. Lett.* **116**, 131102 (2016).
- [268] Callister, T. *et al.* The limits of astrophysics with gravitational wave backgrounds. *Phys. Rev. X* **6**, 031018 (2016).
- [269] Abadie, J. *et al.* (LIGO Scientific Collaboration and Virgo Collaboration). Predictions for the Rates of Compact Binary Coalescences Observable by Ground-based Gravitational-wave Detectors. *Class. Quantum Grav* **27**, 173001–+ (2010).

- [270] Blanchet, L. Gravitational Radiation from Post-Newtonian Sources and Inspiralling Compact Binaries. *Living Rev. Relat.* **17**, 2 (2014).
- [271] Hannam, M. Status of black-hole-binary simulations for gravitational-wave detection. *Class.Quant.Grav.* **26**, 114001 (2009).
- [272] Hinder, I. The Current Status of Binary Black Hole Simulations in Numerical Relativity. *Class.Quant.Grav.* **27**, 114004 (2010).
- [273] Sperhake, U., Berti, E. & Cardoso, V. Numerical simulations of black-hole binaries and gravitational wave emission. *Comptes Rendus Physique* **14**, 306–317 (2013).
- [274] Buonanno, A. *et al.* Comparison of post-Newtonian templates for compact binary inspiral signals in gravitational-wave detectors. *Phys.Rev.* **D80**, 084043 (2009).
- [275] Ohme, F. Analytical meets numerical relativity - status of complete gravitational waveform models for binary black holes. *Class.Quant.Grav.* **29**, 124002 (2012).
- [276] Hannam, M. *et al.* Simple Model of Complete Precessing Black-Hole-Binary Gravitational Waveforms. *Phys. Rev. Lett.* **113**, 151101 (2014).
- [277] Pan, Y. *et al.* Inspiral-merger-ringdown waveforms of spinning, precessing black-hole binaries in the effective-one-body formalism. *Phys. Rev. D* **89**, 084006 (2014).
- [278] Babak, S. *et al.* Searching for gravitational waves from binary coalescence. *Phys. Rev. D* **87**, 024033 (2013).
- [279] Aasi, J. *et al.* Search for gravitational waves from binary black hole inspiral, merger, and ringdown in LIGO-Virgo data from 2009-2010. *Phys. Rev. D* **87**, 022002 (2013).
- [280] Aasi, J. *et al.* Parameter estimation for compact binary coalescence signals with the first generation gravitational-wave detector network. *Phys. Rev. D* **88**, 062001 (2013).
- [281] Veitch, J. *et al.* Parameter estimation for compact binaries with ground-based gravitational-wave observations using the LALInference software library. *Phys. Rev. D* **91**, 042003 (2015).

- [282] Abadie, J. *et al.* First low-latency LIGO+Virgo search for binary inspirals and their electromagnetic counterparts. *Astron. Astrophys.* **541**, A155 (2012).
- [283] Singer, L. P. *et al.* The First Two Years of Electromagnetic Follow-up with Advanced LIGO and Virgo. *Astrophys. J.* **795**, 105 (2014).
- [284] Aasi, J. *et al.* (The LIGO Scientific Collaboration, the Virgo Collaboration). Search for gravitational waves associated with gamma-ray bursts detected by the InterPlanetary Network. *Phys.Rev.Lett.* **113**, 011102 (2014).
- [285] Clark, J. *et al.* Prospects for joint gravitational wave and short gamma-ray burst observations. *Astrophys. J.* **809**, 53 (2015).
- [286] Hannam, M. *et al.* When can Gravitational-wave Observations Distinguish between Black Holes and Neutron Stars? *Astrophys. J. Lett.* **766**, L14 (2013).
- [287] Ohme, F., Nielsen, A. B., Keppel, D. & Lundgren, A. Statistical and systematic errors for gravitational-wave inspiral signals: A principal component analysis. *Phys. Rev. D* **88**, 042002 (2013).
- [288] C, C. & E, F. Gravitational waves from merging compact binaries: How accurately can one extract the binary’s parameters from the inspiral waveform? *Phys. Rev. D* **49**, 2658 (1994).
- [289] Kelley, L. Z. *et al.* The Distribution of Coalescing Compact Binaries in the Local Universe: Prospects for Gravitational-wave Observations. *Astrophys. J. Lett.* **725**, L91–L96 (2010).
- [290] Mandel, I. Parameter estimation on gravitational waves from multiple coalescing binaries. *Phys. Rev. D* **81**, 084029+ (2010).
- [291] Belczynski, K. *et al.* Compact Binary Merger Rates: Comparison with LIGO/Virgo Upper Limits. *Astrophys. J.* **819**, 108 (2016).
- [292] Messenger, C. & Veitch, J. Avoiding selection bias in gravitational wave astronomy. *New Journal of Physics* **15**, 053027 (2013).
- [293] Mandel, I., Kalogera, V. & O’Shaughnessy, R. Unraveling Binary Evolution from Gravitational-Wave Signals and Source Statistics. *ArXiv e-prints* (2010).
- [294] Postnov, K. & Yungelson, L. The Evolution of Compact Binary Star Systems. *Living Rev. Rel.* **6** (2007).

- [295] Kalogera, V. & Baym, G. The maximum mass of a neutron star. *Astrophys. J.* **470**, L61–L64 (1996).
- [296] Rhoades, C. E. & Ruffini, R. Maximum mass of a neutron star. *Phys. Rev. Lett.* **32**, 324–327 (1974). URL <http://link.aps.org/doi/10.1103/PhysRevLett.32.324>.
- [297] Nelemans, G., Tauris, T. M. & van den Heuvel, E. P. J. Constraints on mass ejection in black hole formation derived from black hole X-ray binaries. *Astron. Astrophys.* **352**, L87–L90 (1999).
- [298] Lépine, S. & Moffat, A. F. J. Direct Spectroscopic Observations of Clumping in O-Star Winds. *Astron. J.* **136**, 548–553 (2008).
- [299] Paczynski, B. Common Envelope Binaries. In Eggleton, P., Mitton, S. & Whelan, J., editors, *Structure and Evolution of Close Binary Systems*, volume 73 of *IAU Symposium*, 75 (1976).
- [300] Belczynski, K. *et al.* Cyg X-3: A Galactic Double Black Hole or Black-hole-Neutron-star Progenitor. *Astrophys. J.* **764**, 96 (2013).
- [301] Bulik, T., Belczynski, K. & Prestwich, A. IC10 X-1/NGC300 X-1: The Very Immediate Progenitors of BH-BH Binaries. *Astrophys. J.* **730**, 140–+ (2011).
- [302] Crowther, P. A. *et al.* NGC 300 X-1 is a Wolf-Rayet/black hole binary. *Mon. Not. R. Astron. Soc.* L11+ (2010).
- [303] O’Shaughnessy, R. W., Kim, C., Kalogera, V. & Belczynski, K. Constraining population synthesis models via empirical binary compact object merger and supernovae rates. *Astrophys. J.* **672**, 479–488 (2008).
- [304] Panter, B., Jimenez, R., Heavens, A. F. & Charlot, S. The cosmic evolution of metallicity from the sdss fossil record. *Mon. Not. Roy. Astron. Soc.* **391**, 1117–1126 (2008). URL <http://mnras.oxfordjournals.org/content/391/3/1117.abstract>.
- [305] Dominik, M. *et al.* Double Compact Objects. II. Cosmological Merger Rates. *Astrophys. J.* **779**, 72 (2013).
- [306] Capano, C., Pan, Y. & Buonanno, A. Impact of Higher Harmonics in Searching for Gravitational Waves from Non-Spinning Binary Black Holes. *Phys. Rev.* **D89**, 102003 (2014).

- [307] Bustillo, J. C. *et al.* Comparison of subdominant gravitational wave harmonics between post-Newtonian and numerical relativity calculations and construction of multi-mode hybrids (2015).
- [308] Brady, P. R. & Fairhurst, S. Interpreting the results of searches for gravitational waves from coalescing binaries. *Class. Quantum Grav* **25**, 105002 (2008).
- [309] Poisson, E. & Will, C. M. Gravitational waves from inspiraling compact binaries: Parameter estimation using second postNewtonian wave forms. *Phys. Rev.* **D52**, 848–855 (1995).
- [310] Abadie, J. *et al.* Search for gravitational waves from low mass compact binary coalescence in LIGO’s sixth science run and Virgo’s science runs 2 and 3. *Phys. Rev. D* **85**, 082002 (2012).
- [311] Santamaría, L. *et al.* Matching post-Newtonian and numerical relativity waveforms: systematic errors and a new phenomenological model for non-precessing black hole binaries. *Phys. Rev. D* **82**, 064016 (2010).
- [312] Aasi, J. *et al.* (LIGO Scientific Collaboration and Virgo Collaboration). Possible scenarios for commissioning and early observing with the second generation detectors. Technical Report LIGO-G1000176 (2010). URL <http://dcc.ligo.org/G1000176>.
- [313] Ajith, P. *et al.* Inspiral-Merger-Ringdown Waveforms for Black-Hole Binaries with Nonprecessing Spins. *Phys. Rev. Lett.* **106**, 241101 (2011).
- [314] Bennett, C., Larson, D., Weiland, J. & Hinshaw, G. The 1% Concordance Hubble Constant. *Astrophys. J.* **794**, 135 (2014).
- [315] Hogg, D. W. Distance measures in cosmology. *ArXiv Astrophysics e-prints* (1999). Astro-ph/9905116.
- [316] Kopparapu, R. K. *et al.* Host Galaxies Catalog Used in LIGO Searches for Compact Binary Coalescence Events. *Astrophys. J.* **675**, 1459–1467 (2008).
- [317] Nitz, A. H. *et al.* Accuracy of gravitational waveform models for observing neutron-starblack-hole binaries in Advanced LIGO. *Phys. Rev.* **D88**, 124039 (2013).

- [318] Vallisneri, M. Use and abuse of the Fisher information matrix in the assessment of gravitational-wave parameter-estimation prospects. *Phys. Rev. D* **77**, 042001 (2008).
- [319] Rodriguez, C. L., Farr, B., Farr, W. M. & Mandel, I. Inadequacies of the Fisher information matrix in gravitational-wave parameter estimation. *Phys. Rev. D* **88**, 084013 (2013).
- [320] Mandel, I. *et al.* Parameter estimation on compact binary coalescences with abruptly terminating gravitational waveforms. *Class. Quantum Grav* **31**, 155005 (2014).
- [321] Dal Canton, T. *et al.* Implementing a search for aligned-spin neutron star-black hole systems with advanced ground based gravitational wave detectors. *Phys. Rev. D* **90**, 082004 (2014).
- [322] Chatziioannou, K., Cornish, N., Klein, A. & Yunes, N. Spin-Precession: Breaking the Black Hole–Neutron Star Degeneracy. *Astrophys. J.* **798**, L17 (2015).
- [323] O’Shaughnessy, R. *et al.* Parameter estimation of gravitational waves from precessing black hole-neutron star inspirals with higher harmonics. *Phys. Rev. D* **89**, 102005 (2014).
- [324] Scott, D. W. On optimal and data-based histograms. *Biometrika* **66**, 605–610 (1979). URL <http://biomet.oxfordjournals.org/content/66/3/605.abstract>.
- [325] LIGO Scientific Collaboration. Advanced LIGO anticipated sensitivity curves (2010). <https://dcc.ligo.org/cgi-bin/DocDB/ShowDocument?docid=2974>.
- [326] Farr, W. M., Gair, J. R., Mandel, I. & Cutler, C. Counting And Confusion: Bayesian Rate Estimation With Multiple Populations. *Phys. Rev. D* **91**, 023005 (2015).
- [327] Aso, Y. *et al.* (KAGRA). Interferometer design of the KAGRA gravitational wave detector. *Phys. Rev. D* **88**, 043007 (2013).
- [328] Lipunov, V. M., Postnov, K. A., Prokhorov, M. E. & Bogomazov, A. I. Description of the “Scenario Machine”. *Astronomy Reports* **53**, 915–940 (2009).
- [329] Postnov, K. A. & Yungelson, L. R. The Evolution of Compact Binary Star Systems. *Living Reviews in Relativity* **9**, 6 (2006).

- [330] Sigurdsson, S. & Hernquist, L. Primordial black holes in globular clusters. *Nature* **364**, 423–425 (1993).
- [331] Sadowski, A. *et al.* The Total Merger Rate of Compact Object Binaries in the Local Universe. *Astrophys. J.* **676**, 1162–1169 (2008).
- [332] Poisson, E. & Will, C. M. Gravitational waves from inspiraling compact binaries: Parameter estimation using second-post-Newtonian waveforms. *Phys. Rev. D* **52**, 848–855 (1995).
- [333] Finn, L. S. & Chernoff, D. F. Observing binary inspiral in gravitational radiation: One interferometer. *Phys. Rev. D* **47**, 2198–2219 (1993).
- [334] Mandel, I. *et al.* Model-independent inference on compact-binary observations. *Mon. Not. Roy. Astron. Soc.* **465**, 3254–3260 (2017).
- [335] McClintock, J. E. *et al.* Measuring the spins of accreting black holes. *Class. Quantum Grav.* **28**, 114009 (2011).
- [336] Fragos, T. & McClintock, J. E. The Origin of Black Hole Spin in Galactic Low-mass X-Ray Binaries. *Astrophys. J.* **800**, 17 (2015).
- [337] Miller, M. C. & Miller, J. M. The masses and spins of neutron stars and stellar-mass black holes. *Phys. Rep.* **548**, 1–34 (2015).
- [338] Boss, A. P. Binary stars - Formation by fragmentation. *Comments on Astrophysics* **12**, 169–190 (1988).
- [339] Albrecht, S. *et al.* The spin axes orbital alignment of both stars within the eclipsing binary system V1143 Cyg using the Rossiter-McLaughlin effect. *Astron. Astrophys.* (2007). [Astron. Astrophys.474,565(2007)].
- [340] Albrecht, S., Reffert, S., Snellen, I. A. G. & Winn, J. N. Misaligned spin and orbital axes cause the anomalous precession of DI Herculis. *Nature* **461**, 373–376 (2009).
- [341] Bardeen, J. M. & Petterson, J. A. The Lense-Thirring Effect and Accretion Disks around Kerr Black Holes. *Astrophys. J. Lett.* **195**, L65 (1975).
- [342] Kalogera, V. Spin-orbit misalignment in close binaries with two compact objects. *Astrophys. J.* **541**, 042003 (2000).

- [343] King, A. R., Lubow, S. H., Ogilvie, G. I. & Pringle, J. E. Aligning spinning black holes and accretion discs. *Mon. Not. Roy. Astron. Soc.* **363**, 49–56 (2005).
- [344] Zahn, J.-P. Tidal friction in close binary stars. *Astron. Astrophys.* **57**, 383–394 (1977).
- [345] Hut, P. Tidal evolution in close binary systems. *Astron. Astrophys.* **99**, 126–140 (1981).
- [346] Fragos, T., Tremmel, M., Rantsiou, E. & Belczynski, K. Black Hole Spin-Orbit Misalignment in Galactic X-ray Binaries. *Astrophys. J. Lett.* **719**, L79–L83 (2010).
- [347] Orosz, J. A. *et al.* A Black Hole in the Superluminal Source SAX J1819.3-2525 (V4641 Sgr). *Astrophys. J.* **555**, 489–503 (2001).
- [348] Martin, R. G., Reis, R. C. & Pringle, J. E. Misalignment of the microquasar V4641 Sgr (SAX J1819.3-2525). *Mon. Not. Roy. Astron. Soc.* **391**, L15–L18 (2008).
- [349] Baird, E., Fairhurst, S., Hannam, M. & Murphy, P. Degeneracy between mass and spin in black-hole-binary waveforms. *Phys. Rev. D* **87**, 024035 (2013).
- [350] Farr, B. *et al.* Parameter Estimation on Gravitational Waves from Neutron-star Binaries with Spinning Components. *Astrophys. J.* **825**, 116 (2016).
- [351] Foreman-Mackey, D., Hogg, D. W. & Morton, T. D. Exoplanet Population Inference and the Abundance of Earth Analogs from Noisy, Incomplete Catalogs. *Astrophys. J.* **795**, 64 (2014).
- [352] Farr, W. M., Mandel, I., Aldridge, C. & Stroud, K. The Occurrence of Earth-Like Planets Around Other Stars. *ArXiv e-prints* (2014).
- [353] Lored, T. J. Accounting for Source Uncertainties in Analyses of Astronomical Survey Data. In Fischer, R., Preuss, R. & Toussaint, U. V., editors, *American Institute of Physics Conference Series*, volume 735 of *American Institute of Physics Conference Series*, 195–206 (2004).
- [354] Naoz, S., Farr, W. M. & Rasio, F. A. On the Formation of Hot Jupiters in Stellar Binaries. *Astrophys. J. Lett.* **754**, L36 (2012).

- [355] Hogg, D. W., Myers, A. D. & Bovy, J. Inferring the Eccentricity Distribution. *Astrophys. J.* **725**, 2166–2175 (2010).
- [356] Lieu, M. *et al.* Hierarchical inference of the relationship between Concentration and Mass in Galaxy Groups and Clusters. *ArXiv e-prints* (2017).
- [357] Ramírez-Agudelo, O. H. *et al.* The VLT-FLAMES Tarantula Survey. XXI. Stellar spin rates of O-type spectroscopic binaries. *Astron. Astrophys.* **580**, A92 (2015).
- [358] Mirabel, I. F. Formation of black holes in the dark. *ArXiv e-prints* (2016).
- [359] Kalogera, V. Orbital Characteristics of Binary Systems after Asymmetric Supernova Explosions. *Astrophys. J.* **471**, 352 (1996).
- [360] Schutz, B. F. Networks of gravitational wave detectors and three figures of merit. *Class. Quantum Grav.* **28**, 125023 (2011).
- [361] Berry, C. P. L. *et al.* Parameter Estimation for Binary Neutron-star Coalescences with Realistic Noise during the Advanced LIGO Era. *Astrophys. J.* **804**, 114 (2015).
- [362] Apostolatos, T. A., Cutler, C., Sussman, G. & Thorne, K. Spin-induced orbital precession and its modulation of the gravitational waveforms from merging binaries. *PRD* **49**, 6274–6297 (1994).
- [363] Schmidt, P., Ohme, F. & Hannam, M. Towards models of gravitational waveforms from generic binaries: II. Modelling precession effects with a single effective precession parameter. *Phys. Rev. D* **91**, 024043 (2015).
- [364] Finn, L. S. Detection, measurement and gravitational radiation. *Phys. Rev.* **D46**, 5236–5249 (1992).
- [365] Moore, C. J., Cole, R. H. & Berry, C. P. L. Gravitational-wave sensitivity curves. *Class. Quantum Grav.* **32**, 015014 (2015).
- [366] Farr, B., Ochsner, E., Farr, W. M. & O’Shaughnessy, R. A more effective coordinate system for parameter estimation of precessing compact binaries from gravitational waves. *Phys. Rev. D* **90**, 024018 (2014).
- [367] Miller, B., O’Shaughnessy, R., Littenberg, T. B. & Farr, B. Rapid gravitational wave parameter estimation with a single spin: Systematic uncertainties in parameter estimation with the SpinTaylorF2 approximation. *Phys. Rev. D* **92**, 044056 (2015).

- [368] Veitch, J., Pürrer, M. & Mandel, I. Measuring Intermediate-Mass Black-Hole Binaries with Advanced Gravitational Wave Detectors. *Phys. Rev. Lett.* **115**, 141101 (2015).
- [369] Vallisneri, M. Beyond the Fisher-Matrix Formalism: Exact Sampling Distributions of the Maximum-Likelihood Estimator in Gravitational-Wave Parameter Estimation. *Phys. Rev. Lett.* **107**, 191104 (2011).
- [370] Gerosa, D., Sperhake, U. & Vošmera, J. On the equal-mass limit of precessing black-hole binaries. *Classical and Quantum Gravity* **34**, 064004 (2017).
- [371] MacKay, D. J. C. *Information Theory, Inference and Learning Algorithms*. Cambridge University Press, Cambridge (2003).
- [372] Foreman-Mackey, D., Hogg, D. W., Lang, D. & Goodman, J. emcee: The MCMC Hammer. *Publications of the Astronomical Society of the Pacific* **125**, 306–312 (2013).
- [373] Goodman, J. & Weare, J. Ensemble samplers with affine invariance. *Communications in Applied Mathematics and Computational Science* **5**, 65–80 (2010).
- [374] Vitale, S. *et al.* Parameter estimation for heavy binary-black holes with networks of second-generation gravitational-wave detectors. *Phys. Rev.* **D95**, 064053 (2017).
- [375] Reisswig, C. *et al.* Gravitational-wave detectability of equal-mass black-hole binaries with aligned spins. *Phys. Rev. D* **80**, 124026 (2009).
- [376] Farr, W. M., Kremer, K., Lyutikov, M. & Kalogera, V. Spin Tilts in the Double Pulsar Reveal Supernova Spin Angular-Momentum Production. *Astrophys. J.* **742**, 81 (2011).
- [377] Gerosa, D. & Berti, E. First or second generation? Black hole census with gravitational wave observations. *ArXiv e-prints* (2017).
- [378] Fishbach, M., Holz, D. & Farr, B. Are LIGO’s Black Holes Made From Smaller Black Holes? *ArXiv e-prints* (2017).
- [379] Lipunov, V. M., Postnov, K. A. & Prokhorov, M. E. Formation and coalescence of relativistic binary stars: the effect of kick velocity. *Mon. Not. R. Astron. Soc.* **288**, 245–259 (1997).

- [380] Taracchini, A. *et al.* Effective-one-body model for black-hole binaries with generic mass ratios and spins. *Phys. Rev. D* **89**, 061502 (2014).
- [381] King, A. R. & Kolb, U. The evolution of black hole mass and angular momentum. *Mon. Not. Roy. Astron. Soc.* **305**, 654–660 (1999).
- [382] Podsiadlowski, P., Rappaport, S. & Han, Z. On the formation and evolution of black hole binaries. *Mon. Not. Roy. Astron. Soc.* **341**, 385–404 (2003).
- [383] Zaldarriaga, M., Kushnir, D. & Kollmeier, J. A. Research Note: The Expected Spins of Gravitational Wave Sources With Isolated Field Binary Progenitors. *ArXiv e-prints* (2017).
- [384] Hotokezaka, K. & Piran, T. Implications of the low binary black hole spins observed by LIGO. *ArXiv e-prints* (2017).
- [385] Bogdanović, T., Reynolds, C. S. & Miller, M. C. Alignment of the Spins of Supermassive Black Holes Prior to Coalescence. *Astrophys. J. Lett.* **661**, L147–L150 (2007).
- [386] Albrecht, S. *et al.* The BANANA Project. V. Misaligned and Precessing Stellar Rotation Axes in CV Velorum. *Astrophys. J.* **785**, 83 (2014).
- [387] Martin, R. G., Tout, C. A. & Pringle, J. E. Alignment time-scale of the microquasar GRO J1655-40. *Mon. Not. Roy. Astron. Soc.* **387**, 188–196 (2008).
- [388] Morningstar, W. R. & Miller, J. M. The Spin of the Black Hole 4U 1543-47. *Astrophys. J. Lett.* **793**, L33 (2014).
- [389] Farr, W. M., Kremer, K., Lyutikov, M. & Kalogera, V. Spin Tilts in the Double Pulsar Reveal Supernova Spin Angular-momentum Production. *Astrophys. J.* **742**, 81 (2011).
- [390] Abbott, B. P. *et al.* Effects of waveform model systematics on the interpretation of GW150914. *ArXiv e-prints* (2016).
- [391] Abbott, B. P. *et al.* Directly comparing GW150914 with numerical solutions of Einstein’s equations for binary black hole coalescence. *Phys. Rev. D* **94**, 064035 (2016).